8-2022

A Comparison of Relict and Active Terrestrial Patterned Ground as an Analog for Mars

John Paul Knightly Jr.
University of Arkansas, Fayetteville

Citation

Knightly, J. P. (2022). A Comparison of Relict and Active Terrestrial Patterned Ground as an Analog for Mars. *Graduate Theses and Dissertations* Retrieved from https://scholarworks.uark.edu/etd/4595

A Comparison of Relict and Active Terrestrial Patterned Ground as an Analog for Mars

A dissertation submitted in partial fulfillment
of the requirements for the degree of
Doctor of Philosophy in Space and Planetary Sciences

by

John Paul Knightly Jr
Wichita State University
Bachelor of Science in Geology, 2013

August 2022
University of Arkansas

This dissertation is approved for recommendation to the Graduate Council.

Vincent Chevrier, Ph.D.
Dissertation Director

John Dixon, Ph.D.
Committee Member

Larry Roe, Ph.D.
Committee Member

Jason Tullis, Ph.D.
Committee Member

Abstract

Patterned ground is a ubiquitous landform in periglacial regions of Earth and is also present across the mid to high latitudes of Mars. The association of terrestrial patterned ground to the presence of subsurface water ice in the form of permafrost that develops a seasonal ‘wet’ active layer during the summer thaw prompted further investigation of patterned ground on Mars. The Phoenix spacecraft was sent to the surface of the north polar plains of Mars to investigate an area of patterned ground where water ice was predicted to occur. The confirmation of subsurface water ice at the Phoenix landing site confirmed the hypothesis that water ice and patterned ground on Mars are intricately linked, however outstanding questions remain regarding the mode of formation of martian patterned ground. Dry modification via sublimation and thermal-driven processes are possible under present-day climate conditions, however warmer climate conditions are predicted to have occurred during past periods of high obliquity and could have supported periglacial freeze-thaw modification of patterned ground on Mars. Understanding the extent to which liquid water may have been available in the recent geological history of Mars is important to constraining past habitability as well as identifying resources for future long-duration human exploration. It is suggested that if patterned ground on Mars experienced periglacial modification in the past, then it currently exists in a relict form. This research examines the morphometry and surface roughness parameters of active and relict terrestrial patterned ground sites in conjunction with evaluations of martian patterned ground to identify parameters that may assist with ongoing efforts to determine the age and modes of historical modification of patterned ground on Mars.

Acknowledgements

Funding for field work conducted in the Westfjords and Highlands of Iceland in 2019 was received through a Transnational Access Grant and the Europlanet 2020 Research Initiative, funded by the European Union's Horizon 2020 Research and Innovation Program under grand agreement No. 654208.

Funding for field work conducted at Haughton Crater on Devon Island in Nunavut, Canada in 2017 was received through the Mars Society's Mars 160 Twin Analog Mission Simulation. In addition, the Devon Island field work was performed on ancestral Inuit land and received permission through the Qikiqtani Inuit Association to conduct field work via Certificate of Exemption Q17X014. Minimal disturbance was required to collect samples and collect in-situ measurements and all work areas were restored to their prior condition following the completion of site investigation activities, adhering to the terms and conditions of the Inuit Owned Land access agreement.

Thank you to my committee for their input, guidance, and support while conducting this research and writing my dissertation. I took a non-traditional path through the program and I thank you for trusting me as I undertook this journey.

Thank you to the Mars 160 Crew and The Mars Society for providing me with the opportunity to participate in the Mars 160 Twin Analog Mission Simulation. The mission ignited an interest in conducting further analog field work that served as the basis for the remaining research discussed in this dissertation.

Thank you to my friends in the program, who have helped navigate the ups and downs associated with graduate school as well as making memories that will last a lifetime.

Thank you to my parents for their love and support over the years and for fostering, encouraging, and supporting my love for science over the years.

Finally, I want to thank my wife, Jessica, for her love and support throughout the past several years. I know the weeks (and sometimes months) away from home while collecting field

data were difficult, but the juice was worth the squeeze. Getting to this point has been two decades in the making with some detours along the way, including navigating a challenging work-life balance the past year and a half as I’ve been finishing my research while working full time, but we’ve made it work. I wouldn’t trade where we are today for anything, and I’m excited to see where life takes us as one chapter closes and a new one begins. I truly would not have made it this far without you!

Dedication

To Jessica, Judah, and to my parents, for their love and support all these years. This is for you.

Table of Contents

List of Figures

Chapter 1

Chapter 2

Figure 2-8: Integral image concept and examples of surface roughness under different scenarios. Images A) and B) show a patterned ground survey performed at 7.5 m agl where r_f = 3 in A) and r_f = 100 in B). Images C) and D) represent a different survey area, where data at C) was collected at 7.5 m agl and r_f = 100 and D) was collected over the same area at 85 m agl with the same *rf* = 100.

Figure 2-9: North Pole Pass survey area locations viewed at ground level. NPP-2 (A) had the smallest distance between polygon centers and margins. A cirque is visible along a mountain across the valley looking west from NPP-2. The surface morphology at NPP-4 (images B and C) is representative of the morphology across much of the North Pole Pass area, with vegetated centers hosting grasses and alpine vegetation and largely vegetation-free margins composed of large granitic boulders. NPP-7 (D) was heavily vegetated with hummocks obscured by vegetation growth.

Figure 2-10: From left to right, the NPP-1 orthomosaic, MSR rf=5, survey DTM, and MSR r_f =100 raster outputs. I, and roughness vs r_f (scale) plot. Surface roughness variations between polygon centers, borders, and margins are less apparent however the provincial differences are apparent in the survey DTM. NPP-1 had one of the lower distributions of vegetation across polygon high centers. Soil horizons, where present, are thin enough to permit the topographic expression of underlying boulders in the DTM, which is subsequently reflected in the MSR analysis.

Figure 2-11: From left to right, the NPP-5 orthomosaic, MSR rf=3, survey DTM, and MSR r_f =100 raster outputs. The difference in surface roughness between polygon centers, borders, and margins is maintained at scale in both MSR raster outputs and the survey DTM. The difference in roughness is the result of grass, alpine vegetation, and underlying soil that has established on the polygon high centers. Pore space between large boulders that comprise the borders and margins supports a high transmissivity environment permiting perched water flow during the summer that has potentially prevented the establishment of vegetation along margins over the short-term.

Figure 2-12: Flateyri Patterned Ground (FPG) survey area locations viewed at ground level. Vegetation-dense margins and vegetation free centers at FPG-1 (A) contrast with vegetation-free margins and vegetation-dense centers at FPG-3 (B). Stone stripes (C) and hummocks (D) were present but less common observed morphologies. Morphological variation appeared to be partially controlled by compositional differences in local bedrock. Cairns, posts, and remnant telecommunications lines visible at FPG-1 & 3 and other sites appeared to previously support a telegraph or phone line before falling into disservice. The use of cairns rather than setting the posts in ground could indicate the presence of permafrost in the past.

Figure 2-13: Projected depth to frost line based on subsurface temperature measurements at the Flateyri patterned ground site compared to temperature measurements and permafrost depth in patterned ground on Devon Island. Trenching was only possible to 0.5 m depth at Flateyri due to encountering large boulders that limited excavating deeper with the available equipment.

Figure 2-14: Examples of microsorting in FPG polygons. Intra-polygon microsorting of larger gravels and small boulders was visible in some polygon centers at FPG-1 and other sites (A). Microsorting of small gravels was also observed in vegetation-free polygons at several sites, including FPG-X25 as shown in B-D. The small gravels in the dark centers were covered in reddish-brown clay indicating the sorting had occurred recently, potentially in response to seasonal or diurnal freeze-thaw cycles. Notably, only small round to subrounded gravels were observed in the darker material of the microsorted centers. Angular clasts were rare to absent in the dark microsorted centers that were examined.

Figure 2-15: Orthomosaic, DTM, and MSR raster images for the FPG-5 survey area. The small variation of surface roughness observed between hummock centers and margins is attributed to the relatively homogeneous composition of large clasts across centers and margins.

Figure 2-16: Orthomasic, DTM, and MSR raster images for the FPG-3 survey area. Polygons at FPG-3 were typical of the broader stone circle population that was characterized at Flateyri. Polygon high centers are prominently visible in the survey DTM and translates to some features in the resulting MSR analyses. Large rocks along polygon margins are resolved at r_f =3 and blend across the margins at r_f =100. Lower surface roughness parameters in polygon centers are more apparent at r_f =3.

Figure 2-17: Orthomasic, DTM, and MSR raster images for the FPG-X25 survey area. The highest resolution survey of the project was performed at FPG-X25 at 7.5 m agl. Individual rocks down to 0.02 m across are resolved in the resulting DTM and r_f =3 MSR analysis. Visibility of the largest or most prominent rocks carries through to the r_f =100 MSR analysis. Due to the high detection rate of smaller rocks and gravels in polygon centers, the difference in roughness between centers and margins becomes more visually apparent at higher r_f values.

Figure 2-18: Orthomasic, DTM, and MSR raster images for the FPG-7 survey area. Despite the high level of organization and presence of visible polygonal boundaries between the stone circles at FPG-7 in the survey orthoimagery and DTM, the corresponding surface roughness parameters are comparable to observations of other stone circle populations surveyed at Flateyri.

Figure 2-19: Orthomasic, DTM, and MSR raster images for the FPG-6B survey area. The tight concentration of larger gravels and boulders along polygon margins visible in survey orthoimagery is visible in the MSR analysis at r_f =3, however the roughness variation becomes less apparent at r_f =100.

Figure 2-20: Examples of surface morphology at Highlands polygon (HPOLY) survey areas. Most ice-wedge polygons (IWP) were composed of gravels emplaced by the nearby Blanda River to the west, evident in images A and B and visible between vegetation in image C. IWP margins were frequently the only or most vegetated portions of each survey area, as seen in at HPOLY-5 in A. Lichen mats were the most common on less vegetated sites and became more prevalent across IWP centers as vegetation became more well-established (HPOLY-7 and HPOLY-11, B and C respectively). Alpine vegetation (C) and grasses (D) become more commonplace with the progression of pedogenesis. The topographic variation between IWP centers and margins was also observed to increase in proportion to vegetation coverage and a probable corresponding increase in the erosion of associated soils.

Figure 2-21: Orthomasic, DTM, and MSR raster images for the HPOLY-1 survey area. Topographic variations across polygon margins are reflected in the DTM and in each MSR raster. Roughness magnitudes are observed to increase significantly with scale (r_f =100) along polygon margins. While vegetation and lichen mats are present across polygon centers and margins within the survey area and produce some elevated roughness measurements, the greatest variation in roughness is in areas where topographic variations are also present.

Figure 2-22: Orthomasic, DTM, and MSR raster images for the HPOLY-6 survey area. While lichen mats are prevalent along polygon margins, this does not result in widescale representations in the DTM or MSR r_f =3 raster. When the r_f is increased to 100, a slight increase in surface roughness magnitude is obeserved along some margins, but the trend is not ubiquitous. In contrast to other Highlands survey areas with larger roughness magnitudes on the margins, this suggests that topographic variations along the margins (i.e. downcutting and degradation) provide a larger overall contribution to margin roughness parameters than vegetation or lichens alone.

Figure 2-23: Size distribution of patterned ground by population. The ice wedge polygons were the largest features surveyed at approximately 20 to 30 m in size, followed by patterned ground at North Pole Pass at approximately 4 to 12 m in size. Patterned ground at the Flateyri site was generally between approximately 1 to 2.5 m in size.

Figure 2-24: Circularity distribution of patterned ground by population. Despite the differences in size presented in Figure 23, the NPP and FPG-5 hummocks shared the highest degree of circularity among the characterized populations. The FPG-7 stone polygons had the highest circularity of observed populations. The high vegetation ice wedge polygons in the highlands were observed to be slightly less circular than low vegetation polygons, which may be the result of topographic variations that permit vegetation growth.

Figure 2-25. Comparison of hummocky patterned ground populations between the North Pole Pass, U.S.A. and Flateyri, Iceland sites. Feature circularity was found to decrease in response to a corresponding increase in feature size at both sites.

Figure 2-26. Comparison of low vegetation and high vegetation ice wedge polygons in the Highlands, Iceland. Feature circularity was found to decrease in response to a corresponding increase in feature size among low vegetation polygons.

Figure 2-27: Polygon orientation rose diagrams. Row 1: The orientation of the DTM and vegetation-defined hummocks at North Pole Pass (NPP-DTM and NPP-Veg) are compared to the hummocks at FPG-5. Row 2: The orientation of the broader stone circle population at the Flateyri site (FPG-SC) are compared to stone circles delineated at the FPG-X25 survey and the stone stripes at FPG-6B. Row 3: The orientation of the stone polygons at FPG-7 are compared to low vegetation and high vegetation polygons at the Highlands site (HPOLY-LV and HPOLY-HV).

Figure 2-28: Surface roughness of patterned ground by population. The greatest surface roughness was observed in hummocks at NPP. While the NPP hummocks had a higher surface roughness relative to FPG-5, the FPG-5 hummocks had the greatest surface roughness among the FPG sites. The high-resolution survey at FPG-X25 resulted in higher surface roughness parameters relative to other stone circles at FPG, potentially resulting from the detection of smaller gravels across feature centers. High-vegetation IWPs at the HPOLY site had a higher surface roughness relative to low-vegetation IWPs.

Figure 2-29: Multiscale surface roughness analysis summary of patterned ground populations, with surface roughness displayed in relationship to the cell neighborhood filter radius (r_f). Within most populations, patterned ground centers had consistently lower surface roughness values (smoother) in comparison to higher surface roughness values among feature borders and margins (rougher). This relationship was less conclusive among lower resolution surveys (e.g. Stone Circles, Stone Polygons). Among the FPG-5 hummocks, the relationship is inconclusive due to the low spatial resolution of the survey and the homogeneous distribution of boulders spread throughout hummock centers and margins.

Figure 2-30: Multiscale surface roughness analysis summary of IWPs at the HPOLY site. Despite homogeneous composition and low topographic expression at the surface, vegetation-dense margins and centers exhibited higher surface roughness values relative to low-vegetation centers.

Figure 2-31: Correlation matrix for the evaluated terrestrial patterned ground morphologies. The most common positive correlation was among size-dependent variables including calculated size, length, and width. Circularity was found to be negatively correlated with length and size at some sites, which may be expected as longer patterned ground forms such as stone stripes or nets are typically more oblong.

Figure 2-32: Summary of the PCA for the DTM-defined NPP hummocks. There is a slight positive correlation between feature width and length. Factor scores for the MSR analysis of polygon regions reflect the consistently higher surface roughness values in polygon margins and lower surface roughness values in polygon centers.

Figure 2-33: Summary of the PCA for the Vegetation-defined NPP hummocks. There is a slight positive correlation between feature length and size. Factor scores for the MSR analysis of polygon regions reflect the consistently higher surface roughness values in polygon borders and lower surface roughness values in polygon centers.

Figure 2-34: Summary of the PCA for the FPG Stone Circles population. There is a slight positive correlation between feature width and length. Factor scores for the MSR analysis of polygon regions reflect the consistently higher surface roughness values in polygon margins and lower surface roughness values in polygon centers.

Figure 2-35: Summary of the PCA for the FPG Stone Circles population at FPG-X25. There is a slight positive correlation between feature size, width, and length. Factor scores for the MSR analysis of polygon regions reflect the consistently higher surface roughness values in polygon margins and lower surface roughness values in polygon centers.

Figure 2-36: Summary of the PCA for the FPG Stone Circles population at FPG-X25. There is a slight positive correlation between feature size, width, and length. Factor scores for the MSR analysis of polygon regions reflect the consistently higher surface roughness values in polygon margins and lower surface roughness values in polygon centers.

Chapter 3

Figure 3-1. The locations of HiRISE stereo-pair images that were transformed into digital terrain models. Sites were selected based on the presence of patterned ground with consideration for the potential applicability of the sites for future studies.

Figure 3-2: Key site metadata including site location coordinates, HiRISE image identifiers, population categories, and number of features delinated in each population. ND = nondifferentiated population.

Figure 3-3. (Left-right/top-bottom). HiRISE image and HiRISE DTM-derived shaded relief, slope, aspect, and surface roughness at focal radii of 5 and 100 at Copais Palus. Variations between polygon centers and margins are not visually apparent in the DTM-derived raster datasets.

Figure 3-4. Distribution of polygon long-axis orientations within each population. The red line indicates the mean slope aspect of each population. Orientation trends are apparent at several locations, oftentimes with feature long-axis orientations orthogonal to slope aspect.

Figure 3-5: MSR plot for the polygon centers and margins at Copais Palus. Polygon centers have a smoother roughness profile when compared to the adjacent margins.

Figure 3-6. Copais Palus polygons PCA scree plot and variable loading biplot. There are positive correlations between feature size and length. Slope and roughness (rf = 5) are positively correlated but inversely related to length and size.

Figure 3-7. Comparison of correlation matrix plots for polygon populations at the ten evaluated sites on Mars. The nearly ubiquitous 1:1 positive correlation between length and size provides a test of correlation quality as length and size are expected to increase in parallel. While expected, strong positive correlations between feature slope and surface roughness are common but not universal.

Figure 3-8. (Left-right/top-bottom). HiRISE image and HiRISE DTM-derived shaded relief, slope, aspect, and surface roughness at focal radii of 10 and 100 at Deuteronlius Mensae. Variations between polygon centers and margins are visually apparent in several of the DTM-derived raster datasets.

Figure 3-9: MSR plot for the polygon centers and margins at Deuteronlius Mensae. Polygon centers have a rougher surface when compared to the adjacent margins.

Figure 3-10. Deuteronlius Mensae polygons PCA scree plot and variable loading biplot. There are positive correlations between feature slope and roughness (rf = 10). Length and size are positively correlated but inversely related to slope and roughness.

Figure 3-11. (Left-right/top-bottom). HiRISE image and HiRISE DTM-derived shaded relief, slope, aspect, and surface roughness at focal radii of 5 and 100 at Lethe Vallis. Variations between polygon centers and margins are not visually apparent in the DTM-derived raster datasets.

Figure 3-12: MSR plot for the polygon centers and margins at Lethe Vallis. There is not a significant observable difference in surface roughness between centers and margins, however centers average slightly smoother than the adjacent margins.

Figure 3-13. Lethe Vallis polygons PCA scree plot and variable loading biplot. There are positive correlations between feature size and length, followed by slope and roughness (rf = 5).

Figure 3-14. (Left-right/top-bottom). HiRISE image and HiRISE DTM-derived shaded relief, slope, aspect, and surface roughness at focal radii of 5 and 100 near Lyot Crater. Variations between polygon centers and margins are visually apparent in the DTM-derived raster datasets.

Figure 3-15. (Left-right/top-bottom). HiRISE image and HiRISE DTM-derived shaded relief, slope, aspect, and surface roughness at focal radii of 5 and 100 near Lyot Crater. Variations between polygon centers and margins are not visually apparent in the DTM-derived raster datasets.

Figure 3-16: MSR plot for the polygon centers and margins near Lyot Crater. Large polygon centers have a significantly higher surface roughness relative to the adjacent margins. In contrast, small polygon centers have a lower surface roughness relative to the adjacent margins.

Figure 3-17. Lyot Crater large polygons PCA scree plot and variable loading biplot. There are positive correlations between feature size, length, and orientation. Feature slope, aspect, and roughness (rf = 10) are positively correlated but inversely related to feature size.

Figure 3-18. Lyot Crater small polygons PCA scree plot and variable loading biplot. There are positive correlations between feature size and length. Slope and roughness (rf = 10) are positively correlated but inversely related to size and length.

Figure 3-19. (Left-right/top-bottom). HiRISE image and HiRISE DTM-derived shaded relief, slope, aspect, and surface roughness at focal radii of 5 and 100 at Malea Planum. Variations between polygon centers and margins are visually apparent in the DTM-derived raster datasets. Small incised polygons are visible within the large polygon centers.

Figure 3-20. (Left-right/top-bottom). HiRISE image and HiRISE DTM-derived shaded relief, slope, aspect, and surface roughness at focal radii of 5 and 100 at Malea Planum. Variations between polygon centers and margins are not visually apparent in the DTM-derived raster datasets.

Figure 3-21: MSR plot for the polygon centers and margins at Malea Planum. Large polygon centers have a lower surface roughness relative to the adjacent margins. Small incised polygons centers have a higher surface roughness relative to the adjacent margins. There is no difference in surface roughness between the small non-incised (regular) polygons.

Figure 3-22. Malea Planum large polygons PCA scree plot and variable loading biplot. There are positive correlations between feature slope, orientation, and roughness (rf = 10). Feature size and length are positively correlated but negatively correlated to slope, orientation, and roughness. Relationships with orientation and aspect may be biased as most features were selected on a southward facing slope along the channel.

Figure 3-23. Malea Planum small incised polygons PCA scree plot and variable loading biplot. There are positive correlations between feature size and length. Slope and roughness (rf = 10) are positively correlated but negatively correlated to size and length. Relationships to orientation and aspect may be biased as most features were selected on a southward facing slope along the channel.

Figure 3-24. Malea Planum small non-incised (regular) polygons PCA scree plot and variable loading biplot. There are positive correlations between feature size and length, followed by slope and roughness (rf = 10). Relationships to feature orientation and aspect may be biased as many features were selected on a southward facing slope near the channel.

Figure 3-25. (Left-right/top-bottom). HiRISE image and HiRISE DTM-derived shaded relief, slope, aspect, and surface roughness at focal radii of 10 and 100 at Utopia Planitia. Variations between polygon centers and margins are visually apparent in the DTM-derived raster datasets.

Figure 3-26. (Left-right/top-bottom). HiRISE image and HiRISE DTM-derived shaded relief, slope, aspect, and surface roughness at focal radii of 10 and 100 at Utopia Planitia. Variations between polygon centers and margins are visually apparent in some of the DTM-derived raster datasets.

Figure 3-27: MSR plot for the polygon centers and margins at Utopia Planitia. Both large and small polygon centers had a lower surface roughness relative to the adjacent margins.

Figure 3-28. Utopia Planitia large polygons PCA scree plot and variable loading biplot. With the exception of feature orientation, there are positive correlations among all assessed variables, including roughness (rf = 10). The most likely explanation is that the large polygons at Utopia Planitia are topographically prominent and are distinctly visible in HiRISE DTMs.

Figure 3-29. Utopia Planitia small polygons PCA scree plot and variable loading biplot. There are positive correlations between feature length and size. Slope and roughness (rf = 10) are positively correlated but inversely correlated to length and size. While visually distinct, the small polygons are not as topographically prominent as the larger parent polygons and are not as distinctly visible in HiRISE DTMs.

Figure 3-30. (Left-right/top-bottom). HiRISE image and HiRISE DTM-derived shaded relief, slope, aspect, and surface roughness at focal radii of 5 and 100 at Utopia Rupes Site 1. Variations between polygon centers and margins are visually apparent in several of the DTM-derived raster datasets.

Figure 3-31. (Left-right/top-bottom). HiRISE image and HiRISE DTM-derived shaded relief, slope, aspect, and surface roughness at focal radii of 5 and 100 at Utopia Rupes Site 1. Variations between polygon centers and margins are not visually apparent in the DTM-derived raster datasets.

Figure 3-32: MSR plot for the polygon centers and margins at the Utopia Rupes Site 1. Large polygon centers have a lower surface roughness relative to the adjacent margins. There is no difference in surface roughness between the small polygon centers and margins.

Figure 3-33. Utopia Rupes Site 1 large polygons PCA scree plot and variable loading biplot. There are positive correlations between feature slope and roughness (rf = 10). Length and size are positively correlated but inversely related to aspect, slope, and roughness.

Figure 3-34. Utopia Rupes Site 1 small polygons PCA scree plot and variable loading biplot. There are positive correlations between feature size and length, followed by slope and aspect. Roughness (rf = 10) is orthogonal to slope/aspect and size/length.

Figure 3-35. (Left-right/top-bottom). HiRISE image and HiRISE DTM-derived shaded relief, slope, aspect, and surface roughness at focal radii of 5 and 100 at Utopia Rupes Site 2. Variations between sorted boulder centers and margins are visually apparent in some of the DTM-derived raster datasets.

Figure 3-36. (Left-right/top-bottom). HiRISE image and HiRISE DTM-derived shaded relief, slope, aspect, and surface roughness at focal radii of 5 and 100 at Utopia Rupes Site 2. Variations between polygon centers and margins are not visually apparent in the DTM-derived raster datasets.

Figure 3-37. (Left-right/top-bottom). HiRISE image and HiRISE DTM-derived shaded relief, slope, aspect, and surface roughness at focal radii of 5 and 100 at Utopia Rupes Site 2. Variations between polygon centers and margins are visually apparent in some of the DTM-derived raster datasets.

Figure 3-38: MSR plot for the polygon centers and margins at Utopia Rupes Site 2. Large polygon centers have a lower surface roughness than the adjacent margins. Sorted boulder centers have a higher surface roughness than the adjacent margins. There was no significant difference in surface roughness between small polygon centers and margins.

Figure 3-39. Utopia Rupes Site 2 sorted boulders PCA scree plot and variable loading biplot. There are positive correlations between feature size and length. Slope and roughness (rf = 10) are positively correlated but inversely related to size and length.

Figure 3-40. Utopia Rupes Site 2 small polygons PCA scree plot and variable loading biplot. There are positive correlations between feature roughness (rf = 10), slope, circularity, orientation, and aspect. Length and size are positively correlated but inversely related to the other assessed variables.

Figure 3-41. Utopia Rupes Site 2 large polygons PCA scree plot and variable loading biplot. There are positive correlations between feature length, size, and aspect. Slope and roughness (rf = 10) are positively correlated but negatively correlated to length, size, and aspect.

Figure 3-42. (Left-right/top-bottom). HiRISE image and HiRISE DTM-derived shaded relief, slope, aspect, and surface roughness at focal radii of 5 and 100 at Vastitas Boreals. Variations between polygon centers and margins are not visually apparent in the DTM-derived raster datasets.

Figure 3-43: MSR plot for the polygon centers and margins at Vastitas Borealis. There is no significant difference in surface roughness between polygon centers and the adjacent margins.

Figure 3-44. Vastitas Borealis Site 1 polygons PCA scree plot and variable loading biplot. Feature size and length are positively correlated but negatively related to slope. Slope and roughness (rf = 10) are positively correlated.

Figure 3-45. (Left-right/top-bottom). HiRISE image and HiRISE DTM-derived shaded relief, slope, aspect, and surface roughness at focal radii of 5 and 100 at the *Phoenix* Landing Site in Vastitas Borealis. Variations between polygon centers and margins are not visually apparent in the DTM-derived raster datasets. Small polygons (not delineated in this figure) are inset on the larger polygons delineated in this figure.

Figure 3-46: MSR plot for the polygon centers and margins at the *Phoenix* Landing Site in Vastitas Borealis. Large polygon centers have a lower surface roughness relative to the adjacent margins. Small polygon centers have a higher surface roughness relative to the adjacent margins.

Figure 3-47. Vastitas Borealis Site 2 *(Phoenix* landing site) large polygons PCA scree plot and variable loading biplot. There are positive correlations between feature size and length. Slope and roughness (rf = 5) are positively correlated and related to feature size but negatively related to feature length.

Figure 3-48. Vastitas Borealis Site 2 (*Phoenix* landing site) small polygons PCA scree plot and variable loading biplot. There are positive correlations between feature slope and roughness (rf = 5). Length and size are positively correlated but inversely related to slope and roughness.

Figure 3-49. Top row: size distribution histograms of patterned ground near the *Phoenix* landing site. Bottom row: size vs. circularity of patterned ground near the landing site. Right: Image of subdued patterned ground from the *Phoenix* lander (Image: PIA10690).

Chapter 4

Figure 1 – Haughton Impact Structure and Study Area Location. Overview of the 2017 field season study locations within and near the Haughton Impact Structure relative to FMARS. Abbreviations: DS = Datalogger Station. FMARS = Flashline Mars Arctic Research Station. PAS = *Phoenix* Analog Site. PS = Polygon Site.

Figure 2 – Datalogger Station and Slopewash Streak Locations. A.) Zoomed in view from an aerial photo of Station 1 and the approximate locations of probe deployment locations 1A and 1B. Displaced soil from the installation and retrieval of the dataloggers is visible near the indicated points. B.) Zoomed in view of Station 2 and the approximate locations of probe deployment points 2A and 2B. A rock cairn that was supporting the datalogger station is visible between the indicated points. C.) View of the datalogger monitoring site and the positions of Stations 1, 2, and 3. Station 3 collected atmospheric background measurements between Stations 1 and 2. The proximity of slopewash streaks originating upgradient of the datalogger stations is apparent, with Station 1 located outside of a slopewash pathway and Station 2 located in the middle of a slopewash streak.

Figure 3 – *Phoenix* Analog Sites (PAS). The morphological similarities of PAS 1, 2, 3 to the *Phoenix* landing site. While the hummocks observed within the Haughton Impact Structure of approximately similar dimensions to the hummocks observed near the *Phoenix* lander, the small-scale patterned ground observed within the crater was overwhelmingly composed of larger-grained gravels with interstitial sand relative to finer-grained regolith observed on Mars.

Figure 4 – Polygon Site 1 (PS-1) satellite image (A) and ground-level photo taken from near the middle of the site (B). PS-2 satellite image (C) and ground level photo of subdued polygons taken from a distal portion along the northwest margin of the site. Ground-level photos of polygons at PS-2 (D). PS-3 aerial photo captured on the departure flight from Devon Island on 17 August 2017 (E). While no ground-level photos were acquired of PS-3, it is likely that polygon morphology at the surface resembles a combination of the PS-2 polygons in image (D) and subdued polygons along a distal portion of the PS-1 site (F).

Figure 5 – Datalogger Station Configurations and Schematic. Final deployment configurations of Stations 1, 2, and 3. An annotated idealized station configuration highlighting the components of the datalogger setup.

Figure 6 – Wet vs Dry Comparison of Datalogger Station 1. A.) Image captured on 3 July of the Station 1 location prior to datalogger deployment. Residual snow is visible at the surface near the station deployment location and the slopewash streaks are prominently visible. B.) Image captured on 17 August following the retrieval of the dataloggers. All remaining snow near the dataloggers has melted and while still visible, the slopewash streaks have started to lighten in appearance due to reduced water flow.

Figure 7 – Histograms for the datalogger sites (DS-1 and DS-2; top row) and ice-wedge polygon sites (PS-1, PS-2, and PS-3; bottom row).

Figure 8 – Patterned Ground Soil Temperature. Datalogger temperature observations from Stations 1 and 2. Diurnal temperature trends are evident and there was an approximately 5 to 7

hour lag in temperature response between atmospheric fluctuations detected at the surface and the corresponding temperature change from the temperature sensors at the active layer-permafrost boundary approximately 0.35 to 0.45 meters bgs. The final drop in air temperature prior to retrieval represents the passage of a cold front that brought temperatures below zero for the only sustained period of the study.

Figure 9 – Patterned Ground Soil Moisture Content. Datalogger moisture observations from Stations 1 and 2 relative to atmospheric relative humidity. All of the soil moisture dataloggers recorded saturated conditions of approximately 0.37 to 0.40 mm^3/mm^3 for the majority of the observational period. Fluctuations at Station 2 represent an influx of water moving downgradient along a slopewash streak during a rain event on 22 July.

Figure 10 – Trench Temperature Gradients. A comparison of the observed temperature profiles in trenches excavated at PAS-3 and Polygon Site 1. Over the relatively small depth interval, the temperature profiles follow a nearly linear trend from the surface to the permafrost contact with the active layer.

Figure 11 – Polygon Site 1 Morphology. A.) Several polygons are visible extending from the foreground towards the horizon. Ponding water is visible in the polygon margin (trough) on the left-hand side of the image. Mars 160 crew member Anastasiya Stepanova for scale. B.) Subdued polygon morphology along a distal portion of the site. C.) View looking southeast towards the northern margin of Polygon A – the primary polygon that was the target of trenching and sampling activities. D.) View looking northeast across the center of Polygon A. Small dessication polygons are visible across the surface and were ubiquitous across the observed polygon centers. Vegetation was prevalent throughout the polygon site.

Figure 12 – Polygon Site 1 Trenching and Sampling Photos. A.) Trench excavated into the center of Polygon A and the collection of sample PSA-P1. Permafrost contact at 0.5 m bgs. B.) Trench excavated in the trough north of Polygon A and the collection of sample PSA-P4. Permafrost contact at 0.5 m bgs. C.) Trench excavated along the marginal slope leading from the Polygon A center towards the northern trough. The permafrost contact reflected the ground surface gradient and maintained a consistent, curved profile approximately 0.5 to 0.55 m bgs across the trench. D.) The location of sample PSA-P6 with the Hanna temperature/electrical conductivity and Kelway pH probes shown in a deployed configuration collecting in-situ measurements.

Figure 13 – Thermal Properties (Lab Measured) Relative to Feature Morphology. The distribution of laboratory measured thermal properties of samples collected at patterned ground and ice-wedge polygon locations within the Haughton Impact Structure. While the general distribution of laboratory-measured thermal properties could remain similar relative to theoretical field-measured thermal properties, the exact values will differ due to variations in moisture content, pore space (soil compaction), and prevailing environmental conditions at the time of measurement, including atmospheric temperature and relative humidity. While no firm conclusions can be derived from this dataset in its present form, it is hoped that by making the data freely available it can serve as a comparative dataset to future field-collected measurements or provide input values for future modeling efforts. Tabulated data is presented in full in Appendix A.

Chapter 5

List of Tables

Chapter 2

Chapter 3

Chapter 4

Chapter 1
Introduction

1.0 Introduction

1.1 Patterned Ground on Mars

Patterned ground on Mars has been the subject of frequent investigations over the past two decades. While decameter-scale polygonal terrain with a proposed periglacial origin was resolved in Viking orbiter imagery (Luchitta et al, 1983), it was not until the advent of high spatial resolution imagery from the Mars Orbital Camera (MOC) on Mars Global Surveyor (MGS) that smaller, meter-scale polygons were observed (Hiesinger and Head, 2000; Siebert and Kargel, 2001). The detection of hydrogen bonded to oxygen by the Gamma-Ray Spectrometer on Mars Odyssey (Boynton et al, 2002) further increased interest in studying high-latitude polygons where a suspected connection between the bonded hydrogen and polygons could be indicative of subsurface ice and, potentially, periglacial processes that could indicate the intermittent presence of liquid water. The combination of observed similarities to terrestrial polygons in regions with permafrost and the potential presence of subsurface ground ice touched-off a flurry of investigations into the nature, origin, and distribution of polygons on Mars (Yoshikawa, 2003; Mangold et al, 2004; Burr et al, 2005; Mangold, 2005). The trajectory of polygon investigations were mutually influenced by the results of studies that suggested gullies and other debris flows were formed by the melting of near-surface ground ice during periods of high obliquity (Costard et al, 2002) which could lead to freeze-thaw modification of polygonal terrains (Burr et al, 2005).

Investigations of Martian polygonal ground reached an apex with the Mars *Phoenix* mission to the northern plains of Vastitas Borealis in 2008, where the selected landing site featured an extensive network of small to medium scale polygons (Mellon et al, 2008). During the arctic summer of Mars Year 29, *Phoenix* excavated several trenches in the vicinity of the spacecraft to study the uppermost layers of regolith (Mellon et al, 2009). The presence of subsurface water ice in the vicinity of the spacecraft was confirmed (Smith et al, 2009) and observed to be present at a mean depth of 4.6 cm (Mellon et al, 2009). Ice exposed to the surface was found to sublimate over several sols in subsequent observations of the trench and found to be in vapor-diffusive equilibrium with a mean atmospheric water content of 3.4 x 10^{19} m^{-3} (Mellon et al, 2009).

Environmental monitoring by *Phoenix* provided insight into the present-day climate conditions at the landing site, examining key variables that would provide context into the potential for periglacial processes during the long arctic summer. While the prevailing climate conditions at the landing site are not suitable for the development of wet active layers (Mellon et al, 2009; Sizemore et al, 2009), analysis of the regolith at the landing site found higher than expected concentrations of perchlorate salts which can lower the eutectic point for water (Hecht et al, 2009; Shaw et al, 2009). The presence of liquid water brine in images of the lander struts has been proposed but never definitively confirmed (Renno et al, 2009). Experimental work with the behavior of brines under Mars conditions has continued, building off observations from the *Phoenix* mission (Bryson et al, 2008; Rivera-Valentin and Chevrier, 2015). The combination of experimental work and observations from *Phoenix* and other surface missions (Martinez et al, 2017) suggest that contemporary wet active layer modification via periglacial processes is unlikely on present-day Mars.

Studies of Martian patterned ground continued following the conclusion of the *Phoenix* mission, enabled by the High Resolution Imaging Science Experiment (HiRISE) on the Mars Reconnaissance Orbiter (MRO), which arrived at Mars two years prior to touchdown of the *Phoenix* lander. The ability of HiRISE to deliver imagery with sub-meter spatial resolution enabled detailed evaluations of the morphological parameters, potential formation mechanisms, and spatial distribution of polygonal terrains at several sites across Mars (e.g. Ulrich et al, 2011; Barrett et al, 2018). Several recurring themes can be found in remote sensing studies of Martian patterned ground throughout this period, including the hypothesis that polygons formed via freeze-thaw (periglacial) processes in a similar manner to terrestrial polygons, despite surface observations from *Phoenix* that are unfavorable to the development of so-called “wet” active layers at high latitudes (including Balme et al, 2013; Soare et al, 2014; Soare et al, 2016). The main pillar of the periglacial hypothesis invokes modeling by Laskar et al (2004) in which the historical obliquity cycle of Mars supported more frequent periods of high obliquity between 5 Ma and 20 Ma, when obliquity averaged 35° relative to averaging 25° over the most recent 5 Ma period. The resulting increase in atmospheric pressure and temperature would be capable of altering the water cycle such that freeze-thaw modification of patterned ground by periglacial processes could be possible.

The utilization of terrestrial analogs has been ubiquitous to nearly every Martian patterned ground investigation, with analog sites spanning the globe from Svalbard to Antarctica. Based on *Phoenix* observations, terrestrial sites located in Antarctica are the most likely to be representative of surface conditions in the recent past on Mars (Figure 1-1, from Marchant and Head, 2007). In Figure 1-1, the hyperarid and cold conditions of the Antarctic Dry Valleys (ADV) provide analogs for surface conditions on ancient Mars under 300 mbar and 100 mbar climate scenarios. The characterization of climate conditions in the ADV led to a handful of analog studies to evaluate the properties of polygonal ground and other potential thaw-related features (Levy et al, 2006; Marchant and Head, 2007; Levy et al, 2010). The results of these studies identified thermal contraction and sublimation-driven processes that are largely equilibrium-driven processes and mirror the equilibrium conditions identified on Mars by *Phoenix* (Mellon et al, 2009). While the ADV sublimation and thermal contraction polygons are largely in equilibrium with their associated microclimates, some modification through excess melting and subsequent freezing is expected. This is supportive of polygonal ground on Mars representing a range of active and relict cold-desert processes.

In contrast with contemporary surface observations from *Phoenix*, computational modeling suggests that environmental conditions favorable to freeze-thaw modification of

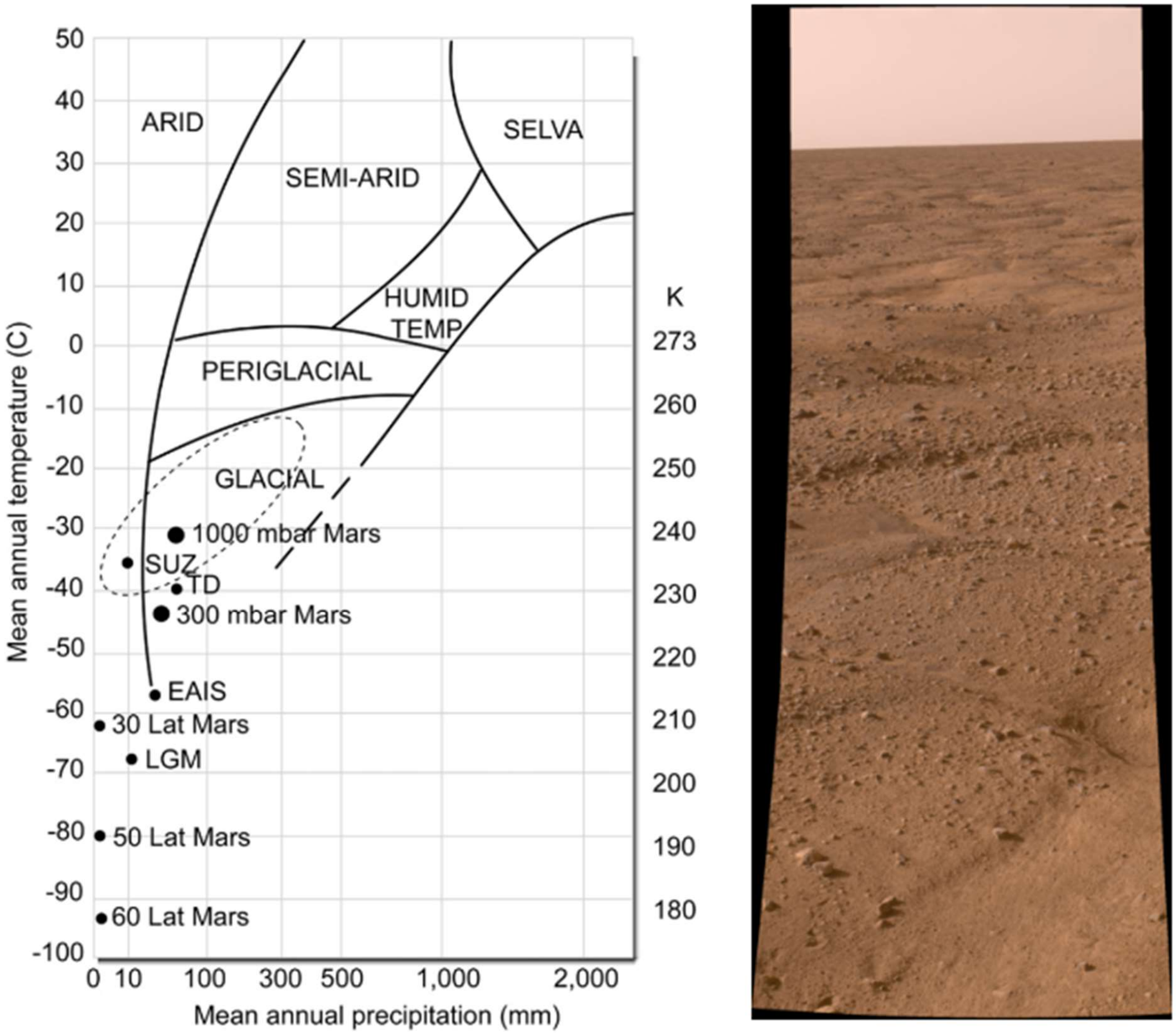

Figure 1-1. Left: Mean annual temperature and precipitation at different latitudes and atmospheric pressures of Mars compared to terrestrial climates (from Marchant and Head, 2007). The dashed line represents ADV climate conditions. Right: Polygonal ground viewed from the Phoenix landing site on the arctic plains of Mars (Image PIA10690).

patterned ground could be possible during periods of high obliquity on Mars (Siebert et al, 2001; Costard et al, 2002; Nakamura and Tajika, 2003; Gallagher et al, 2011; Balme et al 2013). The results of these modeling efforts have, in part, encouraged the use of mostly northern hemisphere terrestrial periglacial landforms as Mars analogs (e.g. Ulrich et al, 2011; Soare et al, 2014; Barrett et al, 2018). These analogs have utility in describing end-member scenarios when periglacial activity involving extensive thawing is possible, however they may overrepresent the role of active freeze-thaw cycles in polygon development on Mars. Each of the evaluated analog studies in

Antarctica and northern hemisphere periglacial sites incorporate features experiencing active modification by sublimation, thermal contraction, or freeze-thaw processes.

Despite the high potential for some patterned ground on Mars to be representative of relict or otherwise inactive processes in the present day, relict patterned ground sites on Earth have not previously been investigated for their applicability to Mars. *Phoenix* observations leave open the possibility that sublimation and thermal contraction processes are active in polygonal ground on Mars today. Even if patterned ground on Mars is assumed to have experienced nearly continuous active sublimation and thermal contraction driven modification (dry processes) over the last several million years, the historical input from periglacial processes (wet processes) from periods of high obliquity relative to dry processes is not well constrained at a feature or site-level. Part of the challenge in assigning contributions of feature modification to wet or dry processes is associated with the overlap of morphological characteristics associated with each formation mechanism. In addition, the degradation and non-wet or dry process modification of relict polygons on Mars is not well defined and not easily ascertained through imagery alone. Evaluating digital terrain models (DTMs) of Martian patterned ground may provide insight into micromorphological characteristics of active and relict polygons to assist with identifying the predominant mode of feature modification. Morphometric parameters based on visual imagery have been previously evaluated (e.g. feature length, circularity, size) in combination with underlying topography (slope and aspect), however surface roughness has not been previously included as a variable in evaluating polygon morphology on Earth or Mars. Surface roughness may provide the specific insight into microtopographic variations that are key to differentiating between active processes (dry active layers modified by sublimation and thermal contraction) and relict processes (wet active layers drive by freeze-thaw periglacial processes).

1.2 Patterned Ground on Earth: Previous Photogrammetric Studies

Active periglacial processes including patterned and polygonal ground have been the focus of research efforts spanning nearly two centuries ranging from the earliest suggested connections between the presence of permafrost and subsequent development of polygonal ground (Baer, 1838) through early studies that sought to characterize feature morphology, distribution, and possible formation mechanisms (Conrad, 1946). The modern era of patterned ground research can trace its lineage to the 1950's (Washburn, 1956) and has leveraged advances in technology to further constrain patterned ground mechanics and modes of formation (e.g. Ray et al., 1983; Kessler et al., 2003; Watanabe et al., 2017).

There was early recognition of the potential applications of using aerial imagery and photogrammetry to identify and study a combination of active and potentially relict patterned ground sites (Knechtel, 1952; Thorén, 1960; Malde, 1964). Some of the earliest attempts to use aerial photography to identify patterned ground sites were stymied by a combination of limitations to the spatial resolution of available aerial imagery and the early state of modern periglacial science at the time. However as high-resolution digital cameras became more widely available, creative attempts were made to characterize patterned ground morphology using cameras mounted to kites (Boike and Yoshiakawa, 2003), pole-mounted cameras coupled with systematic ground surveys (Vopata et al., 2006), and structure-from-motion (SfM) images taken from a step ladder to build 3D feature models to track morphological changes through time (Kääb et al., 2014). Improving technology and lowering costs associated with uncrewed aerial vehicles (UAVs) have opened new opportunities for rapidly characterizing large swaths of patterned ground at a combination of active periglacial sites (Dąbski et al., 2017; Śledź et al., 2021) and relict periglacial sites (Mather et al., 2019).

Research interest of relict patterned ground has remained relatively steady over the past three decades. (Walters, 1994; Kling, 1996; Grab, 2002; Sumner, 2004; Munroe, 2007; Krizek and Uxa, 2013; Pawalec, 2016; Mather et al., 2019; Groos, 2021). Direct comparative studies of active and relict patterned ground are rare, however notable differences have been documented of relict patterned ground in comparison to periglacially active features, including increased vegetation density (Walters, 1994; Munroe, 2007; Mather et al., 2019) and higher rates of pedogenesis (Munroe, 2007). Examining morphological and micromorphological variations between active and relict patterned ground could provide insights into feature evolution with applications to periglacial regions experiencing rapid change in response to warming temperatures. Comparing terrestrial relict and active patterned ground may also assist with the characterization of patterned ground on Mars that may have experienced wet periglacial modification during warmer climates initiated during periods of high obliquity (discussed in Chapter 4). As will be expanded upon in the discussion, there is also a high bar for establishing that patterned ground is periglacially relict, including ruling out seasonal and diurnal processes that can drive substantial pattern formation in the absence of permafrost or periglacial activity. Relict patterned ground in the context of this project is distinguished from active patterned ground on the basis of the presence or absence of permafrost.

1.3 Patterned Ground in the Haughton Impact Structure

The vicinity surrounding Haughton Impact Structure (HIS) provides a unique setting as the largest accessible terrestrial periglacial impact crater, leading to its extensive utilization as an Earth-Mars analog site (Osinski et al., 2001; Lee et al., 2001; Lee and Osinski, 2005; Osinski and Lee, 2005; Osinski et al. 2005; Godin et al., 2019). Dated at approximately 21 to 39 million years old (Sherlock et al., 2005; Young et al., 2013; Erickson et al., 2021), the geology within the crater consists of lacustrine silt, sand, and clay deposits within the upper Haughton Formation overlying impact-derived polymict breccias in the lower Haughton Formation (Osinski and Lee, 2005). The lacustrine deposits originate from a post-impact intracrater lake that featured attendant ouflow channels (Osinski and Lee, 2005), lesser versions of which presently exit the HIS and flow northeast before emptying into the Arctic Ocean at Thomas Lee Inlet.

The Haughton impact structure is situated in an active periglacial environment on Devon Island in the Canadian high arctic (Osinski et al, 2005). The HIS remains one of the best-preserved impact craters owing to relatively cold and dry polar desert conditions that have persisted since its formation (Osinski et al 2005b). Long-term climate data is sparse for the HIS and Devon Island in general, however detailed observations recorded at the Truelove Lowlands approximately 150 km east of HIS provide some context. The modern climate at the HIS is classified as a polar desert that receives approximately 185 mm of precipitation annually, of which roughly 30% is liquid, primarily during the short arctic summer (Ryden, 1977). The combination of mean annual climate conditions, abundance of active periglacial features, geologically recent glacial activity, and the remnants of an intracrater lake make the Haughton impact structure an ideal setting to conduct Earth-Mars analog studies of periglacial morphologies that occur on both planets.

Patterned ground morphology has been extensively studied in the field (Washburn, 1956; Kessler and Werner, 2003; Watanabe et al 2013; Watanabe et al 2017; Uxa et al, 2017). Terrestrial patterned ground has also been utilized as an analog for patterned ground on Mars (Marchant et al, 2002; Mangold, 2005; Levy et al, 2008; Levy et al, 2009a; Levy et al, 2009b; Ulrich et al, 2011; Haltigin et al, 2012; Mellon et al, 2014; Soare et al, 2014; Soare et al, 2016; Barrett et al, 2018; Brooker et al 2018). Modeling patterned ground formation and development on both planets has continued (Ray et al, 1983; Daanen et al, 2008; Peterson and Krantz, 2002; Peterson, 2011). Additional field parameters are necessary in order to refine computational models for patterned ground development (Fisher et al, 2016; Watanabe et al, 2017).

Observations from the *Phoenix* mission indicate that contemporary modification of patterned ground on Mars likely occurs via sublimation-driven processes as subsurface ground ice is currently in vapor-diffusive equilibrium with the atmosphere (Mellon et al., 2009). It has been proposed that periods of high obliquity could result in an increase in atmospheric pressure and temperature enabling polygon modification via periglacial (freeze-thaw) processes to occur on Mars (Laskar et al., 2004; Soare et al., 2014). Further calibration of active layer thermal properties in periglacially-modified patterned ground would therefore benefit modeling efforts to constrain the conditions leading to the onset of periglacial processes on Mars. Analog evaluations of the thermal properties of both smaller-scale features (such as hummocks, stone circles, stone nets) and larger-scale features (such as ice-wedge polygons) would help capture the range of polygon morphologies that are observed on Mars today.

To provide additional measurements to support future modeling efforts, this project collected in-situ data-logged and point observations of the temperature and moisture conditions of the active layer at a variety of sites comprising small- and large-scale patterned groundon Devon Island in the Canadian high arctic. These temperature and moisture observations are used in tandem with measurements collected to derive the thermal properties of material sampled from patterned ground margins and centers during local summer and peak active layer development. Examining the morphology and thermal conditions within individual patterned ground landforms during the terrestrial arctic summer provided data during the seasonal thawing period, an important window of time to understand while testing the wet periglaciation hypothesis for patterned ground development on Mars.

Chapter 2

UAS Photomorphometry and Multiscale Surface Roughness of Patterned Ground at Sites in the Uinta Mountains, Utah, USA and the Westfjords and Highlands, Iceland

Knightly, J.P.[1], Tullis, J.[1], Dixon, J.C.[1], Chevrier, V.F.[1]

[1]University of Arkansas, Center for Space and Planetary Sciences, Fayetteville, AR 72701

1.0 Introduction

Active periglacial processes including patterned and polygonal ground have been the focus of research efforts spanning nearly two centuries ranging from the earliest suggested connections between the presence of permafrost and subsequent development of polygonal ground (Baer, 1838) through early studies that sought to characterize feature morphology, distribution, and possible formation mechanisms (Conrad, 1946). The modern era of patterned ground research can trace its lineage to the 1950's (Washburn, 1956) and has leveraged advances in technology to further constrain patterned ground mechanics and modes of formation (e.g. Ray et al., 1983; Kessler et al., 2003; Watanabe et al., 2017).

There was early recognition of the potential applications of using aerial imagery and photogrammetry to identify and study a combination of active and potentially relict patterned ground sites (Knechtel, 1952; Thorén, 1960; Malde, 1964). Some of the earliest attempts to use aerial photography to identify patterned ground sites were stymied by a combination of limitations to the spatial resolution of available aerial imagery and the early state of modern periglacial science at the time. However as high resolution digital cameras became more widely available, creative attempts were made to characterize patterned ground morphology using cameras mounted to kites (Boike and Yoshiakawa, 2003), pole-mounted cameras coupled with systematic ground surveys (Vopata et al., 2006), and structure-from-motion (SfM) images taken from a step ladder to build 3D feature models to track morphological changes through time (Kääb et al., 2014). Improving technology and lowering costs associated with uncrewed aerial systems (UASs) have opened new opportunities for rapidly characterizing large swaths of patterned ground at a combination of active periglacial sites (Dąbski et al., 2017; Śledź et al., 2021) and relict periglacial sites (Mather et al., 2019).

Research interest of relict patterned ground has remained relatively steady over the past three decades. (Walters, 1994; Kling, 1996; Grab, 2002; Sumner, 2004; Munroe, 2007; Krizek and Uxa, 2013; Pawalec, 2016; Mather et al., 2019; Groos, 2021). Direct comparative studies of active and relict patterned ground are rare, however notable differences have been documented of relict patterned ground in comparison to periglacially active features, including increased vegetation density (Walters, 1994; Munroe, 2007; Mather et al., 2019) and higher rates of pedogenesis (Munroe, 2007). Examining morphological and micromorphological variations between active and relict patterned ground could provide insights into feature evolution with applications to periglacial regions experiencing rapid change in response to warming temperatures. Comparing terrestrial relict and active patterned ground may also assist with the characterization of patterned ground on Mars that may have experienced wet periglacial modification during warmer climates initiated during periods of high obliquity (discussed in Chapter 4). As will be expanded upon in the discussion, there is also a high bar for establishing that patterned ground is periglacially relict, including ruling out seasonal and diurnal processes that can drive pattern formation in the absence of permafrost or periglacial activity.

2.0 Site Selection

Active periglacial patterned ground that is ubiquitous to polar and subpolar terrestrial regions has been extensively studied owing to the level of exposure, preservation, and the relative lack of vegetation. Patterned ground exhibits low-relief topography, which increases the susceptibility to vegetation overgrowth, burial, and erosion by aqueous processes under warming climate conditions and the cessation of periglacial activity. These processes appear to be endemic to the evolution of terrestrial patterned ground sites and serve as significant lines of evidence for deriving the age of relict features. While previous work has mapped weathered relict patterned ground using UAS imaging and photogrammetry (Mather et al., 2019), well-preserved relict patterned ground has yet to be extensively analyzed in this manner. This can largely be attributed to the limited identification of well-preserved relict patterned ground sites that are not substantially weathered or overgrown. A survey of previous studies was undertaken to identify potential relict patterned ground sites for investigation. In order to evaluate the morphology of active and putative relict patterned ground, sites were selected based on meeting the following criteria: degree of surface exposure (absence of or limited burial), the near-absence or limited distribution of vegetation, and low rates of water-driven erosion.

The first category of potentially relict sites that were investigated for inclusion in this project are known weathered or vegetated relict patterned ground sites that are located in agriculturally productive regions in the northern half of the contiguous United States. Prominent vegetated relict polygons have been identified in northeastern Iowa (Walters, 1994) and the Saginaw Lowlands of Michigan, U.S.A. (Lusch et al., 2009). While these vegetated and weathered sites provide evidence of the extent of periglacial conditions along the margins of the Late Wisconsin Glaciation as recently as approximately 14,500 (Lusch et al., 2009) to 16,500 (Walters, 1994) years before present (BP), their locations in agriculturally modified areas have left them at an unsuitable level of preservation for the fine-scale morphological analysis and planetary analog analysis involved with this project. For example, a survey of satellite imagery to locate the relict polygons in northeastern Iowa using location information provided in Walters, 1994 turned up empty-handed as a result of ongoing agricultural practices and land development in the study area that made positive feature identification difficult.

The second category of potential sites involved a survey of older literature that purported to locate potential relict periglacial landforms at accessible low (southern) to mid latitude locations in the contiguous United States. These studies, primarily from the 1950’s to 1960’s, utilized aerial photography to identify potentially relict patterned ground sites (Knechtel, 1952; Malde, 1964).

However, these early attempts to use aerial photography to identify patterned ground sites were stymied by a combination of limitations to the spatial resolution of available aerial imagery, the early state of modern periglacial science, and poor resolution on the spatial extent of periglacial activity during recent ice ages. This resulted in the identification of potential relict patterned ground sites, mima, or pimple mounds that lack characteristic features indicative of cryoturbation

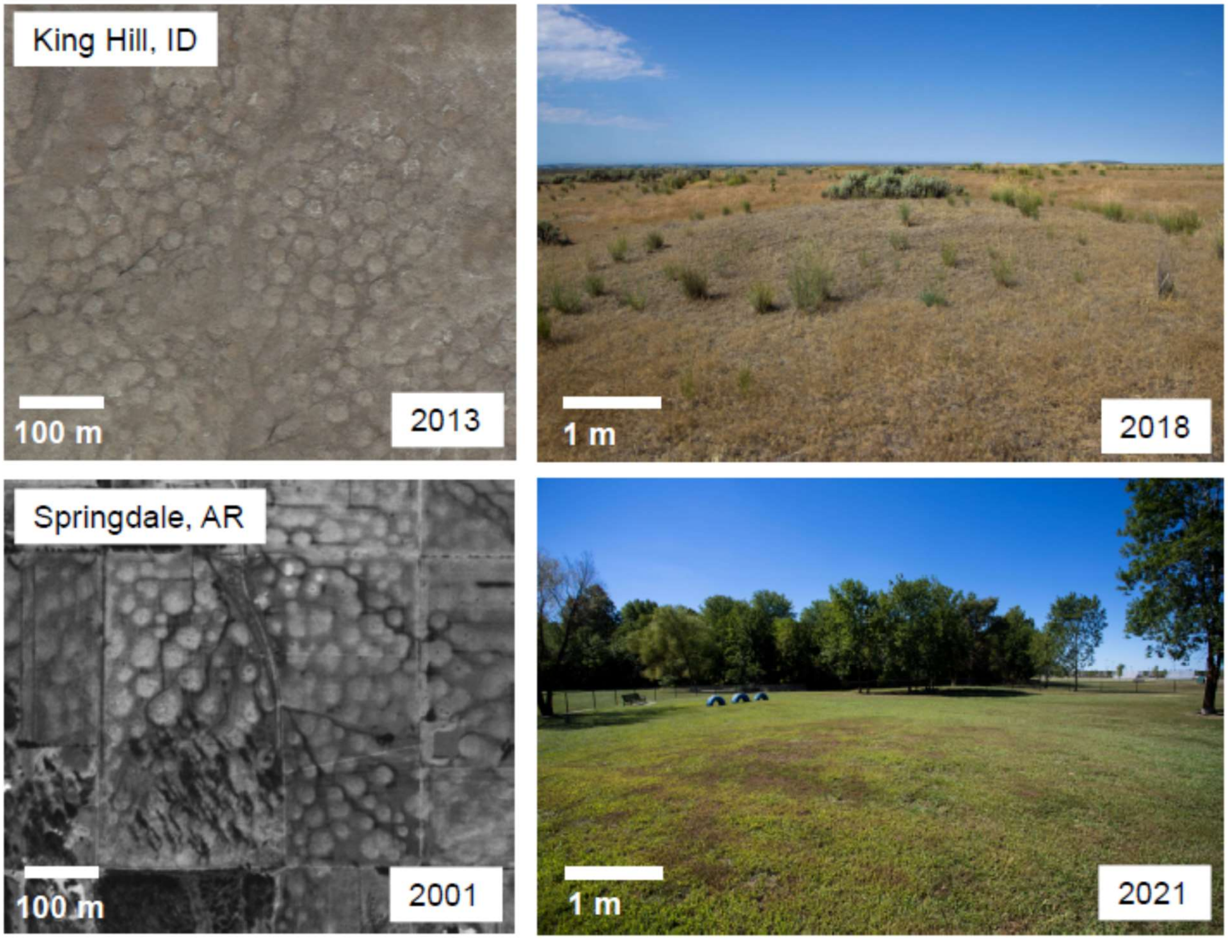

Figure 2-1: Reconnaissance of mounds that were investigated for potential periglacial origins near King Hill, ID and Springdale, AR. Periglacial origins were proposed by Malde (1964) for the King Hill, ID mounds and by Knectel (1952) for mounds in Oklahoma that are similar to those observed in Arkansas. Biological processes (Washburn, 1988) and aeolian orings (Quinn, 1961; Durre et al., 2019) have since been proposed for the origins of similar mounds located in the region of each site, and gopher burrows were observed in the mounds near King Hill during an opportunistic visit in 2018. Regardless of origin and merit for further study, the extent of vegetation and land development precluded further investigation of these and other mid-latitude sites for this project.

(Washburn, 1988) and thus likely have more modest biological and aeolian origins. Proposed origins for mima mounds that are prevalent across the western and central United States that are potentially formed by gopher burrow construction (Washburn, 1988); tree pedestals (Cain, 1974), aeolian deposition (Quinn, 1961), or gilgai processes (Washburn, 1988; Lusch et al., 2009). Opportunistic field reconnaissance visits were conducted at mima and pimple mound sites on public land along the Snake River Valley in Idaho and at a community park close to the University of Arkansas. Extensive pocket gopher burrows were observed at the Snake River Valley site and features measured between approximately 9 m and 15 m across (Figure 2-1). The Arkansas site was more heavily vegetated with feature dimensions ranging from approximately 20 to 50 m across (Figure 2-1). Pimple mounds studied approximately 40 km west of the Springdale site are proposed to have formed via selective erosion and the deposition of eolian material under clumps of bushes (Quinn, 1961; Durre et al., 2019). While these sites are noteworthy in their own regard and perhaps merit further investigation owing to their accessibility, the biological or aeolian origins for the investigated mima and pimple mounds precluded these sites from further investigation under the scope of this project.

The third category of sites that were studied for inclusion in this project are a combination of alpine and high latitude sites that are located along the margin of active periglacial regions and where permafrost is either absent or sporadic. The level of preservation of these patterned ground sites in alpine regions can be attributed to factors including limited revegetation due to absent or sporadic soils (Munroe, 2007) and their location in remote and difficult to access areas that have helped to shield them from anthropogenic disturbance. Prominent examples of variably active to relict alpine patterned ground include locations in the Rocky Mountains in Colorado (Benedict, 1992; Vopata et al., 2006), the Uinta Mountains in Utah (Munroe, 2007), the Krkonose Mountains, Czech Republic (Křížek and Uxa, 2013), the Holy Cross Mountains, Poland (Pawalec, 2016), the Lesotho Highlands in South Africa (Sumner, 2004), northern Sweden (Kling, 1996), the Sanetti Plateau and Bale Mountains in Ethiopia (Groos, 2021), and alpine areas in Iceland (Eztelmüller et al., 2007; Morino et al., 2021). Lower-elevation, high latitude sites that were identified include palsa and polygonal terrains located in sporadic permafrost in the Icelandic highlands (Eztelmüller et al., 2007). The level of preservation and the known variable extent or absence of permafrost at these sites made them ideal for inclusion in this project. Logistical considerations were taken into account for final site selection, including site location and accessibility. Three sites were ultimately selected for further study: alpine patterned ground located near North Pole Pass in the Uinta Mountains, Utah, U.S.A. (previously described by Munroe, 2007); alpine patterned ground located on the Eyrarfjall Peninsula near Flateyri, Iceland; and ice wedge polygons identified along the Blanda River in the Central Highlands of Iceland.

2.1 North Pole Pass, Uinta Mountains, Utah, U.S.A.

A previously studied patterned ground site at approximately 3,700 m near North Pole Pass in the Uinta Mountains (Munroe, 2007) was selected for the first study area (Figure 2-2). While alpine patterned ground has been described throughout the lower Rocky Mountains, steep slopes limit occurrences to small, isolated patches at typically higher elevations. Alpine patterned ground throughout the Uinta Mountains is more widespread owing to relatively flat-topped mountains that dominate the east-west mountain range (locally known as “the bollies”), yielding gentle slopes that are favorable for sustained patterned ground development and evolution. The presence of glacial cirques adjacent to and below many of the patterned ground exposures suggest that these features have remained topographically above the alpine and valley glaciers that would have held a formidable presence during recent glaciations. It is therefore likely that patterned ground in the Uinta Mountains has experienced evolution through multiple glacial-interglacial cycles, punctuated by periods of increased and decreased amounts of cryoturbation (Munroe, 2007).

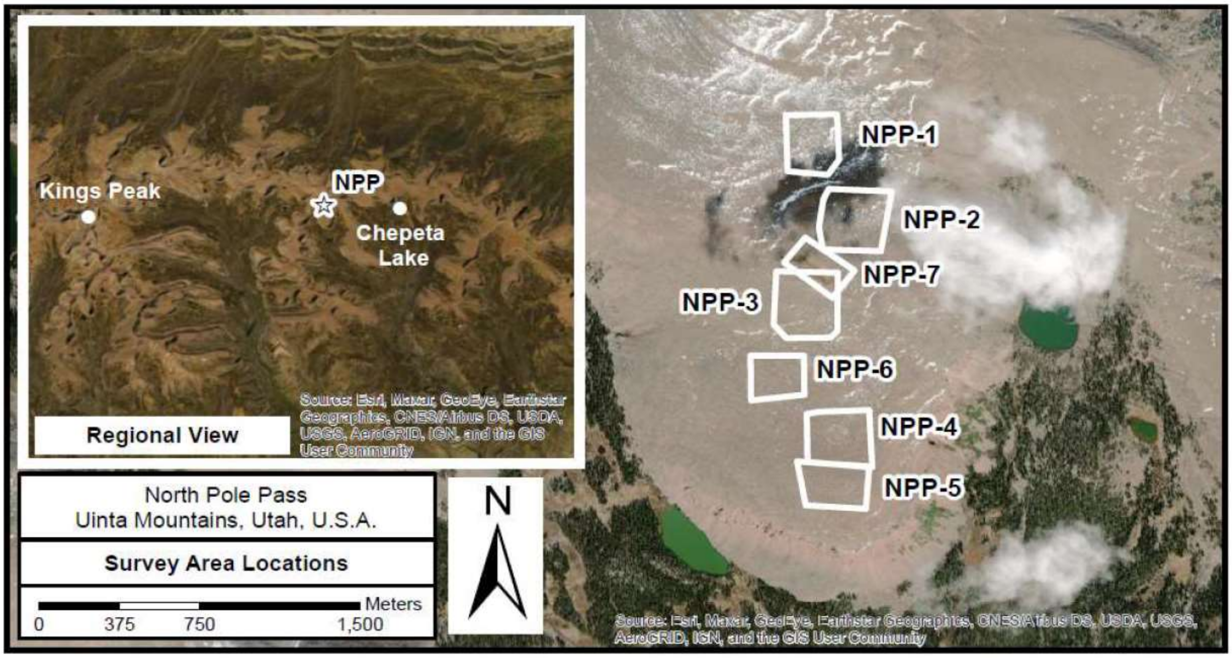

Figure 2-2: North Pole Pass (NPP) survey area locations. Morphometric analyses were performed at all survey areas except for NPP-3 and NPP-7 due to indistinct feature morphologies resulting from extensive vegetative cover.

Following the retreat of adjacent glaciers at the end of the Last Glacial Maximum (LGM), periglacial modification of patterned ground would have likely prevailed under the presence of alpine permafrost, including the seasonal development of a wet active layer. Cryoturbation characteristic of active layer modification was observed in soil profiles near the survey areas (Munroe, 2007). The mean annual atmospheric temperature (MAAT) recorded near the site from 1999 to 2003 was -2.0°C (Munroe 2006), or just slightly below the -1.6°C threshold that has been postulated for active periglacial modification of patterned ground (Grab, 2002). Recurring studies throughout the Uinta Mountains have found only limited evidence to support the presence of alpine permafrost continuing into the present-day and is thus provisionally considered to be absent (Bockheim et al., 2000; Munroe, 2007; Munroe et al., 2021). Despite the apparent lack of contemporary alpine permafrost, several rock glaciers have been characterized along slopes adjacent to the bollies in the present day (Munroe, 2018). The presence of vegetation on some of the feature high centers and the growth of lichen on rock surfaces are further indicators that the features are extremely stable under present climate conditions (Munroe, 2007). While temperatures are still cold enough during the winter to support some seasonal modification, the site is a strong candidate for supporting well-preserved periglacially relict patterned ground.

2.2 Eyrarfjall Peninsula, Westfjords, Iceland (Flateyri)

Building off observations from the North Pole Pass site in the Uinta Mountains, a systematic search of satellite and historical aerial imagery was undertaken using Google Earth and imagery from the National Land Survey of Iceland to identify areas of alpine patterned ground on the broad, level mountaintops in the Westfjords in the northwestern region of Iceland (Figure 2-3). Extensive patterned ground was observed at approximately 600 meters above sea level in the vicinity of glacial cirques approximately 55 km to the west of the Drangajokull Ice Cap and appear to be previously undescribed in existing literature. Located above the small fishing village

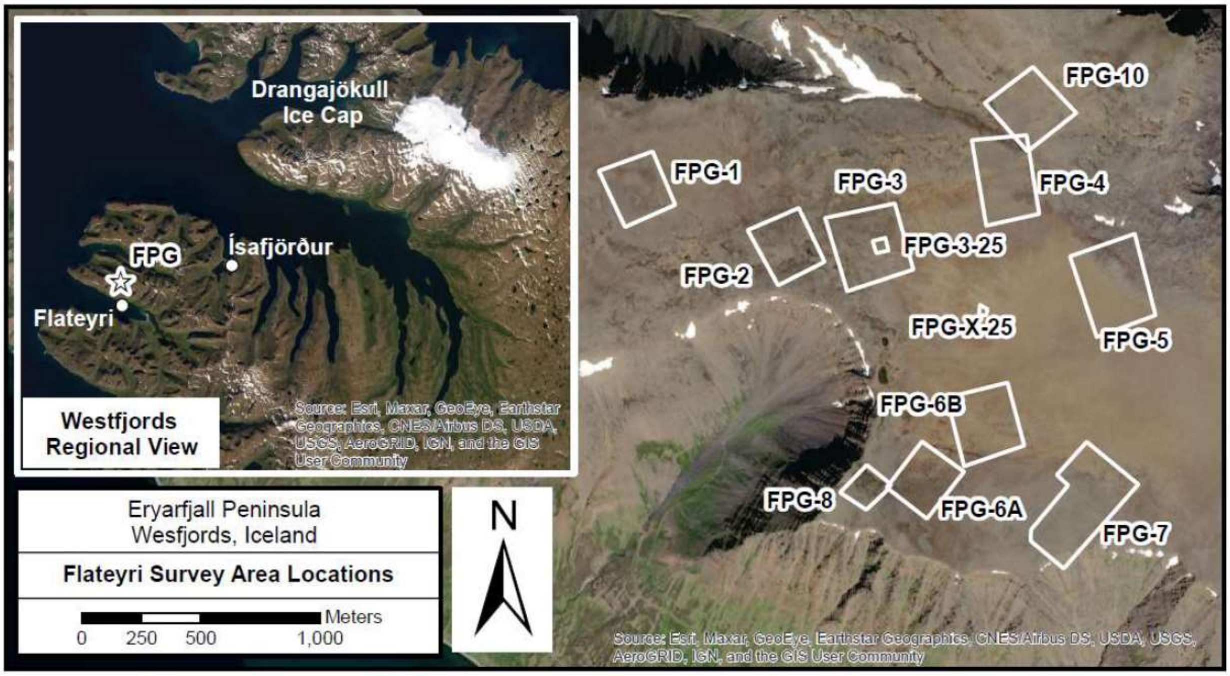

Source: Esri, Maxar, GeoEye, Earthstar Geographics, CNES/Airbus DS, USDA, USGS, AeroGRID, IGN, and the GIS User Community

Source: Esri, Maxar, GeoEye, Earthstar Geographics, CNES/Airbus DS, USDA, USGS, AeroGRID, IGN, and the GIS User Community

Figure 2-3: Flateyri patterned ground (FPG) survey area locations relative to adjacent fjords and the nearby Drangajökull Ice Cap. Morphometric analyses were performed at all survey locations except for FPG-10 and FPG-3-25 due to indistinct feature geometries resulting from extensive vegetative cover. FPG-9 was a planned survey that was not performed due to limited UAV battery life.

of Flateyri, the site is situated on relatively level ground that comprises a broad plateau over much of the Eyrarfjall peninsula, creating a steep coastline that borders the adjacent Önundarfjörður fjord to the south. The geology of the peninsula is poorly described in existing literature, but outcrops visible below the site in an adjacent cirque and eroded subcrop and overburden across the site are consistent with extrusive basalt and derived sediments. A geological map of Iceland (Iceland GeoSurvey, Accessed: 2021) dates the observed basaltic bedrock across much of the Westfjords to the Middle Miocene (older than 11 Ma).

Direct observations of permafrost in the Westfjords are scarce in the literature, however historical permafrost during the Little Ice Age (LIA) was likely prevalent (Eztelmüller et al., 2020) and the presence of contemporary permafrost is hypothesized from climate data and indirect observations (Morino et al., 2021). Regional surface and shallow subsurface temperature observations gathered throughout northern and eastern Iceland suggest that alpine permafrost is generally limited to elevations above 800-900 m above sea level (asl) throughout Iceland, conforming to MAAT isotherms below -3°C (Eztelmüller et al., 2007). Under the same model, sporadic permafrost (palsa) is predicted to occur at lower elevations throughout the Central Highlands and above 800 m asl in the Westfjords (Eztelmüller et al., 2007). However, landslides and molards in the Westfjords that were possibly triggered by permafrost degradation have been observed to originate at significantly lower elevations between 400-500 m asl (Morino et al., 2021). It has been hypothesized that permafrost could prevail at lower elevations in the Westfjords from a combination of exposure to northerly winds, lower summer temperatures, and a corresponding shorter melting season (Glade, 2005; Bryonojolfsson, 2014).

The coastal MAAT in the Westfjords between 1961-1990 was 3.2°C (Glade and Jensen, 2004). Temperature data from higher elevations is scarce, however temperature gradients in the Trollaskagi peninsula in north central Iceland between 1940-1970 demonstrate a MAAT between 2-4°C in coastal areas and MAAT ranging from -2°C to -4°C at mountain summits that approach elevations between 950-1000 m asl (Einarsson, 1984). The highest elevations across the plateau of the Eryrarfjall peninsula range between approximately 450 meters at its northwesternmost tip to approximately 740 meters to the southeast where the peninsula joins the mainland of the Westfjords. The lowermost elevation is consistent with recent observations suggesting the presence of permafrost between 400-500 m asl (Morino et al., 2021). While the presence and extent of permafrost at the site remains unknown, it is conservatively estimated to be present in sporadic to extensive deposits that contribute to at least seasonal modification in the present day. For planning this study, the Westfjords site was initially considered to be an active analog for the potentially relict site at North Pole Pass.

2.3 Blanda River, Central Highlands, Iceland

A review of existing literature describes the presence of sporadic permafrost across the Icelandic Highlands resulting in varied periglacial landforms including ice wedge polygons, palsas, and thofur (Schunke, 1974; Eztelmüller et al., 2007; Emmert, 2020). A survey of historical and present-day aerial and satellite imagery (using data from Google Earth and the National Land Survey of Iceland) was undertaken to search for accessible patterned ground sites across the broader Highlands region. A series of ice-wedge polygons were identified in Google Earth satellite imagery along the overbanks of the Blanda River in the Central Highlands (Figure 2-4) that appear to have been previously described as part of a broader survey by Schunke (1974). An extensive study of polygons and palsa landforms approximately 30 to 40 km to the east near the proglacial margin of the Hofsjokull Glacier was concluded immediately prior to this work and provides extensive in-situ and subsurface measurements of related polygonal landforms (Emmert, 2020). The site is also located along the margins of active glacial activity being positioned approximately 15-30 km northeast of Lagjokull Ice Cap and approximately 20-35 km northwest of the Hofsjokull Ice Cap. A geological map of Iceland has characterized the material across the Blanda River sites as basaltic in origin with intermediate interglacial and supraglacial lava sediments that date from the Middle to Upper Pleistocene, or younger than 0.8 Ma (Iceland GeoSurvey, Accessed: 2021).

Permafrost was likely prevalent across the Highlands during the LIA (Eztelmüller et al., 2020) and tephrachronological dating reported in Icelandic literature suggests that ice-wedge activity was also reactivated during the LIA lasting through at least the end of the Nineteenth Century (Thorarinsson, 1964). As with the Westfjords site, modeling by Eztelmüller et al. (2007) is relied upon for constraining the presence and extent of contemporary permafrost and associated active periglacial terrains. More extensive seasonal temperature records at the surface and boreholes have enabled a more thorough characterization of permafrost at lower elevations throughout the Icelandic Highlands. The MAAT for 1961 to 1990 at the Highlands site is greater than -3°C (Eztelmüller et al., 2007). However, depressed mean annual temperatures of 1.6-1.8°C and winter temperatures of 2.4-2.7°C below the mid-century mean temperatures reported by Schunke (1974) suggest that ice wedge activity was possible at least as recently at the 1960's.

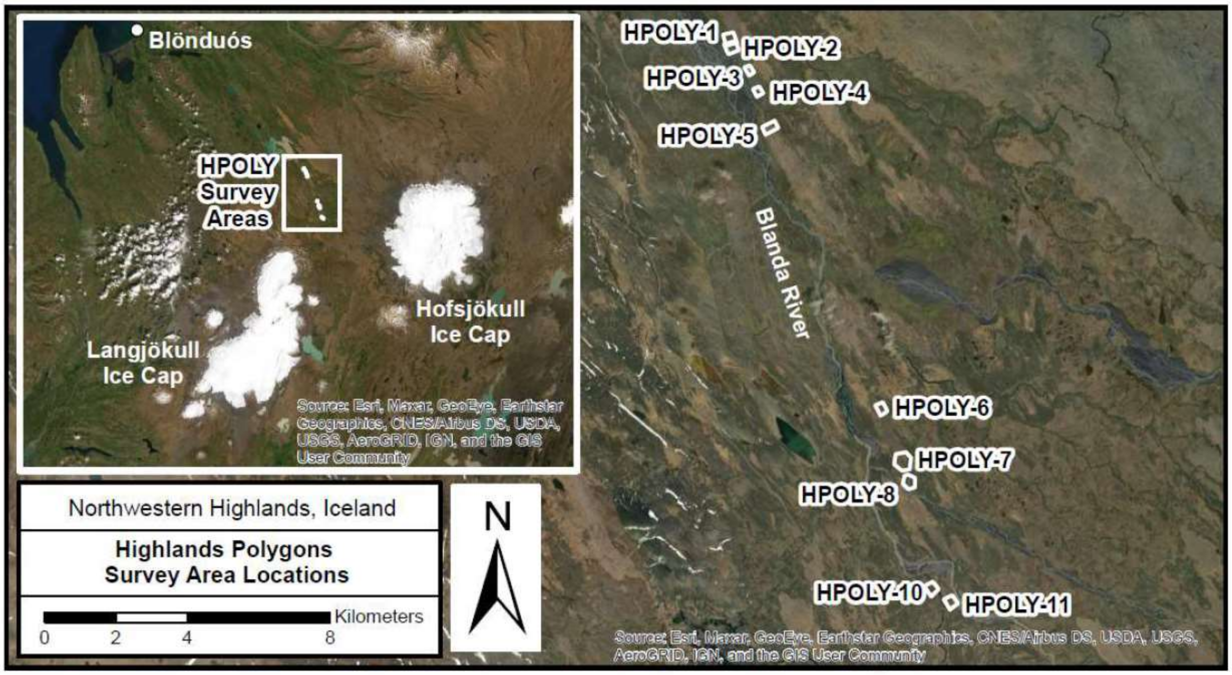

Figure 2-4: Highlands polygons (HPOLY) survey area locations relative to the nearby Langajökull and Hofsjökull Ice Caps. Morphometric analyses were performed at all survey locations except for HPOLY-4 and HPOLY-10 due to indistinct feature geometries resulting from extensive vegetative cover. HPOLY-9 (not shown) was a planned survey that could not be performed as the site was located between two inaccessible water crossings along tributaries of the Blanda River.

3.0 Methods

Previous investigations into the nature of alpine periglacial processes in the Uinta Mountains is extensive (courtesy of Munroe et al.). Overnight backpacking was required to reach the North Pole Pass site so to reduce backpack weight, only the supplies required for the UAS survey were packed in at the expense of collecting any subsurface or in-situ measurements. The Icelandic sites in the Westfjords and Central Highlands could be accessed by either a moderately strenuous day hike (Westfjords) or directly by car on along a gravel road (Highlands). Both Icelandic sites have previously not been described in the literature, however previous investigations into the spatial distribution of permafrost and periglacial landforms elsewhere in Iceland provide some context for the expected prevailing conditions. Limited in-situ measurements were collected at each Icelandic site in the Highlands and Westfjords to compare the expected versus actual site conditions. Shallow trenches were excavated to ascertain temperature and moisture conditions in the uppermost 0.5 meter of overburden at select locations at each site. Temperature measurements were collected near the surface and at the base of the each trench using using a Hanna H198331 temperature and conductivity meter.

3.1 UAS Surveys

The primary focus of the field work was to conduct several UAS surveys at each site to document of areas of interest with the intent to derive photogrammetric site models from acquired imagery. All UAS flights were performed using a DJI Mavic Pro equipped with a stock 12 megapixel camera. While there are other comparably priced commercial UAS platforms with higher resolution sensors, the DJI Mavic Pro was selected for this project as it can be folded into a compact configuration making it extremely favorable to transport in a traditional hiking backpack to remote field sites where backpack weight and space considerations are a significant factor.

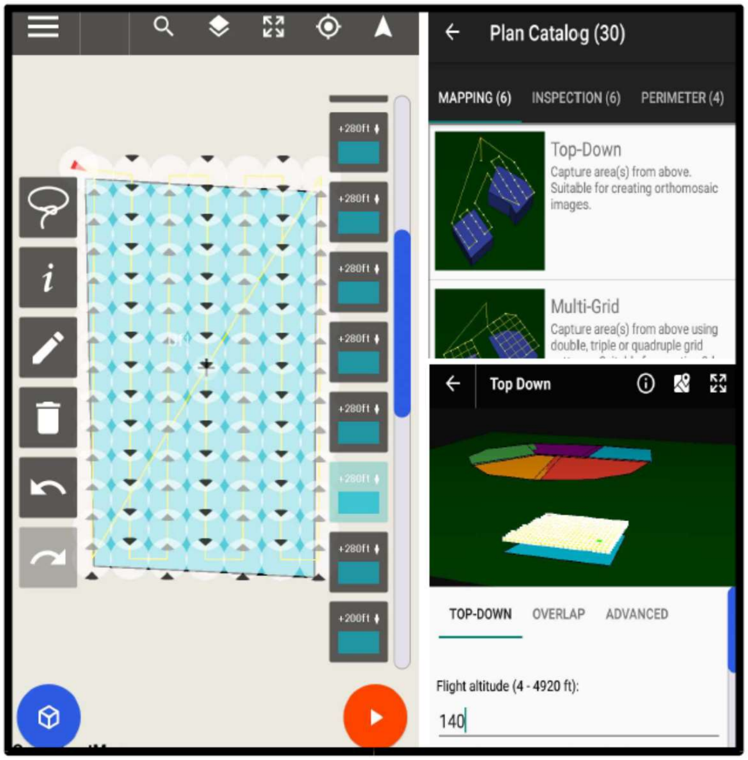

Top-Down
Capture area(s) from above. Suitable for creating orthomosaic images.

Multi-Grid
Capture area(s) from above using double, triple or quadruple grid

Flight altitude (4 - 4920 ft): 140

Survey ID	Approximate Survey Altitude (m agl)	Approximate Survey Area (m^2)
NPP-1	120	67,450
NPP-2	120	81,000
NPP-4	120	73,000
NPP-5	120	65,250
NPP-6	120	49,300
FPG-1	85	41,440
FPG-2	85	31,080
FPG-3	85	62,160
FPG-3-25	7.5	787
FPG-4	85	51,800
FPG-5	85	67,340
FPG-6A	43	31,080
FPG-6B	85	49,210
FPG-7	85	72,520
FPG-8	43	15,540
FPG-X-25	7.5	773
HPOLY-1	85	64,750
HPOLY-2	85	67,340
HPOLY-3	85	28,490
HPOLY-4	85	28,490
HPOLY-5	85	56,980
HPOLY-6	85	44,030
HPOLY-7	85	116,550
HPOLY-8	85	67,340
HPOLY-11	85	62,160

Figure 2-5: Idealized UAV survey footprint and screenshot from the Drone Harmony app (left). Survey properties including flight altitude in meters above ground level (m agl) and the approximate survey area.

The flights were planned and flown using the Drone Harmony application on a Motorola G6 Play smartphone (Figure 2-5). Drone Harmony flight plans are generated in-app on Android-supported mobile devices in three general steps:

First, the bounding area of interest was defined for each flight based on satellite image analysis. For the purpose of this project, all flight areas were plotted in generally rectangular to polygonal shapes ranging in area from approximately 770 to 116,550 square meters. Most flight plans were plotted prior to entering the field due to the absence of internet connectivity at the sites. Each flight plan was designed in a manner to maximize the power budget from the available batteries to conduct the most flights possible and over the widest variety of representative terrain visible at the site in satellite imagery

Second, flight variables were selected based on the make and model of UAS used. During this step, the UAS speed and flight altitude was set, taking into account battery life and the desired spatial resolution of the imagery. The Utah UAS surveys were flown at approximately 120 m above ground surface (ags) and the majority of the Icelandic UAS surveys were flown at approximately 85 m ags. The 85 to 120 m flight altitudes were selected to balance battery life and survey coverage. Follow-up surveys at the Flateyri site were flown at approximately 7.5 m to collect higher resolution imagery in response to an initial analysis of data collected during the initial surveys.

The third step involved uploading the flight plan to the UAS (MavicPro) and instructing it to begin the survey. The UAS executed the automated flight plan by taking photos at the specified intervals adjusted based on the desired final image resolution and tailored based on the flight altitude and speed. At the conclusion of the flight, the UAS returned to the launch point and was landed under manual control.

Due to the remote nature of the study areas, decisions were made to strike a balance between achieving the desired research objectives and accommodating logistical restrictions associated with trekking into remote alpine and highlands sites. Accordingly, the UAS surveys were conducted without the use of ground control points (GCPs) to leave room for critical survival gear. As the UAS surveys collected the highest spatial resolution data available for previously uncharacterized sites, the scope of work was designed as a reconnaissance study from the outset with the intent that the data from these UAS surveys could constrain future site selection for more detailed surveys in the future.

3.2 Photogrammetric Processing

Photogrammetric post-processing of UAS images for each site was accomplished using Agisoft Metashape. Best-practice workflows based on Agisoft guidelines were utilized to render the individual UAS images into a resulting digital site model (DSM), projecting an orthomosaic image of the site onto the derived digital terrain model (DTM). Default settings were generally applied throughout the DSM rendering process in Metashape. The MavicPro is equipped with a consumer-grade GPS receiver and records the latitude, longitude, and altitude (based on take-off location) in addition to the yaw, pitch, and roll of the UAS into the exchangeable image file (EXIF) metadata of each image. While the EXIF data from DJI-manufactured UASs are commonly handled by Metashape, it is still prudent to verify that the camera calibration is recognizing the appropriate sensor associated with the UAS.

During the Align Photos step, the accuracy was set to “High” and the “generic preselection” and “reference preselection” settings were enabled. The “key point limit” was set to 40,000 and “Tie point limit” set to 4,000. “Adaptive camera model fitting” was enabled. Settings for building the dense point cloud were set to “medium” quality with aggressive depth filtering. Once the dense point cloud was generated, the DTM was constructed using the default settings and default coordinate system extracted from the EXIF data. The orthomosaic was generated using the default settings.

During the traditional workflow, there is an option to place markers for GCPs to enable better georeferencing and model fitting results. Prior to commencing field work, it was determined that the on-board GNSS would provide sufficient geodata to accurately locate the resulting derived orthophotos and DTMs. It was understood that not using GCPs would result in geometric distortions that would impact slope-dependent DTM analyses. What was unknown at the outset is that the MavicPro sensor performs on-board image corrections by default, even when shooting to generate a ‘raw’ .DNG output image file. The on-board ‘corrections’ result in an exacerbated doming-effect where the apparent elevation profile of the DTM appears to increase around the center the model. This effect is particularly pronounced on sites where the surveyed topography is relatively level. Conversely, the effect is minimized on sites with a greater level of topographic variability, which causes the doming effect to blend in with or otherwise be obscured by the site’s topography. This magnitude of this effect went unnoticed following the Utah UAS surveys in 2018 due to variably sloped terrain at the survey locations that masked any doming that was present. The doming effect was not fully ascertained until after the completion of field work in Iceland in

2019 due to the comparatively flat nature of most of the Icelandic sites that were surveyed, thus exacerbating the resulting doming effect.

The doming effect in photogrammetric model building has been known for some time and has received growing attention in recent years in parallel with the broader application of UAS surveys. James et al. (2020) developed a model for mitigating systematic doming error in DTMs, however their model currently relies on using GCPs for verification. Other alternatives were brainstormed for mitigating the effects of the resulting doming error of the Utah and Iceland DTMs, but the alternatives would have required additional data collection and the use of GCPs for method verification. Otherwise, the result would yield an unconstrained DTM that while roughly approximating the interpolated topographic surface would impart a higher margin of error onto any derived datasets. The decision was made to perform the data analysis by focusing on variables that were not slope-dependent and thus unaffected by the doming error.

3.3 Morphometric Analysis

The resulting orthomosaics and DTMs were imported into either ArcGIS or QGIS for additional processing. While ArcGIS was used for some data processing, QGIS was used for the majority of data post-processing to enable open-source formatting of the resulting datasets. A modified Dell XPS15 laptop upgraded with a 1 TB solid-state drive and 32 GB of RAM was used to perform the GIS processing procedures outlined in this section. While the hardware was sufficient for performing most operations in a timely and hardware-efficient manner, larger datasets could take upwards of several hours to over a day to process. Hardware capabilities are a paramount consideration prior to replicating this process.

Feature delineation procedures were modeled after similar studies that quantified terrestrial patterned ground observations as a Mars analog (Ulrich et al., 2011; Brooker et al., 2018). Individual patterned ground features were delineated based on morphology, categorizing by feature centers, borders, and inter-feature margins (Figure 2-6). Larger ice-wedge polygons were simply delineated based on feature centers and margins (troughs). However, some ice-wedge polygons preserved smaller polygons layered across the larger polygon centers, which were delineated based on their respective feature centers and margins. Vegetation was present at all sites to some extent, and while it was generally avoided when possible, features were flagged if substantial vegetation was present that could influence the interpretation of results. Upon importing the dataset rasters, the raw DTMs were converted into hillshade DTMs to enable easier feature delineation in areas where feature boundaries were not visually distinct.

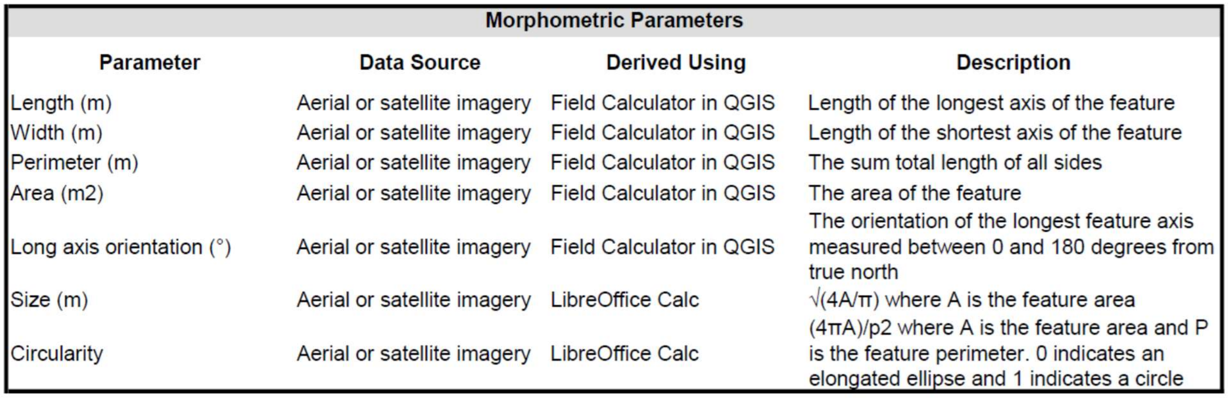

Morphometric Parameters

Parameter	Data Source	Derived Using	Description
Length (m)	Aerial or satellite imagery	Field Calculator in QGIS	Length of the longest axis of the feature
Width (m)	Aerial or satellite imagery	Field Calculator in QGIS	Length of the shortest axis of the feature
Perimeter (m)	Aerial or satellite imagery	Field Calculator in QGIS	The sum total length of all sides
Area (m2)	Aerial or satellite imagery	Field Calculator in QGIS	The area of the feature
Long axis orientation (°)	Aerial or satellite imagery	Field Calculator in QGIS	The orientation of the longest feature axis measured between 0 and 180 degrees from true north
Size (m)	Aerial or satellite imagery	LibreOffice Calc	√(4A/π) where A is the feature area
Circularity	Aerial or satellite imagery	LibreOffice Calc	(4πA)/p2 where A is the feature area and P is the feature perimeter. 0 indicates an elongated ellipse and 1 indicates a circle

Figure 2-6: Morphometric parameters are based on those used by Ulrich et al. (2011) and Brooker et al. (2018). Feature = patterned ground or ice-wedge polygon.

Individual patterned ground features described in the results are colloquially described as polygons, though a distinction is drawn between polygons in small-scale patterned ground located at the North Pole Pass and Flateyri sites and polygons located at the ice-wedge polygon site in the Central Highlands. The macro-composition and organization of patterned ground polygons are described as being sorted or non-sorted. Sorted patterned ground consists of well-defined zones separating large and small grained material, whereas nonsorted polygons consist of uniformly distributed material. The size and distribution of the micro-compositional constituents are estimated based on a combination of UAS and eye-level photography. To avoid conflating the sorted and non-sorted terminology used for describing the macro-compositional organization of features, United Soil Classification System (USCS) nomenclature is utilized to describe the micro-compositional soil and gravel constituents within each feature. In USCS terminology, well-graded gravels and sands are composed of a wide range of well-distributed grain sizes whereas poorly-graded gravels and sands are composed of a limited or uniform range of grain sizes.

3.4 Multiscale Surface Roughness Analysis

Surface roughness is commonly used in planetary science applications to determine the composition and morphology of volcanic terrains (e.g. Cao et al., 2015; Florinsky, 2018) and to aid in estimating the moisture content of soils (e.g. Neelam et al., 2020). Applications using surface roughness as a morphometric property for characterizing periglacial landforms was not readily found in existing literature. The surface roughness of the UAS DTMs was measured to quantify variations across different feature morphologies (i.e. feature centers, borders, and margins). Detectable variations of surface roughness could serve as a diagnostic metric for assessing feature age and level of present-day activity (Figure 2-7).

Initially, surface roughness measurements were calculated as a standard deviation of elevation of the DTM following Equation 1, which is a function of the mean and range of the DTM raster in a procedure outlined by Ascione et al., 2008. This procedure involves creating mean and range rasters of the target DTM using the Focal Statistics tool in the Spatial Analyst toolkit in ESRI ArcMap. The settings in the Focal Statistics tool default to a 3x3 cell neighborhood, though this can be adjusted based on the spatial resolution of the dataset. The Raster Calculator is then used to generate the resulting surface roughness raster as a standard deviation of elevation (Equation 1).

Equation 1:

$$\frac{(\text{"}Mean\ DTM\text{"} - \text{"}DTM\text{"})}{\text{"}Range\ DTM\text{"}} = Standard\ Deviation\ of\ Elevation$$

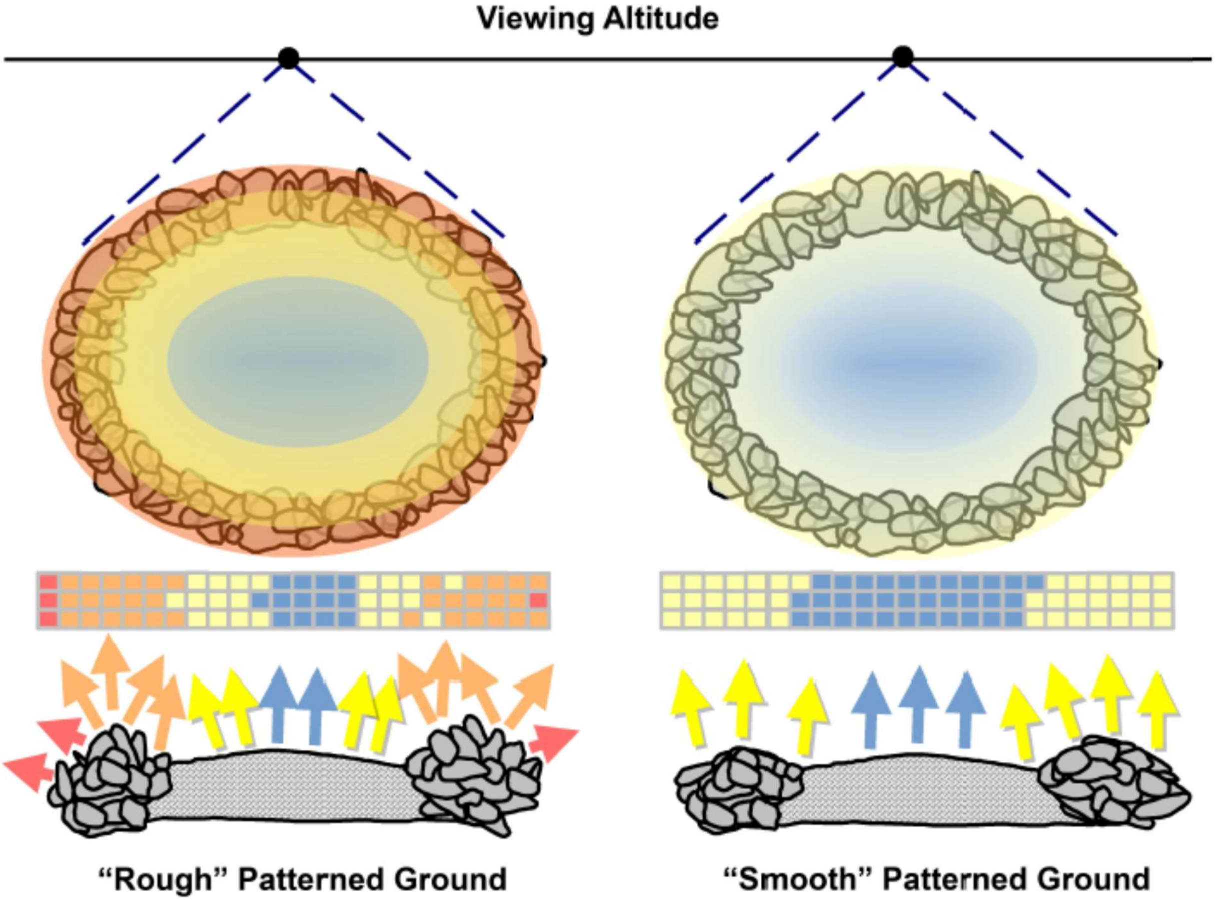

Figure 2-7: Application of surface roughness as a morphometric variable for assessing patterned ground. While variations in surface roughness resulting from the presence or absence of vegetation is expected, variations in micro-surface roughness between similar features could provide insight into feature age and activity in the present-day as a function of feature degradation. In the example above, two visually identical stone circles when viewed from above are differentiated based on variations in surface roughness along the margins.

Surface roughness measurements are scale-dependent in terms of the features being studied and the measurements are a direct reflection of the spatial resolution of the dataset, so calculating the standard deviation of elevation at a fixed scale (local neighborhood or cell neighborhood radius, such as the default 3x3 parameters) is insufficient to account for variations in feature scale and spatial resolutions across different datasets. A manual alternative could involve repeating the steps outlined above but modulating the cell radius of the local neighborhood to account for a range of scenarios applicable to each dataset. The challenge of modulating

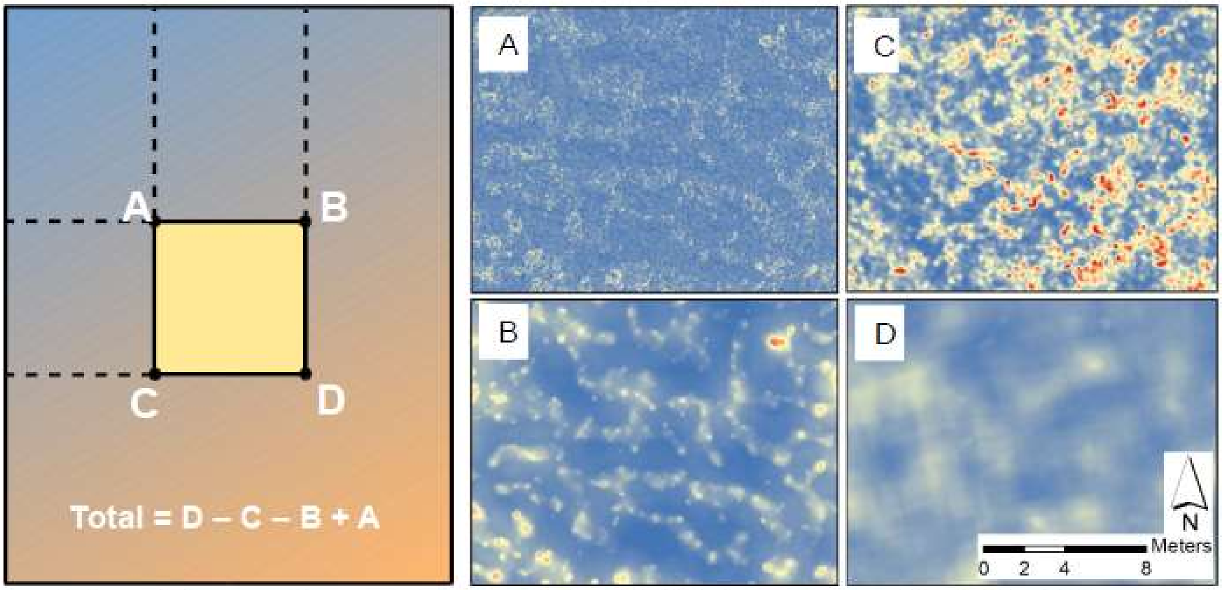

Integral Image Concept (Adapted from Lindsay et al., 2015)

Fixed Altitude Variable Scale

Variable Altitude Fixed Scale

Figure 2-8: Integral image concept and examples of surface roughness under different scenarios. Images A) and B) show a patterned ground survey performed at 7.5 m agl where $r_f = 3$ in A) and $r_f = 100$ in B). Images C) and D) represent a different survey area, where data at C) was collected at 7.5 m agl and $r_f = 100$ and D) was collected over the same area at 85 m agl with the same $r_f = 100$.

iterative surface roughness calculations for variations in scale has been ameliorated via the development of QGIS and ArcGIS tools available within the Whitebox Tools plugin (Lindsay et al., 2019). Lindsay et al. 2019 details a method for utilizing the Multiscale Roughness tool to assess DTMs at a range of scale inputs. This method involves calculating an integral image at a defined filter radius (scale or cell neighborhood radius) with a resulting surface roughness output representing an average roughness (in degrees) at the specified filter radius (r_f) interval (Figure 2-8). In high-resolution UAS datasets, surface roughness at a small scale (or small cell neighborhood radius) can reflect features as small as gravels or boulders depending on the flown survey altitude. At a large filter radius for the same base dataset, the resulting surface roughness will asymptotically approach the average surface roughness of the entire study area such that individual meter-scale features become indistinguishable in the multiscale surface roughness dataset.

3.5 Statistical Analysis

The Zonal Statistics tool was used to calculate, aggregate, and export the resulting geospatial datasets from QGIS. The datasets were exported in a .xlsx file format, so the statistical analysis of the resulting datasets was performed using a combination of built-in tools for Microsoft Excel and the XLSTAT extension developed by Addinsoft. The mean, median, and standard deviation of the baseline morphometric properties and MSR analysis output was tabulated and presented in graphical form. Raw feature orientations were recorded from 0 deg (north) to 180 deg (south), so it was it was necessary to calculate the inverse for each feature orientation in order to plot to a rose diagram. Rose diagrams were plotted using the GeoRose application developed by Yong Technology, Inc.

XLSTAT, an extension for Microsoft Excel developed by Addinsoft, was used to perform a multivariate principal component analysis (PCA) of the resulting datasets to identify, evaluate, and quantify any potential correlations within each polygon population. A principal component analysis was employed in a study of patterned ground by Ulrich et al. (2011) to identify and evaluate potential morphometric trends using a similar set of baseline parameters as this study. The objective of the PCA was to identify and quantify any potential correlations between the baseline morphometric parameters and surface roughness calculations.

4.0 Results

Field work was conducted at North Pole Pass, Utah in September 2018 and at the Westfjords and Highlands sites in Iceland between late June to early July 2019. Orthomosaics and DTMs were generated upon the completion of field work. The final morphometric assessments of the sites were completed upon the establishment of common methodologies. The results of selected UAS surveys are grouped according to each respective site in the following subsections.

4.1 North Pole Pass, Uinta Mountains, Utah, U.S.A.

A total of seven UAS surveys were conducted at the North Pole Pass sites (NPP-Survey Number) over a single day in the field as shown in Figure 2-2. The surveys were conducted under clear skies and calm winds with estimated high temperatures between 10 and 15 °C at site elevation. Six of the surveys were pre-planned prior to entering the field and a seventh survey was plotted in the field based on prevailing observations. UAS survey footprints ranged in area from approximately 47,500 m^2 to 95,500 m^2 . A total of 99 hummocky polygons were characterized from five of the seven surveys during subsequent geospatial dataset processing and analysis.

Water could be heard moving beneath boulders along polygon margins at some locations in NPP-1, NPP-2, and NPP-3. Water was visible at the surface near NPP-3 forming a densely vegetated bog, prompting a field-planned survey to be conducted to provide coverage of the area (NPP-7). It is not clear if the draining water was originating from an upgradient source or from perched groundwater. No residual snow pack was observed on nearby peaks. Climate data from the closest National Weather Service (NWS) monitoring station is located in Vernal, Utah, approximately 60 km southeast of North Pole Pass at approximately 1600 m asl. While precipitation rates in the mountains at the site are likely to have been higher during the seasonal monsoon (which peaks between approximately June and August), the station at Vernal received 0.50 mm of rain during September 2018 compared to a monthly average of 27.43 mm (NWS climate data, accessed 2021).

Vegetation is common across the study area and is nearly ubiquitous for polygon centers (Figure 2-9). Where vegetation is present, grasses and alpine shrubs were observed primarily on the higher ground of well-drained polygon centers and shoulders. The preference for vegetation growth on the polygon high centers creates a visible contrast between many of the feature centers and margins (Figure 2-9, images A-C), however the vegetation growth is irregular and not perfectly constrained by topography. It is for this reason that polygon high centers were delineated based on the UAS-generated DTMs.

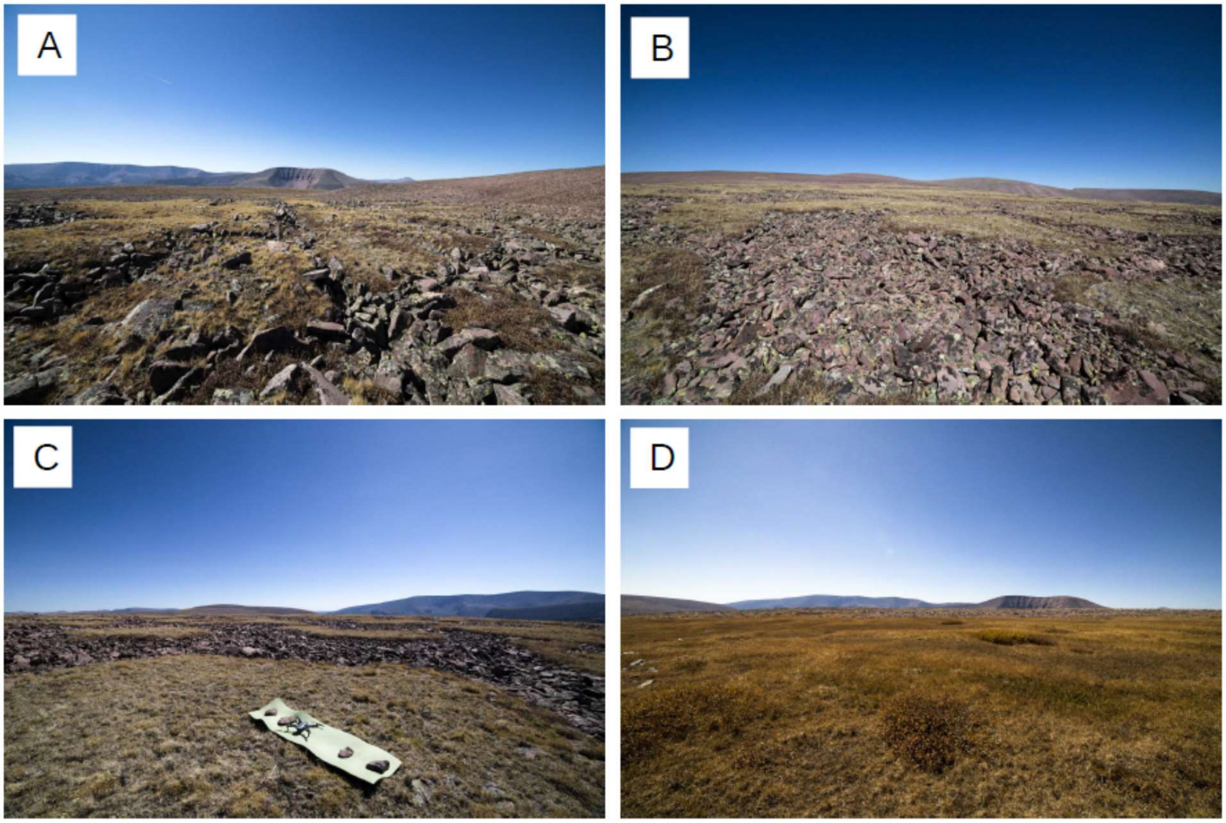

Figure 2-9: North Pole Pass survey area locations viewed at ground level. NPP-2 (A) had the smallest distance between polygon centers and margins. A cirque is visible along a mountain across the valley looking west from NPP-2. The surface morphology at NPP-4 (images B and C) is representative of the morphology across much of the North Pole Pass area, with vegetated centers hosting grasses and alpine vegetation and largely vegetation-free margins composed of large granitic boulders. NPP-7 (D) was heavily vegetated with hummocks obscured by vegetation growth.

Nearly continuous vegetation was present across polygon centers and margins in the NPP-3 survey area and it was not included for further morphometric or surface roughness analyses. The NPP-7 (field-planned) survey was also excluded from further analyses as it covers a boggy area with most of the patterned ground being totally obscured by dense vegetation (Figure 2-9, image D). The geospatial observations for NPP-1 and NPP-5 are representative of the features and morphology observed at the other analyzed survey locations, and they are

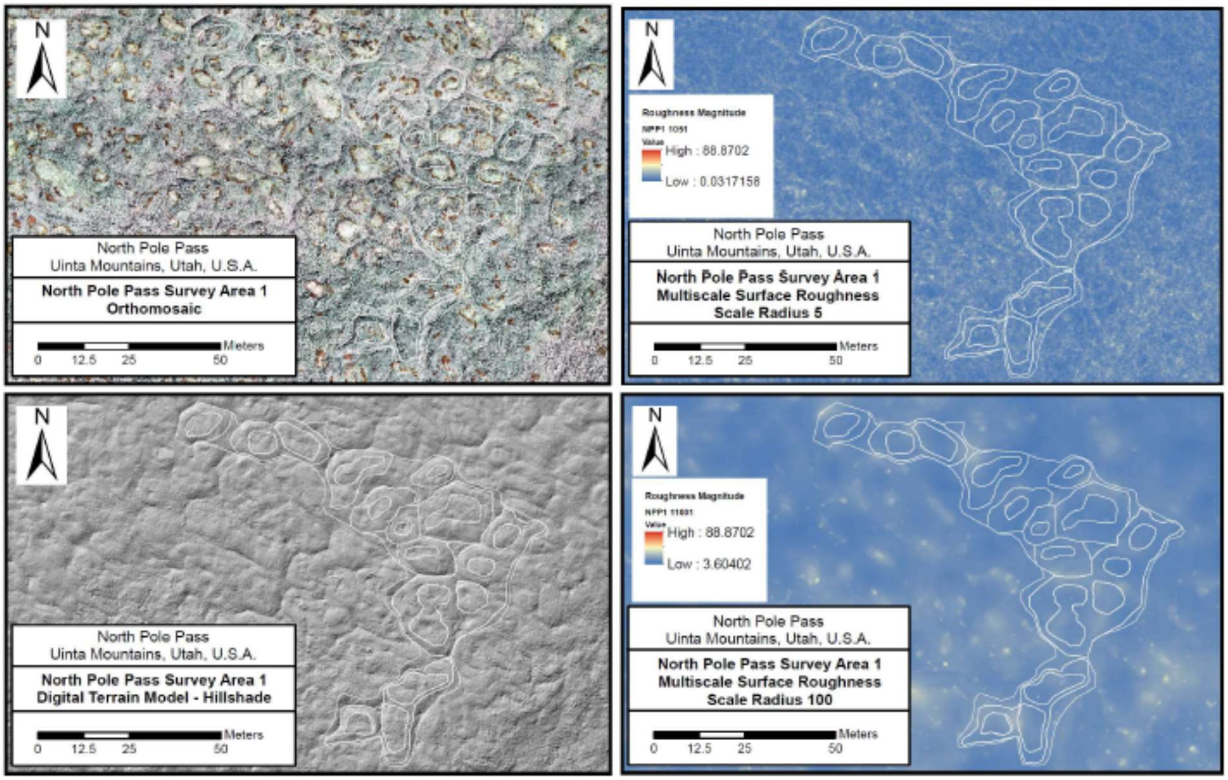

Figure 2-10: From left to right, the NPP-1 orthomosaic, MSR rf=5, survey DTM, and MSR rf=100 raster outputs. I, and roughness vs rf (scale) plot. Surface roughness variations between polygon centers, borders, and margins are less apparent however the provincial differences are apparent in the survey DTM. NPP-1 had one of the lower distributions of vegetation across polygon high centers. Soil horizons, where present, are thin enough to permit the topographic expression of underlying boulders in the DTM, which is subsequently reflected in the MSR analysis.

detailed in Figures 2-10 and 2-11, respectively. The most distinctive surface roughness variations between polygon centers and margins was observed in areas where vegetation was occurring almost exclusively on polygon high centers (i.e. NPP-2, NPP-5 [Figure 2-11], and NPP-6). Where vegetation was distributed partially across high centers and margins, the variation in surface roughness was less well-defined (i.e. NPP-1 [Figure 2-10] and NPP-4). Trenching and soil characterization was not performed during this scope of work, but Munroe 2007 provides a background for soil characteristics at the site.

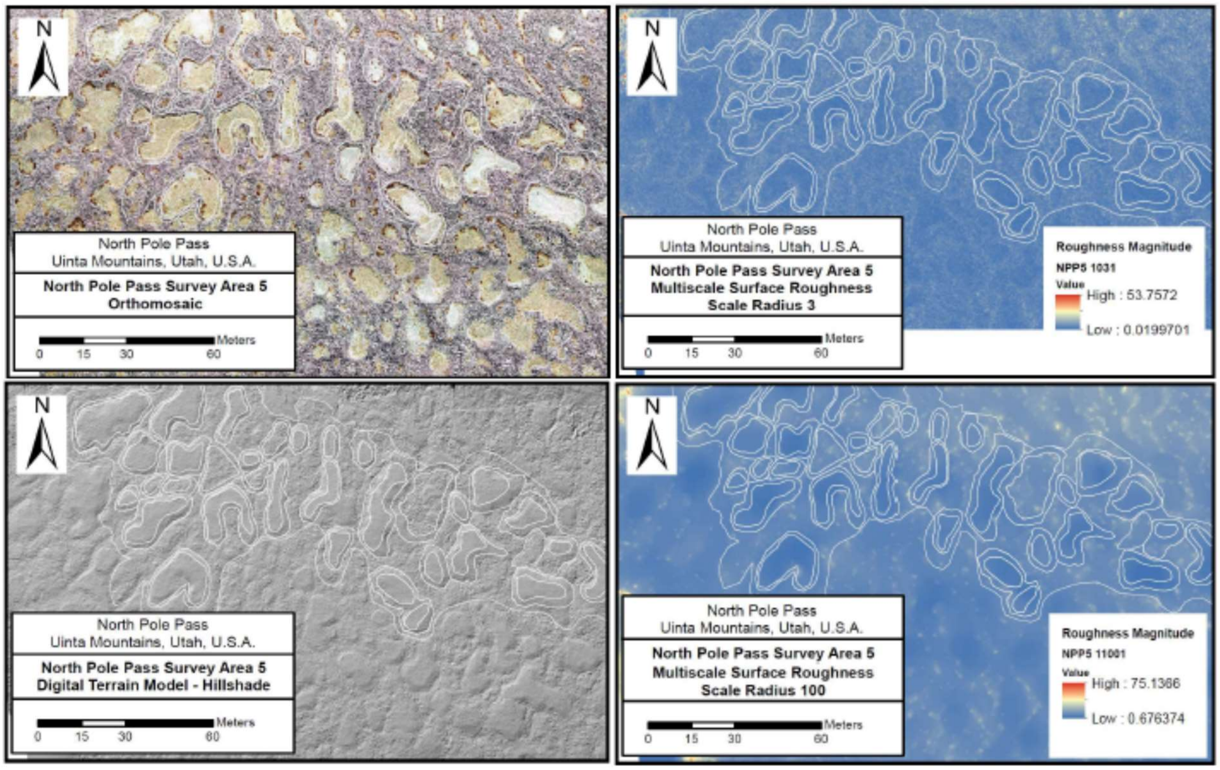

Figure 2-11: From left to right, the NPP-5 orthomosaic, MSR rf=3, survey DTM, and MSR rf=100 raster outputs. The difference in surface roughness between polygon centers, borders, and margins is maintained at scale in both MSR raster outputs and the survey DTM. The difference in roughness is the result of grass, alpine vegetation, and underlying soil that has established on the polygon high centers. Pore space between large boulders that comprise the borders and margins supports a high transmissivity environment permiting perched water flow during the summer that has potentially prevented the establishment of vegetation along margins over the short-term.

The thin nature of soil horizons was evident in some UAS imagery where the shapes of underlying rocks were visible despite dense vegetation coverage.

4.2 Eryrarfjall Peninsula, Westfjords, Iceland

A total of fourteen UAS surveys were conducted over patterned ground on the Eryrarfjall peninsula near Flateyri over two non-consecutive days in July 2019 (Figure 2-3). Surveys were conducted under clear to partly cloudy skies with calm winds during each site visit. Estimated high temperatures ranged from approximately 10°C to 15°C at site elevation. UAS survey footprints ranged in area from approximately 775 m^2 to 72,500 m^2. A total of 449 polygons were characterized from ten of the fourteen UAS survey areas during subsequent geospatial processing and analysis.

Site access partially utilized an abandoned two-track access road that climbs the arc of a glacial cirque northwest of Flateyri. Rock piles (or cairns) supporting the apparent remains of abandoned telegraph or telephone poles run partially parallel the access road on top of the Eryrarfjall plateau (Figure 2-12). The cairns are an apparent testament to the rocky or seasonally frozen ground conditions throughout the area that perhaps prevented setting the poles directly into the ground. A precise age for the derelict poles and cairns is unknown, but the presence of cut segments of wire and several fallen poles suggests the line has been out of service for many years. It is possible that the initial construction could have occurred under colder climate conditions favorable to sustaining shallow permafrost that prevented the stable installation of poles in-ground.

Vegetation is generally sparse across the study areas and its distribution varies where it occurs. Most vegetation occurs along feature margins (Figure 2-12, image A), however in some cases (such as at FPG-7 and FPG-8) vegetation is present in some feature centers (Figure 2-12, image B). While vegetation distribution can vary, survey locations were selected to ensure consistent vegetation distribution across features at each location. Virtually all the surveyed patterned ground is well-sorted featuring defined centers and margins, so polygon centers were delineated based off visual observations and verified against the UAS-generated DTM. While vegetation is present, the observed soil matrix encountered during trench excavation contained a high clay and gravel fraction. Excavating trenches below 0.5 m depth became difficult as larger gravels and boulders were encountered in the matrix. Sufficient equipment was not available for excavating deeper trenches, however spot temperature and soil moisture measurements were made to estimate the depth to the local frost line or permafrost (Figure 2-13).

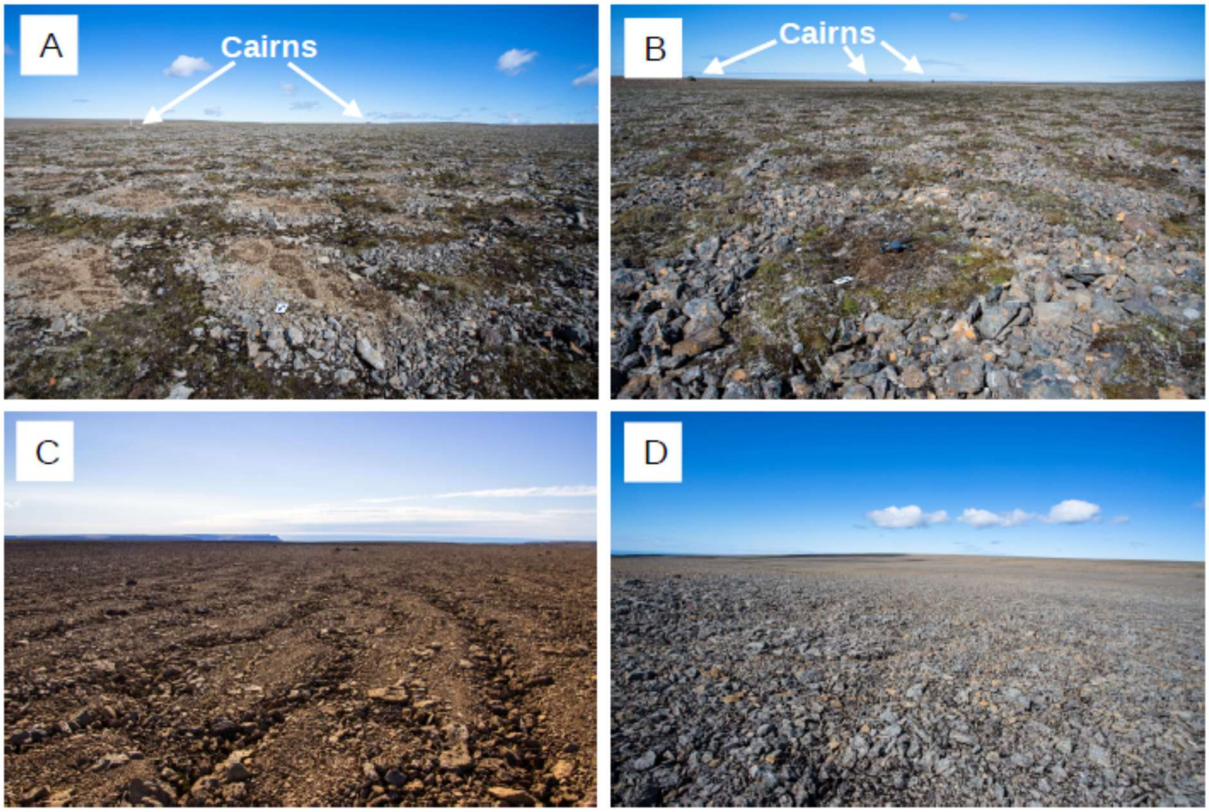

Figure 2-12: Flateyri Patterned Ground (FPG) survey area locations viewed at ground level. Vegetation-dense margins and vegetation free centers at FPG-1 (A) contrast with vegetation-free margins and vegetation-dense centers at FPG-3 (B). Stone stripes (C) and hummocks (D) were present but less common observed morphologies. Morphological variation appeared to be partially controlled by compositional differences in local bedrock. Cairns, posts, and remnant telecommunications lines visible at FPG-1 & 3 and other sites appeared to previously support a telegraph or phone line before falling into disservice. The use of cairns rather than setting the posts in ground could indicate the presence of permafrost in the past.

Microsorting was frequently observed in small, well graded gravels on polygon centers across surveyed areas on the Eryrarfjall Peninsula (Figure 2-14). Similar microsorting has been reported elsewhere in Iceland and most likely form as a result of needle frost and ice from seasonal and diurnal processes when the surface temperature drops to between -1°C and -2°C and is common in subarctic alpine and maritime settings (Lawler, 1988; Dabski, 2005; Ballantyne, 2018; Brooker et al., 2018). In general, the microsorting was only observed in areas where the largest gravels along the microsorted 'margins' ranged from approximately 4 to 6 cm in length.

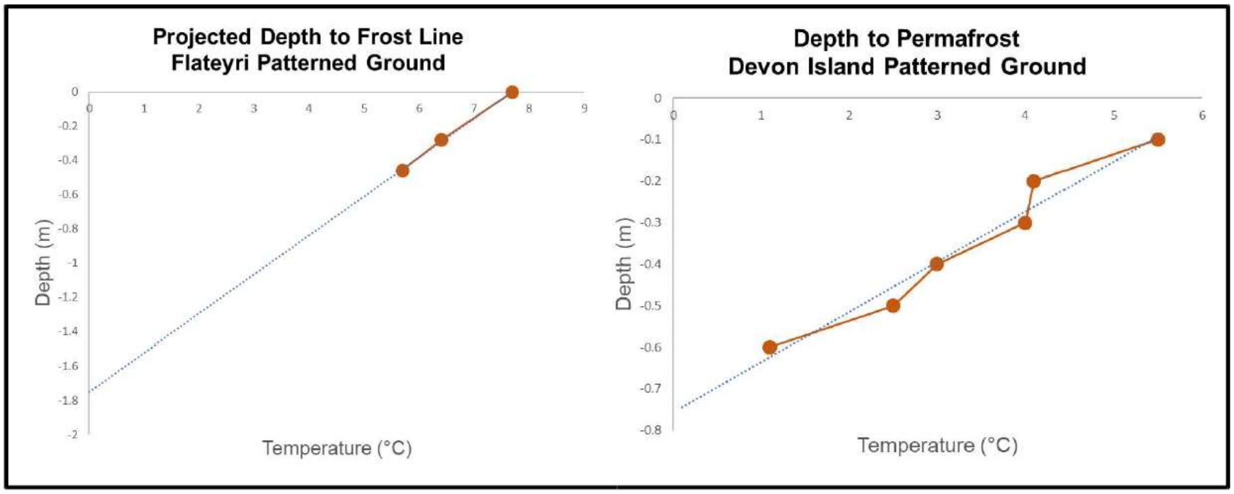

Figure 2-13: Projected depth to frost line based on subsurface temperature measurements at the Flateyri patterned ground site compared to temperature measurements and permafrost depth in patterned ground on Devon Island. Trenching was only possible to 0.5 m depth at Flateyri due to encountering large boulders that limited excavating deeper with the available equipment.

Darker, clay-stained gravels were present in the ‘centers’ of the microsorted polygons and were composed of material ranging in size from fine to coarse grained sands (<1 mm) up to small gravels (10 mm). The clay coating was easily rubbed clean with a small amount of water. The presence of the clay-stained gravel indicates relatively recent exposure to the surface as seasonal rainfall had not washed the gravel clean.

A total of eleven survey areas were assigned sequential Flateyri Patterned Ground (FPG-Survey Number) designations during pre-field flight planning activities. One of the pre-planned survey areas was not visited due to waning battery life towards the end of the first day in the field. An initial rapid processing of the field datasets following the first day of field work identified areas of interest to conduct follow-up surveys. A total of four follow-up surveys were plotted in the field during the second day of field work and were conducted at a lower flight altitudes (7.5 m agl) to record higher resolution data at the areas of interest. Following the generation of survey orthomosaics and DTMs, an assessment of survey quality was performed that looked at factors

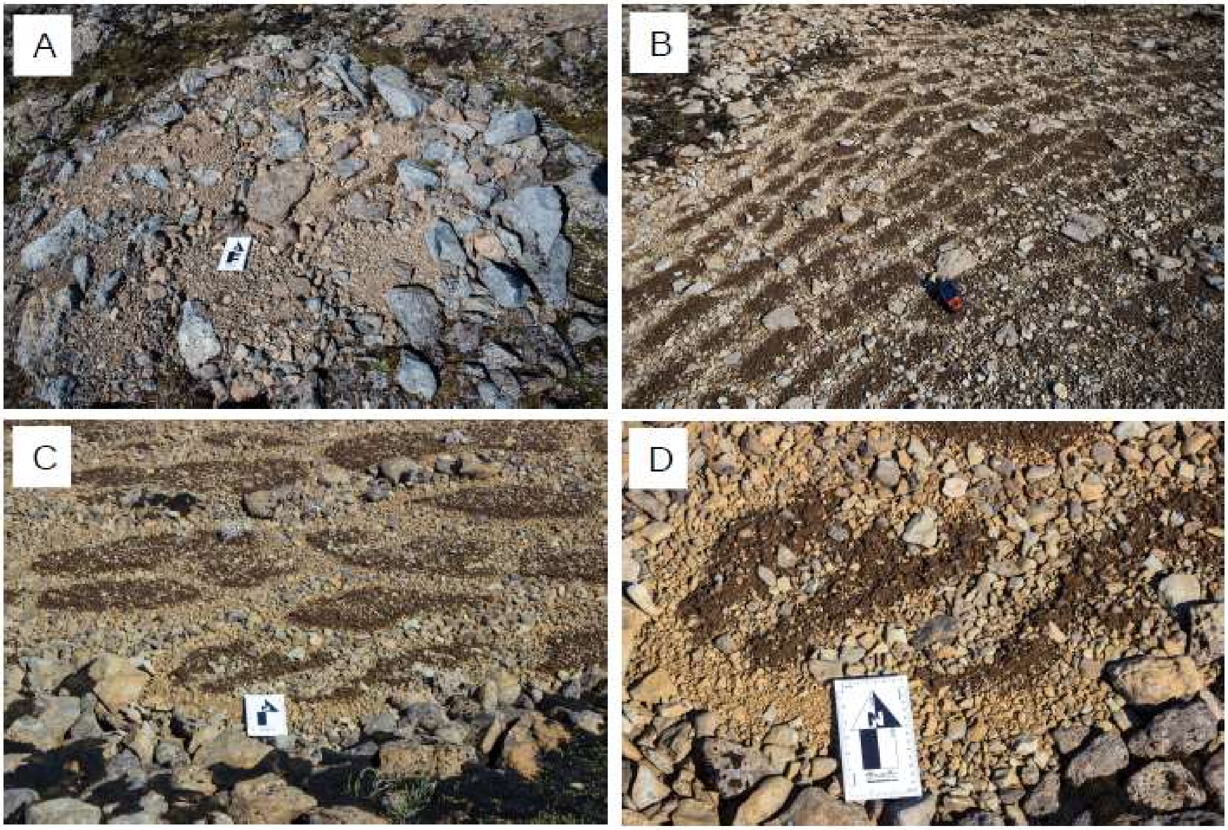

Figure 2-14: Examples of microsorting in FPG polygons. Intra-polygon microsorting of larger gravels and small boulders was visible in some polygon centers at FPG-1 and other sites (A). Microsorting of small gravels was also observed in vegetation-free polygons at several sites, including FPG-X25 as shown in B-D. The small gravels in the dark centers were covered in reddish-brown clay indicating the sorting had occurred recently, potentially in response to seasonal or diurnal freeze-thaw cycles. Notably, only small round to subrounded gravels were observed in the darker material of the microsorted centers. Angular clasts were rare to absent in the dark microsorted centers that were examined.

including image quality, extent of vegetation, and the degree to which individual features could be visually distinguished. The survey quality assessment determined that a combination of four of the pre-planned and follow-up survey locations did not provide adequate coverage of discernible patterned ground features and were thus excluded from further analysis. The 10 survey areas were grouped based on feature morphology into the following subpopulations (with representative figures): Stone Hummocks (Figure 2-15) Stone Circles - Low Resolution Surveys (Figure 2-16), Stone Circles – High Resolution Survey at FPG-X25 (Figure 2-17), Stone Polygons (Figure 2-18), and Stone Stripes (Figure 2-19).

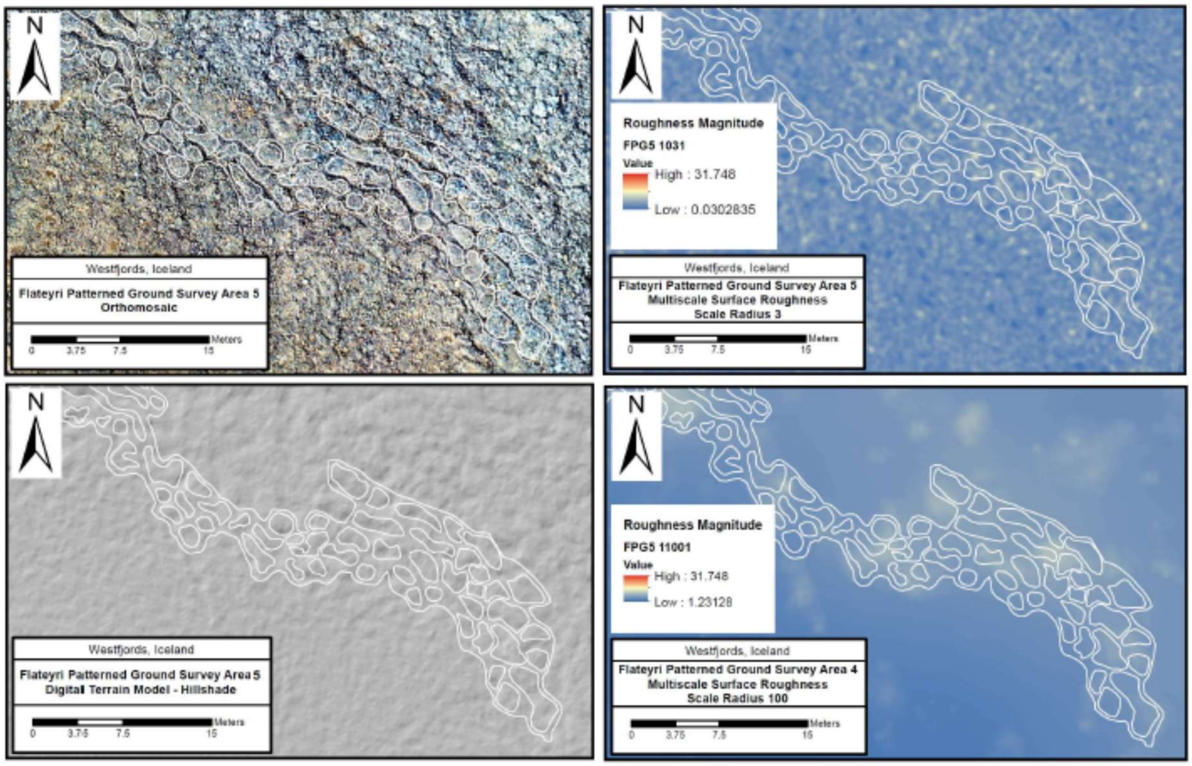

Figure 2-15: Orthomosaic, DTM, and MSR raster images for the FPG-5 survey area. The small variation of surface roughness observed between hummock centers and margins is attributed to the relatively homogeneous composition of large clasts across centers and margins.

The hummocky polygons at FPG-5 were evaluated for their morphological similarities to the hummocky patterned ground observed at NPP. In Figure 2-15, morphometric variations between centers and margins are apparent in the survey orthomosaic and DTM. Results from the MSR analysis at $r_f = 3$ show some variation in surface roughness with higher roughness values occurring within polygon centers and smoother roughness values occurring along polygon margins. At $r_f = 100$ of the MSR analysis, differentiation of surface roughness between polygon centers and margins is not distinct.

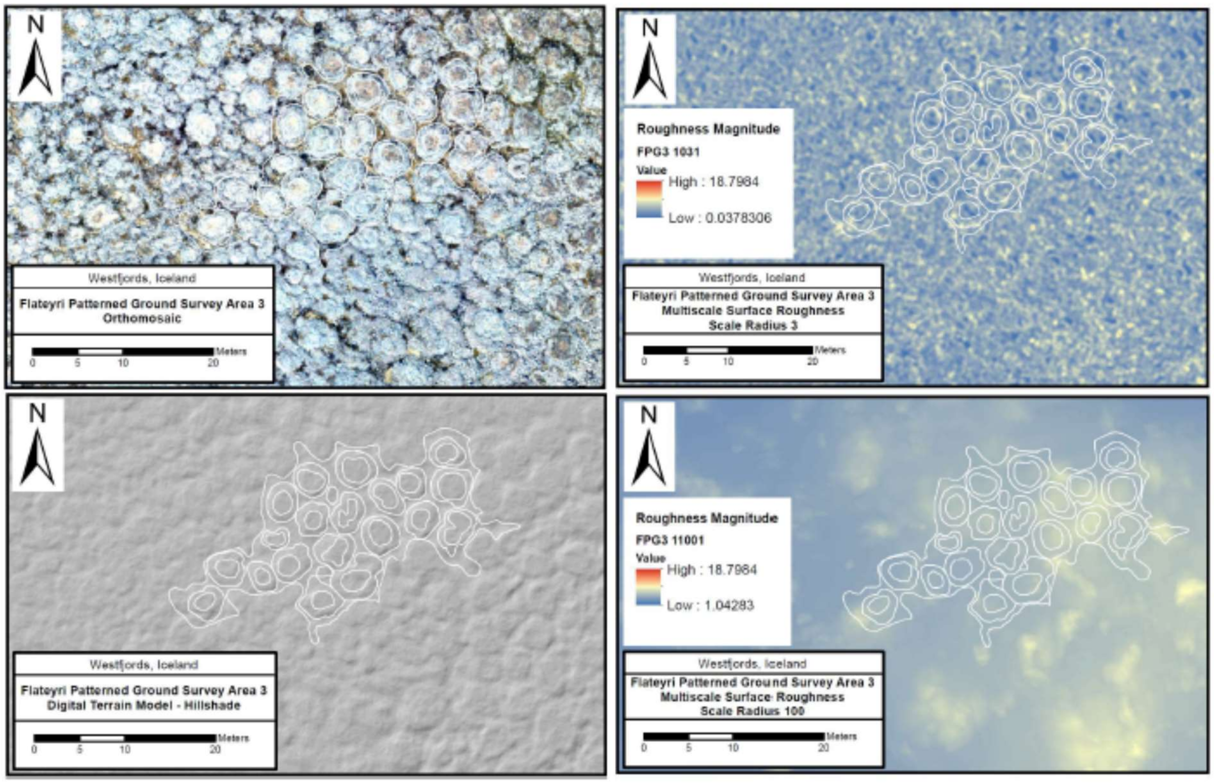

Figure 2-16: Orthomasic, DTM, and MSR raster images for the FPG-3 survey area. Polygons at FPG-3 were typical of the broader stone circle population that was characterized at Flateyri. Polygon high centers are prominently visible in the survey DTM and translates to some features in the resulting MSR analyses. Large rocks along polygon margins are resolved at rf=3 and blend across the margins at rf=100. Lower surface roughness parameters in polygon centers are more apparent at rf=3.

The low-resolution surveys of stone circles comprised the largest population of polygons at the FPG site. Figure 2-16 details a series of stone circles at the FPG-3 survey area that are visually distinct in the survey orthomosaic and DTM. The prominent polygon high centers that are prominently visible in the orthomosaic and DTM translates to some distinct variation in surface roughness in the resulting MSR analysis. Large rocks along polygon margins are resolved at r_f = 3 but start to blend across the margins and centers at r_f = 100. Lower surface roughness values in polygon centers are more visually apparent at r_f = 3.

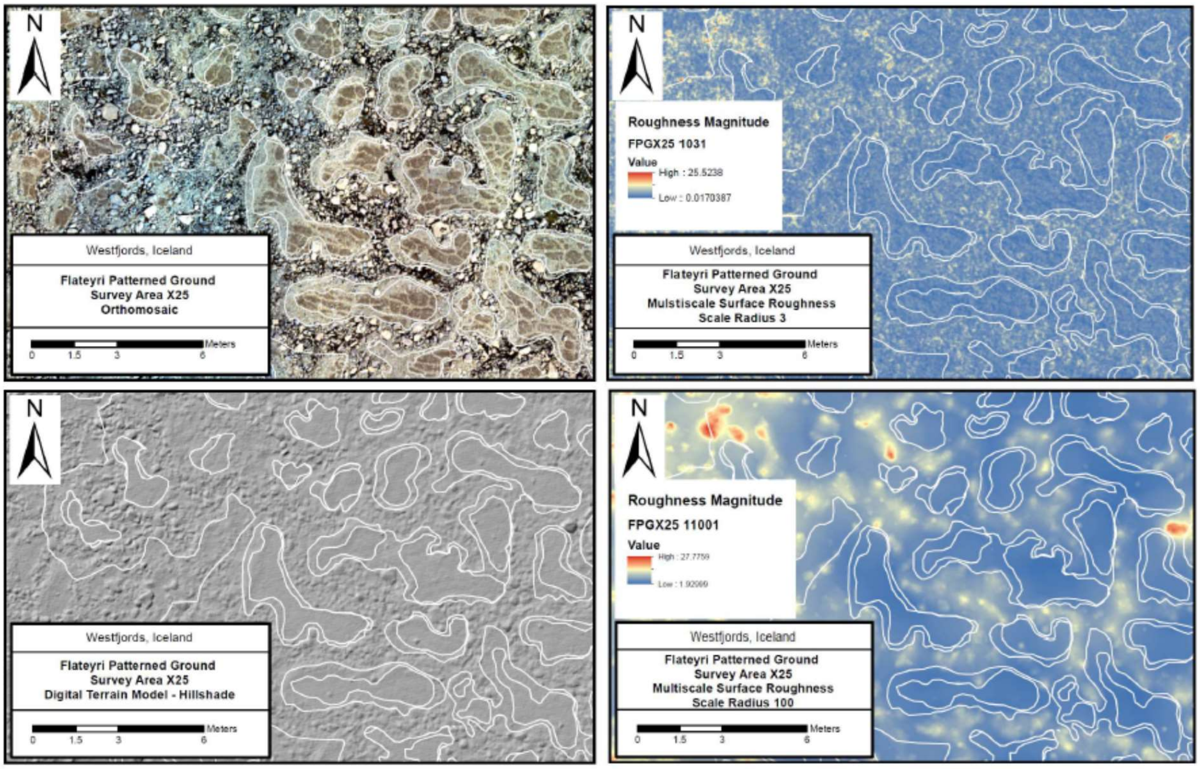

Figure 2-17: Orthomasic, DTM, and MSR raster images for the FPG-X25 survey area. The highest resolution survey of the project was performed at FPG-X25 at 7.5 m agl. Individual rocks down to 0.02 m across are resolved in the resulting DTM and rf=3 MSR analysis. Visibility of the largest or most prominent rocks carries through to the rf=100 MSR analysis. Due to the high detection rate of smaller rocks and gravels in polygon centers, the difference in roughness between centers and margins becomes more visually apparent at higher rf values.

To complement the low resolution surveys of the broader stone circle population, a high resolution UAS survey was performed at 7.5 m agl at the FPG-X25 survey area on a subsequent site visit and is detailed in Figure 2-17. The FPG-X25 survey encompasses polygons that have very little vegetation present along the margins and microsorting resulting from needle-ice modification of the surface is prominently visible in polygon centers. Boulders are prominently visible along the margins in the survey DTM and gravels as small as approximately 2 cm across are resolved in polygon centers. These compositional variations are translated to the MSR analysis across all evaluated scales ranging from r_f = 3 to r_f = 100, corresponding to smoother polygon centers and rougher polygon margins.

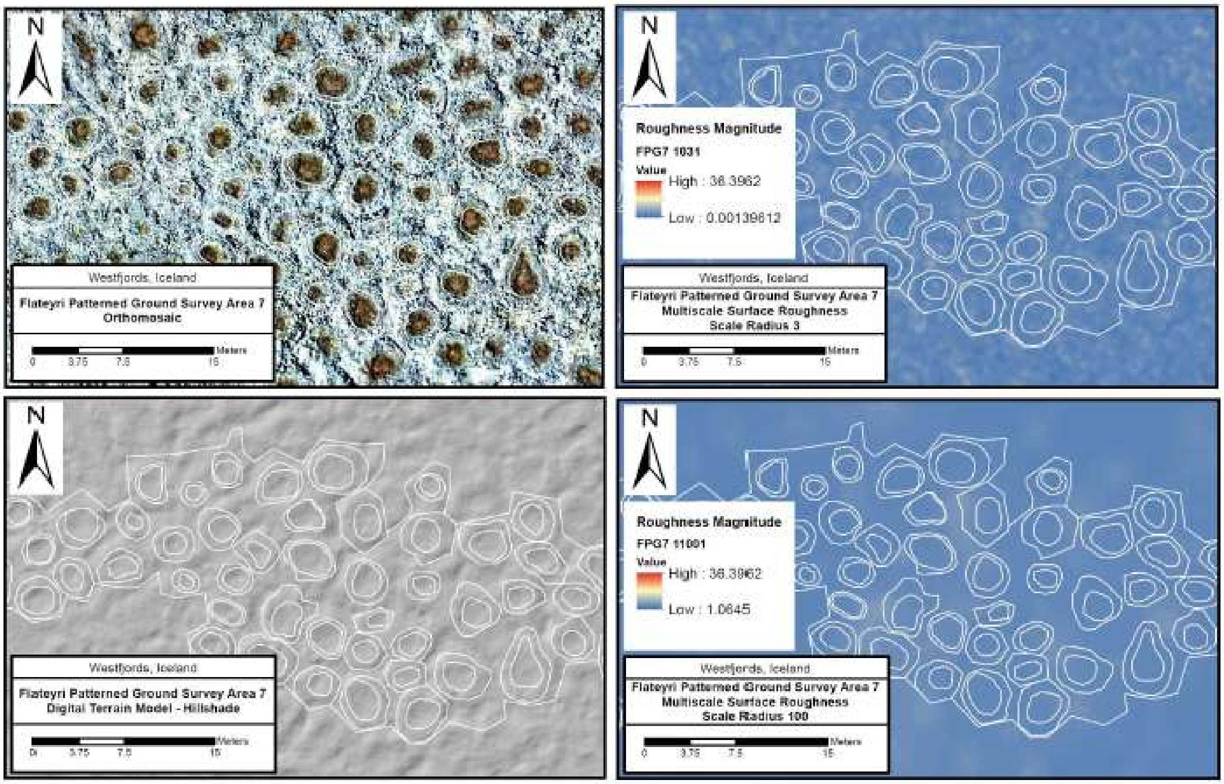

Figure 2-18: Orthomasic, DTM, and MSR raster images for the FPG-7 survey area. Despite the high level of organization and presence of visible polygonal boundaries between the stone circles at FPG-7 in the survey orthoimagery and DTM, the corresponding surface roughness parameters are comparable to observations of other stone circle populations surveyed at Flateyri.

A stone polygon population was characterized at the FPG-7 survey area as a distinct population of stone circles owing to the high level of feature regularity that was observed, including frequently very prominent and sharp boundaries along feature margins that were not observed in any of the other FPG surveys, as shown in Figure 2-18. However, despite the high level of organization and distinct polygon boundaries, the corresponding surface roughness values were comparable to those observed elsewhere at the FPG site.

Stone stripes were observed sporadically where steeper slopes permitted their development, however FPG-6B provided the most distinct stone stripe population that was suitable for individual feature delineation. In Figure 2-19, distinct center, border, and margin regions are visible in the survey orthosmaic and modest surface expressions of varying topography within the stripes are visible the survey DTM. Results from the MSR analysis were not strongly conclusive, however a slight increase in surface roughness is apparent along the border and margin areas of the delineated stone stripes.

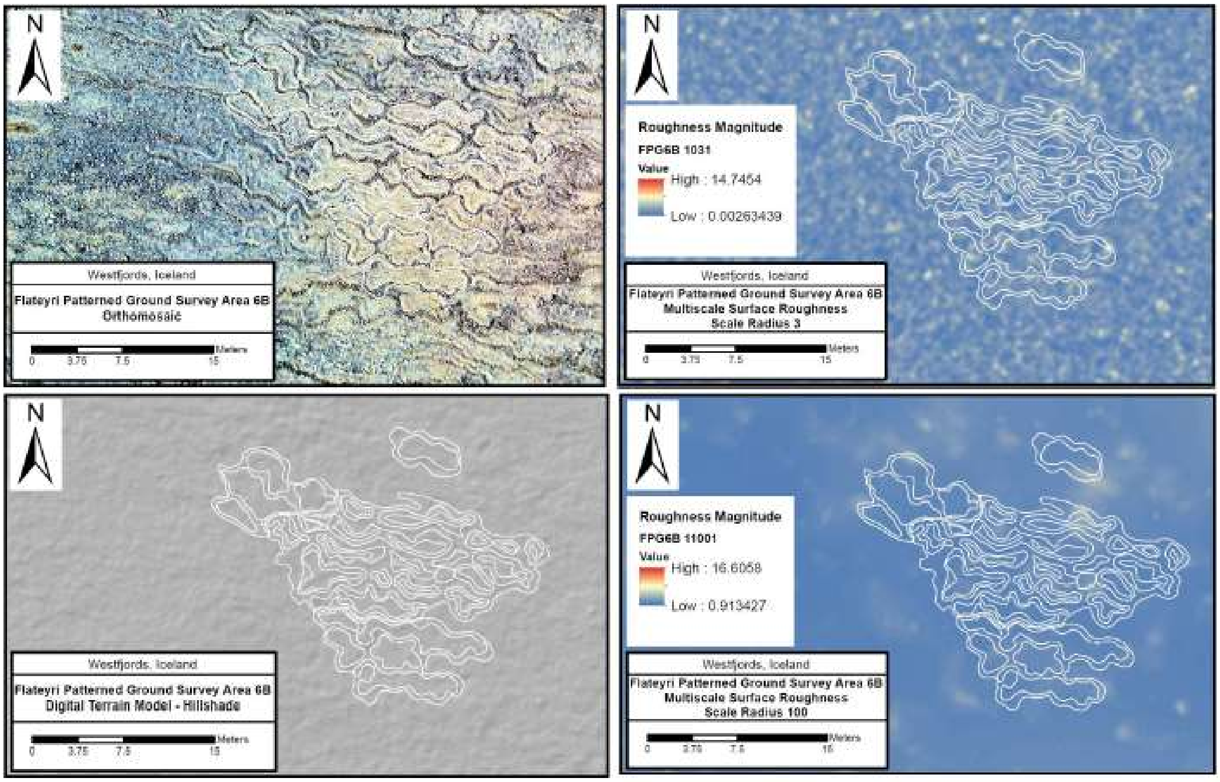

Figure 2-19: Orthomasic, DTM, and MSR raster images for the FPG-6B survey area. The tight concentration of larger gravels and boulders along polygon margins visible in survey orthoimagery is visible in the MSR analysis at rf=3, however the roughness variation becomes less apparent at rf=100.

4.3 Blanda River, Central Highlands, Iceland

A total of ten UAS surveys were performed at ice wedge polygon (IWP) sites located along the Blanda River over three non-consecutive days between late June and early July 2019 (Figure 2-4). Surveys were conducted under clear to cloudy skies with moderate winds. Estimated daytime high temperatures ranged between 7°C and 10°C during the survey work. All of the sites were accessible by a gravel road that allowed for batteries to be recharged in between surveys, enabling larger survey footprints to be achieved. UAS survey footprints ranged in area from approximately 28,500 m^2 to 116,500 m^2. A total of 181 polygons were delineated during subsequent geospatial processing and analysis.

The IWP survey areas are all centered between 200 m and 1,150 m east of the present banks of the Blanda River. While the survey locations were selected based on site accessibility, other well-defined IWPs visible in satellite imagery in the immediate area are also within approximately 1,000 m of the river and its tributaries. The surveyed IWPs are morphologically subdued and can be easily overlooked when viewed from the surface at eye level (Figure 2-20). The IWPs are composed of a combination of well-graded rounded gravels and glacial till deposited by the river. Well-defined IWPs are characterized by having a higher density of vegetation along feature margins, corresponding to areas with a visually higher fraction of fine-grained glacial till and silt exposed at the surface. Vegetation along IWP margins and some IWP centers ranges from sparse to dense and includes a variety of uncharacterized species of grass, lichen, moss, and arctic willow.

A total of eleven survey areas were assigned sequential Highlands Polygon (HPOLY-Survey Number) designations during pre-field flight planning activities. One survey area (HPOLY-9) was inaccessible due to high water levels preventing safe passage at a water crossing along the access road to the site. Following the generation of survey orthomosaics and DTMs, an assessment of survey quality was performed that looked at factors including image quality, extent of vegetation, and the degree to which individual features could be distinguished. The survey quality assessment determined that two of the ten surveyed locations were too extensively vegetated to easily delineate polygons or provide definitive morphometric and surface roughness assessments to non-vegetated polygons and were thus excluded from further analysis.

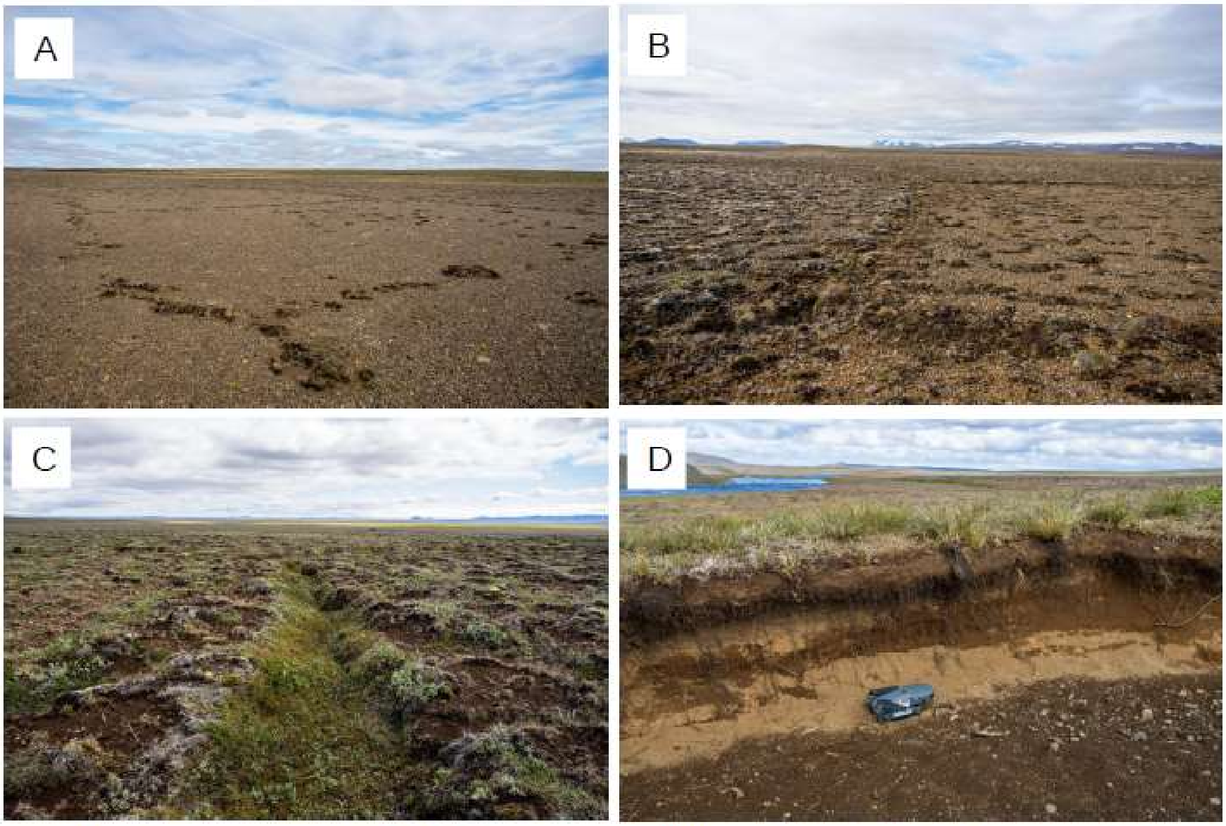

Figure 2-20: Examples of surface morphology at Highlands polygon (HPOLY) survey areas. Most ice-wedge polygons (IWP) were composed of gravels emplaced by the nearby Blanda River to the west, evident in images A and B and visible between vegetation in image C. IWP margins were frequently the only or most vegetated portions of each survey area, as seen in at HPOLY-5 in A. Lichen mats were the most common on less vegetated sites and became more prevalent across IWP centers as vegetation became more well-established (HPOLY-7 and HPOLY-11, B and C respectively). Alpine vegetation (C) and grasses (D) become more commonplace with the progression of pedogenesis. The topographic variation between IWP centers and margins was also observed to increase in proportion to vegetation coverage and a probable corresponding increase in the erosion of associated soils.

Geospatial observations are provided for HPOLY-1 (Figure 2-21) and HPOLY-6 (Figure 2-22) as they feature morphological properties that are common to the polygons surveyed at the other sites. HPOLY-1 is an example of dense-vegetation polygons with a variety of vegetation covering both polygon centers and margins, while HPOLY-6 is an example of polygons with low-vegetation centers and corresponding high-vegetation margins.

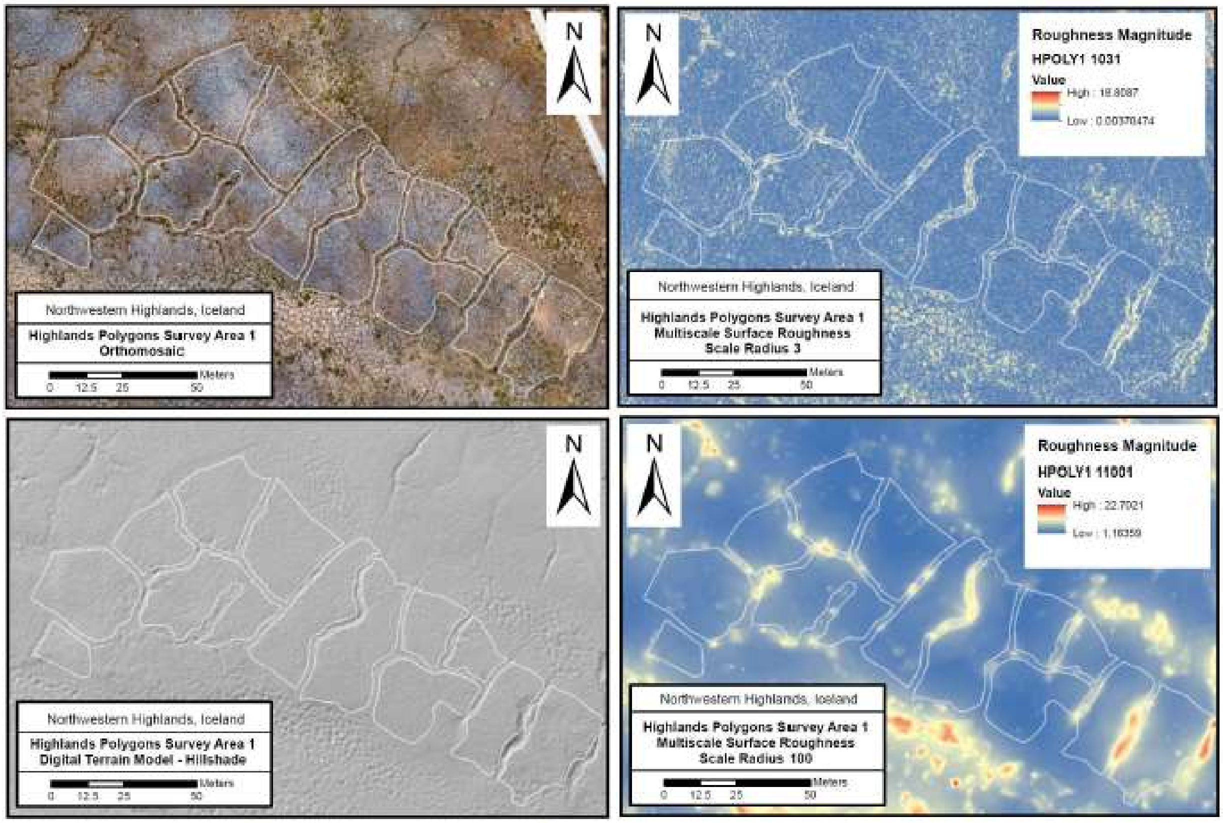

Figure 2-21: Orthomasic, DTM, and MSR raster images for the HPOLY-1 survey area. Topographic variations across polygon margins are reflected in the DTM and in each MSR raster. Roughness magnitudes are observed to increase significantly with scale (rf=100) along polygon margins. While vegetation and lichen mats are present across polygon centers and margins within the survey area and produce some elevated roughness measurements, the greatest variation in roughness is in areas where topographic variations are also present.

At HPOLY-1, visual and topographic variations across polygon centers and margins are apparent in the survey orthomosaic and DTM in Figure 2-21. Variations in surface roughness between polygon centers and margins were consistently visible across all scales of the MSR analysis. Individual clusters of vegetation, larger gravels, and variations in surface topography are visible at $r_f = 3$ with corresponding roughness magnitudes increasing but retaining definition along centers and margins up to $r_f = 100$.

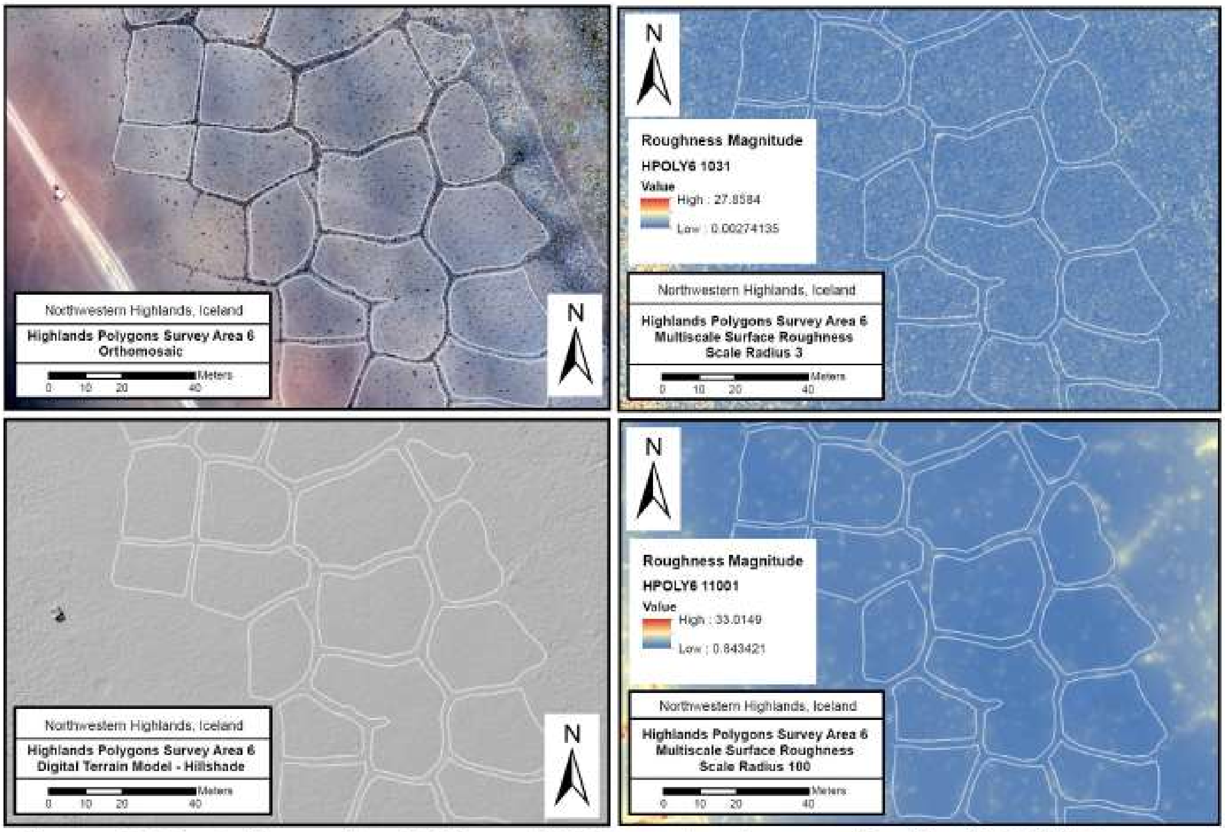

Figure 2-22: Orthomasic, DTM, and MSR raster images for the HPOLY-6 survey area. While lichen mats are prevalent along polygon margins, this does not result in widescale representations in the DTM or MSR rf=3 raster. When the rf is increased to 100, a slight increase in surface roughness magnitude is obeserved along some margins, but the trend is not ubiquitous. In contrast to other Highlands survey areas with larger roughness magnitudes on the margins, this suggests that topographic variations along the margins (i.e. downcutting and degradation) provide a larger overall contribution to margin roughness parameters than vegetation or lichens alone.

While the vegetation and gravels produced some elevated roughness measurements across all scales, the greatest variation in surface roughness is in areas where sharp topographic gradients are present.

At HPOLY-6, lichen mats and vegetation are most concentrated along polygon margins but some vegetation is scattered at a low density across polygon centers, as apparent in the survey orthomosaic in Figure 2-22. While the higher concentration of lichen mats along polygon margins are visibly apparent, this did not translate to visible variations in the DTM or MSR analysis at $r_f = 3$. When the r_f is increased to 100, there is a slight increase in surface roughness that is observed along some of the feature margins. A similar trend is observed at other low-vegetation polygons. The primary difference between the surface roughness variations observed at HPOLY-1 and HPOLY-6 (and similar survey areas) appears to be a higher degree of topographic variability at HPOLY-1 that may be tied to higher rates of feature degradation that is more prevalent among heavily vegetated polygons relative to less vegetated polygons.

Table 2-1

Site	Feature Subpopulation	Number of Features
NPP	DTM-Defined Centers	99
	Vegetation-Defined Centers	120
FPG	Hummocks (FPG-5)	69
	Stone Circles - Low Resolution Surveys	204
	Stone Circles - High Resolution Survey (FPG-X25)	55
	Stone Polygons (FPG-7)	87
	Stone Stripes (FPG-6B)	34
HPOLY	Low-Vegetation Ice-Wedge Polygons	108
	High-Vegetation Ice-Wedge Polygons	73

Table 1: Breakdown of feature subpopulations across the surveyed areas.

5.0 Analysis

5.1 Morphometric Parameters

Following data collection and processing, the morphometric properties of each survey were aggregated and organized into populations for each site that were classified on the basis of shared visual characteristics. A breakdown of the resulting feature classifications are provided in Table 1. Once features were classified into distinct populations, the size, circularity, roughness, and long-axis orientation distributions were assessed for each population. Then the size, circularity, and roughness properties were compared. Finally, the results of the multiscale surface roughness analyses were compared across the assessed filter radius intervals.

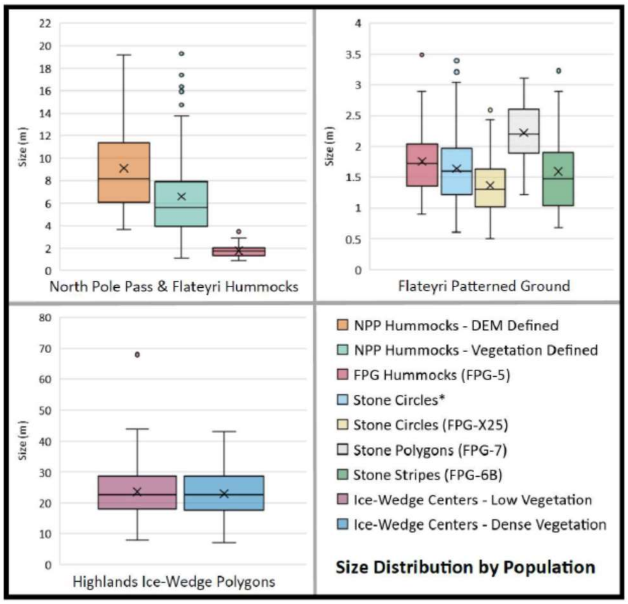

Figure 2-23: Size distribution of patterned ground by population. The ice wedge polygons were the largest features surveyed at approximately 20 to 30 m in size, followed by patterned ground at North Pole Pass at approximately 4 to 12 m in size. Patterned ground at the Flateyri site was generally between approximately 1 to 2.5 m in size.

The size distribution for polygon populations are presented in Figure 2-23. Patterned ground at Flateyri was the smallest ranging from approximately 0.5 to 3.5 m, followed by the hummocky polygons at North Pole Pass that ranged from approximately 1 to 19 m. A comprehensive analysis of orthoimagery from the FPG surveys determined that hummocky patterned ground at FPG-5 shared the strongest visual similarities to the hummocks observed at NPP. While visually similar, the NPP polygons are two to nearly ten times larger than the FPG-5 polygons. The vegetated high centers of the NPP polygons were smaller than polygon high centers that were delineated on the basis of the UAS-derived DTMs.

Circularity was calculated for each polygon as a means of quantifying feature elongation (Figure 2-24). Circularity (or elongation) can be a useful metric in comparison with underlying slope and slope aspect values. However, since slope-specific data was impacted by geometric doming of the DTMs, circularity can serve as a proxy for feature slope. Despite the wide variance in size, the hummocks at FPG-5 and NPP had the most consistent circularity across any population subset, ranging between approximately 0.60 and 0.85.

The circularity is well controlled on the remaining FPG polygon populations. For example, the patterned ground at FPG-7 was the only site to exhibit polygonal morphology with well-defined

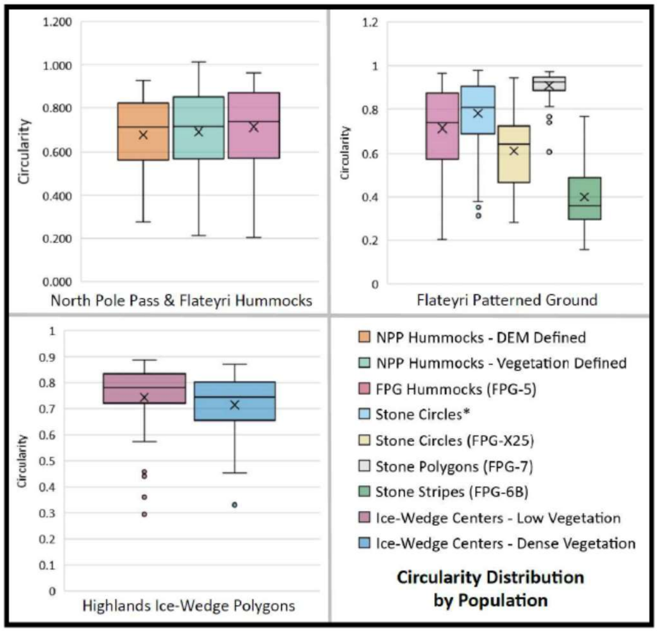

Figure 2-24: Circularity distribution of patterned ground by population. Despite the differences in size presented in Figure 23, the NPP and FPG-5 hummocks shared the highest degree of circularity among the characterized populations. The FPG-7 stone polygons had the highest circularity of observed populations. The high vegetation ice wedge polygons in the highlands were observed to be slightly less circular than low vegetation polygons, which may be the result of topographic variations that permit vegetation growth.

sides. Stone stripes at FPG-6B had the lowest circularity and thus the highest elongation of any feature population. This is consistent with modeling and observations by Kessler and Werner (2003) that stone stripes form on slopes steeper than 10 degrees. The stone stripes also exhibited an observably higher fraction of smaller gravels and lack of vegetation relative to other FPG polygons.

The circularity of low vegetation and dense vegetation IWP in the Highlands were generally similar with vegetated polygons exhibiting slightly lower circularity. One possibility is that polygon degradation and vegetation preferentially establish earlier on slightly sloped ground, which would also allow for greater rates of fluvial transport driving increased erosion rates while also supplying water and potential nutrients for plant life. The other possibility is that the variation is the result of polygon margins becoming more obscured as a result of plant overgrowth. Additional controlled slope and slope aspect data would be required to draw further conclusions.

When size and circularity are compared (Figure 2-25), there is a consistent inverse trend among small-scale patterned ground at NPP and FPG correlating higher circularity with smaller feature size and circularity decreasing in response to an increase in feature size. While this trend is also observed in low-vegetation IWPs at the Highlands site (Figure 2-26), the correlation is

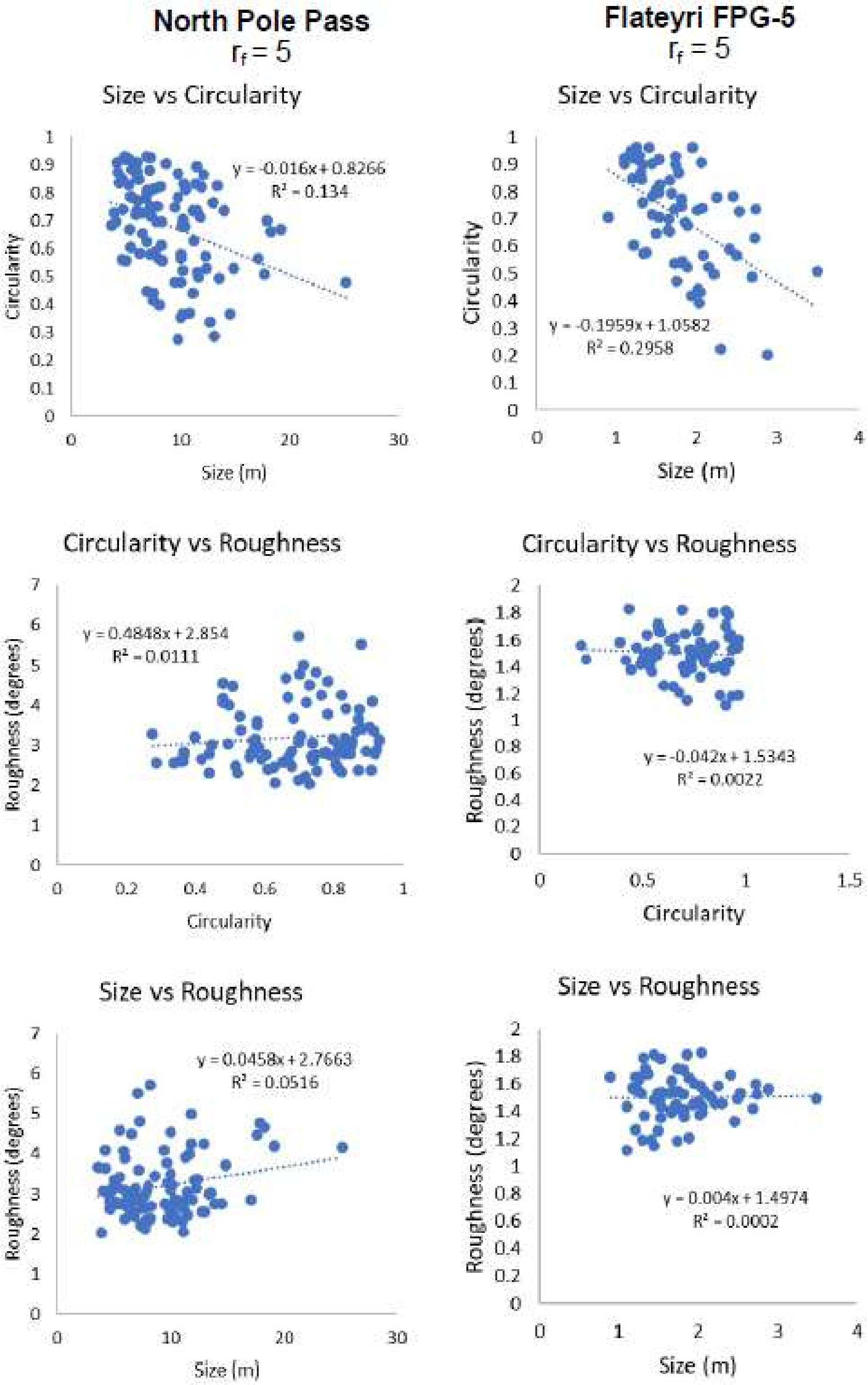

Figure 2-25. Comparison of hummocky patterned ground populations between the North Pole Pass, U.S.A. and Flateyri, Iceland sites. Feature circularity was found to decrease in response to a corresponding increase in feature size at both sites.

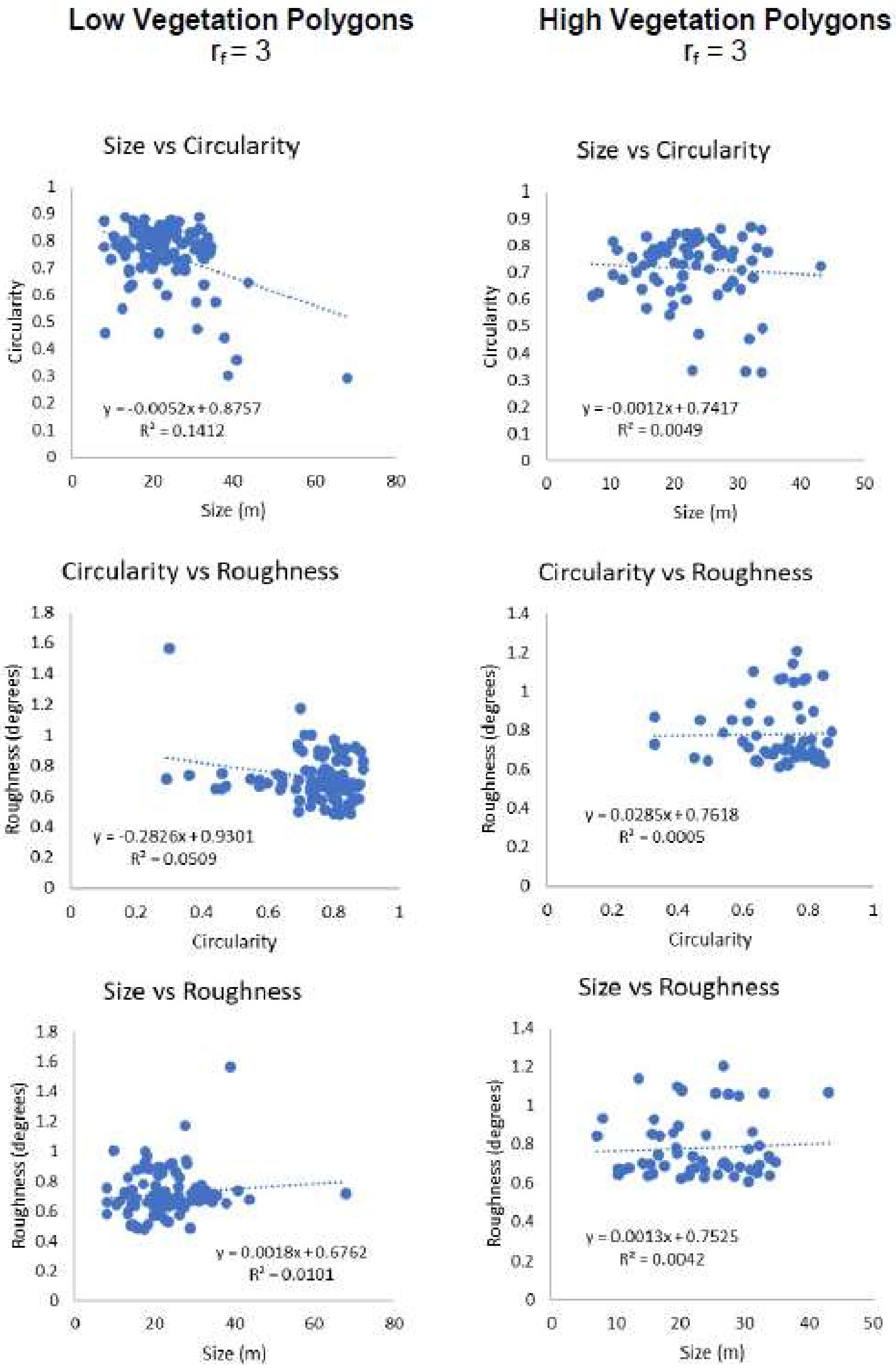

Figure 2-26. Comparison of low vegetation and high vegetation ice wedge polygons in the Highlands, Iceland. Feature circularity was found to decrease in response to a corresponding increase in feature size among low vegetation polygons.

greatly reduced in high-vegetation polygons. As it relates to the observed differences in circularity between the two polygon populations, it is possible that the relative consistency of circularity with size is due to lower landscape slope that allows for the accumulation of water, leading to increased soil moisture content that is favorable for the establishment of lichen mats and other vegetation in feature centers.

Feature orientation was also evaluated (Figure 2-27), however the observations are considered preliminary as feature orientation is often tied to prevailing landscape topography. The DTM-defined NPP polygons had a predominantly southwest to northeast orientation compared to vegetation-defined NPP polygons that did not exhibit a strong directional trend, except for a higher frequency of polygons oriented along a northwest to southeast trend. The elevation across the NPP survey area is understood to be sloped towards the south, ranging from approximately 3700 m asl near NPP-1 to 3600 m asl near NPP-5. The orientation of the NPP hummocks are interpreted to be at least partially transverse relative to prevailing slope of the landscape. The slope underlying the hummocks at the FPG-5 survey area is sloped towards the northwest. The orientation of the FPG-5 hummocks are also interpreted to be partially transverse to the approximate slope of the landscape.

Among the remaining FPG survey areas, the feature orientation was generally along a west to east trend. The downward slope of the Eryrarfjall plateau is generally towards the northwest, with the elevation near the northwesternmost tip starting at approximately 475 m asl and slowly climbing to approximately 655 m asl in the vicinity of the survey areas. Polygon orientation is therefore interpreted to largely coincide with the direction of the prevailing slope of the landscape.

Feature orientation at the HPOLY sites also follow a general west to east trend. This is thought to be at least partially controlled by the slope of the landscape, as the survey areas are all located directly west of the south to north flowing Blanda River. The slope of the landscape in the immediate vicinity of the river would be expected to be slightly towards the river with a slight northward component. What is not clear is if feature orientation coincides with the direction of slope or if polygon orientation is transverse to the direction of the prevailing landscape slope.

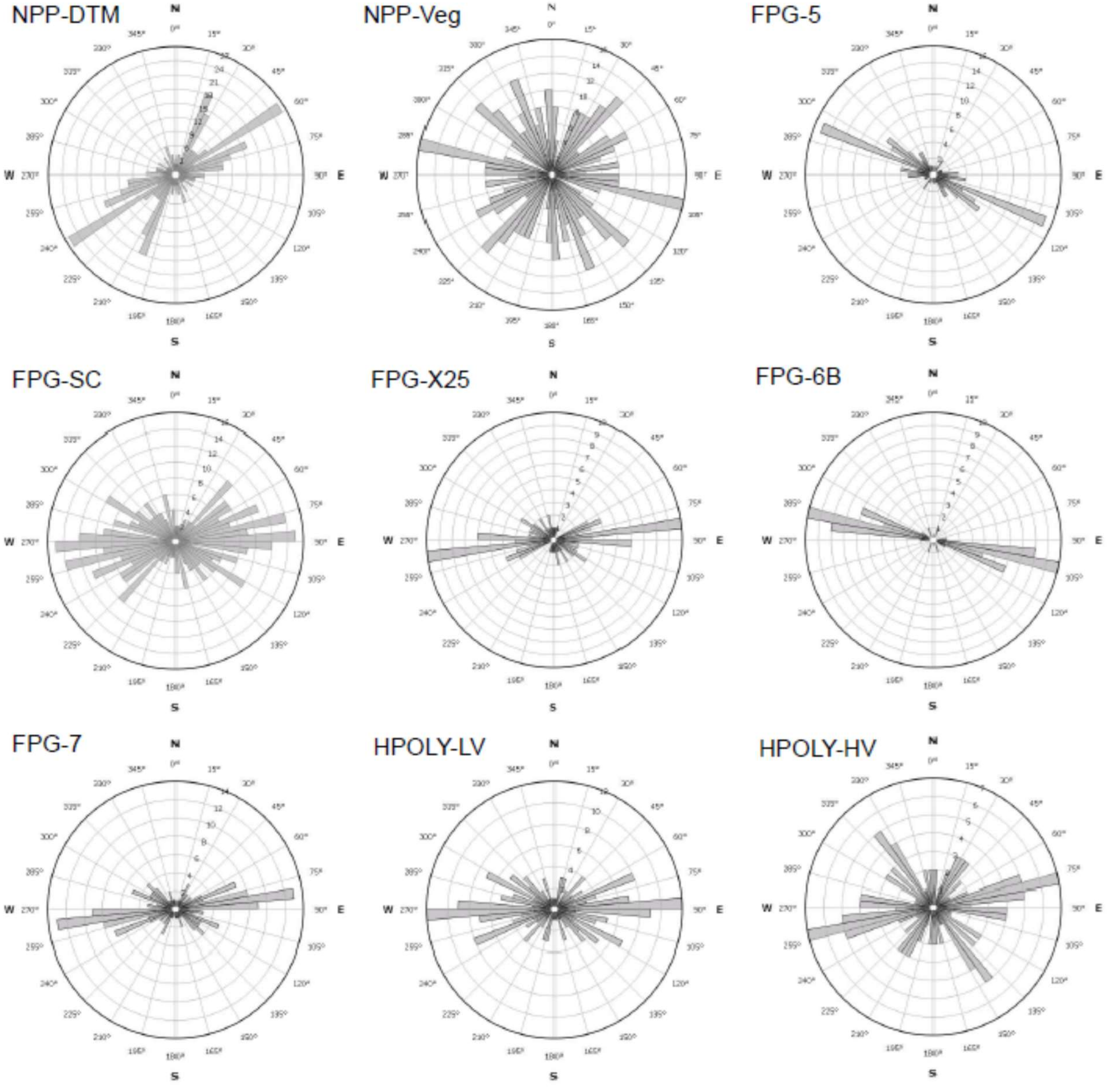
NPP-DTM

NPP-Veg

FPG-5

FPG-SC

FPG-X25

FPG-6B

FPG-7

HPOLY-LV

HPOLY-HV

Figure 2-27: Polygon orientation rose diagrams. Row 1: The orientation of the DTM and vegetation-defined hummocks at North Pole Pass (NPP-DTM and NPP-Veg) are compared to the hummocks at FPG-5. Row 2: The orientation of the broader stone circle population at the Flateyri site (FPG-SC) are compared to stone circles delineated at the FPG-X25 survey and the stone stripes at FPG-6B. Row 3: The orientation of the stone polygons at FPG-7 are compared to low vegetation and high vegetation polygons at the Highlands site (HPOLY-LV and HPOLY-HV).

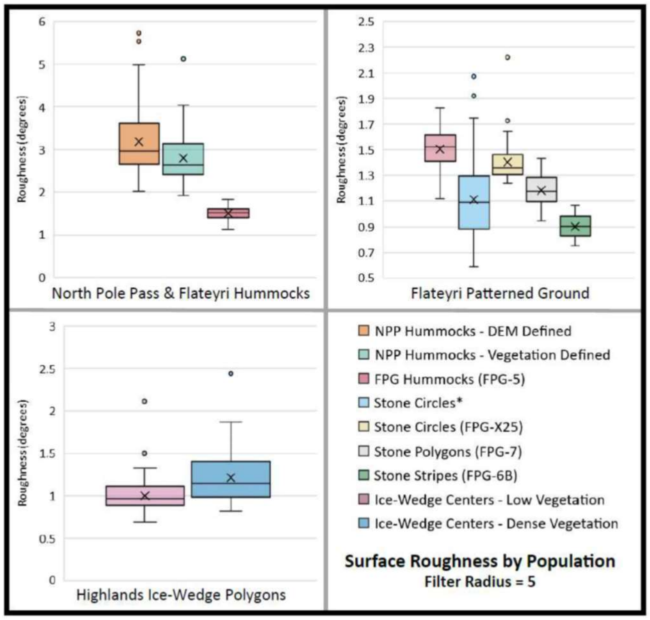

Figure 2-28: Surface roughness of patterned ground by population. The greatest surface roughness was observed in hummocks at NPP. While the NPP hummocks had a higher surface roughness relative to FPG-5, the FPG-5 hummocks had the greatest surface roughness among the FPG sites. The high-resolution survey at FPG-X25 resulted in higher surface roughness parameters relative to other stone circles at FPG, potentially resulting from the detection of smaller gravels across feature centers. High-vegetation IWPs at the HPOLY site had a higher surface roughness relative to low-vegetation IWPs.

5.2 Multiscale Surface Roughness Analysis

The greatest variation across all populations was observed in the results of the multiscale surface roughness (MSR) analysis. Feature centers and margins were delineated based on compositional and topographic variations as differences in surface roughness between feature margins and centers were hypothesized. It was also hypothesized that vegetated features would generally be smoother than non-vegetated features. This hypothesis was verified at NPP where the vegetation-defined centers were on average smoother than the DTM-defined centers (Figure 2-28). However vegetation-dense centers among the Highlands IWPs exhibited a higher surface roughness relative to low-vegetation centers. This discrepancy between the NPP and HPOLY sites can be explained by compositional variations between the hummocks and IWPs. The NPP hummocks are composed of large boulders up to 0.6 to 0.9 m across that create more ‘reflective’ surfaces relative to grass-covered centers when analyzed for roughness. By contrast, the IWPs in the Highlands are composed of well-graded gravels that are rarely larger than 0.07 m across. The surface of the IWPs is reminiscent of a desert pavement with little variation of geological constituents. Lichen mats that grow initially along polygon margins before spreading into centers provide the greatest vertical relief across the polygon centers. It is for this reason that the surface roughness for the majority of the Highlands IWP are less than 2.5 degrees in comparison to the majority of NPP hummocks that have a surface roughness greater than 2.5 degrees.

The patterned ground at Flateyri exhibits surface roughness parameters that fall within a similar range as the Highlands IWPs. As with the NPP hummocks, the hummocky patterned ground at FPG-5 had the highest surface roughness among the greater FPG population as a result of being composed of larger clasts and being free of any vegetation or soil cover. The high-resolution stone circle survey at FPG-X25 had the second highest surface roughness of the FPG subpopulations. The FPG-X25 survey was flown at one of the lowest heights above ground level (7.5 m agl), which when examined at the same $r_f = 5$ as surveys flown at nearly 80 m agl resulted in a higher apparent surface roughness. This is supported by several similar stone circles being captured by the 80 m agl surveys at FPG-2 and FPG-3 and included in the larger stone circles population which has a lower relative surface roughness when compared to FPG-X25. The lowest surface roughness of the FPG population was the stone stripes at FPG-6B, which is most likely attributable to a higher ratio of small gravels in stripe centers with the largest gravels and boulders being confined to smaller, more well-defined feature margins.

While there were consistent variations in surface roughness associated with feature populations, there were no consistent trends when surface roughness was plotted against feature circularity and size (Figure 2-25). Consistent variations are observed when the multiscale surface roughness of feature centers, margins, and borders are plotted (Figure 2-29). In the highest resolution, low-altitude survey at FPG-X25, there is a distinct difference in surface roughness between the centers, borders, and margins of the stone circles. As previously noted in Figure 2-17, individual gravels down to 0.02 m across are resolved in the DTM and resulting MSR analysis at $r_f = 3$, and the contrast between feature margins and centers is visually maintained through at least $r_f = 100$.

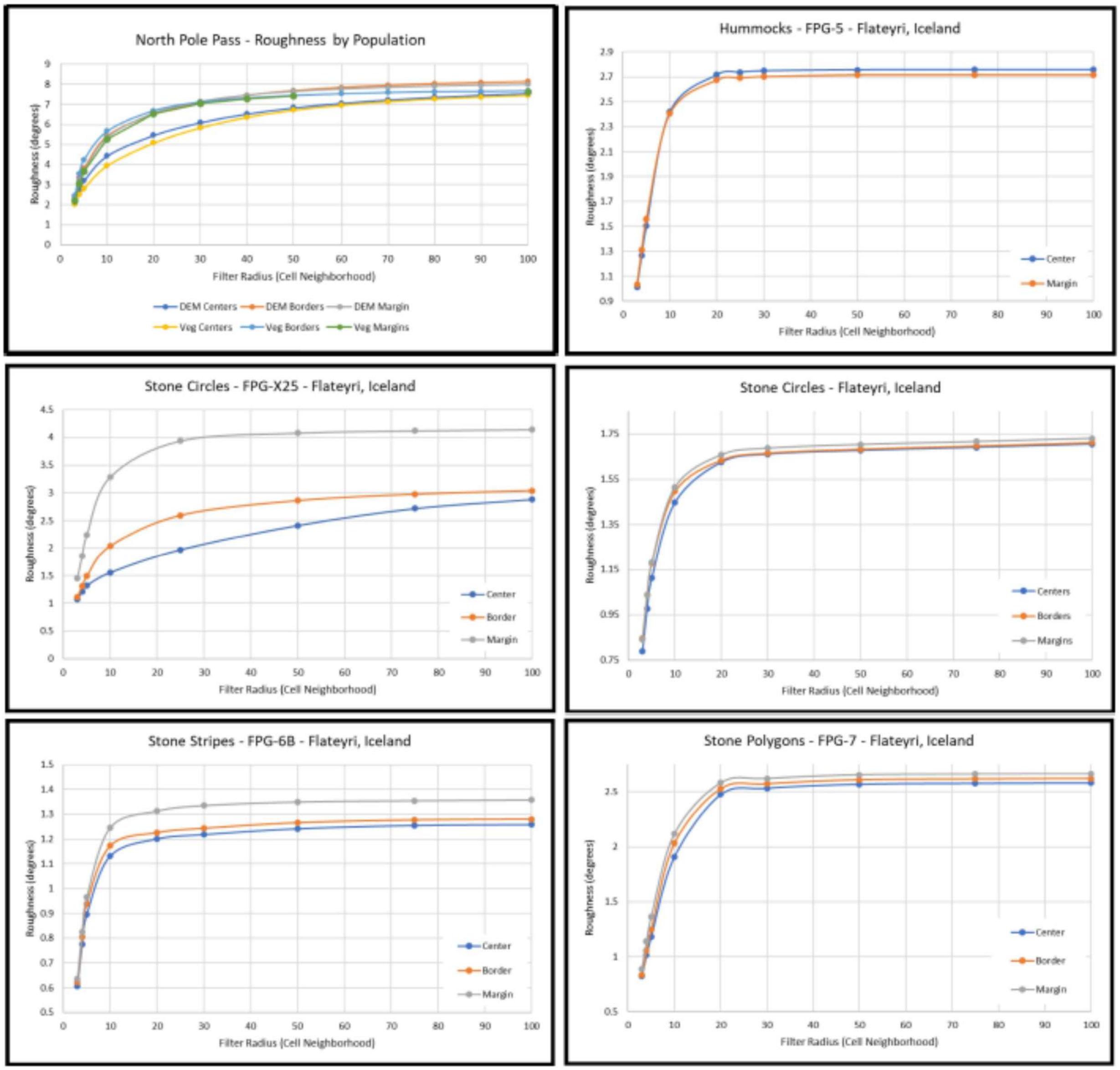

Figure 2-29: Multiscale surface roughness analysis summary of patterned ground populations, with surface roughness displayed in relationship to the cell neighborhood filter radius (r_f). Within most populations, patterned ground centers had consistently lower surface roughness values (smoother) in comparison to higher surface roughness values among feature borders and margins (rougher). This relationship was less conclusive among lower resolution surveys (e.g. Stone Circles, Stone Polygons). Among the FPG-5 hummocks, the relationship is inconclusive due to the low spatial resolution of the survey and the homogeneous distribution of boulders spread throughout hummock centers and margins.

While less profound, similar trends are observed among other Flateyri subpopulations, including FPG-5, FPG-6B, and FPG-7 (Figure 2-29). Comprising the majority of polygons at

Flateyri, the stone circles population has the least distinct variation across polygon centers, borders, and margins, however it retains the same trend as observed at FPG-X25. Stone stripes at FPG-6B had a wider distinction across the observed surface roughness of stripe centers and margins, however this is likely attributed to a sharp contrast in feature composition with centers composed of poorly graded small gravels and margins defined by larger boulders with little transition in material in the border between centers and margins.

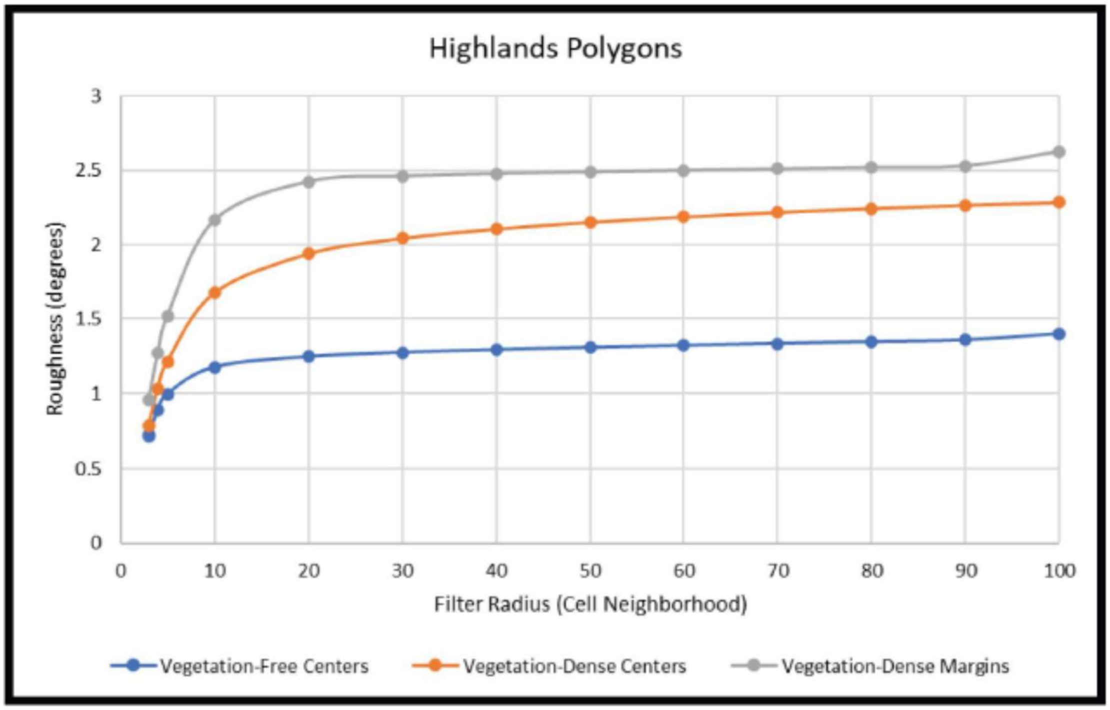

Figure 2-30: Multiscale surface roughness analysis summary of IWPs at the HPOLY site. Despite homogeneous composition and low topographic expression at the surface, vegetation-dense margins and centers exhibited higher surface roughness values relative to low-vegetation centers.

Clear variations in surface roughness were also observed at the Highlands site between low-vegetation and vegetation-dense polygon centers relative to predominantly vegetation-dense margins (Figure 2-30). The observable spread of surface roughness across feature margins was unexpected due to the low relief between most feature centers and margins and that UAS surveys were performed at a similar altitude to the FPG surveys. Considering there is an equitable spread between low and high vegetation polygons, it is likely that the margin results are skewed by the more prominent erosional surfaces of margins with the densest vegetation. This result has implications for performing surface roughness analysis at larger, more defined ice wedge polygons in the future.

5.3 Principal Component Analysis

While notable variations in surface roughness were observed between polygon centers, margins, and borders (as applicable), associations between surface roughness and other morphometric parameters were not immediately clear. A principal component analysis (PCA) was performed to better identify and quantify any potential correlations between morphometric parameters and surface roughness calculations. A correlation matrix for each evaluated morphology is presented in Figure 2-31. A summary of key PCA results for each site are presented in Figures 2-32 to 2-36 and discussed in the following paragraphs.

5.3.1 North Pole Pass, Uinta Mountains, Utah, U.S.A.

At North Pole Pass, polygon centers were delineated based on the photogrammetric DTM and visible distribution of vegetation that appeared to be most concentrated on polygon high centers. Among the morphometric parameters evaluated for DTM-Defined Polygon Centers, a slight positive correlation between polygon width and length is observed (Figure 2-32). This is likely associated with the negative correlation between polygon size and circularity, where polygon circularity is seen to decrease with size as observed in Figure 2-25. Among Vegetation-Defined polygon centers, a similar negative correlation is observed between polygon circularity and size and length, with a slight positive correlation between polygon size and length (Figure 2-32). The variation in surface roughness between polygon centers, margins, and borders that are observed in Figures 2-29 were verified by the factor scores presented in Figures 2-32 and 2-33. While there is some variation between the spread of factor scores between the DTM and Vegetation populations (e.g. DTM-Defined Borders are negative relative to Vegetation-Defined

Borders) the PCA demonstrates the consistency of the observed surface roughness-provincial relationships.

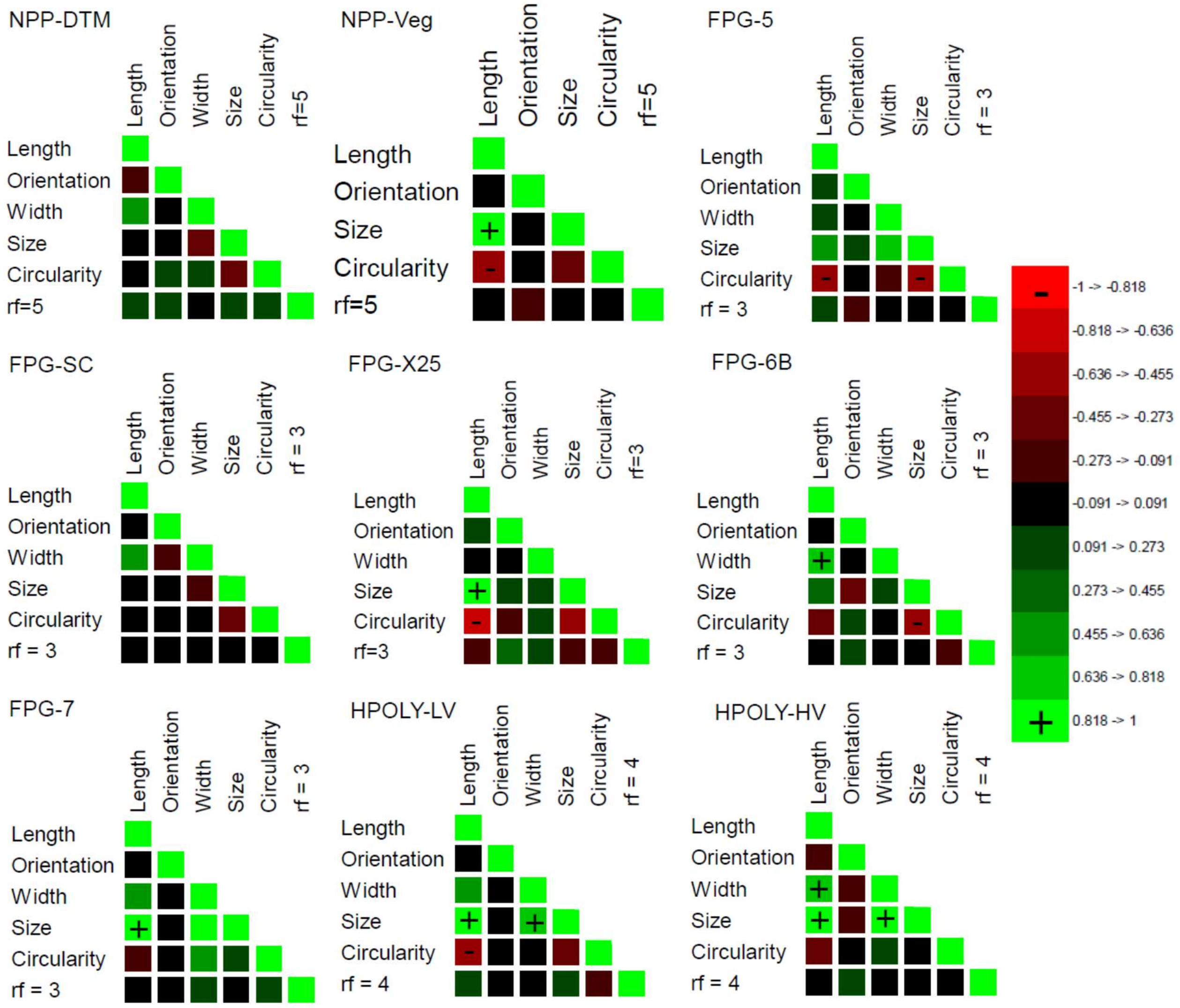

Figure 2-31: Correlation matrix for the evaluated terrestrial patterned ground morphologies. The most common positive correlation was among size-dependent variables including calculated size, length, and width. Circularity was found to be negatively correlated with length and size at some sites, which may be expected as longer patterned ground forms such as stone stripes or nets are typically more oblong.

Morphometric Parameters

Correlation matrix (Pearson (n)):

Variables	Length	Orientation	Width	Size	Circularity	$r_f = 5$
Length	**1**	**-0.240**	**0.526**	-0.054	0.036	**0.215**
Orientation	**-0.240**	**1**	-0.060	-0.036	0.145	0.105
Width	**0.526**	-0.060	**1**	**-0.318**	0.178	0.037
Size	-0.054	-0.036	**-0.318**	**1**	**-0.366**	**0.227**
Circularity	0.036	0.145	0.178	**-0.366**	**1**	0.105
$r_f = 5$	**0.215**	0.105	0.037	**0.227**	0.105	**1**

Values in bold are different from 0 with a significance level alpha=0.05

Eigenvalues:

	F1	F2	F3	F4	F5	F6
Eigenvalue	1.780	1.392	1.201	0.760	0.485	0.383
Variability (%)	29.664	23.197	20.011	12.661	8.087	6.379
Cumulative %	29.664	52.862	72.872	85.533	93.621	100.000

Correlations between variables and factors:

	F1	F2	F3	F4	F5
Length	0.701	0.554	0.038	0.107	0.114
Orientation	-0.149	-0.513	0.590	0.586	0.069
Width	0.833	0.121	-0.046	0.344	0.085
Size	-0.574	0.603	0.264	0.028	0.469
Circularity	0.480	-0.545	0.337	-0.489	0.347
$r_f = 5$	0.111	0.382	0.816	-0.216	-0.346

Polygon Regions & Multiscale Surface Roughness Vectors

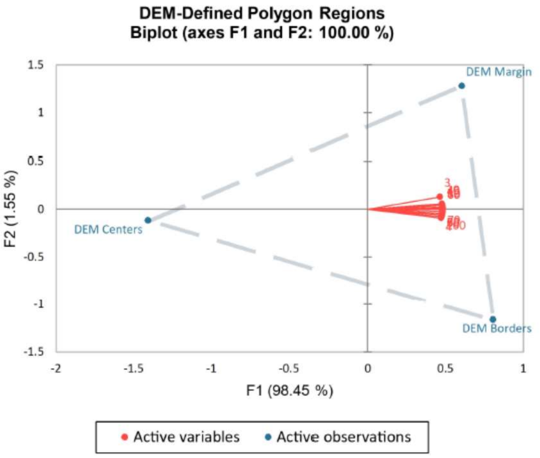

Figure 2-32: Summary of the PCA for the DTM-defined NPP hummocks. There is a slight positive correlation between feature width and length. Factor scores for the MSR analysis of polygon regions reflect the consistently higher surface roughness values in polygon margins and lower surface roughness values in polygon centers.

Morphometric Parameters

Correlation matrix (Pearson (n)):

Variables	Length	Orientation	Size	Circularity	$r_f = 5$
Length	**1**	-0.005	**0.947**	**-0.591**	0.039
Orientation	-0.005	**1**	-0.047	-0.044	-0.166
Size	**0.947**	-0.047	**1**	**-0.443**	0.029
Circularity	**-0.591**	-0.044	**-0.443**	**1**	0.017
$r_f = 5$	0.039	-0.166	0.029	0.017	**1**

Values in bold are different from 0 with a significance level alpha=0.05

Eigenvalues:

	F1	F2	F3	F4	F5
Eigenvalue	2.347	1.173	0.836	0.608	0.036
Variability (%)	46.934	23.470	16.714	12.165	0.717
Cumulative %	46.934	70.403	87.118	99.283	100.000

Correlations between variables and factors:

	F1	F2	F3	F4	F5
Length	0.975	-0.007	-0.002	0.175	-0.140
Orientation	-0.017	0.766	0.634	0.107	0.005
Size	0.927	-0.045	-0.053	0.346	0.124
Circularity	-0.731	-0.127	-0.048	0.668	-0.028
$r_f = 5$	0.041	-0.754	0.655	-0.026	0.003

Polygon Regions & Multiscale Surface Roughness Vectors

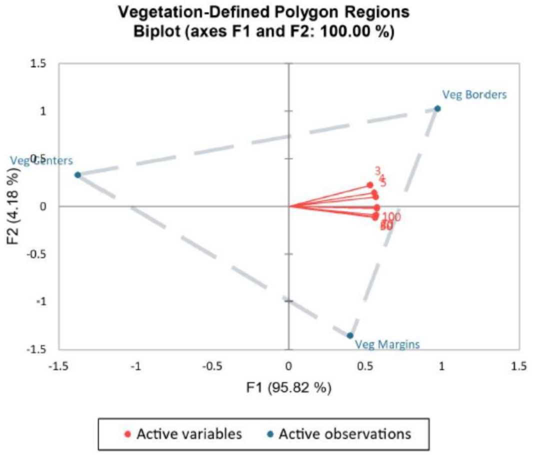

Figure 2-33: Summary of the PCA for the Vegetation-defined NPP hummocks. There is a slight positive correlation between feature length and size. Factor scores for the MSR analysis of polygon regions reflect the consistently higher surface roughness values in polygon borders and lower surface roughness values in polygon centers.

5.3.2 Eryrarfjall Peninsula, Westfjords, Iceland

Several polygon populations were delineated at the site near Flateyri and a variation in surface roughness is apparent between polygon centers and margins in most of the survey data as discussed in Section 5.2. However only the Stone Circle population had a low-altitude UAS survey performed during a follow-up site visit that provides a higher resolution dataset to correspond to the lower resolution surveys. Among the baseline morphometric parameters that were evaluated, positive correlations were detected among polygon lengths and widths in the low-resolution surveys (Figure 2-34) and between polygon length, width, and size in the high resolution surveys (Figure 2-35). Negative correlations were observed between polygon size and circularity in the low-resolution surveys (Figure 2-34) and between polygon size, circularity, and length in the high resolution surveys (Figure 2-35). This correlation is visible along the trendlines in Figure 2-25, where circularity is observed to decrease in response to the increase in feature size among Stone Hummocks. Only Stone Polygons maintain a relatively constant degree of circularity in response to alterations in feature size (Figure 2-24). While slope was not evaluated on the derived-DTMs in this study, the observed negative correlation between circularity and size is probably controlled by terrain slope as polygons tend to elongate and become less circular as slope increases (Kessler and Werner, 2003).

The factor scores for the surface roughness of polygon centers, margins, and borders for the low resolution (Figure 2-34) and high resolution (Figure 2-35) surveys reinforce the stark morphological and compositional differences that exist within each province. The consistency of this relationship is represented by the near equidistant distribution of the factor scores in the biplot for the low-resolution surveys (resulting from the delineation of 203 individual polygons). The relationship of the factor scores for the high-resolution survey in Figure 2-35 are still representative of the strong associations of surface roughness derived from the MSR analysis

Morphometric Parameters

Correlation matrix (Pearson (n)):

Variables	Length	Orientation	Width	Size	Circularity	$r_f = 3$
Length	**1**	0.001	**0.490**	-0.069	-0.056	-0.055
Orientation	0.001	**1**	-0.125	-0.039	0.020	0.017
Width	**0.490**	-0.125	**1**	-0.118	0.023	-0.032
Size	-0.069	-0.039	-0.118	**1**	**-0.340**	-0.010
Circularity	-0.056	0.020	0.023	**-0.340**	**1**	0.038
$r_f = 3$	-0.055	0.017	-0.032	-0.010	0.038	**1**

Values in bold are different from 0 with a significance level alpha=0.05

Eigenvalues:

	F1	F2	F3	F4	F5	F6
Eigenvalue	1.547	1.335	1.000	0.986	0.644	0.487
Variability (%)	25.790	22.249	16.670	16.439	10.729	8.123
Cumulative %	25.790	48.039	64.709	81.148	91.877	100.000

Correlations between variables and factors:

	F1	F2	F3	F4	F5
Length	0.793	-0.267	0.223	0.142	0.056
Orientation	-0.160	0.202	0.932	0.212	0.067
Width	0.841	-0.173	-0.048	0.103	0.098
Size	-0.376	-0.723	-0.014	0.096	0.572
Circularity	0.174	0.798	-0.127	-0.112	0.547
$r_f = 3$	-0.116	0.182	-0.252	0.943	-0.027

Polygon Regions &
Multiscale Surface Roughness Vectors

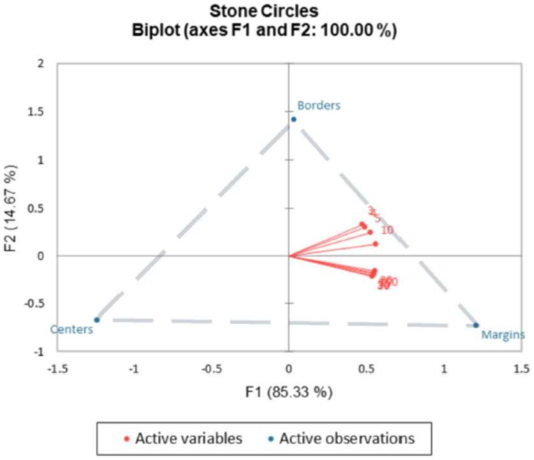

Figure 2-34: Summary of the PCA for the FPG Stone Circles population. There is a slight positive correlation between feature width and length. Factor scores for the MSR analysis of polygon regions reflect the consistently higher surface roughness values in polygon margins and lower surface roughness values in polygon centers.

Morphometric Parameters

Correlation matrix (Pearson (n)):

Variables	Length	Orientation	Width	Size	Circularity	$r_f = 3$
Length	**1**	0.178	-0.017	**0.918**	**-0.765**	-0.125
Orientation	0.178	**1**	-0.003	0.120	-0.253	**0.345**
Width	-0.017	-0.003	**1**	**0.269**	0.136	0.185
Size	**0.918**	0.120	**0.269**	**1**	**-0.596**	-0.105
Circularity	**-0.765**	-0.253	0.136	**-0.596**	**1**	-0.091
$r_f = 3$	-0.125	**0.345**	0.185	-0.105	-0.091	**1**

Values in bold are different from 0 with a significance level alpha=0.05

Eigenvalues:

	F1	F2	F3	F4	F5	F6
Eigenvalue	2.592	1.386	1.127	0.602	0.266	0.027
Variability (%)	43.201	23.100	18.788	10.028	4.439	0.444
Cumulative %	43.201	66.301	85.088	95.117	99.556	100.000

Correlations between variables and factors:

	F1	F2	F3	F4	F5
Length	0.969	-0.163	-0.008	-0.014	0.142
Orientation	0.309	0.694	-0.336	0.556	-0.015
Width	0.069	0.323	0.919	0.105	-0.185
Size	0.912	-0.116	0.307	0.045	0.219
Circularity	-0.849	-0.045	0.273	0.249	0.374
$r_f = 3$	-0.012	0.870	-0.019	-0.466	0.156

Polygon Regions &
Multiscale Surface Roughness Vectors

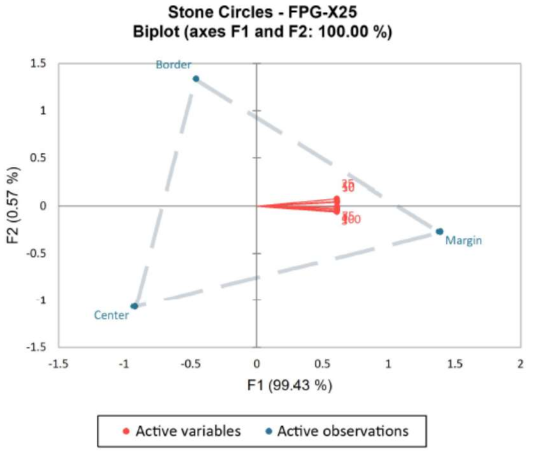

Figure 2-35: Summary of the PCA for the FPG Stone Circles population at FPG-X25. There is a slight positive correlation between feature size, width, and length. Factor scores for the MSR analysis of polygon regions reflect the consistently higher surface roughness values in polygon margins and lower surface roughness values in polygon centers.

presented in Figure 2-29. The similarities in material composition and morphology between polygon centers and borders are evident in the negative distribution of the center and border averages in the biplot presented in Figure 2-34.

5.3.3 Blanda River, Central Highlands, Iceland

The polygons in the Highlands presented distinct visual boundaries between margins and centers for the purpose of feature delineation, however these distinctions were often the result of variable distribution of vegetation. A PCA was performed on the resulting low vegetation and high vegetation polygon center populations (Figure 2-36). A positive correlation between polygon length, width, and size is observed regardless of the presence of vegetation.

The factor scores for the polygon populations indicate there is a potential relationship between polygon circularity, orientation, and surface roughness among the dense vegetation polygon centers. As discussed previously, surface roughness variations between vegetated and non-vegetated provinces can serve as a proxy for quantifying the presence or absence of vegetation in polygon provinces. As discussed in Section 5.2, dense vegetation centers are observed to have a higher surface roughness than low vegetation centers (Figure 2-30). Polygon circularity is tied slope, where polygons on lower slopes tend to have a higher degree of circularity and polygons on steeper slopes tend to be more elongated (Kessler and Werner, 2003). Orientation was recorded from 0 to 180 degrees (where 0=north and 180=south), so an increase in orientation could be indicative of features that are oriented along a northwest to southeast trend. As the Blanda River is located west of the site and flows north, it is likely that feature orientation is controlled by prevailing slope of the landscape. When these factors are considered together, it is possible that the increase in surface roughness corresponds to an increase in vegetation that is partially controlled by the accumulation of water that may occur in response to decreasing slope.

Morphometric Parameters

Low Vegetation Polygon Centers

Correlation matrix (Pearson (n)):

Variables	Length	Orientation	Width	Size	Circularity	$r_f = 4$
Length	**1**	-0.075	**0.596**	**0.931**	**-0.570**	**0.239**
Orientation	-0.075	**1**	-0.089	-0.074	-0.059	0.075
Width	**0.596**	-0.089	**1**	**0.773**	0.008	0.006
Size	**0.931**	-0.074	**0.773**	**1**	**-0.371**	0.141
Circularity	**-0.570**	-0.059	0.008	**-0.371**	**1**	**-0.261**
$r_f = 4$	**0.239**	0.075	0.006	0.141	**-0.261**	**1**

Values in bold are different from 0 with a significance level alpha=0.05

Eigenvalues:

	F1	F2	F3	F4	F5	F6
Eigenvalue	2.786	1.282	0.934	0.772	0.197	0.029
Variability (%)	46.428	21.363	15.569	12.870	3.281	0.490
Cumulative %	46.428	67.791	83.360	96.230	99.510	100.000

Correlations between variables and factors:

	F1	F2	F3	F4	F5
Length	0.964	0.057	-0.030	-0.106	-0.208
Orientation	-0.088	0.480	0.872	-0.039	-0.018
Width	0.741	-0.491	0.259	0.236	0.294
Size	0.962	-0.166	0.100	-0.003	-0.145
Circularity	-0.542	-0.606	0.229	0.490	-0.213
$r_f = 4$	0.283	0.642	-0.209	0.681	0.018

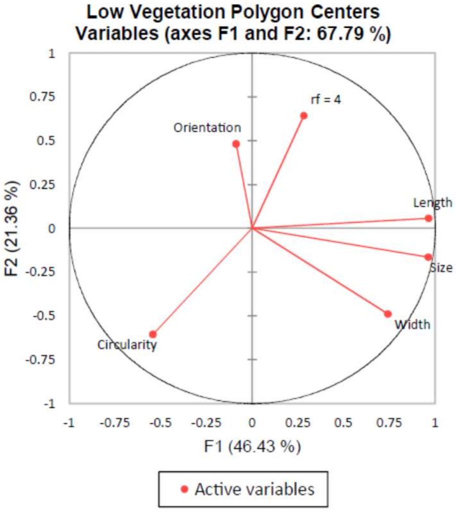
Low Vegetation Polygon Centers
Variables (axes F1 and F2: 67.79 %)

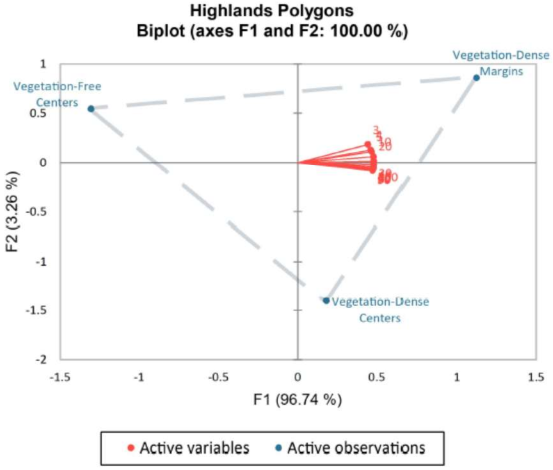
Highlands Polygons
Biplot (axes F1 and F2: 100.00 %)

Dense Vegetation Polygon Centers

Correlation matrix (Pearson (n)):

Variables	Length	Orientation	Width	Size	Circularity	$r_f = 4$
Length	**1**	-0.122	**0.658**	**0.862**	**-0.286**	-0.037
Orientation	-0.122	**1**	-0.155	-0.146	0.065	0.117
Width	**0.658**	-0.155	**1**	**0.838**	0.147	0.018
Size	**0.862**	-0.146	**0.838**	**1**	-0.070	0.008
Circularity	**-0.286**	0.065	0.147	-0.070	**1**	0.014
$r_f = 4$	-0.037	0.117	0.018	0.008	0.014	**1**

Values in bold are different from 0 with a significance level alpha=0.05

Eigenvalues:

	F1	F2	F3	F4	F5	F6
Eigenvalue	2.623	1.146	1.063	0.869	0.218	0.081
Variability (%)	43.720	19.095	17.710	14.485	3.639	1.350
Cumulative %	43.720	62.815	80.525	95.011	98.650	100.000

Correlations between variables and factors:

	F1	F2	F3	F4	F5
Length	0.913	-0.132	-0.186	0.115	-0.286
Orientation	-0.247	0.452	-0.488	0.704	0.030
Width	0.881	0.289	0.162	0.001	0.323
Size	0.967	0.094	-0.028	0.054	-0.041
Circularity	-0.133	0.756	0.618	-0.004	-0.171
$r_f = 4$	-0.025	0.510	-0.617	-0.598	-0.022

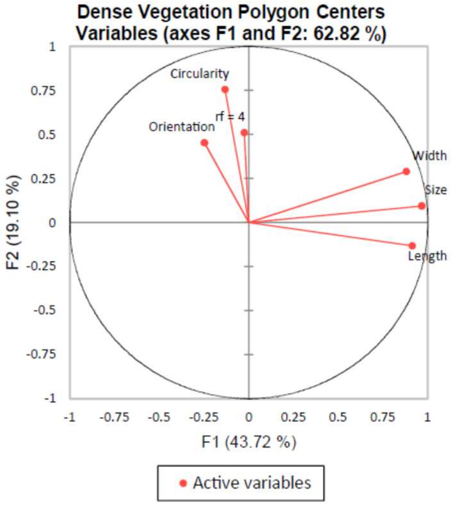
Dense Vegetation Polygon Centers
Variables (axes F1 and F2: 62.82 %)

Figure 2-36. Summary of the PCA for the FPG Stone Circles population at FPG-X25. There is a slight positive correlation between feature size, width, and length. Factor scores for the MSR analysis of polygon regions reflect the consistently higher surface roughness values in polygon margins and lower surface roughness values in polygon centers.

6.0 Discussion

6.1 Observed Variations Between Active and Relict Patterned Ground

Determining whether patterned ground is representative of active or relict periglacial processes (status determination) is complicated by a range of factors. Ballantyne (2018) provides a discussion of most of the variables that can impact this status determination and serves as a guide for the following discussion. Small scale patterns can form through needle-ice formation anywhere that is free of vegetation and with a sufficient distribution of small clasts where overnight ground frost results in surface cooling between -1°C to -2°C (Ballantyne, 2018). As it is not necessary to invoke historical permafrost or periglacial processes that could be rapidly overtaken by vegetation, it is very likely that the small patterns observed near Flateyri and at isolated locations in the Highlands fall into the category of being driven by diurnal to seasonal temperature cycles that promote the formation and sublimation of needle frost.

Evaluating larger-scale patterns presents a wider set of challenges due to their persistence through time. In high polar latitudes, the association of large stone patterns with underlying permafrost is ubiquitous (e.g. Washburn, 1956; Hallet, 2013). The partial role of permafrost in patterned ground development and evolution is that it serves as an aquitard for seasonal active layers that can be waterlogged and capable of reaching the saturation threshold for the associated soils (Chapter 1 of this dissertation). In this manner, a non-permafrost aquitard (such as low-permeability bedrock) can serve the same role in patterned ground development in areas with favorable climate conditions, such as having a MAAT below 1.6 °C or being situated near active glacial margins.

A total of 849 patterned ground features were evaluated between a combination of 23 sites surveyed in Utah and Iceland. The study sites were selected in a manner to survey a combination of active and potentially relict patterned ground to ascertain if micromorphological differences were detectable in surface roughness datasets derived using UAS photogrammetry.

Detectable differences in feature micromorphology would enable rapid and remote monitoring of periglacial sites in the presence of warming temperatures and could provide a framework for establishing metrics for evaluating the level of present-day activity of analogous landforms on Mars (to be discussed in Chapter 4 of this dissertation).

The North Pole Pass site is considered to be periglacially relict due to the absence of observed permafrost in the Uinta Mountains (Munroe, 2007). Atmospheric monitoring at a nearby weather station yielded a MAAT of -2.0°C during the period between January 1999 to December 2003 (Munroe, 2006), yet temperatures below 0°C were not observed in the uppermost 1 m of soil (Munroe, 2007). A conservative interpretation of the prevailing conditions suggests that permafrost could be sporadic and that seasonal modification via non-periglacial processes could be possible, such as through frost heave, diurnal cycles during the transition period between seasons, and freezing and thawing associated with the onset and departure of winter. While these influences may exert small-scale changes in the present-day, the lateral extent and apparent stability of soils and vegetation growth across polygon centers suggest that non-periglacial influences on patterned ground structure are likely minimal in comparison to biological factors (Munroe, 2007). Extensive vegetation and pedogenesis has been observed at a multitude of established relict patterned ground sites (Walters, 1994; Kling, 1996; Munroe, 2007; Mather et al., 2018) in comparison to other rock-dominated active patterned ground sites in which vegetation is sparse (e.g. Ulrich et al., 2011; Uxa et al., 2017). Therefore, the North Pole Pass site is treated as a relict site for the purpose of this discussion.

Interpretations of the extent of permafrost in Iceland varies. Permafrost is generally understood to be sporadic to extensive at varying locations throughout the Highlands (Etzelmuller et al., 2007). The extent of permafrost in the Westfjords varies by interpretation. When taken as an extension of permafrost studies elsewhere on the island, permafrost levels are perhaps as high as 900 to 950 m asl (Etzelmuller et al., 2007). Recent work evaluating permafrost thaw features in fjords near the site suggest permafrost levels as low as 300 m asl (Bell and Glade, 2003; Morino et al., 2021). The sites near Flateyri are located at approximately 600 m asl, placing the site at either just above or below the predicted base elevation for stable permafrost. In-situ temperature observations to 0.5 m bgs suggest the freezing line (or putative ice table) at the Flateyri sites is potentially as shallow as 1.8 m bgs. Despite a relatively large, interpreted depth to permafrost in relationship to the presence of shallow bedrock, the presence of microscale sorting from needle frost at the surface, the high level of feature preservation, and predicted MAAT, the Flateyri sites are considered to be an edge case for periglacial activity for the purpose of this discussion. The Highlands sites are located between approximately 500 and 550 m asl and fit existing models for the presence of at least sporadic permafrost. Studies of polygonal terrain in the latter half of the Twentieth Century that involved tephrachonological dating suggest that polygons were active throughout the LIA and perhaps as recently as the 1960's (Thorarinson, 1964). While the MAAT is higher than would be expected for a periglacial setting, continued recent studies suggest that periglacial activity is ongoing throughout the region (Emmert, 2020) and the Highlands sites are thus considered to be periglacially active for the purposes of this discussion.

The results of the FPG-X25 survey suggest that high resolution surveys resulting in correspondingly high resolution DTMs may yield informative characteristics of patterned ground morphology which does not easily translate to lower resolution datasets. The similarities in material composition and morphology between polygon centers and borders are evident in the negative distribution of the center and border averages in the biplot presented in Figure 2-32 and may be an indication of the suitability of the MSR technique in being able to resolve fine-scale differences in roughness between defined feature provinces, provided that the spatial resolution of the DTM is sufficient. This has important implications for the interpretation of surface roughness parameters derived from high altitude sources (e.g. high altitude UAS surveys or satellite data). There may be echoes of certain trends (such as variations between feature centers and margins) that translate to lower resolution datasets, but spatial resolution ultimately plays the greatest role in determining the utility of such datasets. For instance, if a satellite were able to derive sub-centimeter scale imagery of a patterned ground site at an image overlap sufficient to produce a centimeter scale DTM, then the scalability of the dataset would be comparable or better than a UAS survey performed an altitude of 80 m agl.

6.2 Processing Observations

A few trial datasets were processed using Pix4D early during data post-processing. With a focus on feature micromorphology, recognizing differences between the output resulting from each software's rendering algorithms was important. It was noted that while Pix4D default settings produced better orthomosaics, the resulting DTMs were oversimplified (smoothed) at submeter scales. The Agisoft processing algorithm appears to provide a better 'unfiltered' DTM that captures submeter feature variations in greater detail (without smoothing).

While the MSR Whitebox Tool is capable of rapidly performing multiscale surface roughness calculations, isolated errors were encountered throughout the workflow that required the development of work-arounds. In the worst-case scenario, MSR datasets at lower r_f values of 3 and 4 could not be fully produced for NPP-1, NPP-5, and HPOLY-8. This processing error was repeated on three separate occasions for each dataset with identical output files each time, resulting in narrow to moderately-sized bands of partially processed data along the top and left-hand side of each dataset leaving white space (or "no data") throughout the rest of the file. Part of the "no data" space at NPP-5 is visible at the bottom of the r_f = 3 image in Figure 2-11. The consistent regularity of these "no data" bands suggests that an error within the processing algorithm is the culprit, potentially the result of the algorithm believing that corrupted data had been encountered, thus preventing the full execution of the MSR analysis. The error did not occur at any r_f greater than 5, which points to potential difficulty for the algorithm to handle a high volume of calculations at higher spatial resolutions.

6.3 Future Work

Regarding potential connections between surface roughness and other morphometric factors and environmental parameters, additional data collection would be required. UAS surveys using ground control points or LiDAR-acquired data would be required to develop the surface roughness to slope and slope aspect relationships. The connection between surface roughness and soil moisture content (Neelam et al, 2020) also offers a compelling opportunity to associate specific roughness regimes to polygon centers, borders, and margins. Additional in-situ measurements and time series morphometric observations (such as Kääb et al, 2014) would be required to more fully develop any potential relationships.

7.0 Conclusion

UAS surveys were performed to study patterned ground at 23 sites spanning alpine zones in the Uinta Mountains, Utah, U.S.A. and the Westfjords and Highlands of Iceland. The surveys sought to characterize differences between relict and active patterned ground sites using a combination of established morphometric parameters with the addition of applying a multiscale surface roughness algorithm for assessing minor topographic variations across feature centers and margins. The strongest variations in surface roughness properties were visible under two circumstances: where there is a contrast in material composition in centers and margins, and where vegetation is present across either feature centers or margins. As survey altitudes and filtering scales are increased, the average surface roughness parameters for both centers and margins approach an asymptotic equilibrium that reflects the prevailing surface roughness parameters associated with the local landscape. The method demonstrates the applicability of the MSR algorithm for high resolution datasets as an additional parameter that can be used in association with or to support other common morphometric analyses, such as associating specific surface roughness values with specific size distributions of gravels and boulders. The application of this technique shifts rapidly from deriving feature-specific data to reflecting landscape-scale conditions, corresponding with decreasing dataset resolution. In this manner, it may be possible to layer ultra-high resolution (or low-altitude-acquired) datasets of targeted locations with overlying lower resolution (or high altitude-acquired) datasets at a landscape scale to associate homogenous surface roughness parameters to specific surface conditions (such as gravel-dominated versus boulder-dominated). Using the technique in this manner has applications for characterizing landscapes where ultra-high-resolution datasets are not available, such as on planetary bodies like the Moon or Mars.

References

Ascione, A., Cinque, A., Miccadei, E., Villani, F., and Berti, C. 2008. The Plio-Quaternary uplift of the Appennine chain: new data from the analysis of topography and river valleys in Central Italy. Geomorphology. 102. 105-108.

Baer, K.E. von.1838. Recent Intelligence upon the Frozen Ground in Siberia. The Journal of the Royal Geographical Society of London. Volume 8. 401-406.

Ballantyne, C.K. 2018. Periglacial Geomorphology, First Edition. John Wiley& Sons. Segregated Ice (needle ice) p. 58-60. Sorted Patterned Ground. p. 148-155.

Benedict, J.B. 1992. Field and Laboratory Studies of Patterned Ground in a Colorado Alpine Region. Occasional Paper 49, Institute of Arctic and Alpine Research.

Bertran, P., Andrieux, E., Antoine, P., Deschodt, L., Font, M., and Sicilia, D. 2017. Pleistocene Involutions and Patterned Ground in France: Examples and Analysis Using a GIS Database. Permafrost and Periglacial Processes. 28. 710-725.

Bockheim, J.G., Munroe, J.S., Douglass, D.C., and Koerner, D. 2000. Soil development along an elevational gradient in the southeastern Uinta Mountains, Utah, U.S.A. Catena, 29, p.169-185.

Boike, J. and Yoshikawa, K. 2003. Mapping of Periglacial Geomorphology using Kite/Balloon Aerial Photography. Permafrost and Periglacial Processes. 14.

Brooker, L.M., Balme, M.R., Conway, S.J., Hagermann, A., Barrett, A.M., Collins, G.S., and Soare, R.J. 2018. Clastic polygonal networks around Lyot crater, Mars: Possible formation mechanisms from morphometric analysis. Icarus. 302. 386-406.

Cain, R.H. 1974. Pimple Mounds: A New Viewpoint. Ecology. 55 (1), 178-182.

Cao, W., Cai, Z., and Tang, Z. 2015. Lunar surface roughness based on multiscale morphological method. Planetary and Space Science, 108, p. 13-23. DOI:10.1016/j.pss.2014.09.009

Conrad, V. 1946. Polygon nets and their physical development. American Journal of Science. 244, 4. 277-296.

Dąbski, M. 2005. Small-scale Sorted Nets on Glacial Till, Fláajökull (Southeast Iceland) and Elisbreen (Northwest Spitsbergen). Permafrost and Periglacial Processes. 16. 305-310.

Dąbski, M., Zmarz, A., Pajanek, P., Korczak-Abshire, M., Karsnia, I., and Chwerdorzewska, K.J. 2017. UAV-based detection and spatial analyses of periglacial landforms on Demay Point (King George Island, South Shetland Islands, Antarctica). Geomorphology. 290, 29-38.

Durre, T., Brye, K.R., Wood, L.S., and Gbur, E.E. 2019. Soil moisture regime and mound position effets on soil profile properties in a native tallgrass prairie in northwest Arkansas, USA. Geoderma, 352, 49-60. DOI:10.1016/j.geoderma.2019.05.045

Einarsson, M.A. 1984. Climate of Iceland. Climate of the Oceans, Van Loon H (ed.). Elsevier Science Publishers: Amsterdam, p. 673-698.

Emmert, A.A. 2020. The Internal Structure of Periglacial Landforms: Assessments of Subsurface Variations in Permafrost-related and Frost-related Phenomena by Multi-dimensional Geophysical Investigations. Dissertation, Julius-Maximilians-Universität Würzbürg.

Etzelmüller, B., Farbrot, H. Guđmundsson, A., Humlum, O., Tveito, O.E., and Björnsson, H. 2007. The Regional Distribution of Mountain Permafrost in Iceland. Permafrost and Periglacial Processes. 18. 185-199.

Etzelmüller, B., Patton, H., Schomacker, A., Czekirda, J., Girod, L., Hubbard, A., Lilleøren, K. S., Westermann, S. (2020). Icelandic permafrost dynamics since the Last Glacial Maximum – model results and geomorphological implications. Quaternary Science Reviews, 233.

Farbrot, H., Eztelmüller, B., Shuler, T.V., Guđmundsson, A., Eiken, T., Humlum, O., and Björnsson, H. 2007. Thermal characteristics and impact of climate change on mountain permafrost in Iceland. Journal of Geophysical Research. 112. F03S90.

Farbrot, H., Eztelmüller, B., Shuler, T.V., Guđmundsson, A., Humlum, O., Kellerer-Pirklbauer, A., Eiken, T., and Wangensteen, B. 2007. Rock glaciers and permafrost in Trollaskagi, northern Iceland. Annals of Geomorphology. 51:2. 1-16.

Florinsky, I.V. 2018. Multiscale geomorphometric modeling of Mercury. Planetary and Space Science, 151, p. 56-70. DOI:10.1016/j.psss.2017.11.010

Girod, L., Nuth, C., Kääb, A., Eztelmüller, B., and Kohler, J. 2017. Terrain changes from images acquired on opportunistic flights by SfM photogrammetry. The Cryosphere. 11. 827-840.

Glade, T. 2005. Linking debris-flow hazard assessments with geomorphology. Geomorphology. 66. 189-213.

Glade, T. and Jansen, E.H. 2004. Recommendations for landslie hazard assessments in Bolungarvik and Vesturbyggd, NW-Iceland. Reykjavik.

Grab, S. (2002). Characteristics and palaeoenvironmental significance of relict sorted patterned ground, Drakensberg plateau, southern Africa. Quaternary Science Reviews, 21, 1729-1744.

Groos, A.R., Niederhauser, J., Wraase, L., Hänsel, F., Nauss, T., Akçar, and Veit, H. 2021. The enigma of relict large sorted stone stripes in the tropical Ethiopian Highlands. Earth Surface Dynamics. 9, 145-166.

Guđmundsson, A. 2010. Rock glaciers and relict debris bodies in Central North Iceland. Iceland in the Central Northern Atlantic: hotspot, sea currents, and climate change.

Hallet, B. 2013.

Iceland GeoSurvey. Geological Web Map. Iceland Power Company and Ministry for the Environment and Natural Resources. http://jardfraedikort.is. Accessed: 2021 July 18

James, M.R., Antoniazza, G., Robson, S., and Lane, S.N. 2020. Mitigating systematic error in topographic models for geomorphic change detection: accuracy, precision and considerations beyond off-nadir imagery. Earth Surface Processes and Landforms.

Johnson, H.W. 1990. Ice-Wedge Casts and Relict Patterned Ground in Central Illinois and their Environmental Significance. Quaternary Research. 33 (1), 51-72.

Kääb, A., Girod, L., and Berthling, I. 2014. Surface kinematics of periglacial sorted circles using structure-from-mostion technology. The Cryosphere. 8. 1041-1056.

Kessler, M.A. and Werner, B.T. 2003. Self-Organization of Sorted Patterned Ground. Science, 299, p. 380-383.

Kling, J. 1996. Relict Sorted Patterned Ground in Rostu, Northernmost Sweden. Geografiska Annaler. Series A, Physical Geography. 78 (1), 61-72.

Knechtel, M.M.1952. Pimpled plains of eastern Oklahoma. Bulletin of the Geological Society of America. Volume 63. 689-700.

Křížek, M. and Uxa, T. 2013. Morphology, Sorting and Microclimates of Relict Sorted Polygons, Krkonose Mountains, Czech Republic. Permafrost and Periglacial Processes. 24. 313-321.

Lindsay, J., Cockburn, J, and Russell, H. 2015. An integral image approach to performing multi-scale topographic position analysis. Geomorphology. 245, 51-61.

Lindsay, J.B. and Newman, D.R. 2018. Hyper-scale analysis of surface roughness. Geomorphometry.

Lindsay, J.B., Newman, D.R., and Francioni, A. 2019. Scale-Optimized Surface Roughness for Topographic Analysis. Geosciences. 9, 322.

Lousada, M. Pina, P. Vieira, G., Bandeira, L., and Mora, C. 2018. Evaluation of the use of very high resolution aerial imagery for accurate ice-wedge polygon mapping (Advantdalen, Svalbard). Science of the Total Environment. 615. 1574-1583.

Lusch, D.P., Stanley, K.E., Schaetzl, R.J., Kendall, A.D., Van Dam, R.L., Nielsen, A., Blumer, B.E., Hobbs, T.C., Archer, J.K., Holmstadt, J.L.F., and May, C.L. 2009. Characterization and Mapping of Patterned Ground in the Saginaw Lowlands, Michigan: Possible Evidence for Late-Wisconsin Permafrost. Annals of the Association of American Geographers, 99:3, 445-446.

Malde, H.E. 1964. Patterned Ground in the Western Snake River Plain, Idaho, and Its Possible Cold-Climate Origin. Geological Society of America Bulletin. 75 (3). 191-208.

Mather, A.E., Fyfe, R.M., Clason, C.C., Stokes, M., Mills, S., and Barrows, T.T. 2019. Automated mapping of relict patterned ground: An approach to evaluate morphologically subdued landforms using unmanned-aerial-vehicle and structure-from-motion technologies. Progress in Physical Geography. 43:2. 174-192.

Morino, C., Conway, S.J., Balme, M.R., Helgason, J.K., Þorsteinn, S., Jordan, C., Hillier, J., and Argles, T. 2021. The impact of ground-ice thaw on landslide geomorphology and dynamics: two case studies in northern Iceland. Landslides.

Munroe, J.S. 2006. Investigating the spatial distribution of summit flats in the Uinta Mountains of northeastern Utah, U.S.A. Geomorphology. 75. 437-449.

Munroe, J.S. 2007. Properties of Alpine Soils Associated with Well-Developed Sorted Polygons in the Uinta Mountains, Utah, U.S.A. Arctic, Antarctic, and Alpine Research. 39:4. 578-591.

Munroe, J.S., Klem, C.M., and Bigl, M.F. 2013. A lacustrine sedimentary record of Holocene periglacial activity from the Uinta Mountains, Utah, U.S.A. Quaternary Research. 79. 101-109.

Munroe, J.S. 2018. Distribution, evidence for internal ice, and possible hydrologic significance of rock glaciers in the Uinta Mountains, Utah, USA. Quaternary Research, 90, p. 50-65. DOI:10.1017/qua.2018.24

Munroe, J.S., Norris, E.D., Olson, P.M., Ryan, P.C., Tappa, M.J., and Beard, B.L. 2020. Quantifying the contribution of dust to alpine soils in the periglacial zone of the Uinta Mountains, Utah, U.S.A. Geoderma. 378. 114631.

Munroe, J.S., Ryan, P.C., and Proctor, A. 2021. Pedogenic clay formation from allochthonous parent materials in a periglacial alpine critical zone. Catena. 203. 105234. DOI:10.1016/j.catena.2021.105324

National Weather Service Climate Data – Accessed 2021.

Pawalec, H. and Ludwikowska-Kędzia. 2016. Macro- and Micromorphologic Interpretation of Relict Periglacial Slope Deposits from the Holy Cross Mountains, Poland.

Pereira, F., Marques, J.S., Heleno, S., and Pina, P. 2020. Detection and Delineation of Sorted Stone Circles in Antarctica. Remote Sensing. 12, 160.

Piermattei, L. Carturan, L., de Blasi, F., Tarolli, P., Fontana, G.D., Vettore, A., and Pfiefer, N. 2016. Suitability of ground-based SfM-MVS for monitoring glacial and periglacial processes. Earth Surface Dynamics. 4. 425-443.

Priesnitz, K. and Schunke, E. 1983. The Significance of Periglacial Phenomena in Iceland. Polarforschung. 53, 2. 9-19.

Quinn, J.H. 1961. Prairie mounds of Arkansas. Arkansas Archaeological Society, 2, 1-7.

Ray, R.J., Krantz, W.B., Caine, T.N., and Gunn, R.D. 1983. A Model for Sorted Patterned-Ground Regularity. Journal of Glaciology, 29, 102, p. 317-337.

Schunke, E. 1974. Frostspaltenmakropolygone im westlichen Zentral-Island, ihre klimatischen und edaphischen Bedingungen. Eiszeitalter und Gegenwart, 25: p. 157-165.

Śledź, S., Ewertowski, M.W., and Piekarczyk, J. 2021. Applications of unammned aerial vehicle (UAV) surveys and Structure from Motion photogrammetry in glacial and periglacial geomorphology. Geomorphology. 378. 107620.

Sumner, P. 2004. Relict Sorted Patterned Ground in Lesotho. Permafrost and Periglacial Processes. 15, 89-93.

Thorén, R. 1960. Frost Problems and Photo Interpretation of Patterned Ground. Commission VII (Photographic Interpretation) of the International Society of Photogrammetry – Working Group 3 “Surface Configuration, drainage, soils and geology.” 779-786.

Thorarinson, S. 1964. Additional notes on patterned ground in Iceland, with a particular reference to ice-wedge polygons. Biul. Perygl. 14, p. 107-124.

Tomcyzk A. M., Ewertowski, M. W., Stawska, M., Rachlewicz, G. (2019). Detailed alluvial fan geomorphology in a high-arctic periglacial environment, Svalbard: application of unmanned aerial vehicle (UAV) surveys. Journal of Maps, 15:2, 460-473.

Ulrich, M., Hauber, E., Herzschuch, U., Härtel, S., and Shirrmeister, L. 2011. Polygon pattern geomorphometry on Svalbard (Norway) and western Utopia Planitia (Mars) using high-resolution stereo remote-sensing data. Geomorphology. 134. 197-216.

Vopata, J., Aber, J.S., and Kalm, V. 2006. Patterned ground in the Culebra Range, southern Colorado. Emporia State Research Studies. 43:1. 8-21.

Walters, J.C. 1994. Ice-Wedge Casts and Relict Polygonal Patterned Ground in North-East Iowa, U.S.A. Permafrost and Periglacial Processes. 5. 269-282.

Washburn, 1956. Classification of Patterned Ground and Reivew of Suggested Origins. Bulletin of the Geological Society of America. 67, 823-866.

Washburn, A.L. 1988. Mima Mounds: An Evaluation of Proposed Origins with Special Reference to the Puget Lowland. Washington Division of Geology and Earth Resources Report of Investigations 29.

Watanabe, T., Matsuoka, N., Christiansen, H.H., and Cable, S. 2017. Soil Physical and Environmental Conditions Controlling Patterned-Ground Variability at a Continuous Permafrost Site, Svalbard. Permafrost and Periglacial Processes, 28, p. 433-445. DOI:10.1002/ppp.1924

Chapter 3

An Evaluation of Patterned Ground Morphometry and Surface Roughness Using HiRISE Digital Terrain Models

Knightly, J.P.[1], Tullis, J.[1], Dixon, J.C.[1], Chevrier, V.F.[1]

[1]University of Arkansas, Center for Space and Planetary Sciences, Fayetteville, AR 72701

1.0 Introduction

Patterned ground on Mars has been the subject of frequent investigations over the past two decades. While decameter-scale polygons with a proposed periglacial origin were resolved in Viking orbiter imagery (Luchitta et al, 1983), it was not until the advent of high-resolution imagery from the Mars Orbital Camera (MOC) on Mars Global Surveyor (MGS) that smaller, meter-scale polygons were observed (Hiesinger and Head, 2000; Siebert and Kargel, 2001). The detection of hydrogen bonded to oxygen by the Gamma-Ray Spectrometer on Mars Odyssey (Boynton et al, 2002) further increased interest in studying high-latitude polygons where a suspected connection between the bonded hydrogen and polygons could be indicative of subsurface ice and, potentially, periglacial processes that could indicate the intermittent presence of liquid water. The combination of observed similarities to terrestrial polygons in regions with permafrost and the potential presence of subsurface ground ice touched-off a flurry of investigations into the nature, origin, and distribution of polygons on Mars (Yoshikawa, 2003; Mangold et al, 2004; Burr et al, 2005; Mangold, 2005). The trajectory of polygon investigations were mutually influenced by the results of studies that suggested gullies and other debris flows were formed by the melting of near-surface ground ice during periods of high obliquity (Costard et al, 2002) which could lead to freeze-thaw modification of polygonal terrains (Burr et al, 2005).

Investigations of Martian polygonal ground reached an apex with the Mars *Phoenix* mission to the northern plains of Vastitas Borealis in 2008, where the selected landing site featured an extensive network of small to medium scale polygons (Mellon et al, 2008). During the arctic summer of Mars Year 29, *Phoenix* excavated several trenches in the vicinity of the spacecraft to study the uppermost layers of regolith (Mellon et al, 2009). The presence of subsurface water ice in the vicinity of the spacecraft was confirmed (Smith et al, 2009) and observed to be present at a mean depth of 4.6 cm (Mellon et al, 2009). Ice exposed to the surface was found to sublimate over several sols in subsequent observations of the trench and found to be vapor-diffusive equilibrium with a mean atmospheric water content of 3.4×10^{19} m^{-3} (Mellon et al, 2009).

Environmental monitoring by *Phoenix* provided insight into the present-day climate conditions at the landing site, examining key variables that would provide context into the potential for periglacial processes during the long arctic summer. While the prevailing climate conditions at the landing site are not suitable for the development of wet active layers (Mellon et al, 2009; Sizemore et al, 2009), analysis of the regolith at the landing site found higher than expected concentrations of perchlorate salts which can lower the eutectic point for water (Hecht et al, 2009; Shaw et al, 2009). The presence of liquid water brine in images of the lander struts has been proposed but never definitively confirmed (Renno et al, 2009). Experimental work with the behavior of brines under Mars conditions has continued, building off observations from the *Phoenix* mission (Bryson et al, 2008; River-Valentin and Chevrier, 2015). The combination of experimental work and observations from *Phoenix* and other surface missions (Martinez et al, 2017) suggest that contemporary wet active layer modification via periglacial processes is unlikely on present-day Mars.

Studies of Martian patterned ground continued following the conclusion of the *Phoenix* mission, enabled by the High Resolution Imaging and Science Experiment (HiRISE) on the Mars Reconnaissance Orbiter (MRO), which arrived at Mars two years prior to touchdown of the *Phoenix* lander. The ability of HiRISE to deliver imagery with sub-meter spatial resolution enabled detailed evaluations of the morphological parameters, potential formation mechanisms, and spatial distribution of polygonal terrain at several sites across Mars (Levy et al, 2008; Levy et al, 2009; Balme et al, 2009; Levy et al, 2010; Gallagher et al, 2011; Ulrich et al, 2011; Johnsson et al, 2012; Balme et al, 2013; Korteniemi and Kreslavsky, 2013; Orloff et al, 2013a; Orloff et al, 2013b; Haltigin et al, 2014; Soare et al, 2014; Soare et al, 2016; Barrett et al, 2018; Soare et al, 2020). Several recurring themes can be found in remote sensing studies of Martian patterned ground throughout this period, including the hypothesis that polygons formed via freeze-thaw (periglacial) processes in a similar manner to terrestrial polygons, despite surface observations from *Phoenix* that are unfavorable to the development of so-called “wet” active layers at high latitudes (including Balme et al, 2013; Soare et al, 2014; Soare et al, 2016). The main pillar of the periglacial hypothesis invokes modeling by Laskar et al (2004) in which the historical obliquity cycle of Mars supported more frequent periods of high obliquity between 5 Ma and 20 Ma, when obliquity averaged 35° relative to averaging 25° over the most recent 5 Ma period.

The utilization of terrestrial analogs has been ubiquitous to nearly every Martian patterned ground investigation, with analog sites spanning the globe from Svalbard to Antarctica. Based on *Phoenix* observations, terrestrial sites located in Antarctica are the most likely to be representative of surface conditions in the recent past on Mars (Figure 1-1, from Marchant and Head, 2007). In Figure 1-1, the hyperarid and cold conditions of the Antarctic Dry Valleys (ADV) provide analogs for surface conditions on ancient Mars under 300 mbar and 100 mbar climate scenarios. The characterization of climate conditions in the ADV led to a handful of analog studies to evaluate the properties of polygonal ground and other potential thaw-related features (Levy et al, 2006; Marchant and Head, 2007; Levy et al, 2010). The results of these studies identified thermal contraction and sublimation-driven processes that are largely equilibrium-driven processes and mirror the equilibrium conditions identified on Mars by *Phoenix* (Mellon et al, 2009). While the ADV sublimation and thermal contraction polygons are largely in equilibrium with their associated microclimates, some modification through excess melting and subsequent freezing is expected. This is supportive of polygonal ground on Mars representing a range of active and relict cold-desert processes.

In contrast with contemporary surface observations from *Phoenix*, computational modeling suggests that environmental conditions favorable to freeze-thaw modification of patterned ground could be possible during periods of high obliquity on Mars (Siebert et al, 2001; Costard et al, 2002; Nakamura and Tajika, 2003; Gallagher et al, 2011; Balme et al 2013). The results of these modeling efforts have, in part, encouraged the use of mostly northern hemisphere terrestrial periglacial landforms as Mars analogs (e.g. Ulrich et al, 2011; Soare et al, 2014; Barrett et al, 2018). These analogs have utility in describing end-member scenarios when periglacial activity involving extensive thawing is possible, however they may overrepresent the role of active freeze-thaw cycles in polygon development on Mars. Each of the evaluated analog studies in Antarctica and northern hemisphere periglacial sites incorporate features experiencing active modification by sublimation, thermal contraction, or freeze-thaw processes.

Despite the high potential for some patterned ground on Mars to be representative of relict or otherwise inactive processes in the present day, relict patterned ground sites on Earth have not previously been investigated for their applicability to Mars. *Phoenix* observations leave open the possibility that sublimation and thermal contraction processes are active in polygonal ground on Mars today. Even if patterned ground on Mars is assumed to have experienced nearly continuous active sublimation and thermal contraction driven modification (dry processes) over the last several million years, the historical input from periglacial processes (wet processes) from periods of high obliquity relative to dry processes is not well constrained at a feature or site-level. Part of the challenge in assigning contributions of feature modification to wet or dry processes is associated with the overlap of morphological characteristics associated with each formation mechanism. In addition, the degradation and non-wet or dry process modification of relict polygons on Mars is not well defined and not easily ascertained through imagery alone. Evaluating digital terrain models (DTMs) of Martian patterned ground may provide insight into micromorphological characteristics of active and relict polygons to assist with identifying the predominant mode of feature modification. Morphometric parameters based on visual imagery have been previously evaluated (e.g. feature length, circularity, size) in combination with underlying topography (slope and aspect), however surface roughness has not been previously included as a variable in evaluating polygon morphology on Earth or Mars. Surface roughness may provide the specific insight into microtopographic variations that are key to differentiating between active processes (dry active layers modified by sublimation and thermal contraction) and relict processes (wet active layers drive by freeze-thaw periglacial processes).

2.0 Methods

This project relied exclusively on using HiRISE imagery and DTMs to evaluate polygon morphometry and surface roughness. Project methodology is divided into the following categories: site selection criteria, HiRISE DTM generation, morphometric analysis, multiscale surface roughness (MSR) analysis, and a statistical evaluation of feature morphometry and surface roughness achieved through performing a principal component analysis (PCA) of each site. All methods with the exception of site selection criteria are discussed in Chapter 2.

2.1 Site Selection Criteria

Previous studies of patterned ground and polygonal terrain on Mars have largely focused on surveys of single sites or a small collection of related sites (Balme et al, 2009; Ulrich et al, 2011; Soare et al, 2014; Soare et al, 2016; Barrett et al, 2017; Brooker et al, 2018; Soare et al, 2020). The utility of single-site surveys is valuable in supporting a thorough characterization of landforms at a particular location. However, a singule site typically only features a handful of subcategories of polygonal terrain and does not capture the full spectrum of patterned ground that has been observed to date across the planet. As a trial for determining the efficacy and potential for incorporating multiscale surface roughness as a parameter for evaluating patterned ground, a total of 10 sites with patterned ground were selected from a pool of 68 candidate site locations with existing HiRISE stereo-pair image coverage. The sites are in the following regions:

Copais Palus, Deutoronlius Mensae, Lethe Vallis, Lyot Crater, Malea Planum, Utopia Planitia, Utopia Rupes, and Vastitas Borealis.

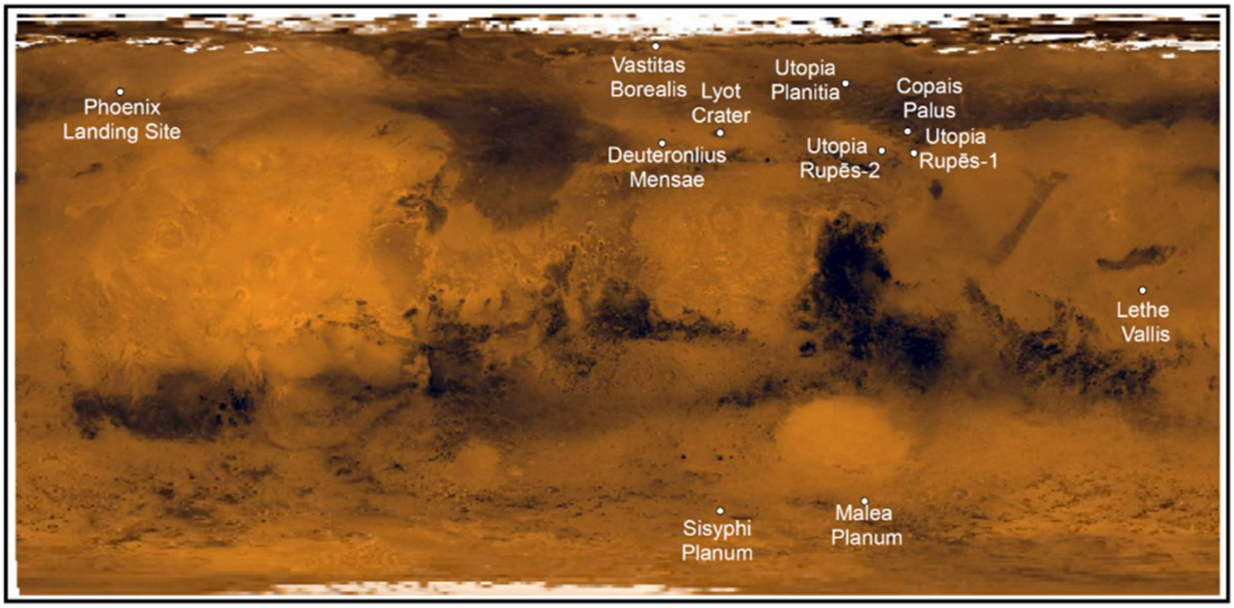

Figure 3-1. The locations of HiRISE stereo-pair images that were transformed into digital terrain models. Sites were selected based on the presence of patterned ground with consideration for the potential applicability of the sites for future studies.

The final site locations (Figure 3-1) were selected on the basis of providing coverage for different subtypes of patterned ground and for their applicability to previous work (e.g. *Phoenix* landing site) and future work as part of ongoing efforts to characterize subsurface ground ice for potential in-situ resource utilization (ISRU) on future crewed missions to Mars (Morgan et al, 2021). A comparison of the various polygon morphologies captured at the selected sites are featured in (Figure 3-2). Polygon morphologies that are represented by the selected sites include clastic stone polygons (Lyot Crater), hummocky patterned ground (*Phoenix* landing site), high centered polygons (Deuteronlius Mensae, Utopia Planitia), and polygons amid pitted and scalloped terrain (Utopia Rupes). A diversity of subdued and prominent polygon morphologies were selected in order to assess the viability of using HiRISE DTMs at a range of vertical and horizontal scales.

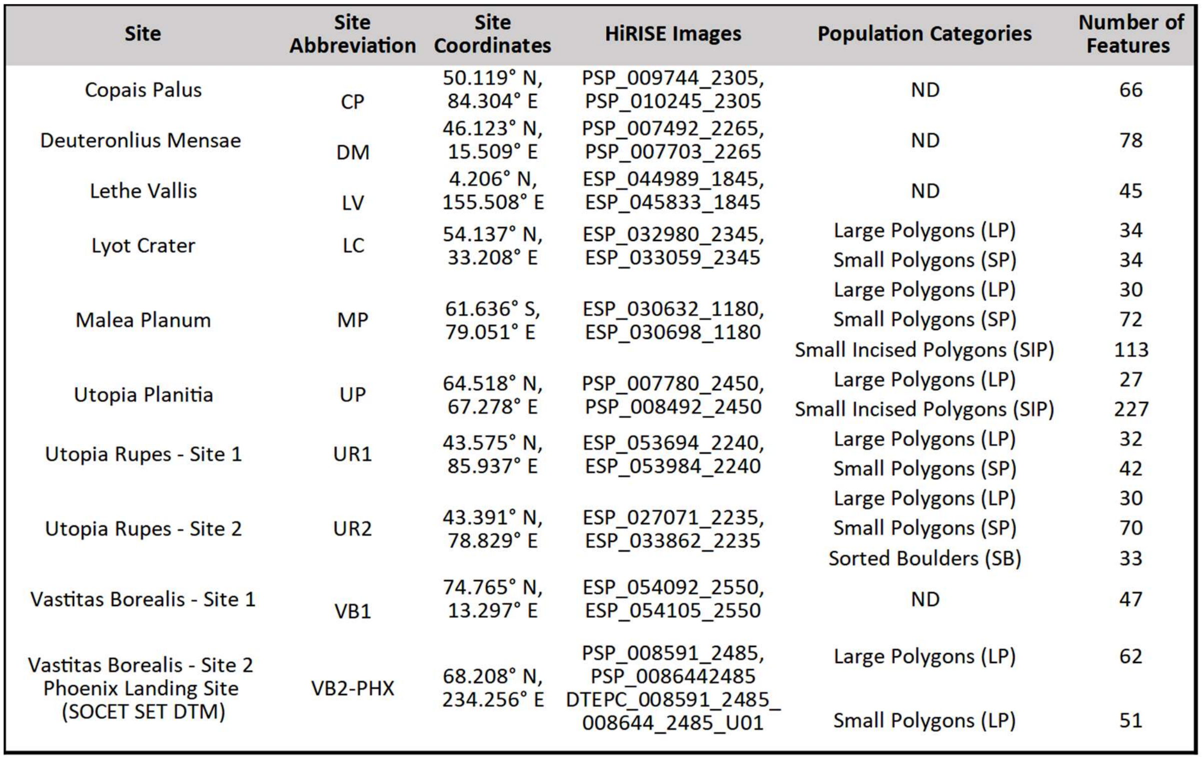

Site	Site Abbreviation	Site Coordinates	HiRISE Images	Population Categories	Number of Features
Copais Palus	CP	50.119° N, 84.304° E	PSP_009744_2305, PSP_010245_2305	ND	66
Deuteronlius Mensae	DM	46.123° N, 15.509° E	PSP_007492_2265, PSP_007703_2265	ND	78
Lethe Vallis	LV	4.206° N, 155.508° E	ESP_044989_1845, ESP_045833_1845	ND	45
Lyot Crater	LC	54.137° N, 33.208° E	ESP_032980_2345, ESP_033059_2345	Large Polygons (LP)	34
				Small Polygons (SP)	34
Malea Planum	MP	61.636° S, 79.051° E	ESP_030632_1180, ESP_030698_1180	Large Polygons (LP)	30
				Small Polygons (SP)	72
				Small Incised Polygons (SIP)	113
Utopia Planitia	UP	64.518° N, 67.278° E	PSP_007780_2450, PSP_008492_2450	Large Polygons (LP)	27
				Small Incised Polygons (SIP)	227
Utopia Rupes - Site 1	UR1	43.575° N, 85.937° E	ESP_053694_2240, ESP_053984_2240	Large Polygons (LP)	32
				Small Polygons (SP)	42
Utopia Rupes - Site 2	UR2	43.391° N, 78.829° E	ESP_027071_2235, ESP_033862_2235	Large Polygons (LP)	30
				Small Polygons (SP)	70
				Sorted Boulders (SB)	33
Vastitas Borealis - Site 1	VB1	74.765° N, 13.297° E	ESP_054092_2550, ESP_054105_2550	ND	47
Vastitas Borealis - Site 2 Phoenix Landing Site (SOCET SET DTM)	VB2-PHX	68.208° N, 234.256° E	PSP_008591_2485, PSP_0086442485 DTEPC_008591_2485_008644_2485_U01	Large Polygons (LP)	62
				Small Polygons (LP)	51

Figure 3-2: Key site metadata including site location coordinates, HiRISE image identifiers, population categories, and number of features delinated in each population. ND = nondifferentiated population.

2.2 Digital Terrain Model Generation

One of the most powerful derived products from HiRISE are high resolution digital terrain models (DTMs) constructed from stereo image pairs. Over 6,285 stereo pairs are catalogued in the Planetary Data System (PDS), however only 709 DTMs have been generated and catalogued. This discrepancy is almost entirely due to the massive amount of computer time and work hours required to properly generate a DTM from a single stereo image pair. Traditionally, HiRISE DTMs have been generated exclusively by using the BAE Systems SOCET SET (now SOCET GXP) photogrammetric processing software. The invested time and effort is worth the reward – a high resolution DTM for areas of interest that exceeds the spatial and vertical resolution of existing laser altimetry-derived topographic datasets for Mars. However, SOCET SET licenses are thinly distributed throughout the planetary science community due to the high licensing expenses associated with the program. This results in vastly more DTMs to be generated then there are dedicated computers and personnel to handle the task.

This is where an alternative, open-source method comes into play. The NASA Ames Stereo Pipeline (ASP) was developed to support photogrammetric processing from a wide range of source inputs, from terrestrial satellites to martian and lunar orbiters. In contrast to the graphical user interface (GUI) that serves as the basis for SOCET SET, ASP is operated entirely through the command line on Linux and Unix-based operating systems. This limits the level of visual interaction during the image and DTM processing workflow, but it also allows for a high degree of flexibility in customizing the program to handle different data sources. Integrating ASP with the United States Geological Survey (USGS) Integrated Software for Imagers and Spectrometers (ISIS) makes the program compatible with interplanetary datasets, including the HiRISE and CTX datasets pertinent to this project.

While the earliest versions of ASP can be traced to Broxton et al (2008), two years after the arrival of MRO and HiRISE at Mars in 2006, it has only been within the last several years that the larger-scale application of ASP to processing HiRISE images has been realized. This is likely from a confluence of factors, but among the more significant has been the steep reduction in hardware cost that has lowered the barrier to building computers with large enough and fast enough hard drives in addition to the large amounts of random access memory (RAM) required to handle the demanding task of generating HiRISE DTMs. Hepburn et al (2019) details the community best-practice work flows for building HiRISE DTMs and found the resulting DTM output to be comparable to existing photogrammetric methods. The methods prescribed by Hepburn et al (2019) and the Ames Stereo Pipeline User Manual (2019) were adhered to for generating the non-SOCETSET DTMs used for this project.

2.2.1 Hardware Requirements

Hardware capabilities are the primary rate-limiting factor to efficiently processing HiRISE DTMs. The final hardware configuration that was utilized for this project was a modified Dell XPS15 laptop with a 2.20 GHz Intel® Core^{TM} i7-8750H CPU. The disk and memory were upgraded to a 1 TB solid-state drive (SSD) and 32 GB RAM. Depending on other tasks the computer is expected to handle, a smaller SSD could be used however many of the base installation files for ISISv3 occupy several hundred gigabytes of space depending on what base files are required. Many of the intermediary files generated during the HiRISE DTM workflow in ASP are several tens of gigabytes in size. An early issue while establishing minimum hardware requirements was the lack of drive space available for processing. A minimum of 75 to 100 GB of free drive space was required for efficient processing of the datasets in this project.

Additionally, ASP and ISISv3 are Linux-based programs that optimally need a dedicated Linux or Macintosh operating system environment. Attempts were made to initially run ASP through a dual-boot setup (Windows/Ubuntu) and the Windows Subsystem for Linux (WSL) and difficulties were encountered with both configurations. The common limitation with both the dual-boot and WSL configurations was sharing the same early storage space restrictions prior to upgrading the laptop SSD. Trials using WSL to proess smaller ConTeXt Camera (CTX) DTMs were promising. For the WSL environment to operate concurrently with Windows, it must be 'quarantined' from the underlying Windows OS. This translates to adding several additional steps to the workflow to import raw imagery for processing and for exporting final datasets. Ultimately, the most efficient DTM processing for this project occurred via a dedicated (unpartitioned) 1 TB SSD running Ubuntu 16.4.

2.2.2 Ames Stereo Pipeline Workflow

The Intelligent Robotics Group (IRG) at the NASA Ames Research Center has been developing the Ames Stereo Pipeline (ASP) for over a decade to support past and ongoing missions including the Mars Exploration Rovers, Lunar Reconnaissance Orbiter, and Mars Reconnaissance Orbiter. While ASP was initially developed for ground control and scientific visualization applications, it has evolved in its capability to address a variety of photogrammetric applications. The expanding photogrammetric capabilities of ASP includes an open source and streamlined workflow for building HiRISE DTMs that would otherwise involve more intensive processing using licensed software (e.g. SOCET SET). SOCET SET (now SOCET GXP) workflows are well established in the planetary science photogrammetry community (e.g. Kirk et al, 2008). ASP workflows are well-documented for terrestrial applications (Shean et al, 2016) and non-terrestrial planetary applications (Broxton et al, 2008; Moratto et al, 2010; Hepburn et al, 2019). These publications and version 2.6.1 of the Ames Stereo Pipeline user guide (published 8 August 2018) were referenced extensively throughout the HiRISE DTM generation workflow used for this project.

ASP is operated as a workflow pipeline in the Integrated Software for Imagers and Spectrometers (ISIS), which is a unix-based program developed the United States Geological Survey (USGS). USGS ISIS version 3 (ISISv3) was installed to run on a modified Dell XPS 15 laptop described in the following section. While ISISv3 is capable of building image mosaics and DTMs from HiRISE imagery, some of the required scripts are not available to general public. ASP has resolved this by providing the missing scripts (e.g. hiedr2mosiac.py) that takes Planetary Data System available HiRISE experiment data record (EDR) products through the pre-processing steps required prior to running the ASP stereo program. The following outline (from the ASP User Guide v. 2.6.1, 2018) summaries the key steps within the hiedr2mosaic.py workflow to prepare the image mosaics for stereo processing:

```
hi2isis          # Import HiRISE IMG to ISIS
hical            # Calibrate
histitch         # Assemble who-CCD images from the channels
spiceinit
spicefit         # For good measure
noproj           # Project images into perspective of RED5 (middle HiRISE image)
hijitreg         # Wok out alignment between CCDs
```

```
handmos                  # Mosaic to single file
cubenorm                 # Normalize the mosaic
```

Once complete, hiedr2mosiac.py yields a single mosaic file for each image with the file extension .mos_hijitreged.norm.cub. With the upgraded computer hardware described in Section 2.2.2, the processing times for hiedr2mosaic.py generally took less than half an hour.

The next step involves preparing the resulting HiRISE mosaics for ingestion into the stereo program by map-projecting the images. The cam2map4stereo.py script removes any large disparity in differences between HiRISE images and leaves the calculation of smaller details for ASP. ISISv3 works backwards through the map-projection process when applying the camera model, thus the geometric integrity of the images are not sacrificed through the map-projection process. The time to process both image mosaics through cam2map4stereo.py generally took between 1.5 to 2 hours to process both images as a batch routine. The output from this step consists of georeferenced .map.cub files for each image mosaic.

The next step is to run the resulting .map.cub files through the stereo program. This step is the most time and resource intensive if the entire image mosaics are processed. Stereo processing times for the full field of view for the image mosaics took between 20 to upwards of 100 hours. The stereo program results in approximately ___ output files, including several intermediate files that are integrated into the processing routine. Of the resulting output files, only the DEM-output file is required for final processing in the into a DTM .tiff file point2dem program. The resulting DTM.tiff can be used in other GIS programs for subsequent processing and analysis. The full processing workflow is summarized as follows:

```
ISIS 3> hiedr2mosaic.py  HiRISE_Image_1_RED*.IMG
ISIS 3> hiedr2mosaic.py  HiRISE_Image_2_RED*.IMG
ISIS 3> cam2map4stereo.py      HiRISE_Image_1_RED.mos_hijitreged.norm.cub \
                               HiRISE_Image_2_RED.mos_hijitreged.norm.cub
ISIS 3> stereo                 HiRISE_Image_1.map.cub     HiRISE_Image_2.map.cub
                               result/output
ISIS 3> point2dem              output-DEM
```

2.3 Morphometric Analysis

The resulting image mosaics and DTMs were imported into either ArcGIS or QGIS for additional processing. While ArcGIS was used for some data processing, QGIS was used for most of the data post-processing to enable open-source formatting of the resulting datasets. A modified Dell XPS15 laptop upgraded with a 1 TB solid-state drive and 32 GB of RAM was used to perform the GIS processing procedures outlined in this section. While the hardware was sufficient for performing most operations in a timely and hardware-efficient manner, larger datasets could take upwards of several hours to over a day to process. Hardware capabilities are a paramount consideration prior to replicating this process. Feature delineation procedures were modeled after similar studies that quantified terrestrial patterned ground observations as analogs for patterned ground on Mars (Ulrich et al., 2011; Brooker et al., 2018). Individual patterned ground features were delineated based on morphology, categorized by feature centers and inter-feature margins (Figure 2-6).

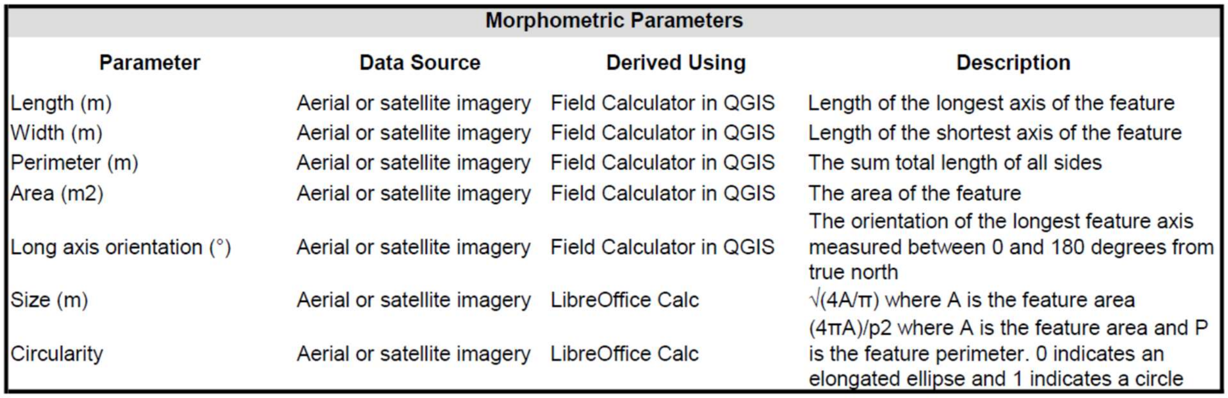

Morphometric Parameters

Parameter	Data Source	Derived Using	Description
Length (m)	Aerial or satellite imagery	Field Calculator in QGIS	Length of the longest axis of the feature
Width (m)	Aerial or satellite imagery	Field Calculator in QGIS	Length of the shortest axis of the feature
Perimeter (m)	Aerial or satellite imagery	Field Calculator in QGIS	The sum total length of all sides
Area (m2)	Aerial or satellite imagery	Field Calculator in QGIS	The area of the feature
Long axis orientation (°)	Aerial or satellite imagery	Field Calculator in QGIS	The orientation of the longest feature axis measured between 0 and 180 degrees from true north
Size (m)	Aerial or satellite imagery	LibreOffice Calc	$\sqrt{(4A/\pi)}$ where A is the feature area
Circularity	Aerial or satellite imagery	LibreOffice Calc	$(4\pi A)/p2$ where A is the feature area and P is the feature perimeter. 0 indicates an elongated ellipse and 1 indicates a circle

Figure 2-6: Morphometric parameters are based on those used by Ulrich et al. (2011) and Brooker et al. (2018). Feature = patterned ground or ice-wedge polygon.

2.4 Multiscale Surface Roughness Analysis

Surface roughness is commonly used in planetary science applications to determine the composition and morphology of volcanic terrains (e.g. Cao et al., 2015; Florinsky, 2018) and to aid in estimating the moisture content of soils (e.g. Neelam et al., 2020). Applications using surface roughness as a morphometric property for characterizing periglacial landforms was not readily found in existing literature. The surface roughness of the UAV DTMs was measured to quantify variations across different feature morphologies (i.e. feature centers, borders, and margins). Detectable variations of surface roughness could serve as a diagnostic metric for assessing feature age and level of present-day activity (Figure 3-4).

Initially, surface roughness measurements were calculated as a standard deviation of elevation of the DTM following Equation 1, which is a function of the mean and range of the DTM raster in a procedure outlined by Ascione et al., 2008. This procedure involves creating mean and range rasters of the target DTM using the Focal Statistics tool in the Spatial Analyst toolkit in ESRI ArcMap. The settings in the Focal Statistics tool default to a 3x3 cell neighborhood, though this can be adjusted based on the spatial resolution of the dataset. The Raster Calculator is then used to generate the resulting surface roughness raster as a standard deviation of elevation (Equation 1). While this process was ultimately abandoned in favor of a multiscale surface roughness procedure described below, it provides a simplified numerical formula for conceptualizing surface roughness parameters.

$$\frac{(\text{"}Mean\ DEM\text{"} - \text{"}DEM\text{"})}{\text{"}Range\ DEM\text{"}} = Standard\ Deviation\ of\ Elevation \qquad (1)$$

Surface roughness measurements are scale-dependent in terms of the features being studied and the measurements are a direct reflection of the spatial resolution of the dataset, so calculating the standard deviation of elevation at a fixed scale (local neighborhood or cell neighborhood radius, such as the default 3x3 parameters) is insufficient to account for variations in feature scale and spatial resolutions across different datasets. A manual alternative could involve repeating the steps outlined above but modulating the cell radius of the local neighborhood to account for a range of scenarios applicable to each dataset.

The challenge of modulating iterative surface roughness calculations for variations in scale is addressed through the development of the QGIS and ArcGIS-compatible Whitebox Tools plugin

(Lindsay et al., 2019). Lindsay et al. 2019 details a method for utilizing the Multiscale Roughness tool to assess DTMs at a range of scale inputs and it useful for handling datasets of varying resolution covering features of varying scale. The method developed by Lindsay et al. seeks to reconcile two similar and often interchanged dimensions of surface roughness. The first dimension is surface ruggedness, as denoted by the variability of local elevation. Surface ruggedness related to ranges in elevation often relies on the standard deviation of elevation previously described. The second dimension is surface complexity, which is a measure of topographic texture. Surface complexity is often quantified by developing a topographic roughness index or the by evaluating the variability in surface normal vectors (e.g. slope and slope aspect). The scale-dependency of both surface ruggedness and complexity is exacerbated by variable being defined over fixed areas rather than by singular points.

The Multiscale Roughness algorithm uses a locally adaptive and scale-optimized approach to capture surface ruggedness and complexity into a single operation. The basis for the operation is as follows:

A three-dimensional surface can be modeled into three vectors (x, y, and z) that are derived from the slope (S) and aspect (a) of the surface such that:

$$x = \sin(a) \times \sin(S) \qquad y = \cos(a) \times \sin(S) \qquad z = \cos(S) \tag{2}$$

In the case of processing DTMs using geospatial software, the vector components can be calculated directly from the elevations within the standard 3 x 3 window surrounding each grid cell. In this simplified model the angular spread among a normal distribution of vector components (n) can be represented by the spherical standard deviation (σ_s) where:

$$\sigma_s = \sqrt{-2\ln\left(\frac{R}{n}\right) \times \left(\frac{180}{\pi}\right)} \tag{3}$$

The resulting σ_s is measured in degrees where zero represents a flat or flat inclined plane and where σ_s values greater than zero can increase infinitely in response to greater surface complexity. The resultant vector length, R, is derived from the sum of the x, y, and z components for each of the normal vectors within a specified filter radius such that:

$$R = \sqrt{\left(\sum_i^n x\right)^2 + \left(\sum_i^n y\right)^2 + \left(\sum_i^n z\right)^2} \qquad (4)$$

As scale-dependent operations, the filter radius (r_f) is defined as $D = 2r_f + 1$, where D is the filter size used to calculate the summations in Equation (4) and where $n = D^2$. In this manner, $r_f = 1$ would correspond to a filter size of 3 x 3, $r_f = 2$ would correspond to a 5 x 5 filter, and so on. This procedure can be applied to derive the maximum σ_s ($\sigma_{s\,max}$) for a range of spatial scales set between lower (r_L) and upper (r_U) filter radius bounds where a locally adaptive measure of surface roughness is defined by:

$$\sigma_{s\,max} = \max\left[\sigma_s(r_f) : r_f = r_L \ldots r_U\right] \qquad (5)$$

The final resulting Multiscale Roughness algorithm involves calculating an integral image at a defined filter radius (as a function of the filter scale or cell neighborhood radius) with a resulting surface roughness output representing an average roughness (in degrees) at the specified filter radius (r_f) interval (Figure 2-8). In high-resolution UAS datasets, surface roughness at a small scale (or small cell neighborhood radius) can reflect features as small as gravels or boulders depending on the flown survey altitude. At a large filter radius for the same base dataset, the resulting surface roughness will asymptotically approach the average surface roughness of the entire study area such that individual meter-scale features become indistinguishable in the multiscale surface roughness dataset.

2.5 Statistical Analysis

The Zonal Statistics tool was used to calculate, aggregate, and export the resulting geospatial datasets from QGIS. The datasets were exported in a .xlsx file format. Despite sharing a common workflow, the differences in types of features present at each site resulted in the creation of several different feature categories. For expediency and process consistency in addressing category variations between each site, the results were compiled in an Excel database. The statistical analysis of the resulting datasets was performed using a combination of built-in tools for Microsoft Excel and the XLSTAT extension developed by Addinsoft. The mean, median, and standard deviation of the baseline morphometric properties and MSR analysis output were tabulated and presented in graphical form using standard Excel workflows and formulas. Raw feature orientations were recorded from 0 deg (north) to 180 deg (south), so it was necessary to calculate the inverse for each feature orientation to plot to a rose diagram. Rose diagrams were plotted using the GeoRose application developed by Yong Technology, Inc.

XLSTAT was used to perform a multivariate principal component analysis (PCA) of the resulting datasets to identify, evaluate, and quantify any potential correlations within each polygon population. A principal component analysis was employed in a study of patterned ground by Ulrich et al. (2011) to identify and evaluate potential morphometric trends and served as the baseline for identifying the morphometric parameters evaluated in this study. The objective of the PCA was to identify and quantify any potential correlations between the baseline morphometric parameters and surface roughness calculations. The correlation matrix and the loading biplot based on the primary and secondary principal components are presented for each site.

3.0 Results

A total of ten sites with existing HiRISE stereo pair coverage were selected to evaluate potential applications of MSR analyses in conjunction with morphometric parameters of polygon centers and margins. The results of the survey at each site are summarized in the following subsections and highlight each respective morphometric analysis, multiscale surface roughness analysis, and principal component analysis.

3.1 Copais Palus

An ASP DTM was generated from HiRISE images PSP_009744_2305 and PSP_010245_2305, which are centered near 50.119° N, 84.304° E in Copais Palus (Figure 3-2). A population of 66 polygons spread across three similarly sized clusters were identified and delineated using the HiRISE imagery in Figure 3-2. While the location is notable for the presence of gullies in the surrounding crater wall, the surveyed polygons are all located in scalloped depressions on the crater floor and treated as a single group. Summary statistics are presented in Table 3-1 for polygon centers. A sample of the delineated features in HiRISE imagery, shaded relief, slope, slope aspect, and surface roughness analysis for $r_f = 10$ and $r_f = 100$ are presented in Figure 3-3.

The polygons average approximately 10.63 m in length, 56.49 m^2 in area, 8.040 m in size, and have a circularity of 0.71. The surveyed polygons have an average long-axis orientation of 71.86° compared to an average slope aspect of 235.8° (Figure 3-4). The average slope aspect of margins is approximately 228.4°. Polygon centers have an average slope of 13.23° compared to an average slope of 15.10° for margins. The multiscale surface roughness analysis of the polygons at the site are summarized Figure 3-5. Polygon centers range from approximately 2.48° at $r_f = 5$ to 5.37° at $r_f = 100$. Polygon margins range from approximately 2.85° to 5.91° within each respective focal radius interval. The MSR analysis of the total surveyed polygon population at the Copais Palus site reveals that surface roughness is slightly lower among the surveyed polygon centers relative to the adjacent margins. A PCA was performed to determine if there are any correlations between the observed morphometric and roughness parameters for the polygon centers (Figure 3-6). Among the surveyed polygons, there are positive correlations between feature size and length. Slope and roughness are positively correlated but inversely related to feature length and size. The resulting correlation matrix is presented in Figure 3-7.

		CP	DM	LV	LC Large	LC Small	MP Large	MP Small Incised	MP Small Regular	UR1 Large	UR1 Small	UR2 Boulders	UR2 Large	UR2 Small	UP Large	UP Small	VB	VB PHX Large	VB PHX Small
Area	**Min**	10.5	3375	14.7	674	74.9	415	11.8	7.6	1310	12.6	54.3	200	10.6	4704	11.3	7.37	52.3	4.14
	Max	242	88007	610	50653	1123	10770	148	147	22917	130	536	26139	118	85529	292	113	2108	142
	Mean	56.5	27608	135	14481	308	3926	47.3	64.0	9587	35.0	173	8273	45.2	22283	76.0	45.8	414	23.3
	Median	48.0	22308	61.8	11974	241	4058	42.6	60.0	9431	26.9	158	5981	40.2	19700	66.8	40.0	265	16.9
	SD	41.2	16939	151	11375	217	2565	26.1	27.8	4686	24.5	92.9	6995	23.6	14215	41.0	23.4	417	22.2
Perimeter	**Min**	13.2	267	14.8	104	31.6	92.5	13.7	12.4	167	14.1	30.1	86.3	13.5	296	13.3	10.8	30.3	9.06
	Max	94.2	1318	154	851	256	457	53.51	69.6	829	63.3	120	1035	70.0	1192	88.7	65.6	296	112
	Mean	31.3	668	46.8	481	74.4	254	27.76	31.3	399	23.9	55.1	392	29.5	583	35.3	27.4	84.8	24.7
	Median	30.4	616	34.0	481	59.2	257	26.48	30.3	386	20.3	51.6	370	26.7	571	33.2	25.4	66.3	19.1
	SD	13.9	222	35.3	210	46.2	103	8.33	8.55	120	10.4	18.5	200	11.7	166	11.6	8.88	54.0	18.1
Length	**Min**	4.02	102	5.06	37.1	10.6	31.9	3.94	4.60	70.9	4.32	10.1	40.4	4.70	92.88	4.33	2.92	11.0	3.24
	Max	33.6	457	45.0	294	89.4	166	22.23	22.5	238	22.1	42.0	326	207.09	399	38.5	18.3	95.8	19.1
	Mean	10.6	225	16.5	170	27.7	83.7	9.34	10.4	127	8.26	19.7	134	13.7	189	11.9	9.26	29.0	7.95
	Median	9.37	197	12.9	167	20.9	76.6	8.75	10.2	127	7.60	18.1	118	9.90	184	10.6	8.38	23.1	6.93
	SD	5.44	81.92	10.3	71.5	18.9	37.6	3.26	3.10	36.6	3.37	6.77	61.9	23.9	64.4	5.07	3.15	16.7	3.78
Size	**Min**	3.66	65.56	4.33	29.3	9.76	23.0	3.87	3.11	40.8	4.01	8.31	15.9	3.67	77.4	3.79	3.06	8.16	2.30
	Max	17.5	335	27.9	254	37.8	117	13.7	13.7	171	12.9	26.1	182	12.2	330	19.28	12.0	51.8	13.4
	Mean	8.04	180	11.5	125	18.9	66.3	7.50	8.80	107	6.38	14.4	94.5	7.35	162	9.53	7.41	21.0	5.07
	Median	7.82	169	8.87	123	17.5	71.8	7.37	8.74	110	5.85	14.2	87.2	7.15	158	9.23	7.13	18.4	4.63
	SD	2.72	54.2	6.36	54.8	5.83	24.9	2.02	2.01	27.8	1.98	3.62	40.8	1.90	46.4	2.45	1.86	9.34	2.02
Circularity	**Min**	0.339	0.476	0.278	0.375	0.216	0.404	0.464	0.333	0.419	0.326	0.408	0.296	0.284	0.640	0.325	0.302	0.243	0.139
	Max	0.882	0.877	0.923	0.881	0.946	0.854	0.912	0.972	0.871	0.933	0.934	0.892	0.893	0.850	0.934	0.900	0.953	0.925
	Mean	0.706	0.726	0.721	0.677	0.784	0.696	0.737	0.800	0.725	0.755	0.720	0.615	0.672	0.763	0.750	0.755	0.719	0.558
	Median	0.754	0.743	0.784	0.673	0.875	0.724	0.762	0.840	0.731	0.793	0.697	0.642	0.708	0.768	0.778	0.787	0.760	0.527
	SD	0.143	0.099	0.171	0.131	0.206	0.118	0.100	0.115	0.097	0.131	0.159	0.156	0.152	0.052	0.119	0.127	0.193	0.217
Slope	**Min**	7.44	3.13	1.36	4.48	3.82	6.46	3.90	5.45	1.78	1.06	1.25	1.60	1.03	1.65	1.43	1.29	1.03	0.62
	Max	28.3	6.33	5.56	17.29	13.63	9.67	25.64	16.47	3.87	5.35	10.56	3.14	6.38	3.67	4.89	9.56	2.98	4.86
	Mean	13.2	4.23	2.76	8.16	7.56	7.98	10.22	9.40	2.58	2.75	3.48	2.20	3.17	2.18	2.47	3.59	1.75	1.92
	Median	11.2	4.05	2.76	6.66	6.55	7.78	9.22	9.23	2.45	2.91	3.11	2.23	2.94	2.08	2.35	3.38	1.64	1.88
	SD	5.31	0.630	0.861	3.52	2.46	0.800	4.01	2.45	0.530	0.882	2.13	0.420	1.23	0.414	0.602	1.91	0.468	0.866
Aspect	**Min**	192	175	67.7	119	118	134	126	122	69.0	92.4	72.8	66.6	42.9	179	142	137	134	80.2
	Max	276	235	277	266	201	239	280	251	293	340	274	292	277	181	205	298	266	321
	Mean	236	203	169	170	158	168	168	154	134	270	182	194	193	180	179	233	197	187
	Median	231	203	173	163	159	162	161	147	118	280	190	197	224	180	179	233	195	187
	SD	19.2	12.3	44.1	35.9	19.0	28.0	30.5	24.8	54.6	50.7	50.3	60.5	73.6	0.417	9.06	30.2	25.4	62.9
Orientation	**Min**	0.184	0.386	1.36	3.90	11.7	4.24	2.73	1.57	3.51	6.92	13.7	2.68	2.94	1.73	0.561	0.876	5.13	3.42
	Max	179	180	177	178	178	177	176	170	180	175	180	180	180	177	180	179	178	180
	Mean	71.9	94.3	54.8	82.7	97.8	82.4	78.4	80.7	103	59.2	86.1	101	91.1	70.0	104	93.4	105	86.4
	Median	44.0	108	33.3	70.7	90.9	80.8	61.2	59.8	105	36.6	81.8	150	69.6	53.5	125	98.2	118	83.0
	SD	59.8	56.8	55.6	54.8	50.9	56.1	47.6	56.5	55.1	45.2	49.6	75.7	70.0	54.1	55.09	56.4	51.84	52.7

Table 3-1: Summary statistics of the evaluated morphometric parameters of the selected HiRISE DTMs.

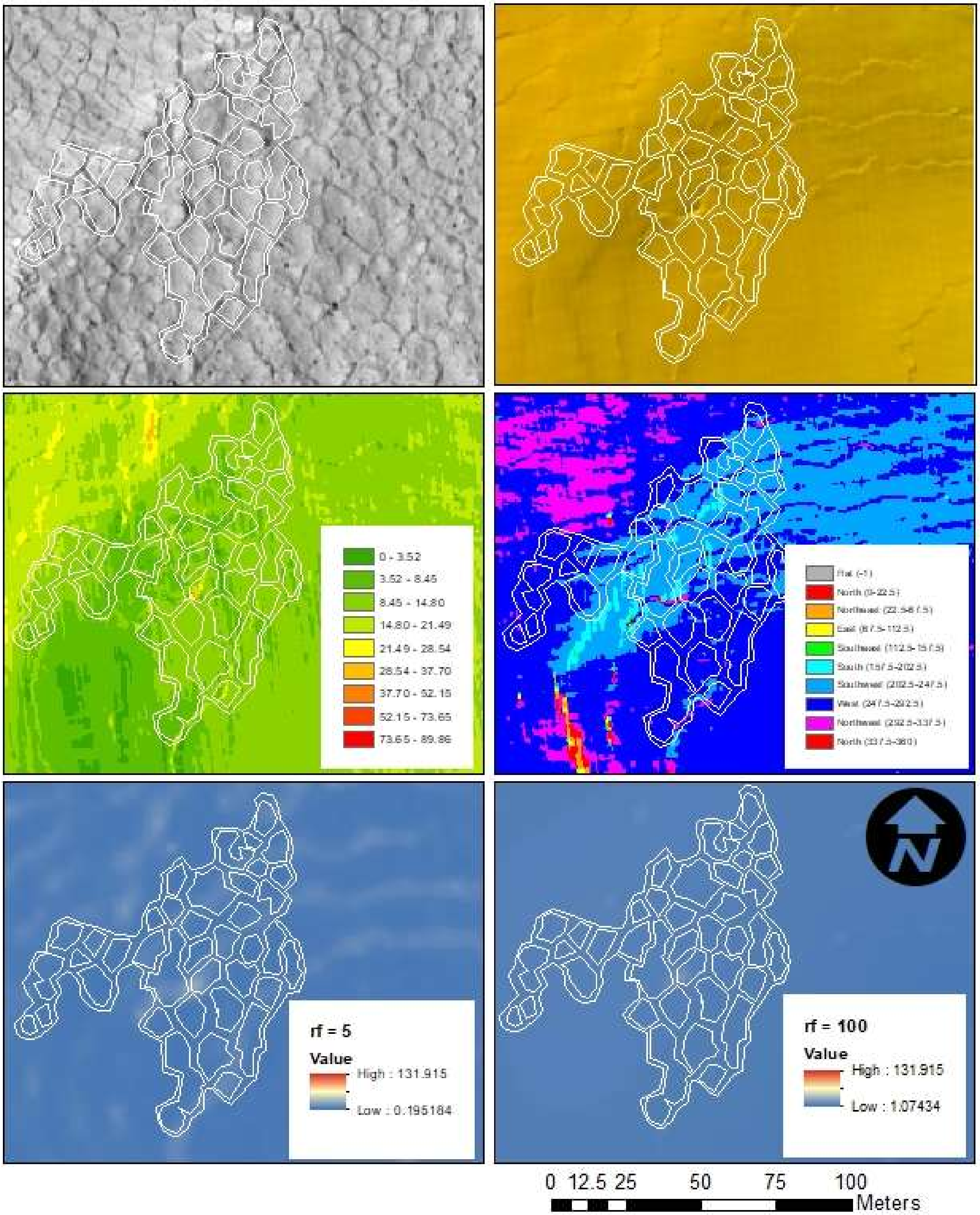

Figure 3-3. (Left-right/top-bottom). HiRISE image and HiRISE DTM-derived shaded relief, slope, aspect, and surface roughness at focal radii of 5 and 100 at Copais Palus. Variations between polygon centers and margins are not visually apparent in the DTM-derived raster datasets.

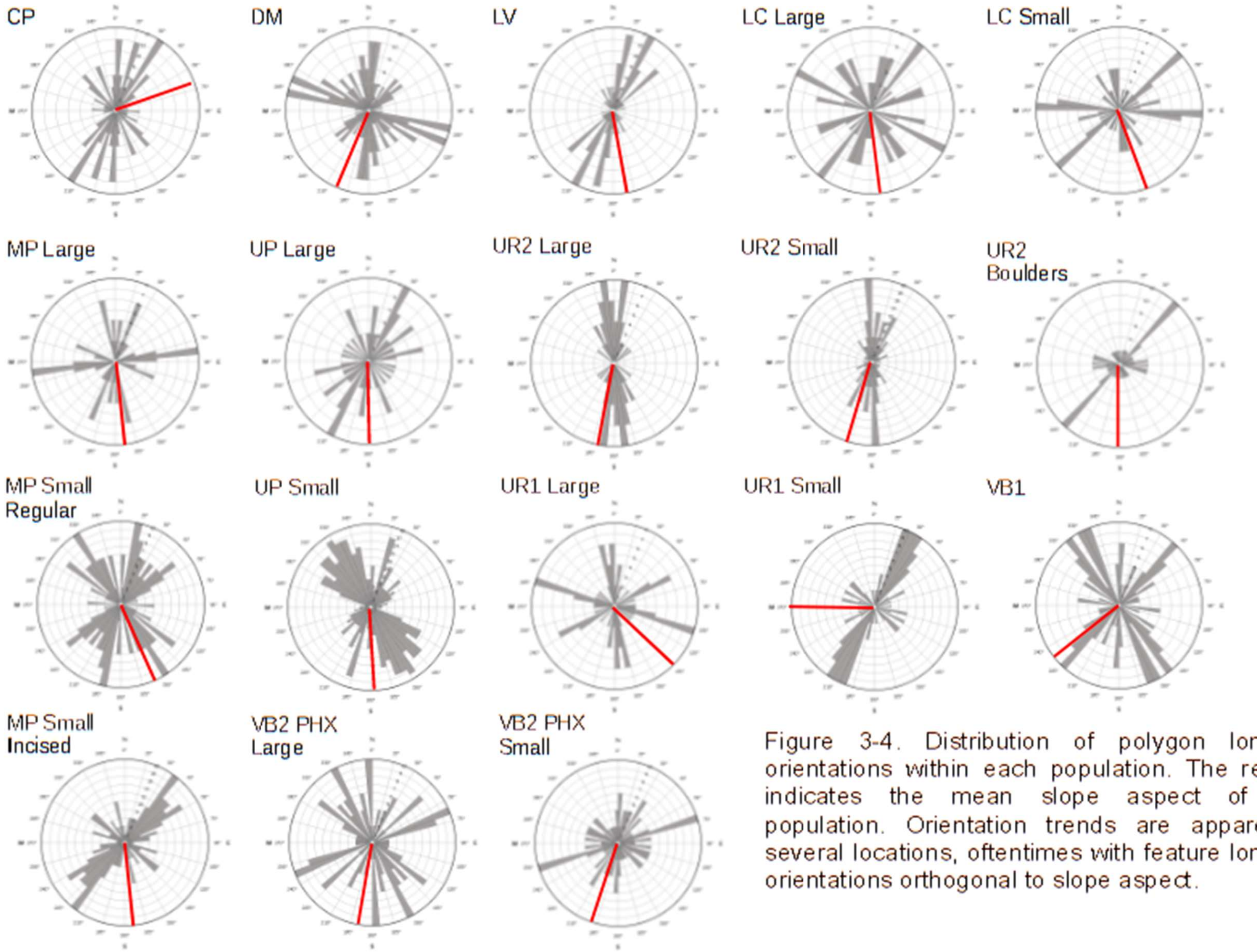

Figure 3-4. Distribution of polygon long-axis orientations within each population. The red line indicates the mean slope aspect of each population. Orientation trends are apparent at several locations, oftentimes with feature long-axis orientations orthogonal to slope aspect.

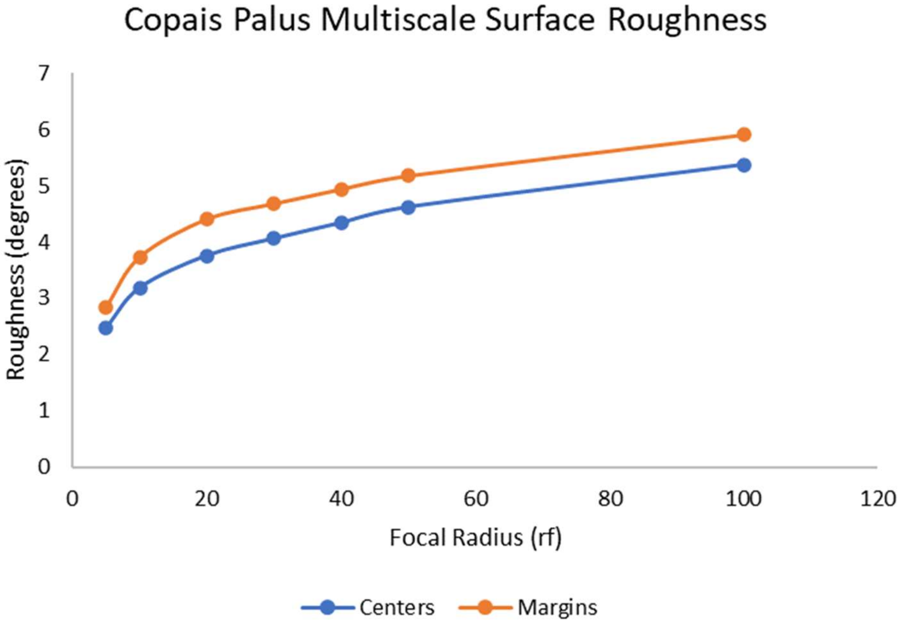

Figure 3-5: MSR plot for the polygon centers and margins at Copais Palus. Polygon centers have a smoother roughness profile when compared to the adjacent margins.

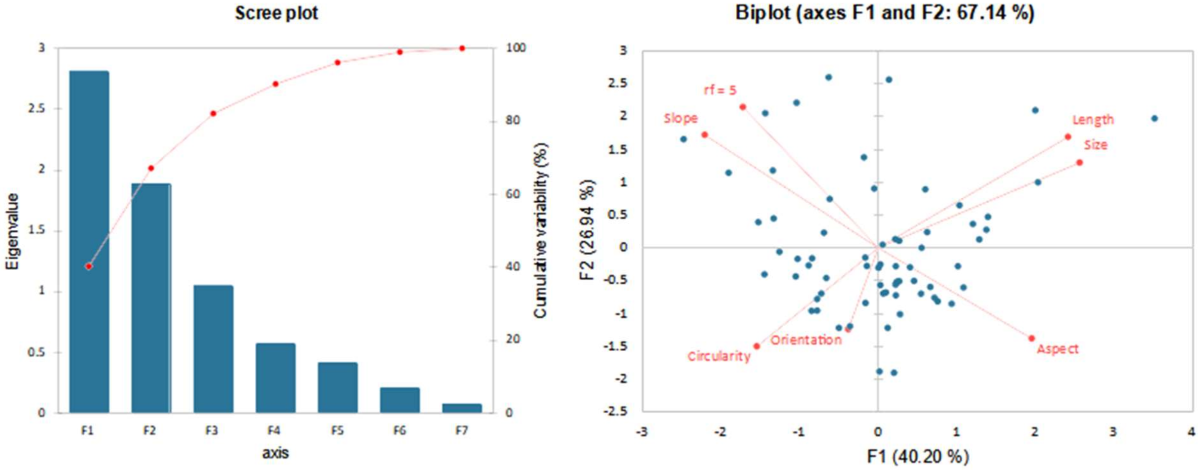

Eigenvectors

	F1	F2	F3	F4	F5
Length	0.468	0.400	0.040	0.196	-0.188
Slope	-0.428	0.408	0.063	0.266	0.238
Aspect	0.379	-0.328	-0.250	0.553	0.615
Orientation	-0.074	-0.295	0.806	0.464	-0.200
Size	0.497	0.307	-0.057	0.208	-0.401
Circularity	-0.300	-0.357	-0.518	0.396	-0.566
rf = 5	-0.334	0.508	-0.105	0.412	0.083

Factor Loadings

	F1	F2	F3	F4	F5
Length	0.785	0.549	0.041	0.147	-0.121
Slope	-0.719	0.560	0.064	0.200	0.152
Aspect	0.635	-0.450	-0.256	0.416	0.394
Orientation	-0.124	-0.405	0.826	0.349	-0.128
Size	0.833	0.422	-0.058	0.157	-0.257
Circularity	-0.503	-0.490	-0.531	0.298	-0.363
rf = 5	-0.561	0.697	-0.108	0.310	0.053

Figure 3-6. Copais Palus polygons PCA scree plot and variable loading biplot. There are positive correlations between feature size and length. Slope and roughness (r_f = 5) are positively correlated but inversely related to length and size.

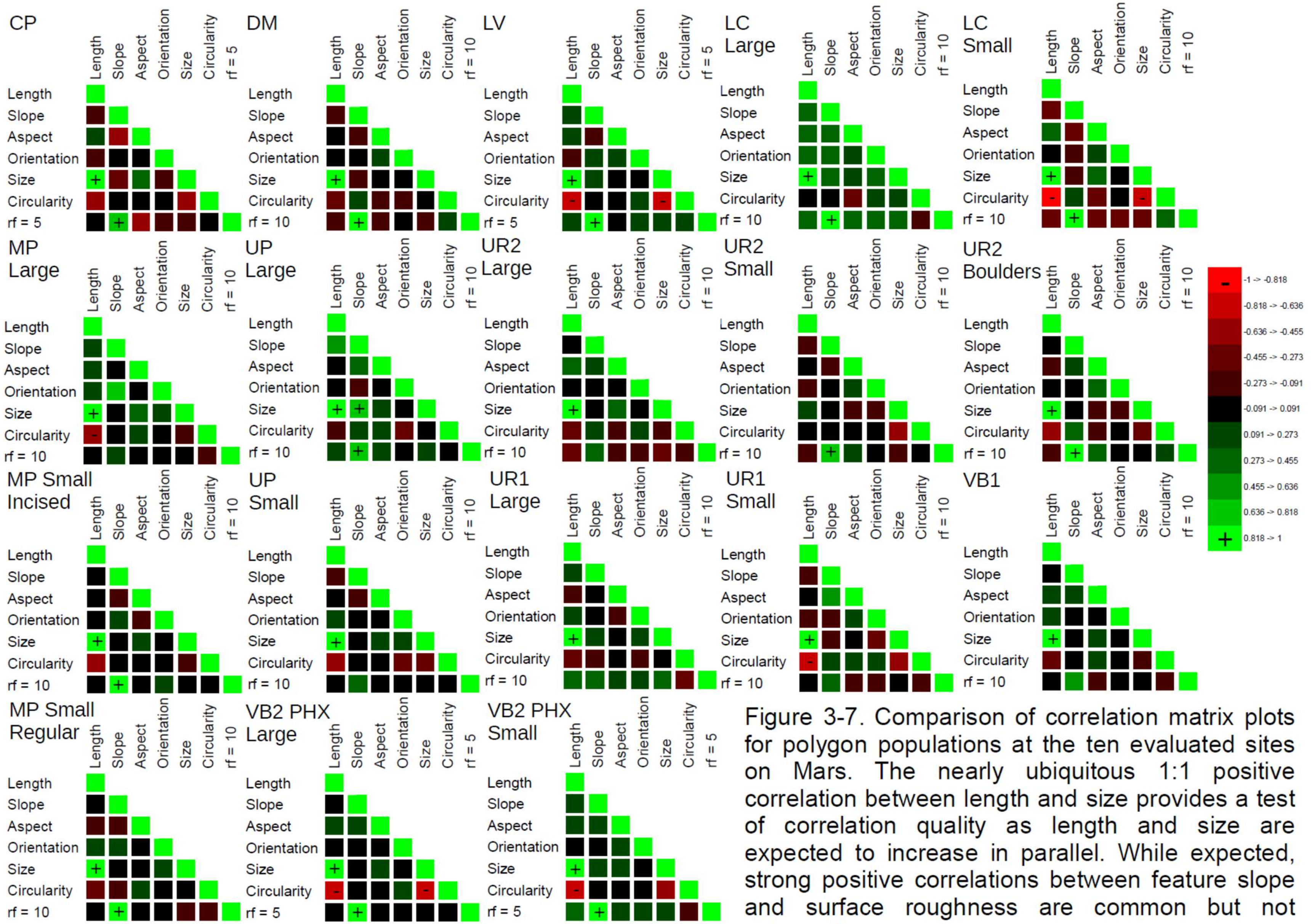

Figure 3-7. Comparison of correlation matrix plots for polygon populations at the ten evaluated sites on Mars. The nearly ubiquitous 1:1 positive correlation between length and size provides a test of correlation quality as length and size are expected to increase in parallel. While expected, strong positive correlations between feature slope and surface roughness are common but not universal.

3.2 Deuteronilus Mensae

An ASP DTM was generated from HiRISE images PSP_007492_2265 and PSP_007703_2265, which are centered near 46.123° N, 15.509° E in Deuteronilus Mensae. A population of 78 polygons spread across four variably sized (one large and three smaller) clusters and were identified and delineated using the HiRISE imagery in Table 1. Summary statistics are presented in Table 3-1 for polygon centers and Table 3-2 for polygon margins. A sample of the delineated features in HiRISE imagery, shaded relief, slope, slope aspect, and surface roughness analysis for $r_f = 10$ and $r_f = 75$ are presented in Figure 3-8.

The surveyed population of polygons are relatively large and uniform in type and are thus grouped into a single category for the site. The polygons average approximately 225.2 m in length, 27,608 m^2 in area, 179.6 m in size, and have a circularity of 0.73. The surveyed Deuteronilus Mensae polygons have an average long-axis orientation of 94.30° compared to an average slope aspect of 202.5° (Figure 3-4). The average slope aspect of margins is approximately 217.2°. Polygon centers have an average slope of 4.23° compared to an average slope of 3.76° for margins. The multiscale surface roughness analysis of the polygons at the site is summarized in Figure 3-9. The polygon centers range from approximately 2.67° at $r_f = 10$ to 4.22° at $r_f = 75$ compared to margins range from approximately 2.11° to 3.51° at the same focal radius range. The MSR analysis at the Deuteronlius Mensae shows the polygon centers have a slightly higher surface roughness in comparison to polygon margins. A PCA was performed to determine

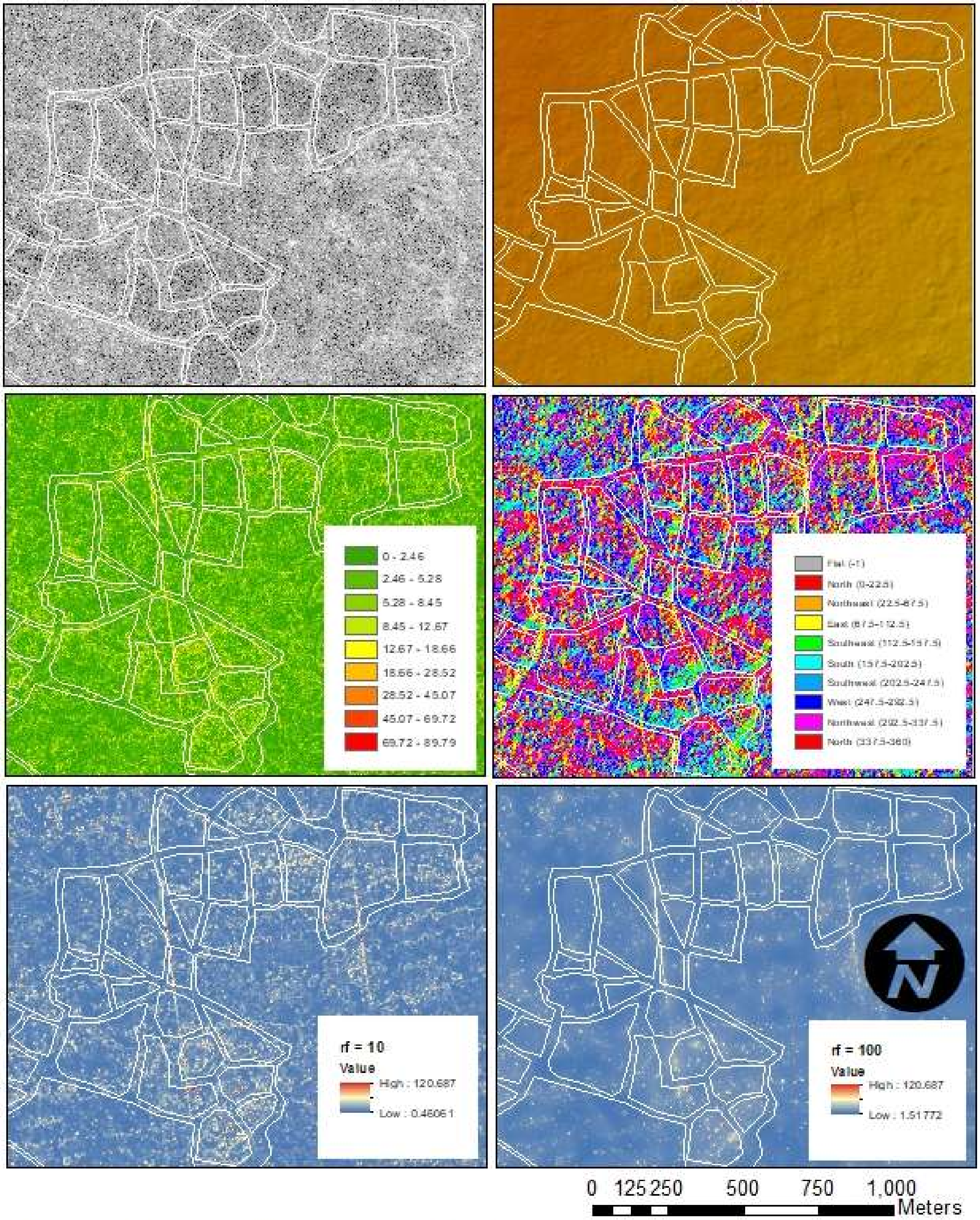

Figure 3-8. (Left-right/top-bottom). HiRISE image and HiRISE DTM-derived shaded relief, slope, aspect, and surface roughness at focal radii of 10 and 100 at Deuteronlius Mensae. Variations between polygon centers and margins are visually apparent in several of the DTM-derived raster datasets.

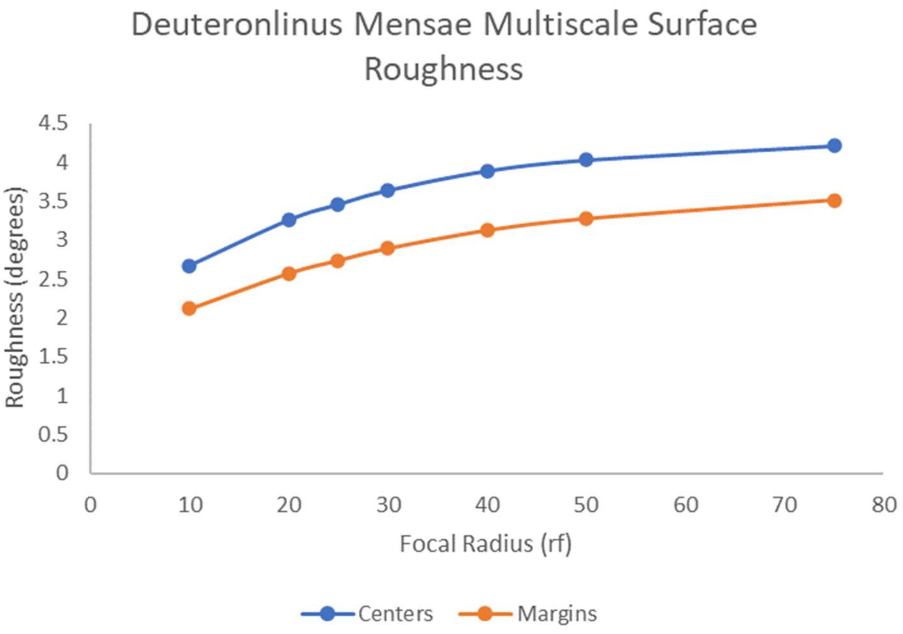

Figure 3-9: MSR plot for the polygon centers and margins at Deuteronlius Mensae. Polygon centers have a rougher surface when compared to the adjacent margins.

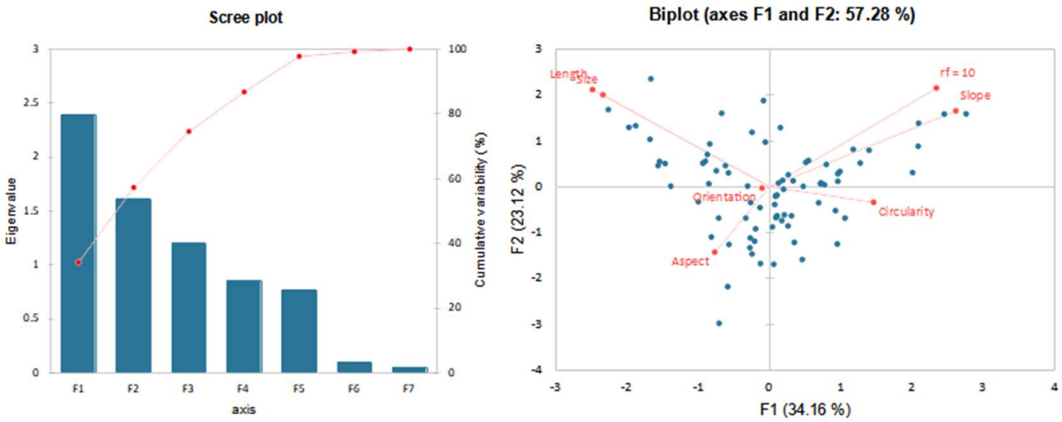

Eigenvectors

	F1	F2	F3	F4	F5
Length	-0.482	0.499	0.068	0.036	0.050
Slope	0.506	0.390	0.237	-0.020	0.192
Aspect	-0.150	-0.336	0.479	0.140	0.780
Orientation	-0.021	-0.008	0.699	0.477	-0.525
Size	-0.453	0.472	-0.133	0.301	0.175
Circularity	0.282	-0.081	-0.430	0.809	0.127
rf = 10	0.453	0.507	0.134	-0.073	0.170

Factor Loadings

	F1	F2	F3	F4	F5
Length	-0.745	0.635	0.075	0.034	0.044
Slope	0.782	0.496	0.261	-0.018	0.168
Aspect	-0.232	-0.428	0.527	0.129	0.685
Orientation	-0.033	-0.010	0.769	0.441	-0.461
Size	-0.701	0.600	-0.146	0.278	0.154
Circularity	0.436	-0.103	-0.473	0.748	0.112
rf = 10	0.700	0.645	0.147	-0.067	0.149

Figure 3-10. Deuteronlius Mensae polygons PCA scree plot and variable loading biplot. There are positive correlations between feature slope and roughness (r_f = 10). Length and size are positively correlated but inversely related to slope and roughness.

if there are any correlations between the observed morphometric and roughness parameters associated with the polygon centers (Figure 3-10). Among the surveyed polygons, there are potential positive correlations between feature slope and surface roughness and between feature length and size. While length and size are positively correlated, they are inversely correlated to slope and roughness. The resulting correlation matrix is presented in Figure 3-7.

3.3 Lethe Vallis

An ASP DTM was generated from HiRISE images ESP_044989_1845 and ESP_045833_1845, which are centered near 4.206° N, 155.508° E in Lethe Vallis. A population of 45 polygons spread across four similarly sized clusters were identified and delineated using the HiRISE imagery in Table 1. Summary statistics are presented in Table 3-1 for polygon centers and Table 3-2 for polygon margins. A sample of the delineated features in HiRISE imagery, shaded relief, slope, slope aspect, and surface roughness analysis for $r_f = 10$ and $r_f = 100$ are presented in Figure 3-11.

The polygons average approximately 16.47 m in length, 134.9 m^2 in area, 11.50 m in size, and have a circularity of 0.72. The surveyed polygons have an average long-axis orientation of 54.82° compared to an average slope aspect of 169.3° (Figure 3-4). The average slope aspect of margins is approximately 173.3°. Polygon centers have an average slope of 2.76° compared to an average slope of 2.82° for margins. The multiscale surface roughness analysis of the polygons at the site are summarized Figure 3-12.

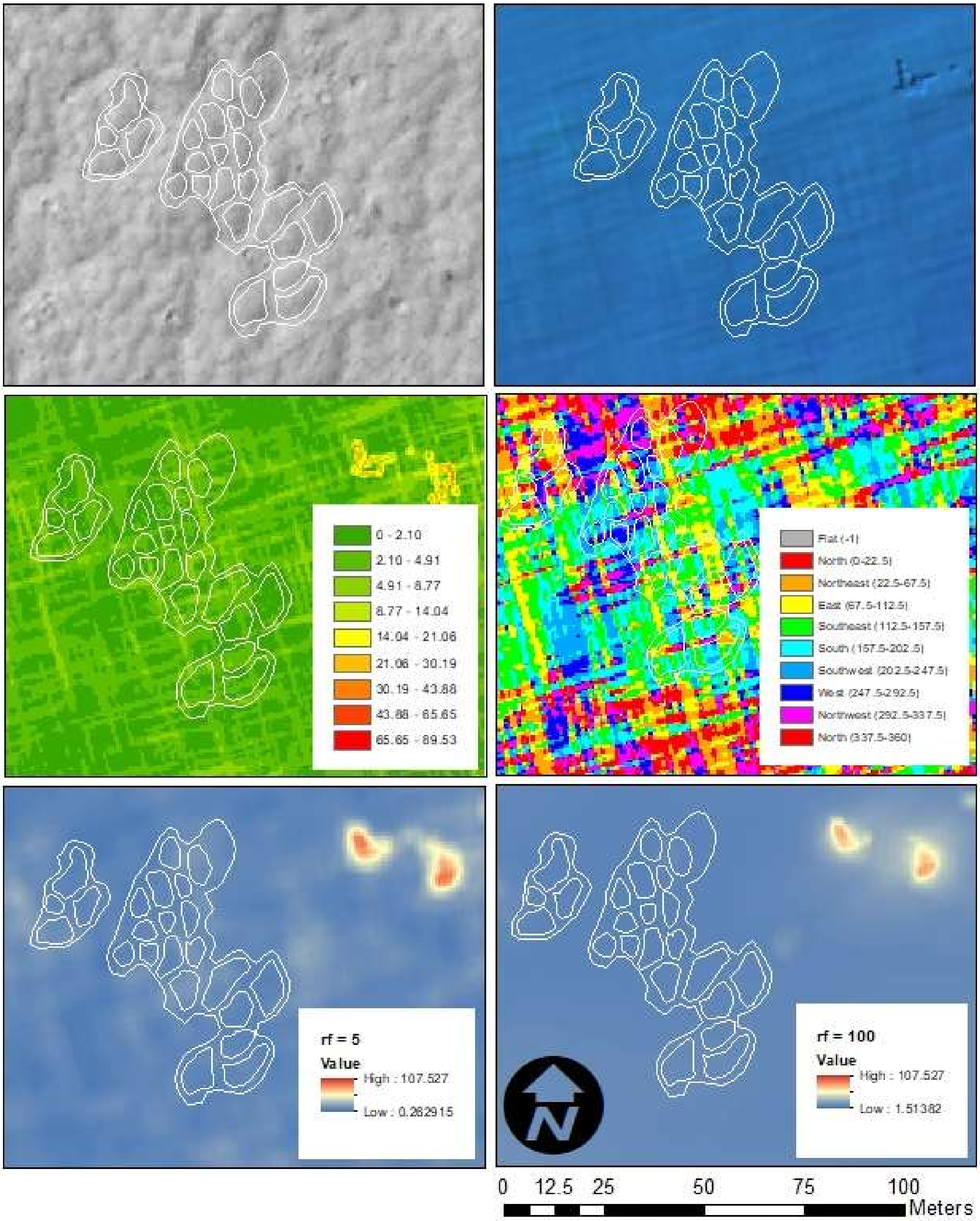

Figure 3-11. (Left-right/top-bottom). HiRISE image and HiRISE DTM-derived shaded relief, slope, aspect, and surface roughness at focal radii of 5 and 100 at Lethe Vallis. Variations between polygon centers and margins are not visually apparent in the DTM-derived raster datasets.

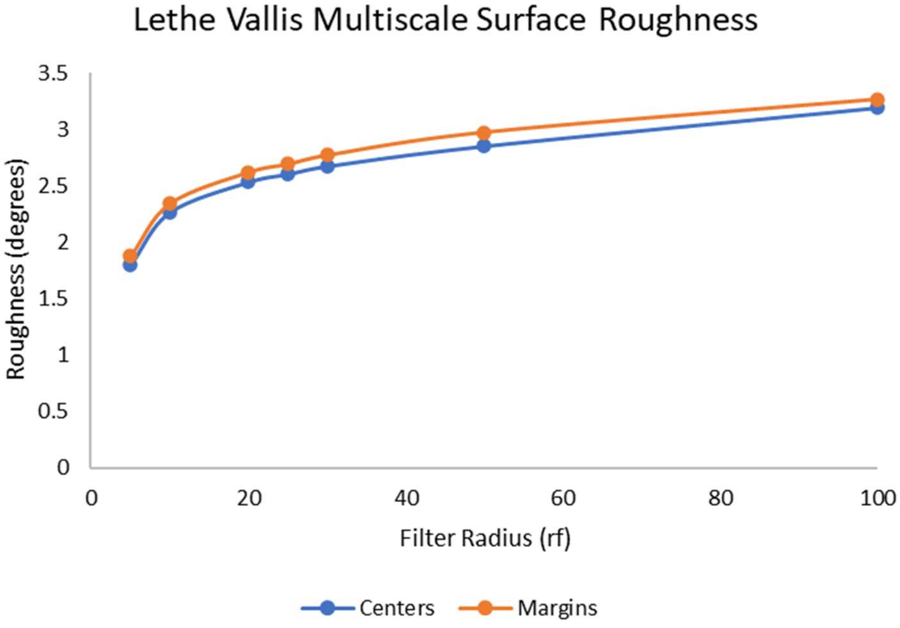

Figure 3-12: MSR plot for the polygon centers and margins at Lethe Vallis. There is not a significant observable difference in surface roughness between centers and margins, however centers average slightly smoother than the adjacent margins.

Polygon centers range from approximately 1.79° at $r_f = 5$ to 3.19° at $r_f = 100$. Polygon margins range from approximately 1.88° to 3.27° at the same focal radius intervals. While polygon centers have a consistently lower surface roughness relative to polygon margins, the variation in surface roughness between centers and margins is extremely slight. A PCA was performed to determine if there are any correlations between the observed parameters for the characterized polygon centers (Figure 3-13). Among the surveyed polygons, there are positive correlations between feature slope and roughness. Feature length and size are positively correlated but inversely correlated to slope and roughness. The resulting correlation matrix is presented in Figure 3-7.

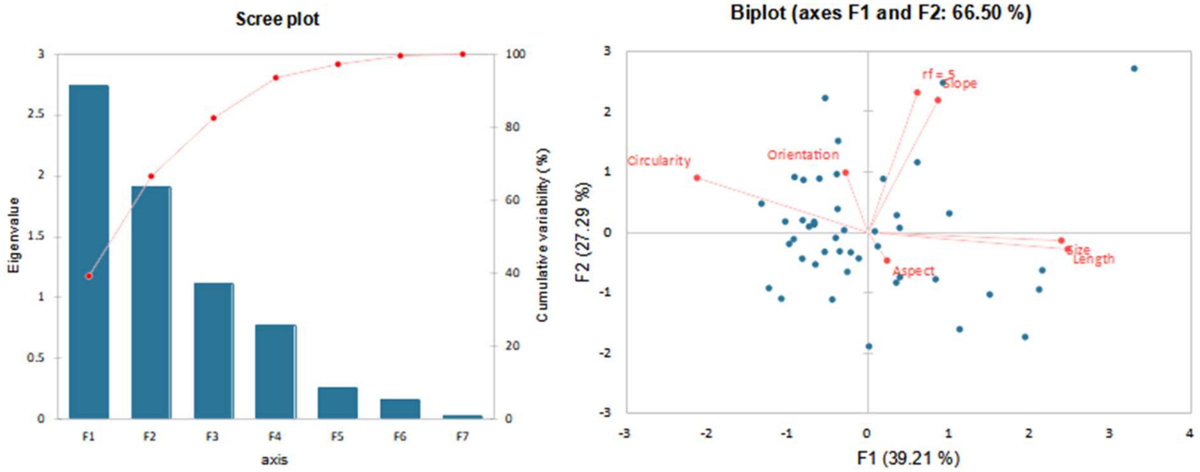

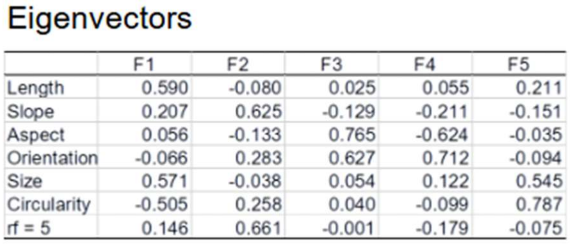

Eigenvectors

	F1	F2	F3	F4	F5
Length	0.590	-0.080	0.025	0.055	0.211
Slope	0.207	0.625	-0.129	-0.211	-0.151
Aspect	0.056	-0.133	0.765	-0.624	-0.035
Orientation	-0.066	0.283	0.627	0.712	-0.094
Size	0.571	-0.038	0.054	0.122	0.545
Circularity	-0.505	0.258	0.040	-0.099	0.787
rf = 5	0.146	0.661	-0.001	-0.179	-0.075

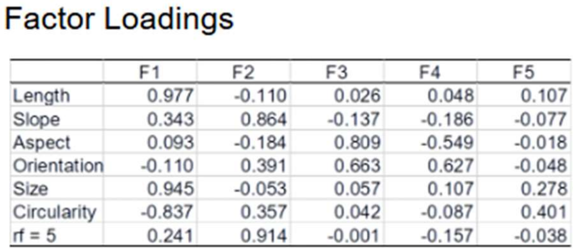

Factor Loadings

	F1	F2	F3	F4	F5
Length	0.977	-0.110	0.026	0.048	0.107
Slope	0.343	0.864	-0.137	-0.186	-0.077
Aspect	0.093	-0.184	0.809	-0.549	-0.018
Orientation	-0.110	0.391	0.663	0.627	-0.048
Size	0.945	-0.053	0.057	0.107	0.278
Circularity	-0.837	0.357	0.042	-0.087	0.401
rf = 5	0.241	0.914	-0.001	-0.157	-0.038

Figure 3-13. Lethe Vallis polygons PCA scree plot and variable loading biplot. There are positive correlations between feature size and length, followed by slope and roughness (r_f = 5).

3.4 Lyot Crater

An ASP DTM was generated from HiRISE images ESP_032980_2345 and ESP_033059_2345, which are centered near 54.137° N, 33.208° E near Lyot Crater. A population of 69 polygons spread across four clusters were identified and delineated using the HiRISE imagery in Table 1. Visible polygons in the stereo-pair imagery are separated into two separate classes consisting of large (34) and small (35) polygons, respectively. Summary statistics are presented in Table 3-1 for polygon centers and Table 3-2 for polygon margins. A sample of the delineated features in HiRISE imagery, shaded relief, slope, slope aspect, and surface roughness analysis for r_f = 10 and r_f = 100 are presented for the large polygon population in Figure 3-14 and the small polygon population in Figure 3-15. Summary statistics are presented in Table 3-1 for polygon centers and Table 3-2 for polygon margins.

The 34 large polygons average approximately 169.9 m in length, 14,481 m^2 in area, 124.6 m in size, and have a circularity of 0.68. The 35 small polygons average approximately 27.73 m in length, 307.6 m^2 in area, 18.94 m in size, and have a circularity of 0.78. The larger polygons that were surveyed have an average long-axis orientation of 82.73° compared to an average slope aspect of 170.3° (Figure 3-4). The smaller polygons have an average long-axis orientation of 97.80° compared to an average slope aspect of 158.23°. The average slope aspect of large polygon margins are approximately 6.855° compared to approximately 8.613° for small polygon margins. Large polygon centers have an average slope of 8.162° compared to an average slope of 210.1° for the adjacent margins. Small polygon centers have an average slope of 7.56° compared to an average slope of 154.1° for the adjacent margins.

The multiscale surface roughness analysis of the both polygon populations at the site is summarized in Figure 3-16. Large polygon centers range from approximately 9.53° at $r_f = 10$ to 12.5° at $r_f = 100$ compared to large polygon margins that range from approximately 5.51° to 10.4° at the same focal radius interval. Small polygon centers range from approximately 9.96° to 12.6° and small polygon margins range from approximately 11.3° to 13.8° at the same cell neighborhood intervals. The MSR analysis at the Lyot Crater site does shows that surface roughness values for small and large polygon centers are roughly similar while small margins had a slightly higher surface roughness relative to small polygon centers and large polygon margins had a smoother surface relative to large polygon centers.

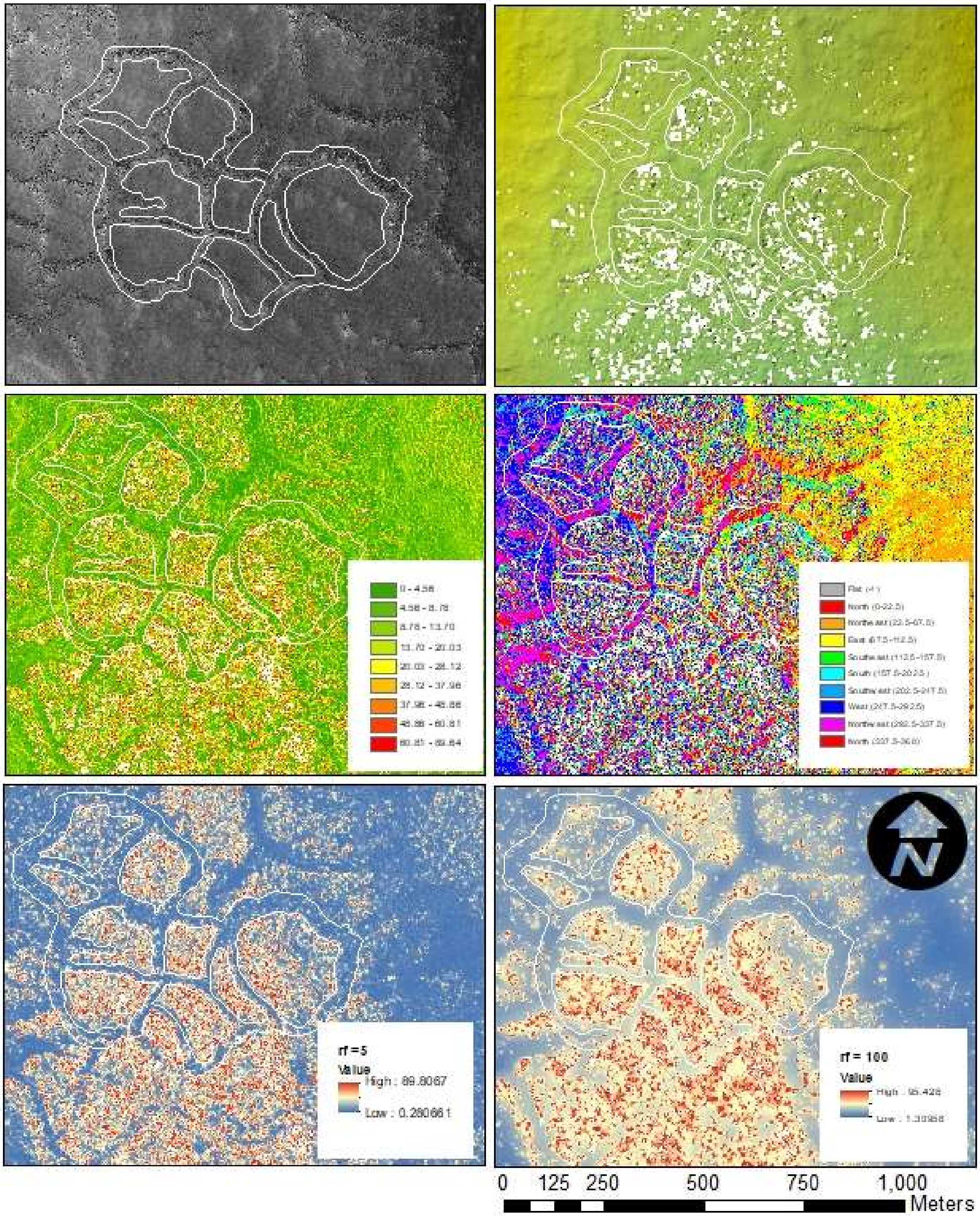

Figure 3-14. (Left-right/top-bottom). HiRISE image and HiRISE DTM-derived shaded relief, slope, aspect, and surface roughness at focal radii of 5 and 100 near Lyot Crater. Variations between polygon centers and margins are visually apparent in the DTM-derived raster datasets.

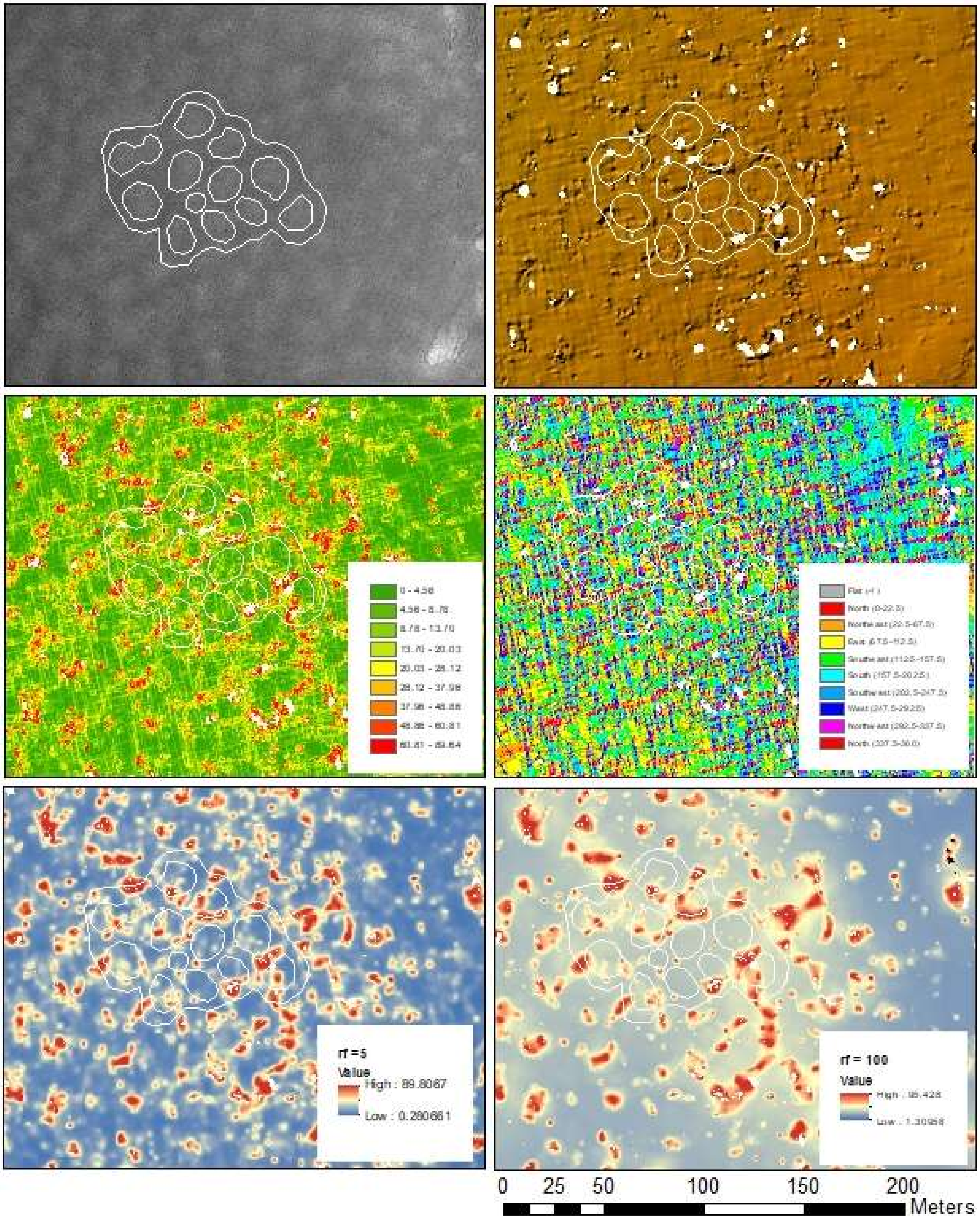

Figure 3-15. (Left-right/top-bottom). HiRISE image and HiRISE DTM-derived shaded relief, slope, aspect, and surface roughness at focal radii of 5 and 100 near Lyot Crater. Variations between polygon centers and margins are visually apparent in the DTM-derived raster datasets.

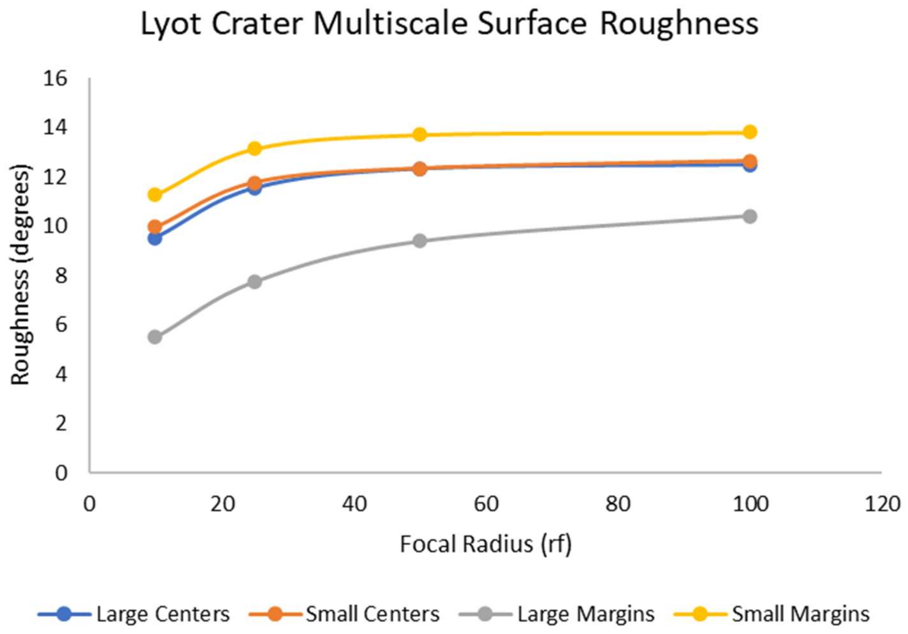

Figure 3-16: MSR plot for the polygon centers and margins near Lyot Crater. Large polygon centers have a significantly higher surface roughness relative to the adjacent margins. In contrast, small polygon centers have a lower surface roughness relative to the adjacent margins.

Two separate PCAs were performed to determine if there are any correlations between the observed parameters for the large polygons (Figure 3-17) and small polygons (Figure 3-18). Among the surveyed large polygons, there are positive correlations between feature length, size, and orientation. Feature slope, aspect, and surface roughness are positively correlated but inversely correlated with feature size. Among the surveyed small polygons, there are positive correlations between feature size and length. Slope and roughness are positively correlated but inversely correlated to both size and length. Among the small polygons, there was a notable inverse correlation between slope aspect, slope, and surface roughness. The resulting correlation matrix for each feature subpopulation is presented in Figure 3-7.

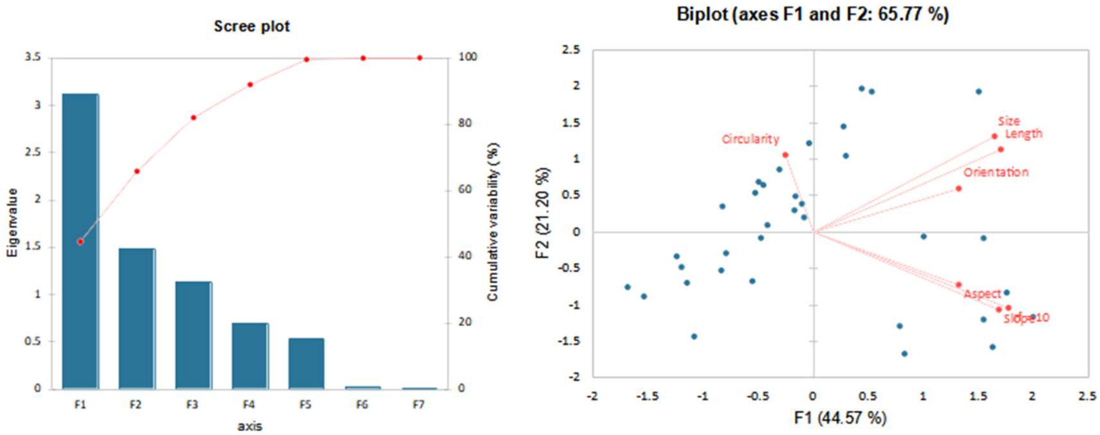

Eigenvectors

	F1	F2	F3	F4	F5
Length	0.437	0.421	-0.262	-0.249	-0.098
Slope	0.433	-0.396	0.353	-0.197	-0.123
Aspect	0.339	-0.270	-0.382	0.297	0.758
Orientation	0.339	0.221	0.132	0.838	-0.336
Size	0.423	0.488	-0.106	-0.295	0.064
Circularity	-0.065	0.393	0.734	0.027	0.525
rf = 10	0.456	-0.388	0.306	-0.141	-0.087

Factor Loadings

	F1	F2	F3	F4	F5
Length	0.773	0.513	-0.279	-0.208	-0.072
Slope	0.765	-0.483	0.376	-0.164	-0.090
Aspect	0.599	-0.329	-0.407	0.248	0.553
Orientation	0.599	0.270	0.140	0.699	-0.245
Size	0.747	0.594	-0.113	-0.246	0.047
Circularity	-0.115	0.479	0.781	0.022	0.383
rf = 10	0.805	-0.473	0.325	-0.118	-0.064

Figure 3-17. Lyot Crater large polygons PCA scree plot and variable loading biplot. There are positive correlations between feature size, length, and orientation. Feature slope, aspect, and roughness ($r_f = 10$) are positively correlated but inversely related to feature size.

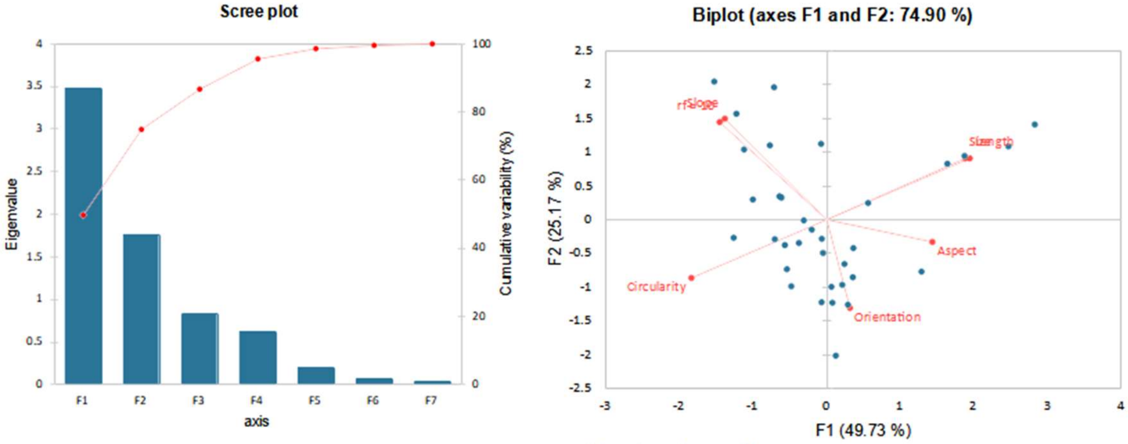

Eigenvectors

	F1	F2	F3	F4	F5
Length	0.473	0.311	0.008	-0.215	0.129
Slope	-0.337	0.512	0.356	0.080	-0.041
Aspect	0.349	-0.114	0.294	0.880	0.022
Orientation	0.076	-0.447	0.813	-0.362	0.047
Size	0.457	0.311	0.046	-0.130	0.621
Circularity	-0.448	-0.296	-0.110	0.134	0.766
rf = 10	-0.354	0.495	0.334	0.089	0.076

Factor Loadings

	F1	F2	F3	F4	F5
Length	0.882	0.412	0.007	-0.169	0.059
Slope	-0.629	0.679	0.324	0.063	-0.019
Aspect	0.651	-0.151	0.267	0.694	0.010
Orientation	0.142	-0.593	0.739	-0.285	0.021
Size	0.853	0.412	0.041	-0.103	0.283
Circularity	-0.836	-0.392	-0.100	0.106	0.349
rf = 10	-0.660	0.657	0.303	0.070	0.035

Figure 3-18. Lyot Crater small polygons PCA scree plot and variable loading biplot. There are positive correlations between feature size and length. Slope and roughness ($r_f = 10$) are positively correlated but inversely related to size and length.

3.5 Malea Planum

An ASP DTM was generated from HiRISE images ESP_030632_1180 and ESP_030698_1180, which are centered near 61.636° S, 79.051° E on a channel floor in Malea Planum. A population of 208 polygons spread across eleven variably-sized clusters were identified and delineated using the HiRISE imagery in Table 1. The surveyed population of polygons can be subdivided into three categories: large polygons (23), small polygons that are incised into larger polygons (113), and small non-incised polygons that are not part of a larger polygonal feature (72). Summary statistics are presented in Table 3-1 for polygon centers and Table 3-2 for polygon margins. A sample of the delineated features in HiRISE imagery, shaded relief, slope, slope aspect, and surface roughness analysis for $r_f = 10$ and $r_f = 30$ are presented for the large, small incised, and small non-incised (regular) polygon populations in Figures 3-19, 3-20, and 3-21, respectively. A smaller maximum focal radius was used at Malea Planum as processing times for the smaller focal radius intervals indicated that processing times for larger intervals would be time-prohibitive and previous multiscale surface roughness evaluations of HiRISE DTMs are observed to begin stabilizing between a focal radius of 30 and 50.

The large polygons average approximately 83.73 m in length, 3,926 m^2 in area, 66.32 m in size, and have a circularity of 0.70. The surveyed polygons have an average long-axis orientation of 100.5° compared to an average slope aspect of 168.4° (Figure 3-4). The average slope aspect of margins is approximately 170.2°. Polygon centers have an average slope of 7.976° compared to an average slope of 9.230° for margins. The multiscale surface roughness analysis of the polygons at the site are summarized Figure 3-22. Large polygon centers range from approximately 6.72 at $r_f = 10$ to 8.24 at $r_f = 30$. Large polygon margins range from approximately 8.59° to 10.06° at the same focal radius intervals. The MSR analysis for the large polygons at Malea Planum demonstrate the centers have a consistently lower surface roughness relative to the adjacent margins.

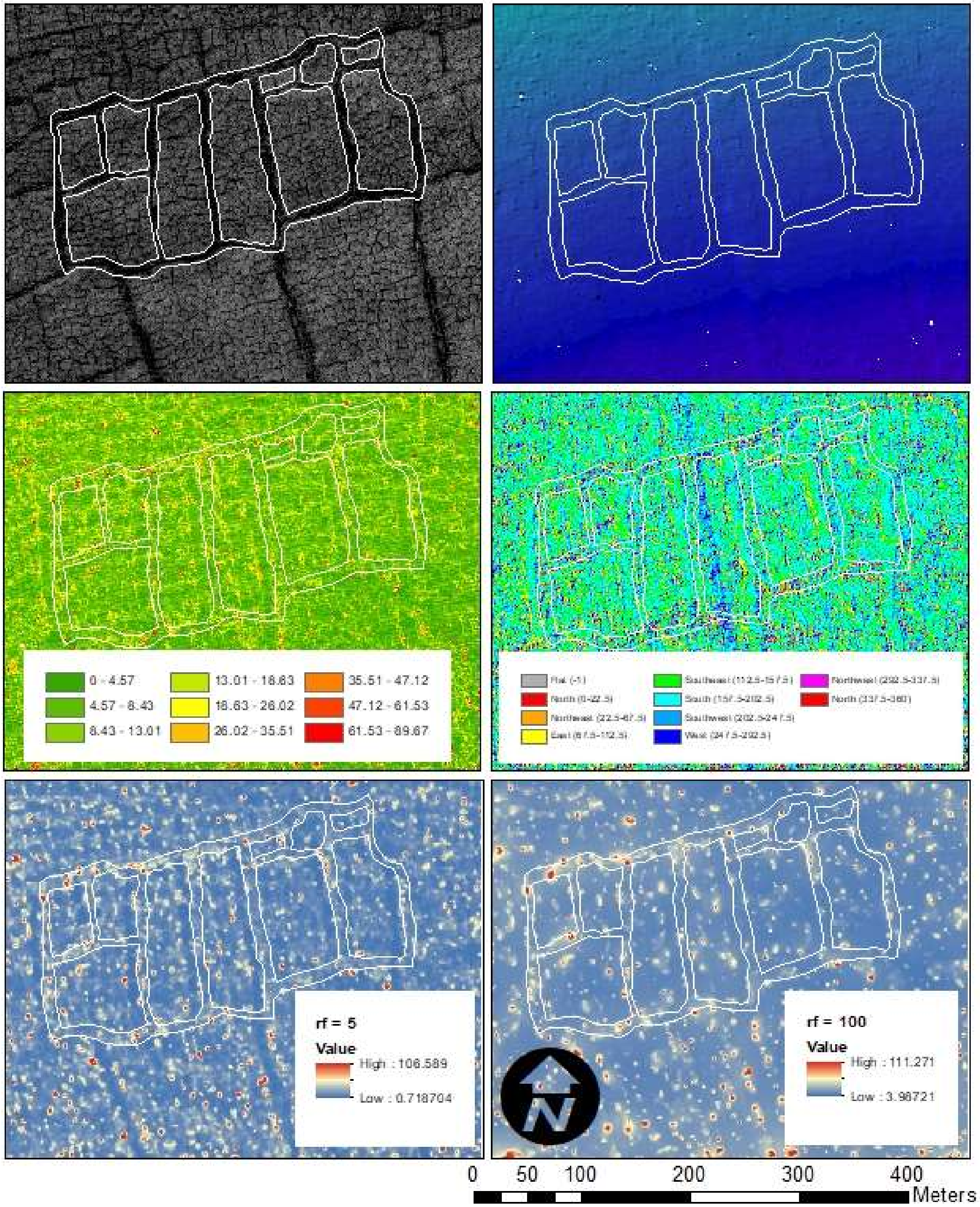

Figure 3-19. (Left-right/top-bottom). HiRISE image and HiRISE DTM-derived shaded relief, slope, aspect, and surface roughness at focal radii of 5 and 100 at Malea Planum. Variations between polygon centers and margins are visually apparent in the DTM-derived raster datasets. Small incised polygons are visible within the large polygon centers.

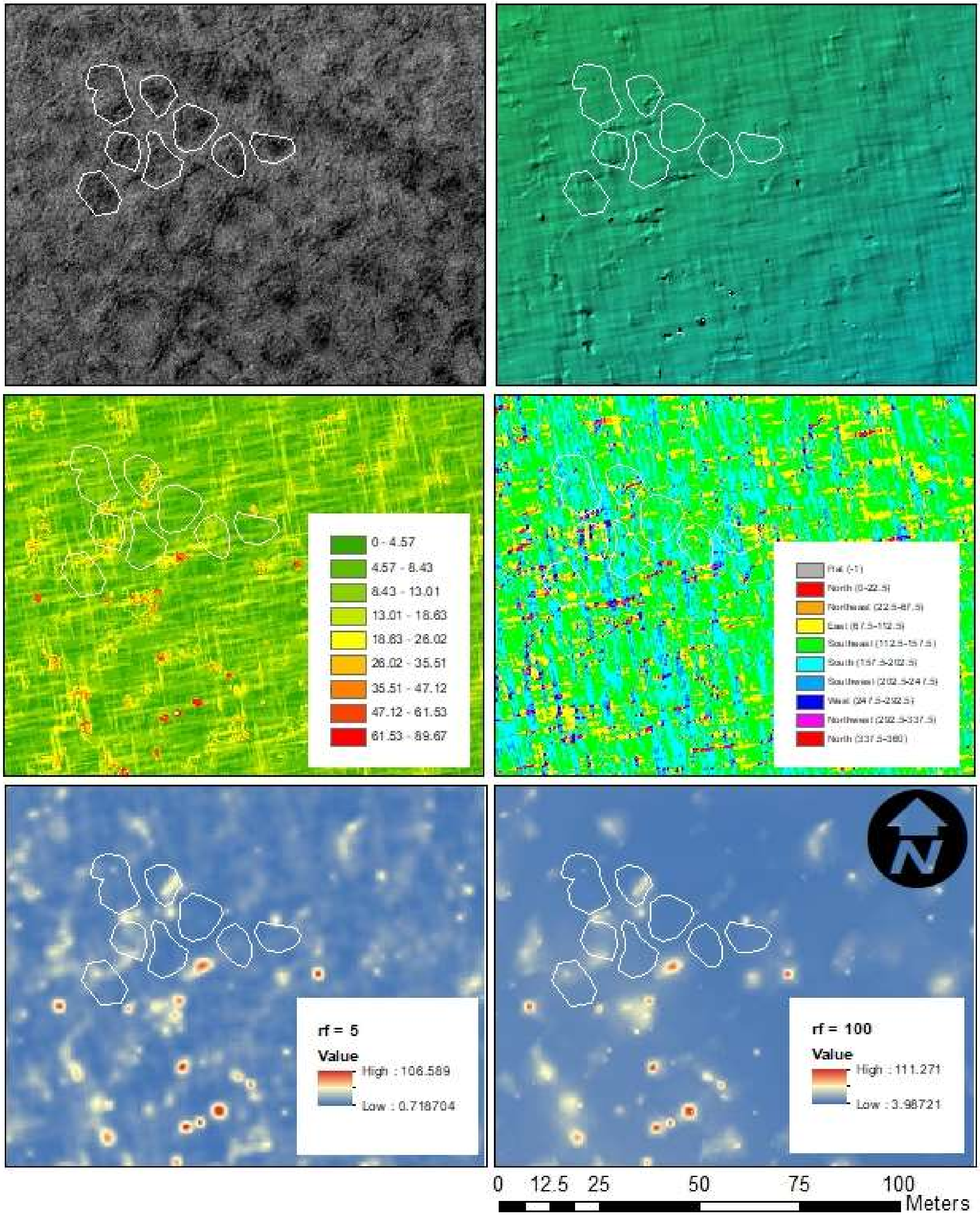

Figure 3-20. (Left-right/top-bottom). HiRISE image and HiRISE DTM-derived shaded relief, slope, aspect, and surface roughness at focal radii of 5 and 100 at Malea Planum. Variations between polygon centers and margins are not visually apparent in the DTM-derived raster datasets.

The PCA for the large polygons (Figure 3-23) found a positive correlation between feature slope, orientation and roughness. Feature size and length are positively correlated but inversely correlated to slope, orientation, and roughness. The observed relationships between orientation and aspect in the PCA may be biased as most features in this population were selected on southward facing slopes along the channel. The resulting correlation matrix is presented in Figure 3-7.

The small incised polygons average approximately 9.335 m in length, 47.31 m^2 in area, 7.497 m in size, and have a circularity of 0.74. The surveyed polygons have an average long-axis orientation of 78.356° compared to an average slope aspect of 168.5° (Figure 3-4). The average slope aspect of margins is approximately 155.5°. Polygon centers have an average slope of 10.22° compared to an average slope of 9.659° for margins. The multiscale surface roughness analysis of the polygons at the site are summarized Figure 3-22. Small incised polygon centers range from approximately 8.96 at r_f = 10 to 10.53 at r_f = 30. The adjacent margins for the small incised polygons range from approximately 7.52° to 8.74° at the same focal radius intervals. The MSR analysis for the small incised polygons at Malea Planum demonstrate that the centers have a slightly higher surface roughness relative to the adjacent margins. The PCA for the small incised polygons (Figure 3-24) found a positive correlation between feature size and length. Slope and roughness are positively correlated but are inversely correlated to size and length. As with the large polygons, the observed relationships between orientation and aspect in the PCA may be biased as most features in this population were selected on a southward facing slopes along the channel. The resulting correlation matrix is presented in Figure 3-7.

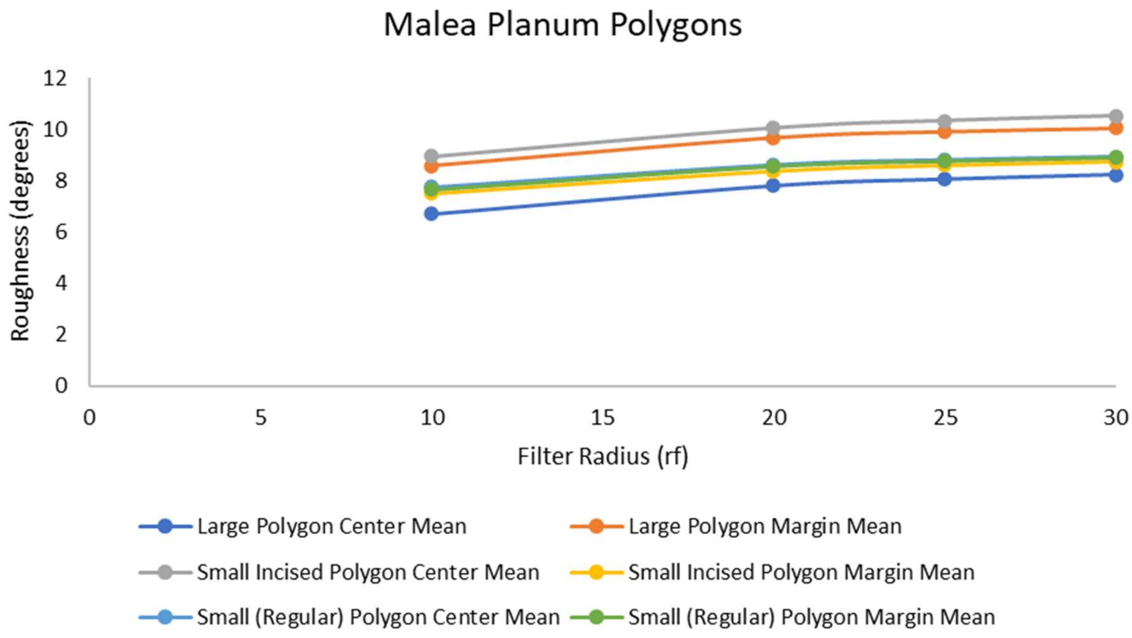

Figure 3-21: MSR plot for the polygon centers and margins at Malea Planum. Large polygon centers have a lower surface roughness relative to the adjacent margins. Small incised polygons centers have a higher surface roughness relative to the adjacent margins. There is no difference in surface roughness between the small non-incised (regular) polygons.

The small non-incised (regular) polygons average approximately 10.45 m in length, 64.01 m^2 in area, 8.804 m in size, and have a circularity of 0.80. The surveyed polygons have an average long-axis orientation of 80.69° compared to an average slope aspect of 153.9° (Figure 3-4). The average slope aspect of margins is approximately 186.4°. Polygon centers have an average slope of 9.405° compared to an average slope of 8.740° for margins. The multiscale surface roughness analysis of the polygons at the site are summarized Figure 3-22. Centers for small (non-incised) polygons range from approximately 7.76° at r_f = 10 to 8.95° at r_f = 30. The adjacent margins for the small (non-incised) polygons range from approximately 7.761° to 8.91° at the same focal radius intervals. The MSR analysis for the small (non-incised) polygons at Malea Planum demonstrate that the surface roughness across the centers and adjacent margins is nearly identical.

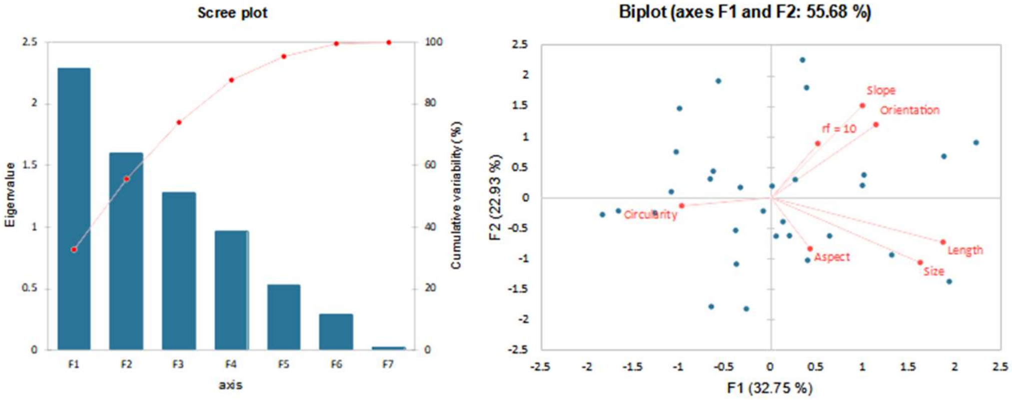

Eigenvectors

	F1	F2	F3	F4	F5
Length	0.597	-0.279	-0.133	-0.125	0.096
Slope	0.318	0.575	0.257	0.050	-0.155
Aspect	0.136	-0.319	0.424	0.669	-0.489
Orientation	0.365	0.457	0.365	-0.240	-0.054
Size	0.518	-0.406	0.143	-0.076	0.361
Circularity	-0.310	-0.050	0.669	0.055	0.604
rf = 10	0.163	0.338	-0.367	0.684	0.479

Factor Loadings

	F1	F2	F3	F4	F5
Length	0.904	-0.353	-0.151	-0.122	0.070
Slope	0.481	0.728	0.292	0.050	-0.114
Aspect	0.206	-0.405	0.481	0.657	-0.357
Orientation	0.552	0.579	0.413	-0.236	-0.040
Size	0.784	-0.514	0.163	-0.075	0.264
Circularity	-0.469	-0.064	0.758	0.054	0.442
rf = 10	0.247	0.429	-0.417	0.672	0.350

Figure 3-22. Malea Planum large polygons PCA scree plot and variable loading biplot. There are positive correlations between feature slope, orientation, and roughness (r_f = 10). Feature size and length are positively correlated but negatively correlated to slope, orientation, and roughness. Relationships with orientation and aspect may be biased as most features were selected on a southward facing slope along the channel.

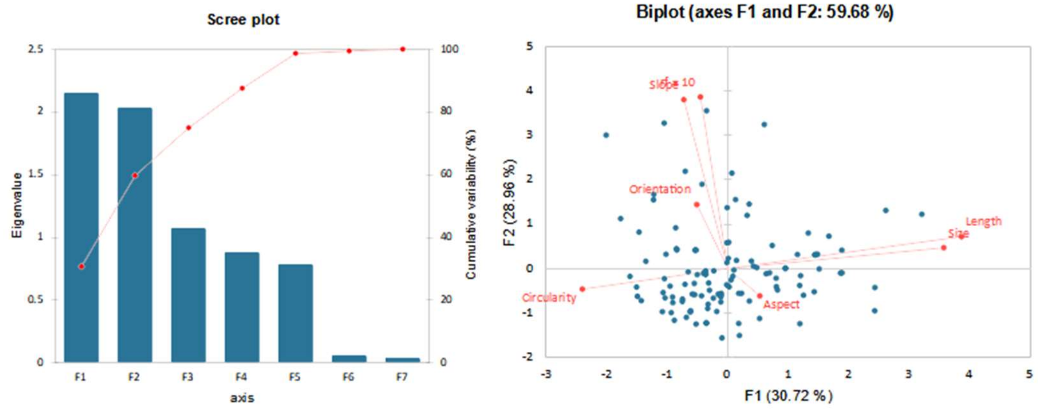

Eigenvectors

	F1	F2	F3	F4	F5
Length	0.656	0.126	-0.047	0.059	0.121
Slope	-0.123	0.664	0.151	-0.168	0.053
Aspect	0.090	-0.107	0.789	0.441	-0.395
Orientation	-0.087	0.251	-0.493	0.810	-0.157
Size	0.606	0.081	0.090	0.149	0.437
Circularity	-0.408	-0.081	0.256	0.302	0.781
rf = 10	-0.077	0.675	0.189	-0.059	-0.038

Factor Loadings

	F1	F2	F3	F4	F5
Length	0.961	0.179	-0.049	0.056	0.107
Slope	-0.180	0.946	0.156	-0.157	0.047
Aspect	0.132	-0.153	0.816	0.413	-0.349
Orientation	-0.128	0.358	-0.510	0.759	-0.139
Size	0.888	0.116	0.093	0.139	0.386
Circularity	-0.598	-0.116	0.265	0.283	0.689
rf = 10	-0.112	0.961	0.196	-0.055	-0.034

Figure 3-23. Malea Planum small incised polygons PCA scree plot and variable loading biplot. There are positive correlations between feature size and length. Slope and roughness (r_f = 10) are positively correlated but negatively correlated to size and length. Relationships to orientation and aspect may be biased as most features were selected on a southward facing slope along the channel.

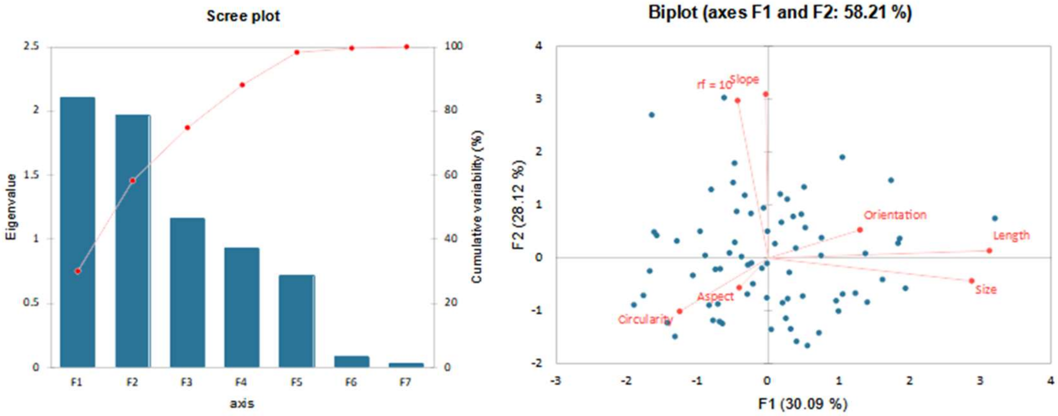

Eigenvectors

	F1	F2	F3	F4	F5
Length	0.671	0.031	-0.037	0.153	0.110
Slope	-0.007	0.688	0.084	-0.038	0.143
Aspect	-0.088	-0.124	0.629	0.660	-0.348
Orientation	0.279	0.118	0.422	-0.626	-0.576
Size	0.618	-0.096	0.220	0.090	0.373
Circularity	-0.269	-0.224	0.579	-0.334	0.597
rf = 10	-0.093	0.661	0.185	0.168	0.140

Factor Loadings

	F1	F2	F3	F4	F5
Length	0.974	0.044	-0.040	0.148	0.093
Slope	-0.010	0.965	0.090	-0.036	0.121
Aspect	-0.128	-0.174	0.677	0.638	-0.294
Orientation	0.405	0.166	0.454	-0.605	-0.486
Size	0.897	-0.134	0.237	0.087	0.315
Circularity	-0.391	-0.314	0.623	-0.322	0.504
rf = 10	-0.135	0.928	0.199	0.162	0.118

Figure 3-24. Malea Planum small non-incised (regular) polygons PCA scree plot and variable loading biplot. There are positive correlations between feature size and length, followed by slope and roughness (r_f = 10). Relationships to feature orientation and aspect may be biased as many features were selected on a southward facing slope near the channel.

The PCA for the small regular polygons (Figure 3-25) found a positive correlation between feature size and length as well as slope and roughness. While a less prominent correlation is observed with feature orientation and aspect, the observed relationships between orientation and aspect in the PCA may be biased as most features in this population are selected on southward facing slopes north of the channel. The resulting correlation matrix is presented in Figure 3-7.

3.6 Utopia Planitia

An ASP DTM was generated from HiRISE images PSP_007780_2450 and PSP_008492_2450, which are centered near 64.518° N, 67.278° E in Utopia Planitia. A total population of 253 polygons subdivided by 34 large polygons and 227 small polygons spread across three clusters and were identified and delineated using the HiRISE imagery in Table 3-1. Summary statistics are presented in Table 3-1 for polygon centers and Table 3-2 for polygon margins. A sample of the delineated features in HiRISE imagery, shaded relief, slope, slope aspect, and surface roughness analysis for rf = 10 and rf = 100 are presented for the large and small polygon populations in Figures 3-25 and 3-26, respectively.

The surveyed population of polygons were subdivided into two separate categories observable in stereo-pair images of the site: 34 large polygons and 227 small polygons that, as a whole population, are co-located with and inset onto the centers of the large polygons. While the surveyed polygons represent a sample of each respective population, the small polygons are observed to greatly outnumber the large polygon population in the imagery. The large polygons average approximately 188.6 m in length, 22,283 m^2 in area, 162.1 m in size, and have a circularity of 0.76. The small polygons average approximately 11.95 m in length, 76.03 m2 in area, 9.53 m in size, and have a circularity of 0.75. The large polygons have an average long-axis orientation of 70.02° compared to an average slope aspect of 180.0°. The small polygons have an average long-axis orientation of 104.3° compared to a slope aspect of 178.9° (Figure 3-26). The average slope aspect of large polygon margins is approximately 179.8° and the slope aspect for small polygon margins is approximately 183.5°. Large polygon centers have an average slope of 2.17° compared to an average slope of 2.99° for the adjacent margins. Small polygon centers have an average slope of 2.47° compared to an average slope of 2.92° for the adjacent margins.

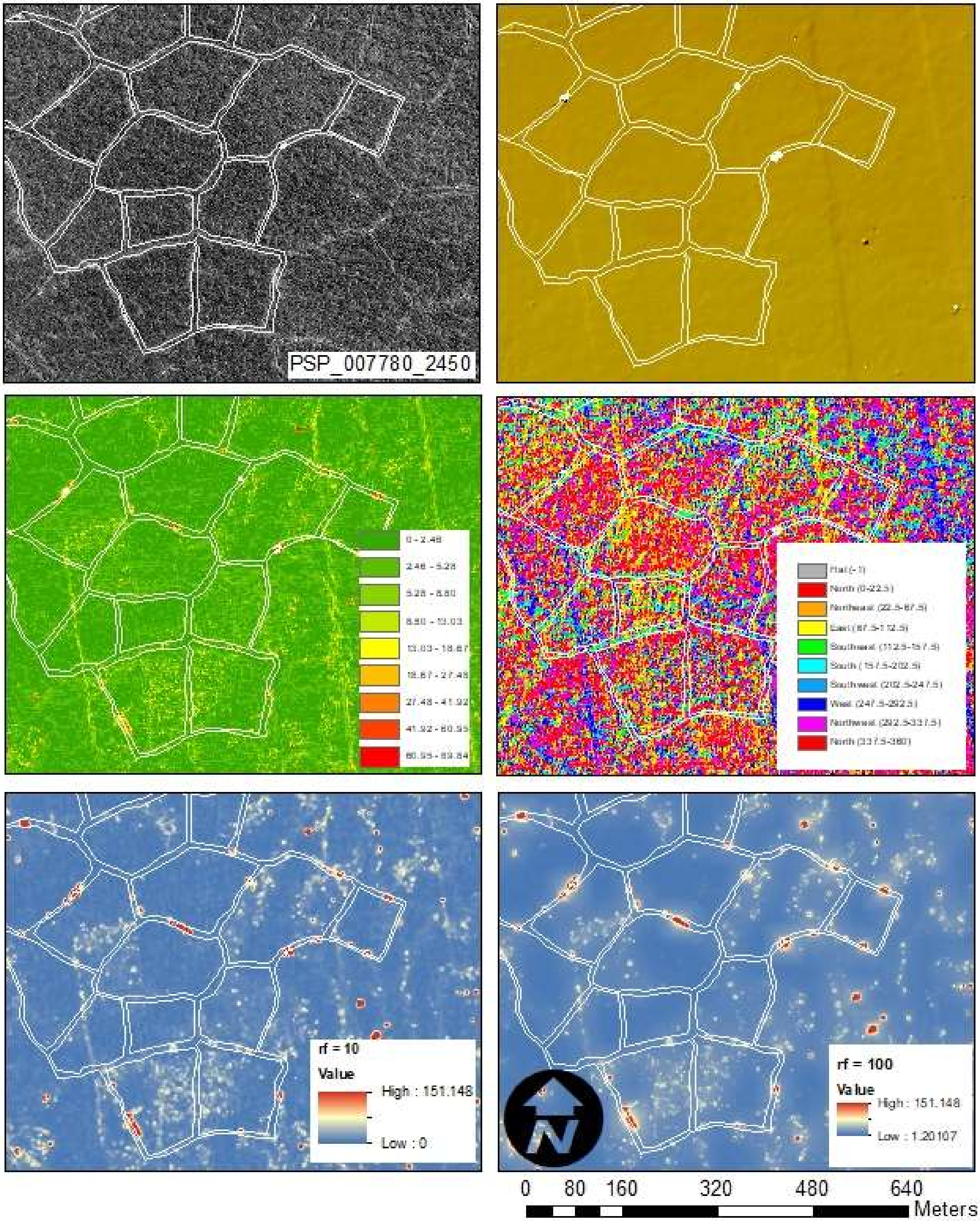

Figure 3-25. (Left-right/top-bottom). HiRISE image and HiRISE DTM-derived shaded relief, slope, aspect, and surface roughness at focal radii of 10 and 100. Variations between polygon centers and margins are visually apparent in several of the DTM-derived raster datasets.

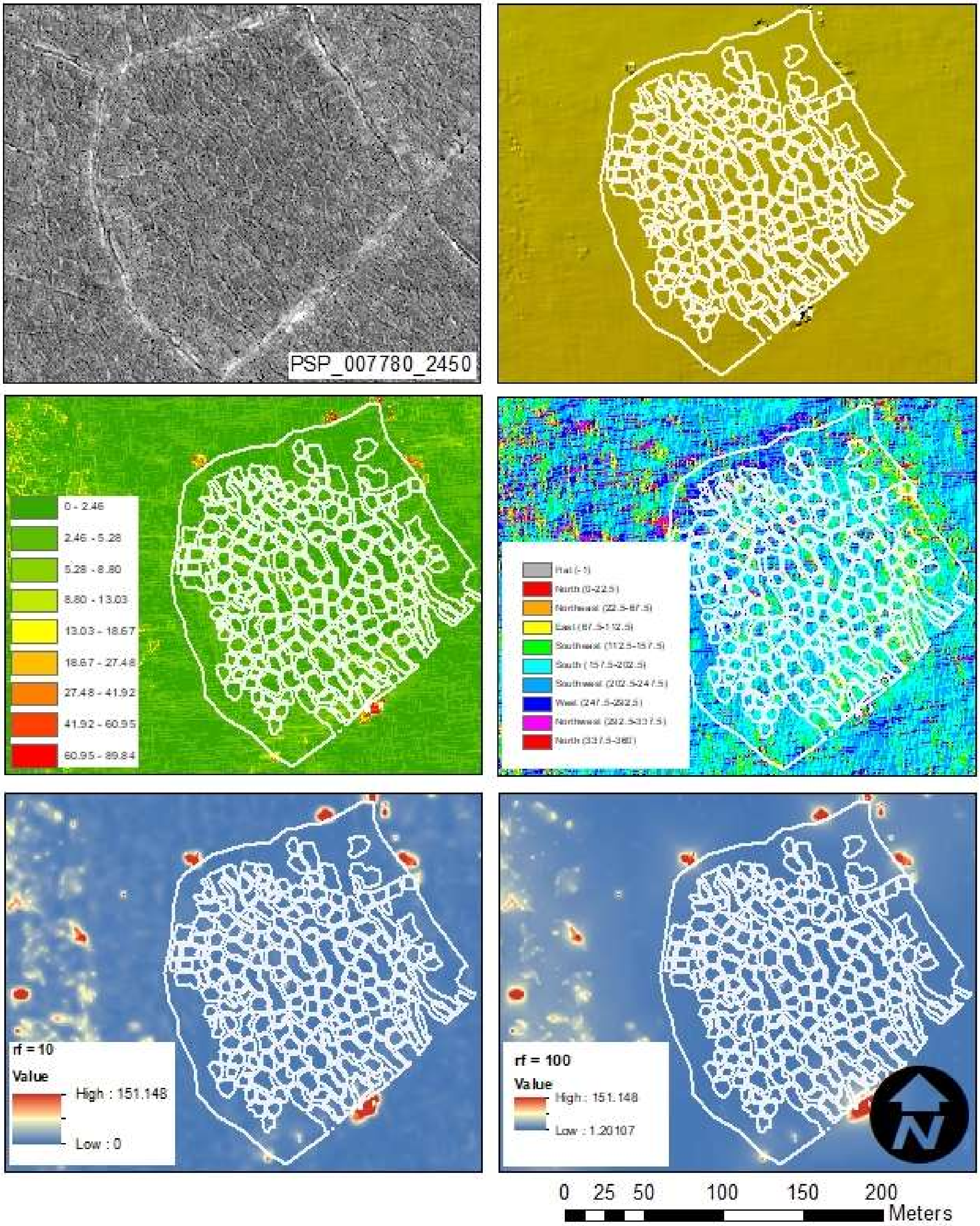

Figure 3-26. (Left-right/top-bottom). HiRISE image and HiRISE DTM-derived shaded relief, slope, aspect, and surface roughness at focal radii of 10 and 100 at Utopia Planitia. Variations between polygon centers and margins are not visually apparent in the DTM-derived raster datasets.

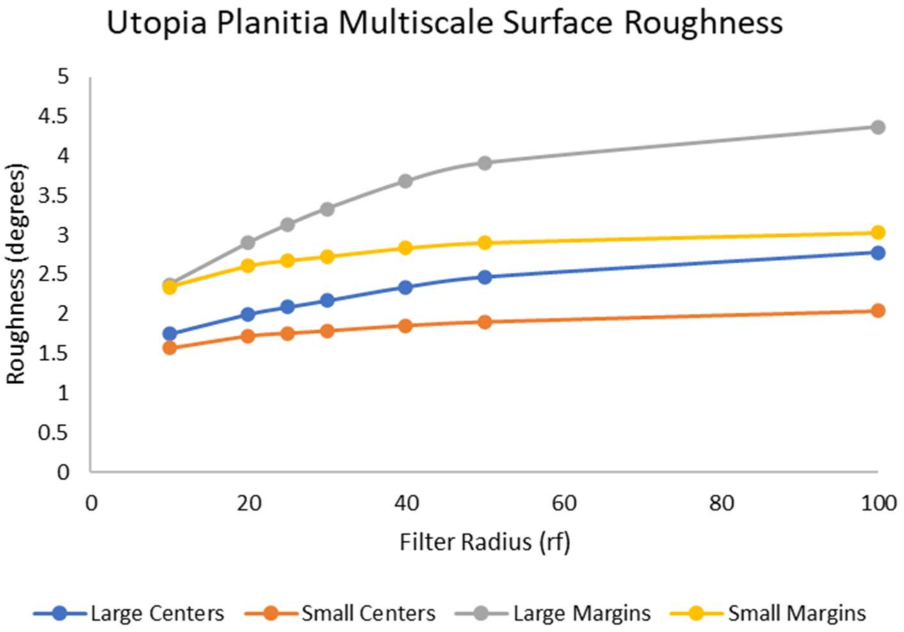

Figure 3-27: MSR plot for the polygon centers and margins at Utopia Planitia. Both large and small polygon centers had a lower surface roughness relative to the adjacent margins.

The multiscale surface roughness analysis of the polygons at the site is summarized in Figure 3-27. Large polygon centers that range from approximately 1.75° at rf = 10 to 2.78° at rf = 100 and the associated polygon margins range from approximately 2.38° to 4.37° at the same focal radius intervals. Small polygon centers range from approximately 1.57° and 2.04° compared to associated polygon margins that range from 2.34° to 3.03° at the same focal radius intervals. The MSR analysis at the Utopia Planitia site demonstrates a correlation between lower surface roughness values and the centers for both large and small polygons relative to higher surface roughness values with the associated polygon margins. A summary of key PCA results for the UP site are presented in Figures 3-28 and 3-29. Among the evaluated morphometric and surface roughness parameters for the centers of the UP-LP population, there was a positive correlation between the slope, length, and size of each feature, and there was also a potential positive correlation between the slope and surface roughness magnitude.

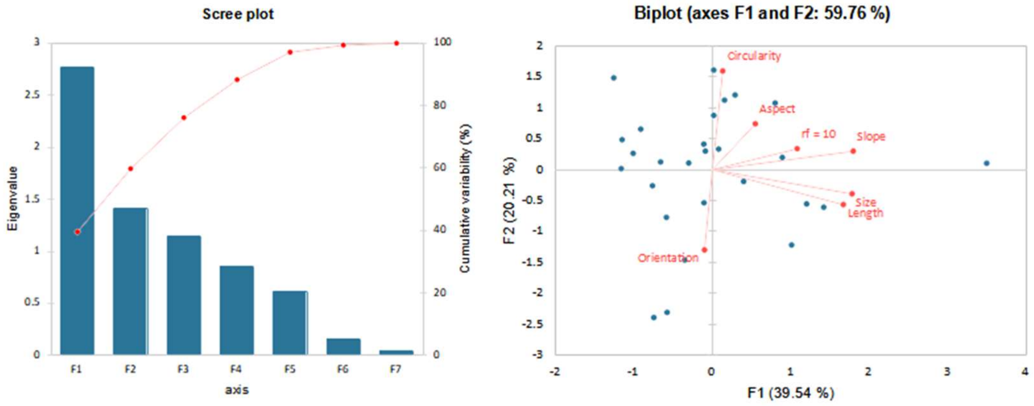

Eigenvectors

	F1	F2	F3	F4	F5
Length	0.511	-0.243	-0.336	0.165	0.015
Slope	0.549	0.127	0.152	-0.150	-0.040
Aspect	0.168	0.316	0.503	0.708	-0.311
Orientation	-0.031	-0.557	0.495	0.198	0.630
Size	0.545	-0.169	-0.269	0.157	0.112
Circularity	0.040	0.682	-0.154	0.089	0.702
rf = 10	0.331	0.145	0.519	-0.615	-0.011

Factor Loadings

	F1	F2	F3	F4	F5
Length	0.850	-0.289	-0.359	0.153	0.012
Slope	0.914	0.151	0.163	-0.139	-0.031
Aspect	0.279	0.376	0.538	0.655	-0.244
Orientation	-0.052	-0.663	0.529	0.183	0.494
Size	0.906	-0.201	-0.288	0.145	0.088
Circularity	0.067	0.811	-0.165	0.083	0.550
rf = 10	0.551	0.172	0.555	-0.569	-0.009

Figure 3-28. Utopia Planitia large polygons PCA scree plot and variable loading biplot. With the exception of feature orientation, there are positive correlations among all assessed variables, including roughness (r_f = 10). The most likely explanation is that the large polygons at Utopia Planitia are topographically prominent and are distinctly visible in HiRISE DTMs.

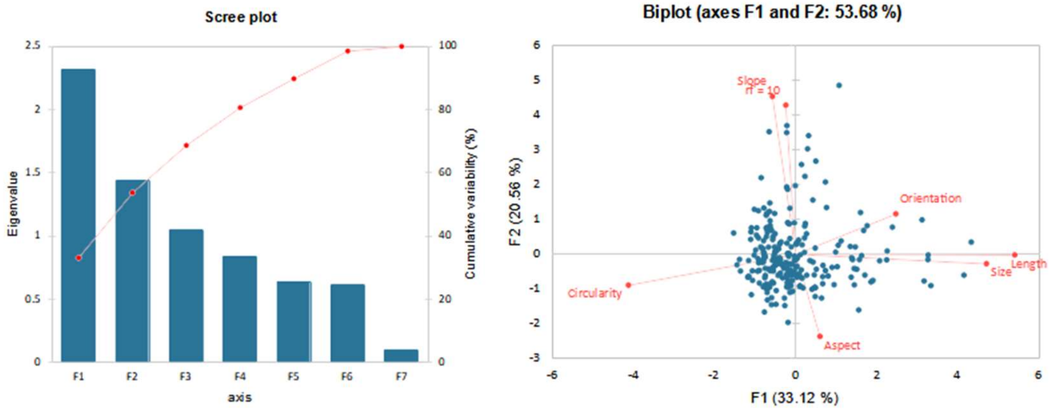

Eigenvectors

	F1	F2	F3	F4	F5
Length	0.623	-0.003	0.110	-0.186	0.021
Slope	-0.067	0.663	0.173	0.086	0.343
Aspect	0.069	-0.346	0.635	0.679	0.096
Orientation	0.284	0.169	-0.584	0.570	0.386
Size	0.543	-0.041	0.251	-0.348	0.409
Circularity	-0.476	-0.131	0.126	-0.218	0.705
rf = 10	-0.028	0.627	0.368	0.061	-0.241

Factor Loadings

	F1	F2	F3	F4	F5
Length	0.948	-0.004	0.112	-0.171	0.017
Slope	-0.102	0.796	0.177	0.079	0.274
Aspect	0.105	-0.415	0.650	0.622	0.077
Orientatior	0.433	0.203	-0.598	0.522	0.309
Size	0.826	-0.049	0.257	-0.319	0.327
Circularity	-0.725	-0.157	0.129	-0.200	0.563
rf = 10	-0.043	0.752	0.377	0.056	-0.192

Figure 3-29. Utopia Planitia small polygons PCA scree plot and variable loading biplot. There are positive correlations between feature length and size. Slope and roughness (r_f = 10) are positively correlated but inversely correlated to length and size. While visually distinct, the small polygons are not as topographically prominent as the larger parent polygons and are not as distinctly visible in HiRISE DTMs.

3.7 Utopia Rupes Site 1

An ASP DTM was generated from HiRISE images ESP_053694_2240 and ESP_053984_2240, which are centered near 43.575° N, 85.937° E in scalloped terrain in Utopia Rupēs. A population of 44 polygons grouped into sub-populations of large polygons (32) and small polygons (42) were identified and delineated using the HiRISE imagery in Table 1. Summary statistics are presented in Table 3-1 for polygon centers and Table 3-2 for polygon margins. A sample of the delineated features in HiRISE imagery, shaded relief, slope, slope aspect, and surface roughness analysis for $r_f = 10$ and $r_f = 30$ are presented for the large and small polygon populations in Figures 3-31 and 3-32, respectively. As with Malea Planum, a smaller maximum focal radius was used at Utopia Rupēs Site 1 as processing times for the smaller focal radius intervals indicated that processing times for larger intervals would be time-prohibitive and previous multiscale surface roughness evaluations of HiRISE DTMs are observed to begin stabilizing between a focal radius of 30 and 50.

The large polygons average approximately 127.2 m in length, 9,587 m^2 in area, 107.1 m in size, and have a circularity of 0.73. The surveyed polygons have an average long-axis orientation of 102.5° compared to an average slope aspect of 134.3° (Figure 3-4). The average slope aspect of the adjacent margins is approximately 131.1°. Large polygon centers have an average slope of 2.584° compared to an average slope of 3.705° for margins. The multiscale surface roughness analysis of the large polygons at the site are summarized Figure 3-33. Polygon centers range from approximately 1.56 at $r_f = 10$ to 2.17 at $r_f = 30$. The adjacent margins range from approximately 2.34° to 3.62° at the same focal radius intervals. cell neighborhood intervals. The MSR analysis for the large polygons at Utopia Rupēs Site 1 show a slight correlation of lower surface roughness values associated with feature centers versus slightly higher surface roughness values within the adjacent margins. The PCA of the large polygons (Figure 3-34) found a positive correlation between feature slope and roughness. While feature length and size are positively correlated, they are inversely correlated to aspect, slope, and roughness. The resulting correlation matrix is presented in Figure 3-7.

The small polygons average approximately 8.260 m in length, 35.03 m^2 in area, 6.385 m in size, and have a circularity of 0.76. The surveyed polygons have an average long-axis orientation of 59.20° compared to an average slope aspect of 270.5° (Figure 3-4). The average slope aspect of margins is approximately 277.2°. Small polygon centers have an average slope of 2.75° compared to an average slope of 2.78° for margins. The multiscale surface roughness analysis of the small polygons at the site are summarized Figure 3-33. Polygon centers range from approximately 1.70° at r_f = 10 to 2.12° at r_f = 30. The adjacent margins range from approximately 1.69° to 2.08° at the same focal radius intervals. The MSR analysis of the small polygons at Utopia Rupēs Site 1 site does not show a distinction between the surface roughness values of feature centers and margins. A PCA of the small polygons (Figure 3-35) found positive correlations between feature length and size in addition to slope and aspect. Roughness was found to have a slightly orthogonal positive correlation to feature length and size. The resulting correlation matrix is presented in Figure 3-7.

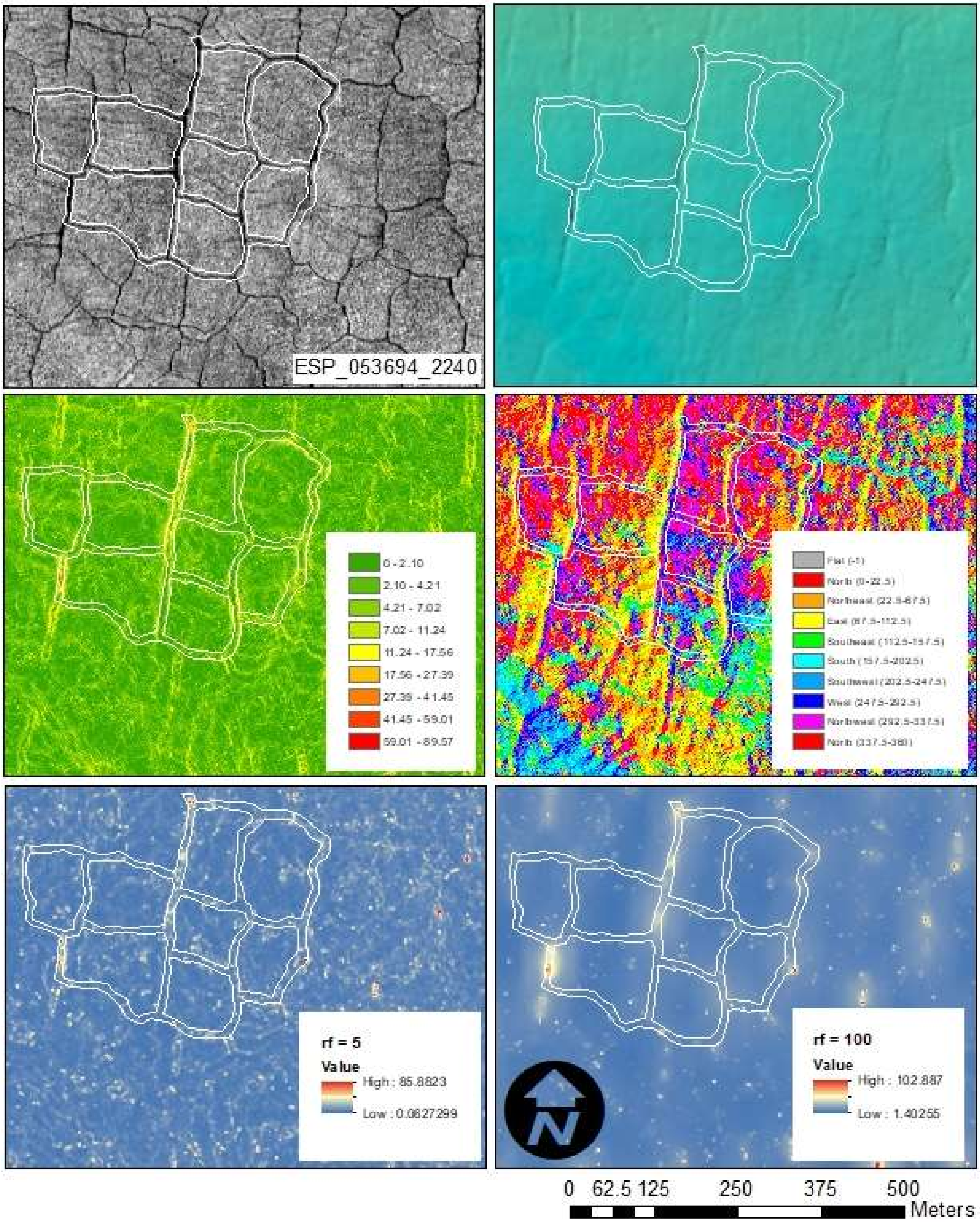

Figure 3-30. (Left-right/top-bottom). HiRISE image and HiRISE DTM-derived shaded relief, slope, aspect, and surface roughness at focal radii of 5 and 100 at Utopia Rupes. Variations between polygon centers and margins are visually apparent in several of the DTM-derived raster datasets.

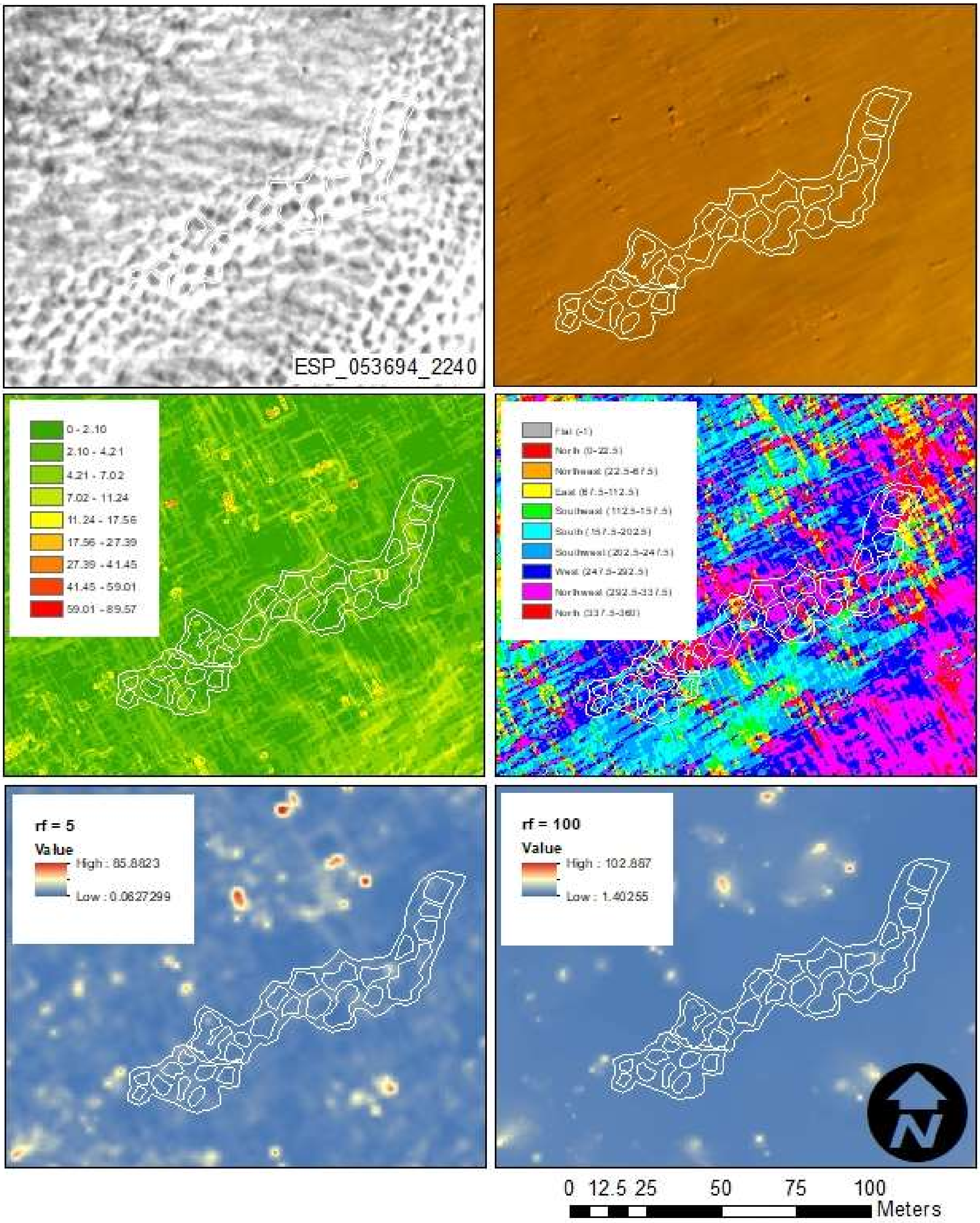

Figure 3-31. (Left-right/top-bottom). HiRISE image and HiRISE DTM-derived shaded relief, slope, aspect, and surface roughness at focal radii of 5 and 100 at Utopia Rupes. Variations between polygon centers and margins are not visually apparent in the DTM-derived raster datasets.

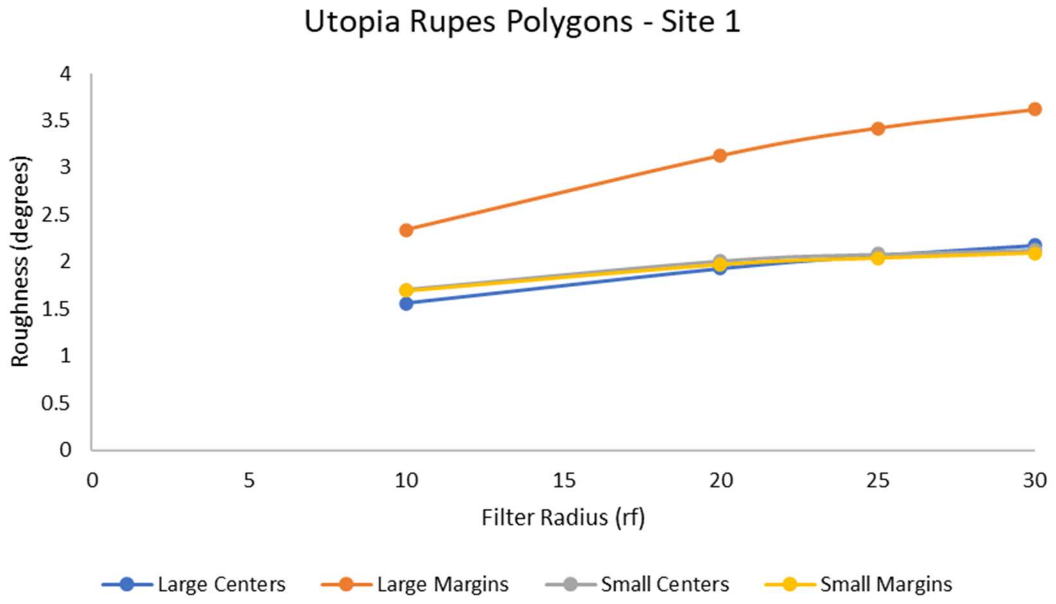

Figure 3-32: MSR plot for the polygon centers and margins at the Utopia Rupes Site 1. Large polygon centers have a lower surface roughness relative to the adjacent margins. There is no difference in surface roughness between the small polygon centers and margins.

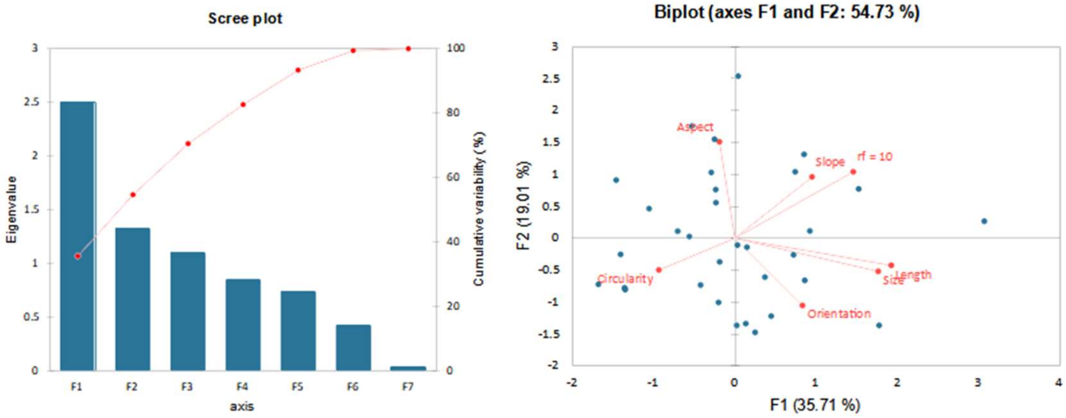

Eigenvectors

	F1	F2	F3	F4	F5
Length	0.569	-0.172	0.254	-0.196	-0.165
Slope	0.280	0.389	-0.045	0.798	-0.103
Aspect	-0.056	0.613	0.366	-0.316	0.546
Orientation	0.246	-0.426	-0.345	0.162	0.777
Size	0.522	-0.210	0.458	-0.075	-0.041
Circularity	-0.276	-0.201	0.658	0.438	0.219
rf = 10	0.431	0.422	-0.194	-0.021	0.104

Factor Loadings

	F1	F2	F3	F4	F5
Length	0.900	-0.198	0.267	-0.181	-0.143
Slope	0.443	0.449	-0.048	0.736	-0.089
Aspect	-0.089	0.707	0.386	-0.292	0.472
Orientation	0.388	-0.492	-0.363	0.149	0.671
Size	0.825	-0.242	0.482	-0.069	-0.035
Circularity	-0.437	-0.232	0.692	0.404	0.189
rf = 10	0.681	0.486	-0.204	-0.019	0.089

Figure 3-33. Utopia Rupes Site 1 large polygons PCA scree plot and variable loading biplot. There are positive correlations between feature slope and roughness (r_f = 10). Length and size are positively correlated but inversely related to aspect, slope, and roughness.

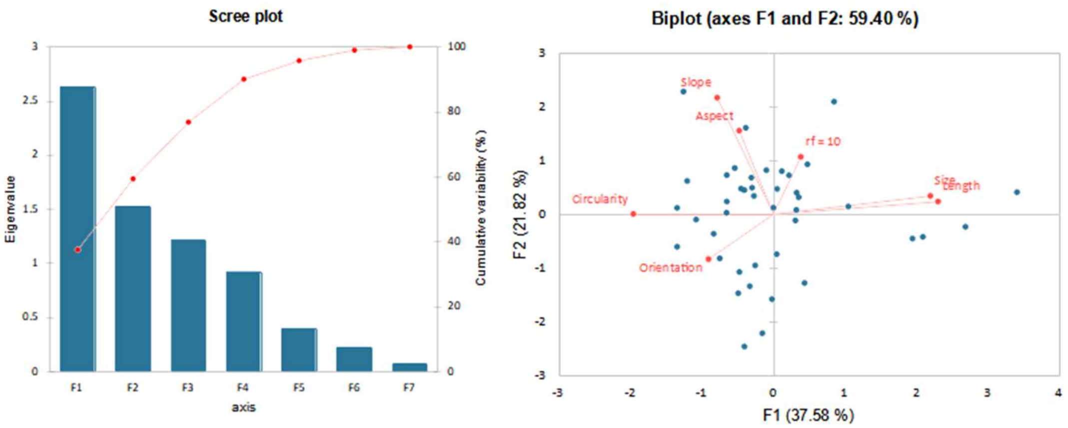

Eigenvectors

	F1	F2	F3	F4	F5
Length	0.580	0.078	-0.181	0.048	0.220
Slope	-0.198	0.717	0.069	-0.016	-0.181
Aspect	-0.120	0.514	-0.615	0.164	-0.052
Orientation	-0.229	-0.277	-0.276	0.819	0.128
Size	0.552	0.113	-0.249	-0.045	0.385
Circularity	-0.493	0.002	-0.113	-0.322	0.786
rf = 10	0.096	0.354	0.658	0.439	0.366

Factor Loadings

	F1	F2	F3	F4	F5
Length	0.941	0.097	-0.200	0.046	0.139
Slope	-0.321	0.887	0.076	-0.015	-0.114
Aspect	-0.195	0.636	-0.679	0.158	-0.033
Orientation	-0.371	-0.342	-0.305	0.789	0.081
Size	0.896	0.139	-0.275	-0.043	0.242
Circularity	-0.800	0.003	-0.125	-0.310	0.496
rf = 10	0.156	0.438	0.727	0.423	0.231

Figure 3-34. Utopia Rupes Site 1 small polygons PCA scree plot and variable loading biplot. There are positive correlations between feature size and length, followed by slope and aspect. Roughness (r_f = 10) is orthogonal to slope/aspect and size/length.

3.8 Utopia Rupes Site 2

An ASP DTM was generated from HiRISE images ESP_027071_2235 and ESP_033862_2235, which are centered near 43.391° N, 78.829° E in Utopia Rupēs. A population of 133 polygons spread across three sub-populations were identified and delineated using the HiRISE imagery in Table 1. The three sub-populations are sorted boulders (33), large polygons (30), and small polygons (70). Summary statistics are presented in Table 3-1 for polygon centers and Table 3-2 for polygon margins. A sample of the delineated features in HiRISE imagery, shaded relief, slope, slope aspect, and surface roughness analysis for r_f = 10 and r_f = 30 are presented for the sorted boulders, large, and small polygon populations in Figures 3-36, 3-37, and 3-38 respectively. As with Malea Planum and Utopia Rupēs Site 1, a smaller maximum focal radius was used at Utopia Rupēs Site 2 as processing times for the smaller focal radius intervals indicated that processing times for larger intervals would be time-prohibitive and previous multiscale surface roughness evaluations of HiRISE DTMs are observed to begin stabilizing between a focal radius of 30 and 50.

The sorted boulders average approximately 19.65 m in length, 173.3 m^2 in area, 14.42 m in size, and have a circularity of 0.72. The surveyed polygons have an average long-axis orientation of 86.08° compared to an average slope aspect of 181.9° (Figure 3-4). The average slope aspect of margins is approximately 192.8°. Polygon centers have an average slope of 3.477° compared to an average slope of 2.307° for margins. The multiscale surface roughness analysis of the sorted boulders at the site are summarized Figure 3-39. The centers of the sorted boulders range from approximately 3.21° at $r_f = 10$ to 3.88° at $r_f = 30$. The adjacent margins of the boulders range from approximately 2.42° to 3.41° at the same focal radius intervals. While the MSR analysis for the sorted boulders at Utopia Rupēs Site 2 suggests that the centers of the sorted boulders have a higher surface roughness relative to the boulder margins, visual inspection of the shaded relief for the DTM highlights several processing artifacts (pits) overlying feature centers that could be the cause (Figure 3-35). A PCA of the sorted boulders (Figure 3-40) found positive correlations between feature size and length. Slope and roughness are positively correlated but inversely related to feature length and size. The resulting correlation matrix is presented in Figure 3-7.

The small polygons average approximately 13.66 m in length, 45.20 m^2 in area, 7.347 m in size, and have a circularity of 0.67. The surveyed polygons have an average long-axis orientation of 91.11° compared to an average slope aspect of 192.7° (Figure 3-4). The average slope aspect of margins is approximately 197.3°. Polygon centers have an average slope of 3.166° compared to an average slope of 2.935° for margins. The multiscale surface roughness analysis of the polygons at the site are summarized Figure 3-39. Small polygon centers range from approximately 1.72 at $r_f = 10$ to 1.98 at $r_f = 30$. The adjacent polygon margins range from approximately 1.75° to 2.03° at the same focal radius intervals.

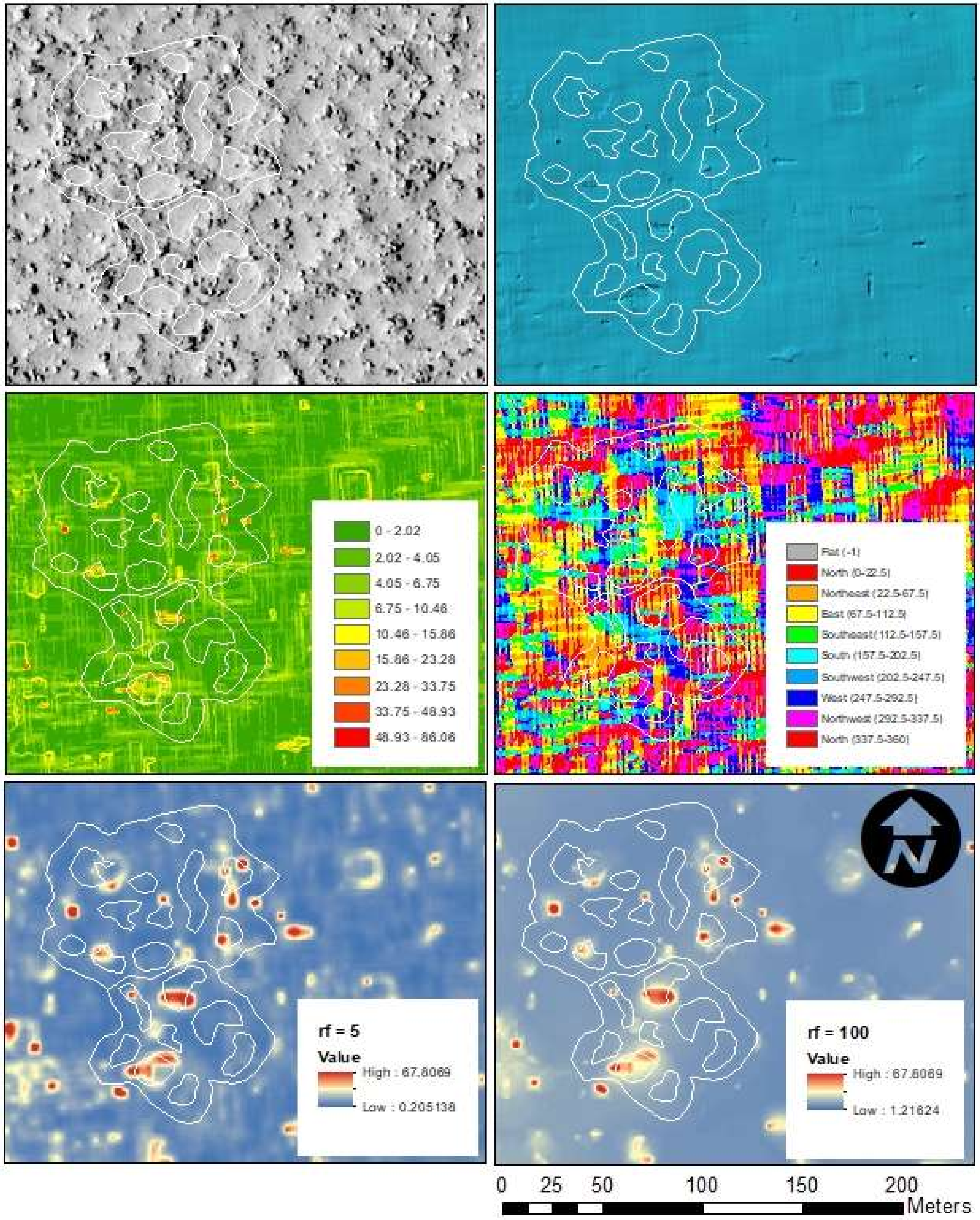

Figure 3-35. (Left-right/top-bottom). HiRISE image and HiRISE DTM-derived shaded relief, slope, aspect, and surface roughness at focal radii of 5 and 100 at Utopia Rupes. Variations between sorted boulder centers and margins are visually apparent in some of the DTM-derived raster datasets.

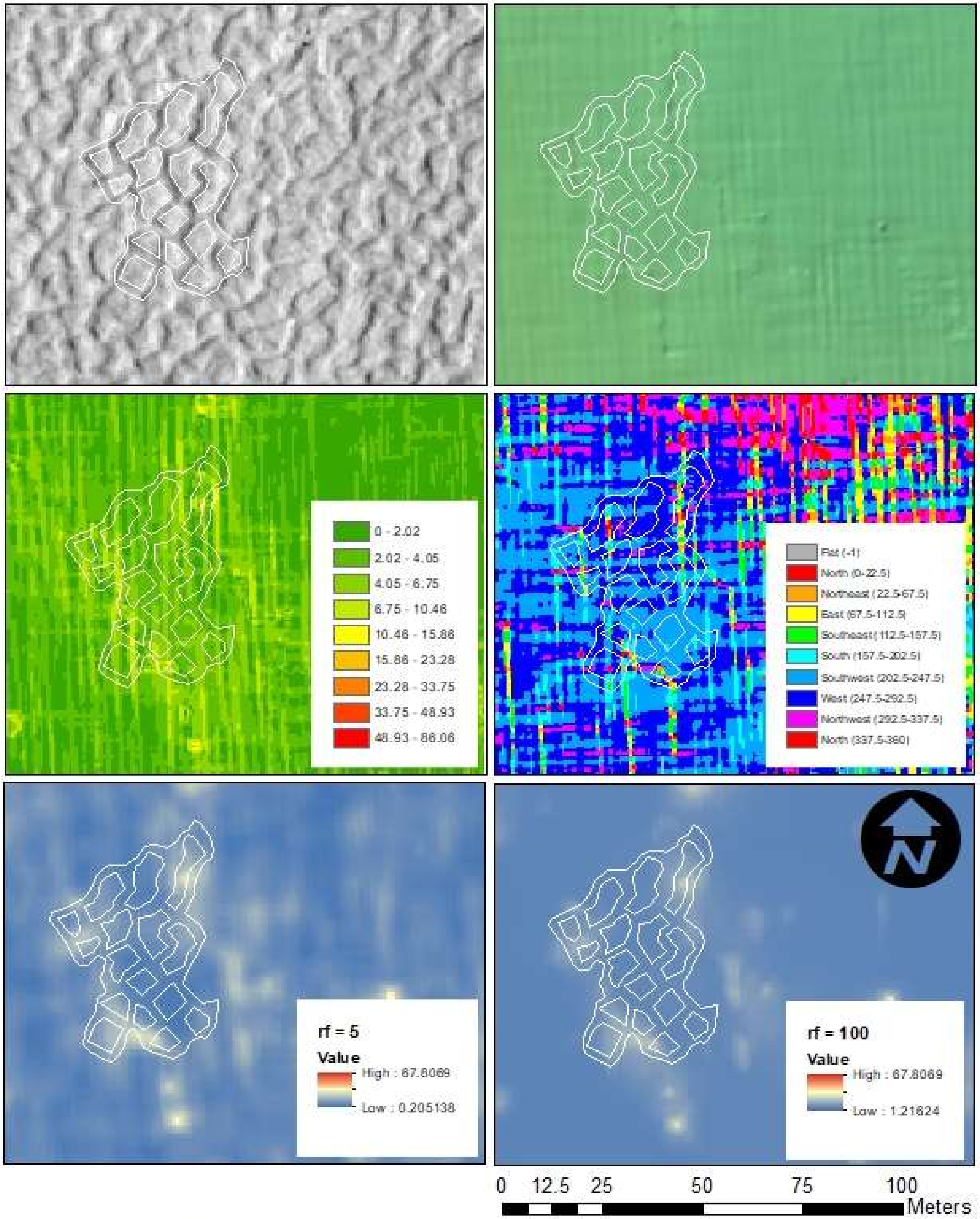

Figure 3-36. (Left-right/top-bottom). HiRISE image and HiRISE DTM-derived shaded relief, slope, aspect, and surface roughness at focal radii of 5 and 100 at Utopia Rupes. Variations between polygon centers and margins are not visually apparent in the DTM-derived raster datasets.

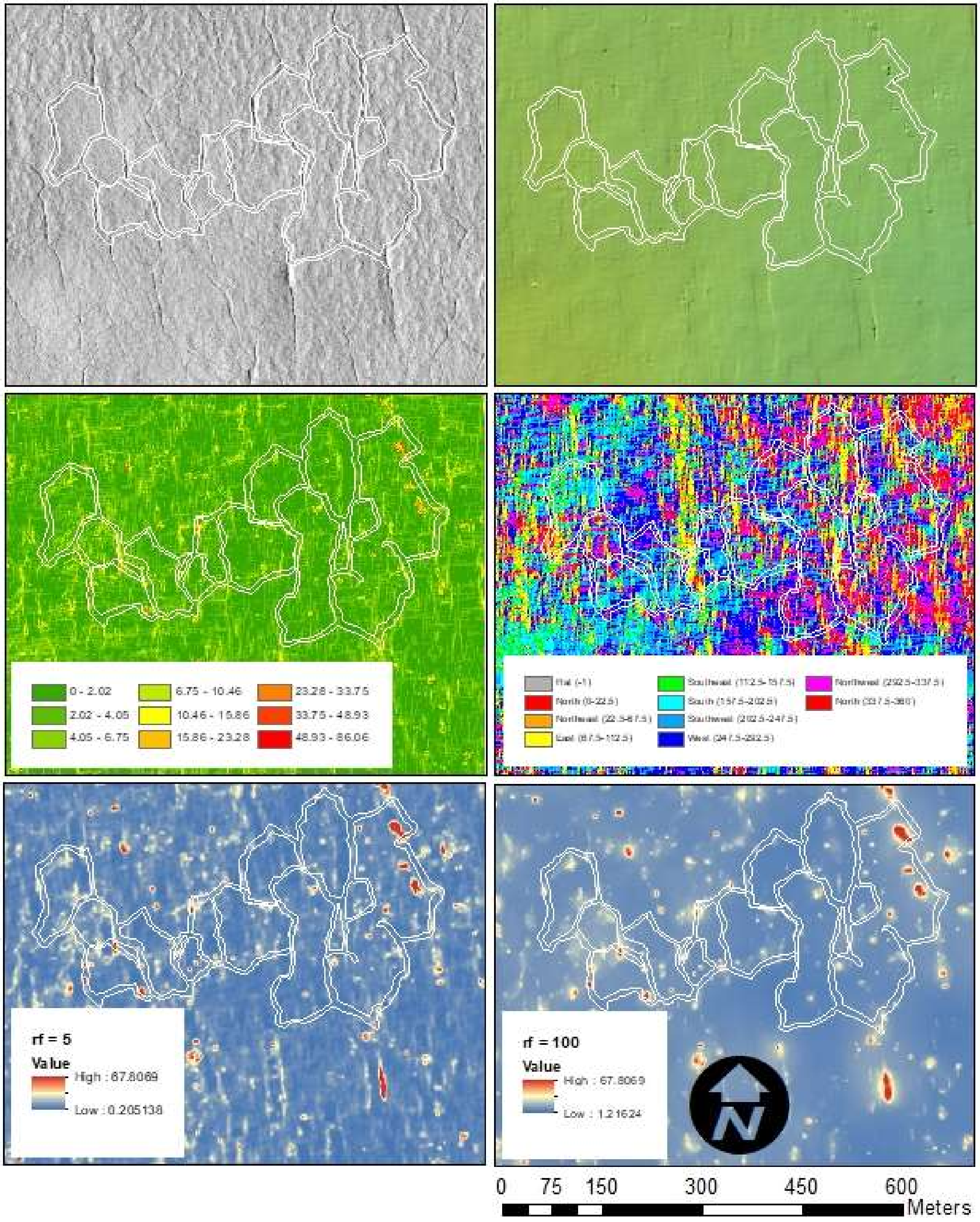

Figure 3-37. (Left-right/top-bottom). HiRISE image and HiRISE DTM-derived shaded relief, slope, aspect, and surface roughness at focal radii of 5 and 100 at Utopia Rupes. Variations between polygon centers and margins are visually apparent in some of the DTM-derived raster datasets.

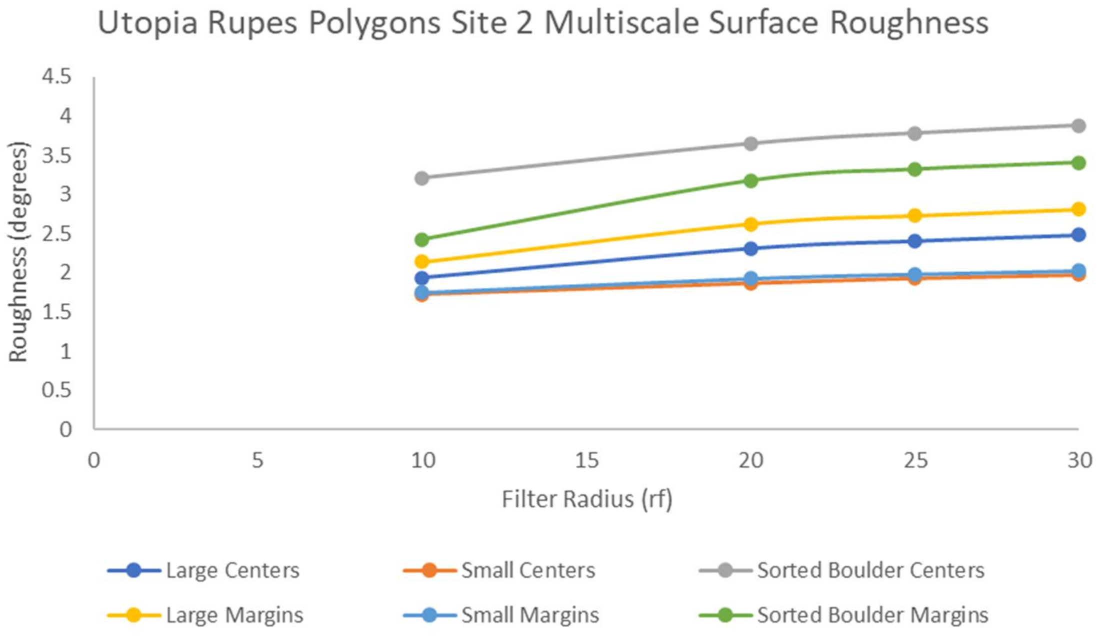

Figure 3-38: MSR plot for the polygon centers and margins at Utopia Rupes Site 2. Large polygon centers have a lower surface roughness than the adjacent margins. Sorted boulder centers have a higher surface roughness than the adjacent margins. There was no significant difference in surface roughness between small polygon centers and margins.

The MSR analysis of the small polygons at Utopia Rupēs Site 2 does not show a clear correlation of surface roughness values between polygon centers and margins. A PCA of the small polygons (Figure 3-41) found a positive correlation between feature roughness, slope, circularity, and orientation. Feature length and size are positively correlated but inversely related to other assessed variables. The correlation matrix is presented in Figure 3-7.

The large polygons average approximately 133.5 m in length, 8,273 m^2 in area, 94.49 m in size, and a circularity of 0.61. The surveyed polygons have an average long-axis orientation of 100.73° compared to an average slope aspect of 193.9° (Figure 3-4). The average slope aspect of margins is approximately 229.8°. Polygon centers have an average slope of 2.197° compared to an average slope of 2.660° for margins. The multiscale surface roughness analysis of the polygons at the site are summarized Figure 3-39. Large centers range from approximately 1.94 at r_f = 10 to 2.49 at r_f = 30. The adjacent polygon margins range from approximately 2.14° to 2.81

at the same focal radius intervals. The MSR analysis at the large polygons at Utopia Rupēs Site 2 show a slight correlation of slightly lower surface roughness values in polygon centers compared to slightly higher surface roughness values along the adjacent polygon margins. A PCA of the large polygons (Figure 3-42) found a positive correlation between feature length, size, and aspect. Slope and roughness are positively correlated but inversely correlated to length, size, and aspect. The resulting correlation matrix is presented in Figure 3-7.

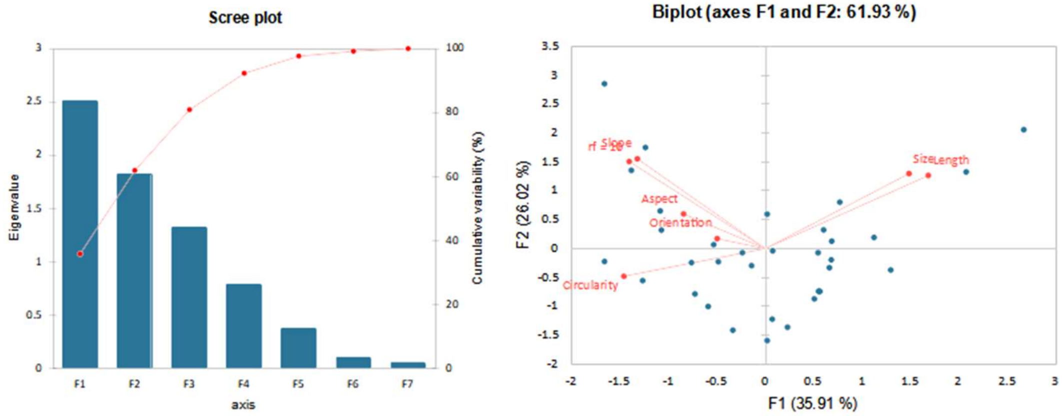

Eigenvectors

	F1	F2	F3	F4	F5
Length	0.489	0.432	0.031	0.155	-0.047
Slope	-0.384	0.530	-0.207	-0.015	-0.193
Aspect	-0.245	0.205	0.633	-0.378	0.578
Orientatior	-0.144	0.059	0.650	0.652	-0.336
Size	0.432	0.443	-0.100	0.278	0.451
Circularity	-0.424	-0.164	-0.317	0.567	0.529
rf = 10	-0.408	0.514	-0.154	-0.098	-0.174

Factor Loadings

	F1	F2	F3	F4	F5
Length	0.775	0.583	0.036	0.138	-0.029
Slope	-0.609	0.715	-0.239	-0.014	-0.118
Aspect	-0.389	0.276	0.730	-0.337	0.354
Orientation	-0.228	0.079	0.749	0.581	-0.206
Size	0.684	0.598	-0.115	0.248	0.276
Circularity	-0.673	-0.221	-0.365	0.505	0.324
rf = 10	-0.647	0.694	-0.177	-0.087	-0.107

Figure 3-39. Utopia Rupes Site 2 sorted boulders PCA scree plot and variable loading biplot. There are positive correlations between feature size and length. Slope and roughness (r_f = 10) are positively correlated but inversely related to size and length.

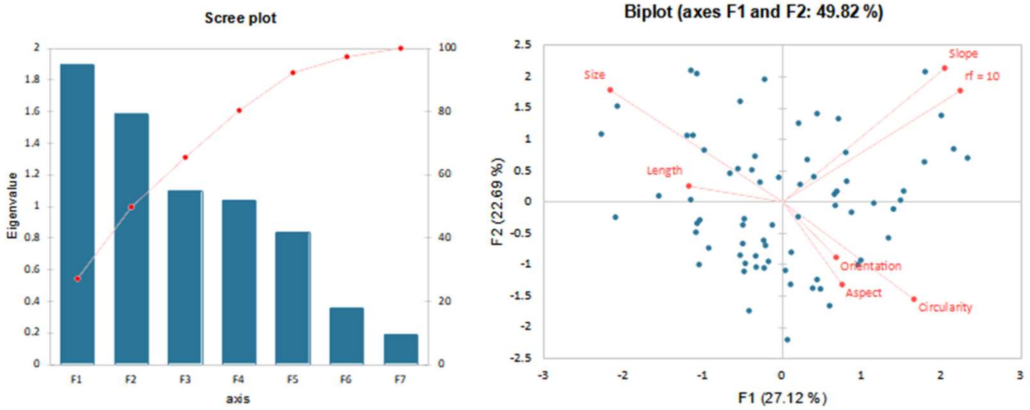

Eigenvectors

	F1	F2	F3	F4	F5
Length	-0.271	0.063	-0.454	0.424	0.724
Slope	0.468	0.535	-0.069	-0.106	0.178
Aspect	0.172	-0.331	0.314	0.766	-0.107
Orientation	0.155	-0.222	0.616	-0.298	0.655
Size	-0.497	0.448	0.150	0.007	-0.027
Circularity	0.379	-0.390	-0.532	-0.198	0.046
rf = 10	0.513	0.445	0.071	0.308	-0.003

Factor Loadings

	F1	F2	F3	F4	F5
Length	-0.373	0.080	-0.476	0.431	0.661
Slope	0.645	0.675	-0.072	-0.108	0.163
Aspect	0.237	-0.417	0.330	0.780	-0.098
Orientation	0.213	-0.280	0.646	-0.304	0.598
Size	-0.685	0.565	0.157	0.008	-0.024
Circularity	0.523	-0.491	-0.558	-0.202	0.042
rf = 10	0.707	0.561	0.075	0.313	-0.002

Figure 3-40. Utopia Rupes Site 2 small polygons PCA scree plot and variable loading biplot. There are positive correlations between feature roughness (r_f = 10), slope, circularity, orientation, and aspect. Length and size are positively correlated but inversely related to the other assessed variables.

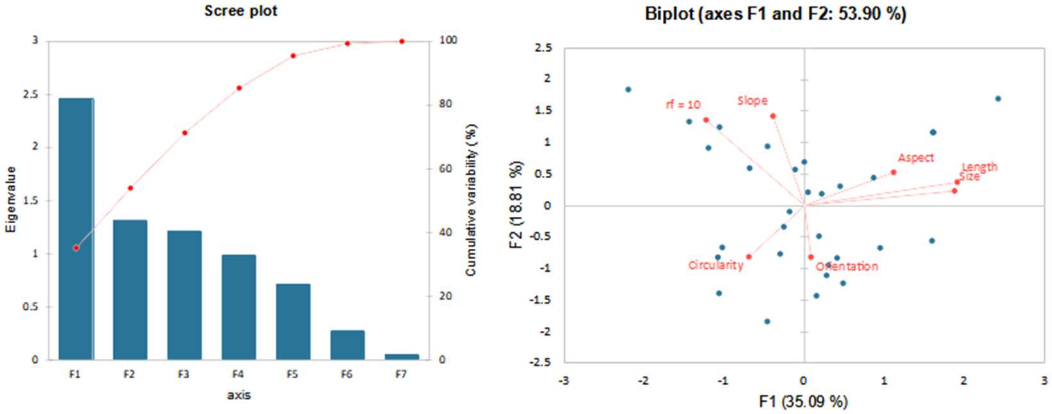

Eigenvectors

	F1	F2	F3	F4	F5
Length	0.588	0.154	-0.066	0.221	-0.228
Slope	-0.121	0.596	0.567	0.144	-0.137
Aspect	0.343	0.221	0.297	-0.322	0.774
Orientation	0.025	-0.345	0.246	0.835	0.341
Size	0.577	0.098	0.156	0.069	-0.369
Circularity	-0.213	-0.344	0.692	-0.210	-0.278
rf = 10	-0.378	0.570	-0.150	0.283	0.007

Factor Loadings

	F1	F2	F3	F4	F5
Length	0.921	0.177	-0.073	0.219	-0.192
Slope	-0.189	0.684	0.625	0.143	-0.116
Aspect	0.538	0.254	0.327	-0.319	0.653
Orientation	0.039	-0.396	0.271	0.828	0.288
Size	0.905	0.112	0.172	0.068	-0.311
Circularity	-0.334	-0.395	0.762	-0.208	-0.234
rf = 10	-0.592	0.654	-0.166	0.280	0.006

Figure 3-41. Utopia Rupes Site 2 large polygons PCA scree plot and variable loading biplot. There are positive correlations between feature length, size, and aspect. Slope and roughness (r_f = 10) are positively correlated but negatively correlated to length, size, and aspect.

3.9 Vastitas Borealis Site 1

An ASP DTM was generated from HiRISE images ESP_054092_2550 and ESP_054105_2550, which are centered near 74.765° N, 13.297° E in a dune field in Vastitas Borealis. A population of 47 polygons spread across four variably-sized clusters and were identified and delineated using the HiRISE imagery in Table 1. Summary statistics are presented in Table 3-1 for polygon centers and Table 3-2 for polygon margins. A sample of the delineated features in HiRISE imagery, shaded relief, slope, slope aspect, and surface roughness analysis for r_f = 10 and r_f = 100 are presented in Figure 3-43.

The groups of surveyed polygons at the Vastitas Borealis site share similar morphometric characteristics and are thus treated as a single undivided population. The polygons average approximately 9.260 m in length, 45.79 m^2 in area, 7.411 m in size, and have a circularity of 0.75. The surveyed Vastias Borealis polygons have an average long-axis orientation of 93.40° compared to an average slope aspect of 232.7° (Figure 3-4). The average slope aspect of margins is approximately 238.9°. Polygon centers have an average slope of 3.590° compared to an average slope of 3.272° for margins. The multiscale surface roughness analysis of the polygons at the site are summarized Figure 3-44. Polygon centers range from approximately 1.515 at r_f = 10 to 2.554 at r_f = 100. The adjacent polygon margins range from approximately 1.511° to 2.475° at the same filter radius intervals. The MSR analysis at the Vastitas Borealis site does not show a correlation of surface roughness values between feature centers and margins at the spatial resolution of the ASP-generated HiRISE DTM, representing one of the more homogeneous MSR datasets of this study. A PCA was performed to determine if there are any correlations between the observed parameters for the characterized polygon centers (Figure 3-45). Among the characterized polygons, feature size and length are positively correlated but inversely related to slope. Slope and roughness are positively correlated. The resulting correlation matrix is presented in Figure 3-7.

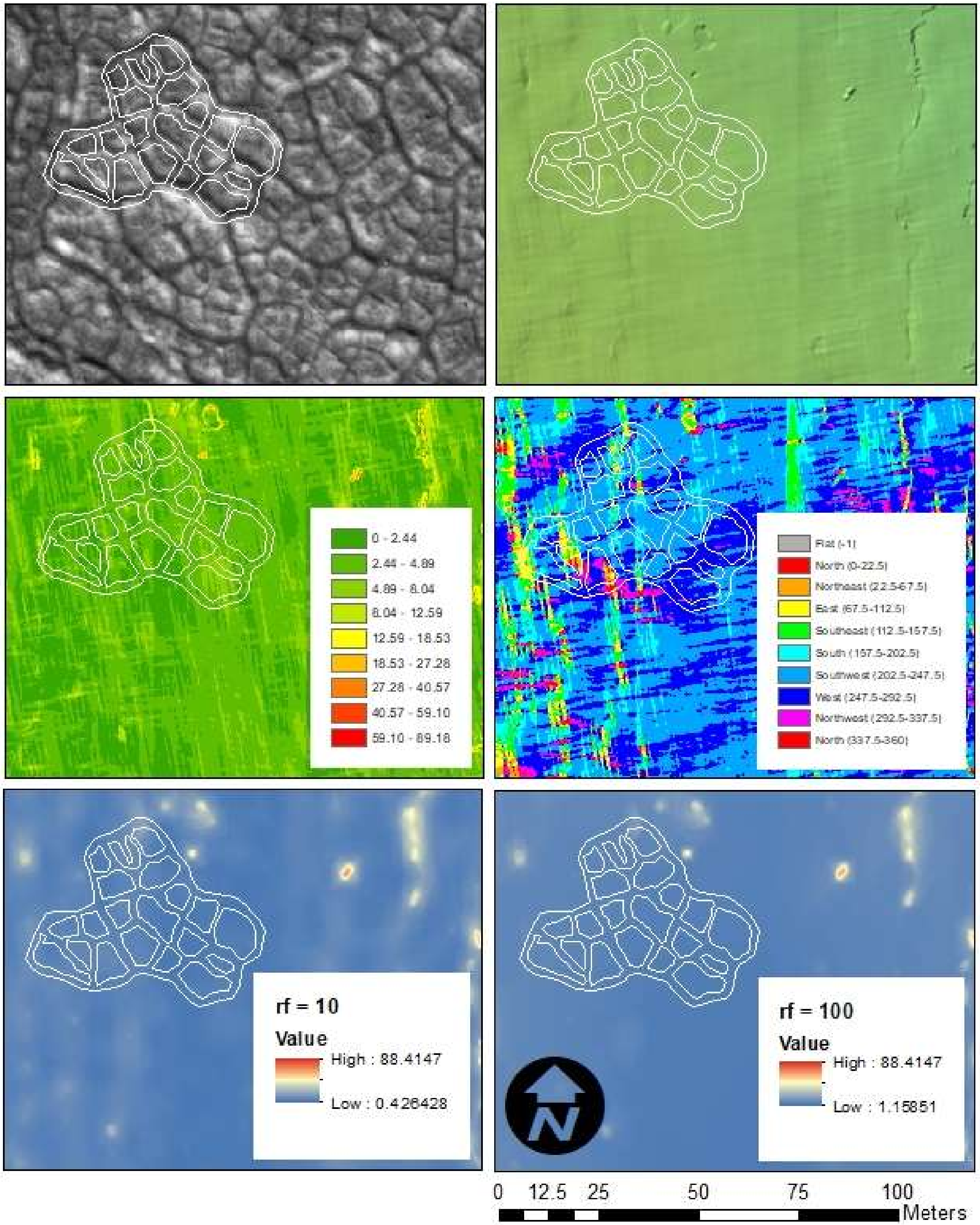

Figure 3-42. (Left-right/top-bottom). HiRISE image and HiRISE DTM-derived shaded relief, slope, aspect, and surface roughness at focal radii of 5 and 100 at Vastitas Borealis. Variations between polygon centers and margins are not visually apparent in the DTM-derived raster datasets.

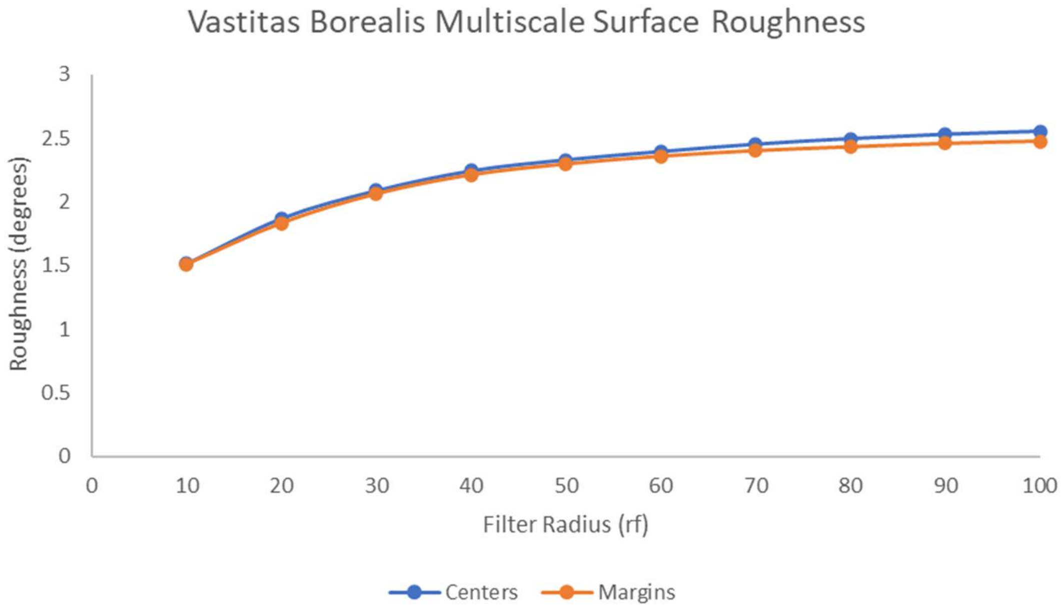

Figure 3-43: MSR plot for the polygon centers and margins at Vastitas Borealis. There is no significant difference in surface roughness between polygon centers and the adjacent margins.

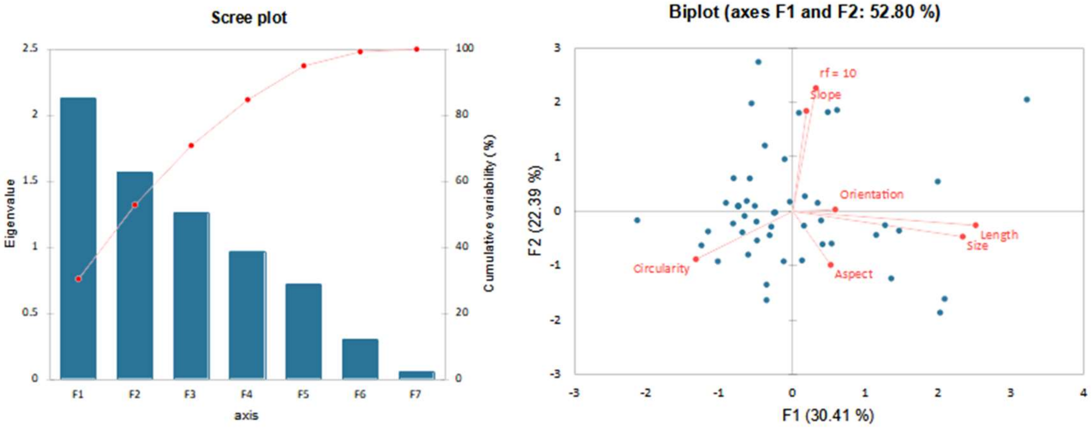

Eigenvectors

	F1	F2	F3	F4	F5
Length	0.665	-0.080	-0.093	0.008	0.096
Slope	0.050	0.567	0.524	-0.094	-0.207
Aspect	0.138	-0.305	0.696	-0.247	-0.317
Orientation	0.154	0.009	0.242	0.948	-0.024
Size	0.618	-0.144	0.070	-0.164	0.358
Circularity	-0.352	-0.272	0.409	0.015	0.744
rf = 10	0.084	0.696	0.038	-0.071	0.407

Factor Loadings

	F1	F2	F3	F4	F5
Length	0.970	-0.100	-0.105	0.008	0.081
Slope	0.073	0.710	0.589	-0.092	-0.176
Aspect	0.201	-0.382	0.781	-0.243	-0.269
Orientation	0.225	0.011	0.272	0.934	-0.020
Size	0.902	-0.180	0.078	-0.161	0.303
Circularity	-0.513	-0.341	0.459	0.015	0.630
rf = 10	0.123	0.871	0.042	-0.070	0.345

Figure 3-44. Vastitas Borealis Site 1 polygons PCA scree plot and variable loading biplot. Feature size and length are positively correlated but negatively related to slope. Slope and roughness ($r_f = 10$) are positively correlated.

3.10 Vastitas Borealis Site 2 – *Phoenix* Landing Site

The *Phoenix* landing site was selected for an initial trial of project methodologies by using an existing SOCET SET-generated DTM that was built from stereo pair images PSP_008591_2485 and PSP_00864_2485, resulting in the HiRISE DTM product DTEPC_008591_2485_008644_2485_U01. Polygons in the vicinity of the *Phoenix* lander are well-characterized providing ground-truth observations that can be correlated with the DTMs and DTM-byproducts. The existing SOCET SET DTM is centered near 68.208° N, 234.256° E. A population of 105 polygons spread across four locations ranging from approximately 0.8 km northeast, 1.8 km northwest, and 2 km northeast of the *Phoenix* landing site that were identified and delineated using the processed HiRISE imagery in Table 1. The locations were selected in part to avoid adverse influences on image and DTM quality resulting from engine exhaust blast deposits in the immediate vicinity of the *Phoenix* landing site and the heat shield and parachute backshell impact sites. Summary statistics are presented in Table 3-1 for polygon centers and Table 3-2 for polygon margins. A sample of the delineated features in HiRISE imagery, shaded relief, slope, slope aspect, and surface roughness analysis for $r_f = 10$ and $r_f = 100$ are presented in Figure 3-46.

The surveyed population of polygons are subdivided into two observable subcategories visible in HiRISE imagery (Figure 3-46): 62 large polygon centers that are an average of approximately 29.0 m in length, 413.8 m^2 in area, 21.0 m in size, and an average circularity of 0.72, compared to 51 small polygon centers that are inset on the centers of the larger polygons and are an average of approximately 7.9 m in length, 23.3 m^2 in area, 5.1 m in size, and an average circularity of 0.56. Large polygon centers have an average long-axis orientation of 105.3° compared to an average slope aspect of 197.2°. Small polygon centers have an average long-axis orientation of 86.4° compared to an average slope aspect of 187.3°. The average slope of large polygon centers is 1.75° compared to small polygon centers that have an average slope of

1.92°. For the large polygon margins, the average slope and slope aspect are 1.77° and 187.4°, respectively, compared to small polygon margins where the average slope and slope aspect are 1.61° and 195.3°, respectively.

The multiscale surface roughness analysis of the large and small polygons at the site is summarized in Figure 3-47. For large polygons, centers range from approximately 1.19° at $r_f = 10$ to 1.90° at $r_f = 100$ compared to polygon margins that range from 1.21° to 1.92° at the same focal radius intervals. For small polygons, centers range from approximately 1.35° at $r_f = 10$ to 2.07° at $r_f = 100$ compared to polygon margins that range from approximately 1.24° to 2.03° at the same focal radius intervals. The MSR analysis at the *Phoenix* landing site does not show a clear correlation of surface roughness values between feature centers and margins at the spatial resolution of the SOCET SET-generated HiRISE DTM.

A PCA was performed to determine if there are any correlations between the observed morphometric and roughness parameters associated with the large and small polygon centers (Figures 3-48 and 3-49, respectively). Among the surveyed large polygons, there are positive correlations between feature size and length. Slope and roughness are positively correlated and related to feature size but inversely related to feature length. Among the surveyed small polygons, there are positive correlations between feature slope and roughness. Feature length and size are positively correlated but inversely related to slope and roughness. The resulting correlation matrix is presented in Figure 3-7.

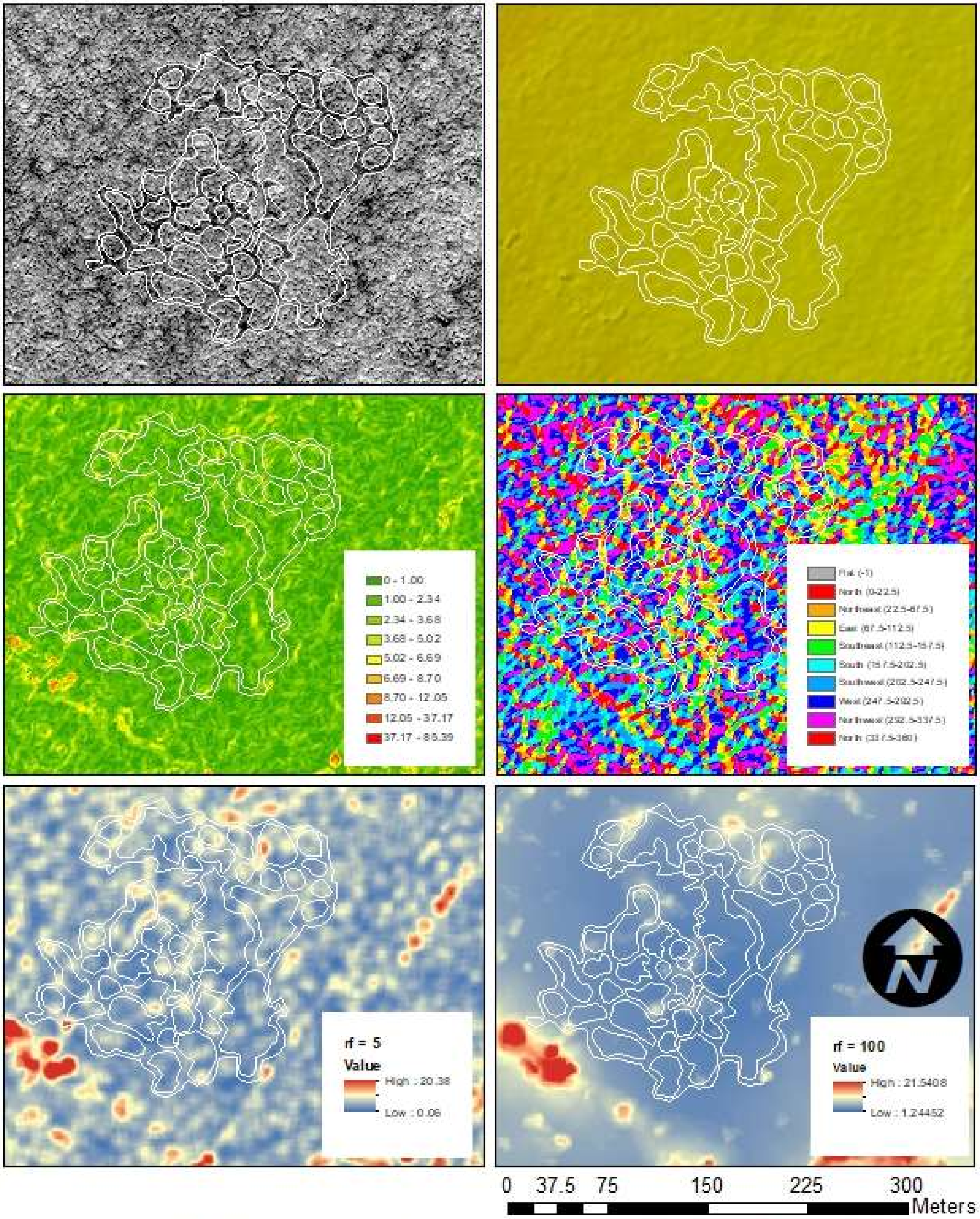

Figure 3-45. (Left-right/top-bottom). HiRISE image and HiRISE DTM-derived shaded relief, slope, aspect, and surface roughness at focal radii of 5 and 100 at the Phoenix Landing Site in Vastitas Borealis. Variations between polygon centers and margins are not visually apparent in some of the DTM-derived raster datasets. Small polygons are inset on the larger polygons delineated in this figure.

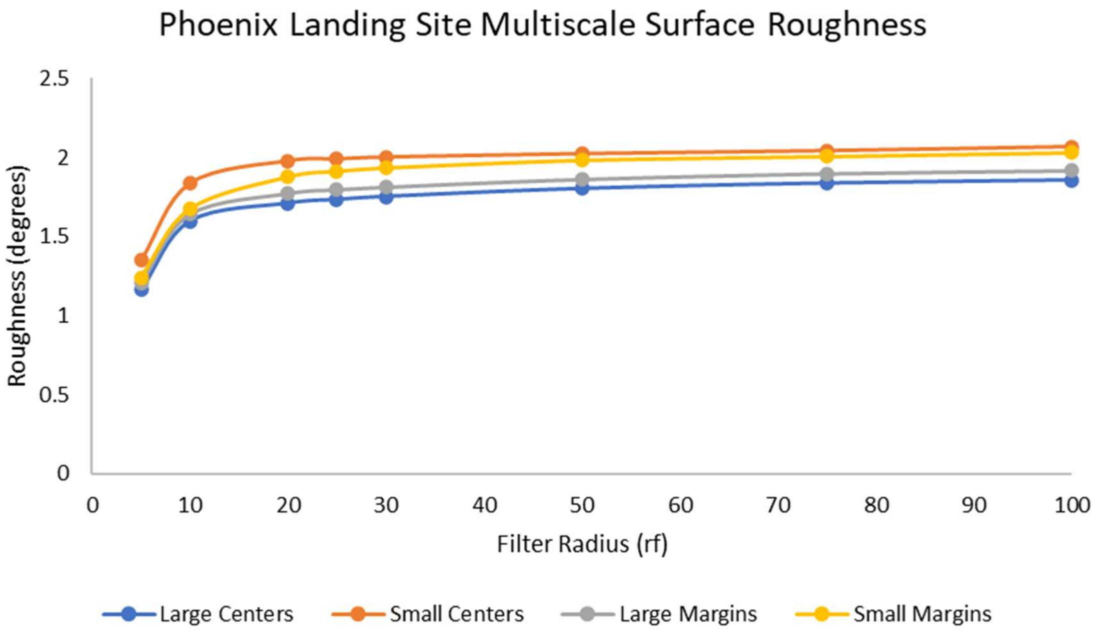

Figure 3-46: MSR plot for the polygon centers and margins at the Phoenix Landing Site in Vastitas Borealis. Large polygon centers have a lower surface roughness relative to the adjacent margins. Small polygon centers have a higher surface roughness relative to the adjacent margins.

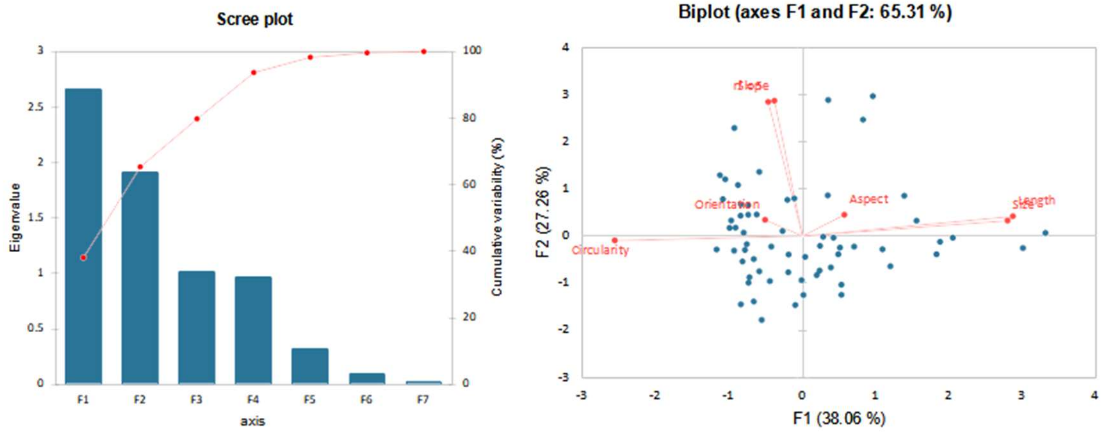

Eigenvectors

	F1	F2	F3	F4	F5
Length	0.591	0.100	0.117	0.021	0.256
Slope	-0.079	0.697	-0.054	-0.065	-0.086
Aspect	0.117	0.108	-0.529	0.819	-0.135
Orientation	-0.105	0.083	0.829	0.507	-0.193
Size	0.576	0.079	0.127	0.070	0.467
Circularity	-0.528	-0.024	-0.007	0.214	0.806
rf = 5	-0.096	0.691	0.007	-0.128	0.068

Factor Loadings

	F1	F2	F3	F4	F5
Length	0.964	0.139	0.117	0.021	0.146
Slope	-0.129	0.963	-0.055	-0.064	-0.049
Aspect	0.192	0.150	-0.532	0.807	-0.077
Orientation	-0.172	0.115	0.834	0.500	-0.110
Size	0.940	0.109	0.128	0.069	0.266
Circularity	-0.862	-0.033	-0.007	0.211	0.459
rf = 5	-0.157	0.955	0.007	-0.126	0.039

Figure 3-47. Vastitas Borealis Site 2 (Phoenix landing site) large polygons PCA scree plot and variable loading biplot. There are positive correlations between feature size and length. Slope and roughness ($r_f = 5$) are positively correlated and related to feature size but negatively related to feature length.

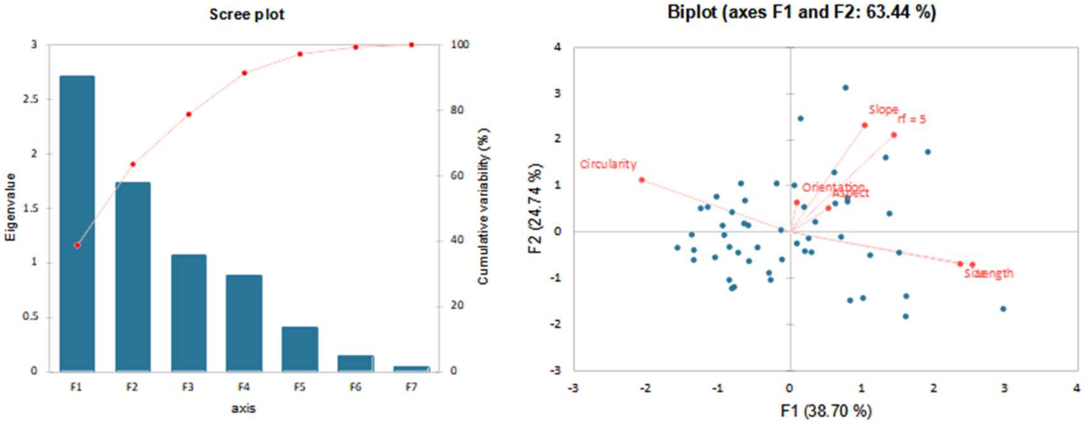

Eigenvectors

	F1	F2	F3	F4	F5
Length	0.571	-0.200	0.032	-0.097	0.144
Slope	0.234	0.648	-0.222	0.010	0.075
Aspect	0.120	0.144	0.630	0.752	-0.046
Orientation	0.021	0.179	0.727	-0.651	-0.068
Size	0.533	-0.196	0.029	-0.015	0.602
Circularity	-0.464	0.316	0.058	0.007	0.750
rf = 5	0.325	0.590	-0.142	-0.038	-0.204

Factor Loadings

	F1	F2	F3	F4	F5
Length	0.939	-0.263	0.033	-0.091	0.092
Slope	0.384	0.853	-0.229	0.009	0.048
Aspect	0.198	0.190	0.651	0.707	-0.029
Orientation	0.035	0.236	0.752	-0.613	-0.043
Size	0.877	-0.257	0.030	-0.014	0.385
Circularity	-0.763	0.416	0.060	0.007	0.479
rf = 5	0.535	0.777	-0.147	-0.036	-0.130

Figure 3-48. Vastitas Borealis Site 2 (Phoenix landing site) small polygons PCA scree plot and variable loading biplot. There are positive correlations between feature slope and roughness (r_f = 5). Length and size are positively correlated but inversely related to slope and roughness.

4.0 Discussion

4.1 Morphometric and Multiscale Surface Roughness Analyses

Polygon centers were evaluated using a common set of metrics that have been employed on previous morphometric evaluations of patterned ground on Mars and Earth (Ulrich et al, 2011; Brooker et al, 2018). Comparisons of polygon morphology must take into consideration variations between different polygon subtypes. For example, large ice-wedge polygons on Earth that are composed of fine-grained material spanning several tens of meters in size will have different morphometric and surface roughness parameters than sorted stone circles that span 2-5 meters in size. Due to fundamental variations in feature composition and size, cross-evaluation between different morphologies should, on average, yield neutral results. In the case of evaluating the surface roughness of polygon centers based on the feature classifications in this study, there are

8 polygon subpopulations with surface roughness greater than the adjacent margins and there are 6 polygon subpopulations with a surface roughness that is less than the adjacent margins. There are 4 polygon populations with surface roughness values that are too close to the roughness of the adjacent margins to make a definitive conclusion.

A similar outcome is observed among polygon margins where the results are the inverse of the polygon center results. Polygon margins were delineated as single features defined by the space between polygon centers. While polygon margin perimeter, area, size, and circularity were recorded, these parameters are determined by the space surrounding the polygon centers that were chosen for delineation and do not represent a quantitative trend beyond providing a comparison for the total area evaluated between polygon centers and margins with the objective of evaluating nearly equal area regions among each feature class. The slope and slope aspect of the margins are interpreted to be more informative in a broader comparison of surface roughness between centers and margins.

Cross-evaluations between polygon subtypes may provide informative insights when paired with other observational objectives, such as investigating the depth and extent of subsurface ground ice in context with surface morphology. Three of the surveyed sites (Lethe Vallis, Utopia Planitia, and the *Phoenix* Landing Site) provide important insight into the broader results with implications for consideration in future morphometric and surface roughness evaluations of patterned ground on Mars.

The Lethe Vallis site is notable for the co-location of the polygons within a crater outflow channel at an equatorial location. The greater abundance of both large and small impact craters relative to the other sites in this project suggest an older landscape. The high level of crater preservation coupled with the lack of indicators that craters have been periglacially modified (e.g. absence of obvious crater pedestals) suggest either a periglacial origin for the polygons that pre-dates younger putative periglacial landscapes at higher latitudes or that the polygons were formed through non-periglacial processes entirely. Non-periglacial formation mechanisms including desiccation cracking that occurs in playa settings on Earth have been proposed for some intracrater and channel settings on Mars (see El-Maary et al, 2010, 2012, 2013, 2014, and 2015). This appears to be a viable formation mechanism at Lethe Vallis when the colocation of the polygons within a fluvial outflow channel are taken into consideration when evaluating polygon morphology. The visual similarities between polygons of periglacial and non-periglacial origins presents some challenge in assigning specific modes of formation at mid to high latitude sites where ground ice is known to occur. Clear morphometric differences between the two periglacial and nonperiglacial polygons would be beneficial to aid in feature characterization under more ambiguous scenarios, however multiple lines of evidence derived from the location of polygons and evidence of either periglacial or evaporite modification would still be required and, for the time, are probably more reliable indicators of polygon origin than evaluating polygon morphology alone.

The polygons at Utopia Planitia provide a case study for larger polygons with excess ice accumulating along polygon margins. The presence of exposed ice suggests, at a minimum, surface processes that are conducive to the accumulation and short-term preservation of ice. Recurring monitoring of the Utopia Planitia site could provide additional insight into the nature and stability of the exposed ice. Ice sublimation observed at the *Phoenix* landing site indicates ice tables on Mars are in vapor-diffusive equilibrium with the atmosphere (Mellon et al, 2009). The small incised polygons are visually similar to terrestrial sublimation polygons observed in Antarctica, however morphometric parameters for the latter are not extensive (Marchant et al, 2002; Levy et al, 2006). Updated measurements collected by UAS survey or LiDAR would be beneficial for performing a quantitative analysis with the data evaluated in this study.

The polygons evaluated near the *Phoenix* landing site can be directly associated with surface observations from the lander and provide an interesting comparison between orbital and surface assessed parameters. Polygons measured at the *Phoenix* landing site in this study ranged from approximately 3 to 19 m. In contrast, polygons measured by the *Phoenix* spacecraft at the surface range from approximately 2 to 3 m in diameter. The difference between the *Phoenix*-measured polygon diameters and HiRISE-measured long axis lengths and size (calculated as a proxy for diameter for irregular features in this study) can be attributed to a combination of feature selection bias and recording a higher frequency of larger polygons that tend to decrease in circularity in response to increasing length (Figure 3-49). The smallest polygons approaching 3.24 m in length are comparable to *Phoenix* observations (Figure 3-49). The outcome of the surface roughness evaluation is reinforced by imagery acquired by the *Phoenix* spacecraft of subdued polygons with approximately 0.2 to 0.5 m of vertical relief between margins and centers in the immediate vicinity of the landing site (Figure 3-49). The polygons are primarily composed of fine-grained regolith and gravel-sized rocks are uniformly distributed across the surface and generally not concentrated along feature margins (Shaw et al, 2009).

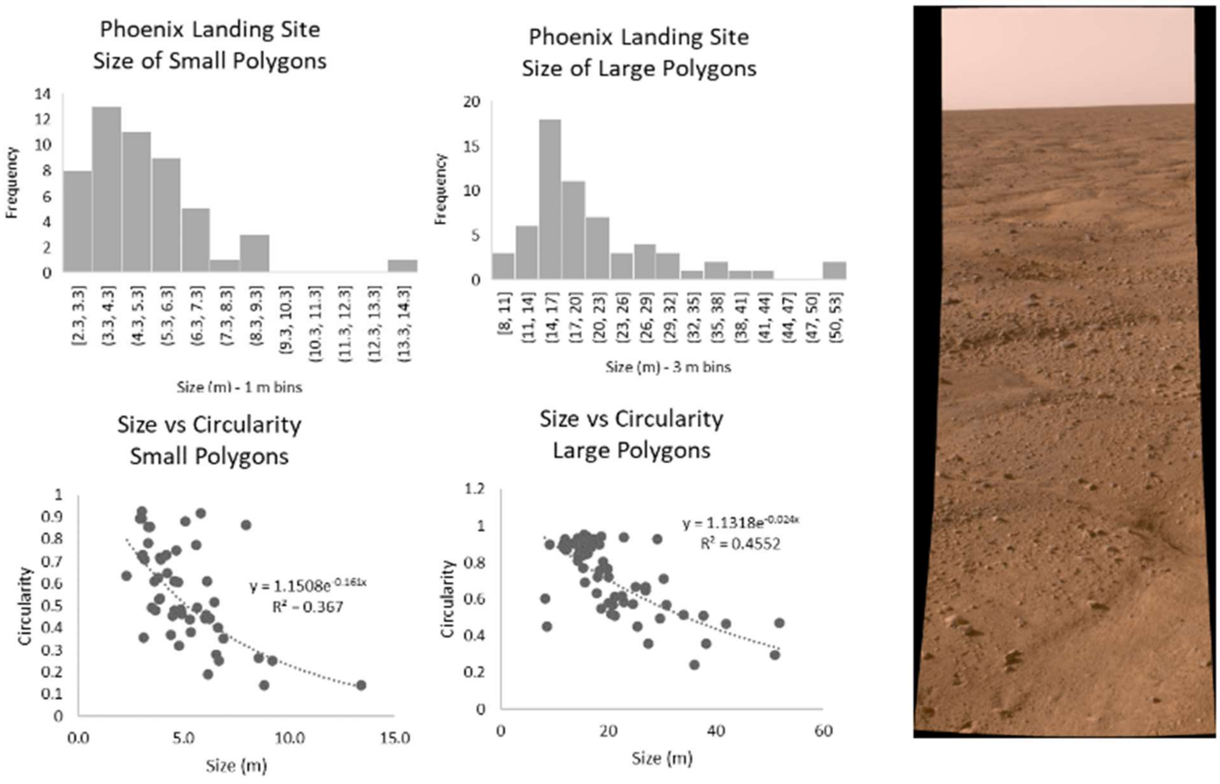

Figure 3-49. Top row: size distribution histograms of patterned ground near the Phoenix landing site. Bottom row: size vs. circularity of patterned ground near the landing site. Right: Image of subdued patterned ground from the Phoenix lander (Image: PIA10690).

While the larger polygons at the *Phoenix* landing site are discernable in terms of contrast variations of regolith between the centers and margins (Figure 3-45), the smaller polygons appear to comprise the “unit cells” that, in aggregate, form the larger polygons. Therefore, the variations between the large polygon centers and margins are likely to be more subtle and smaller in scale relative to the variations between the smaller polygon centers and margins. The challenge in characterizing the differences across the polygons near the landing site is exemplified by differences between small polygon centers and margins that are discernable at ground level in imagery from the *Phoenix* spacecraft, however the 0.2 to 0.5 m topographic relief is readily detectable in larger features on the HiRISE DTMs (Figure 3-45). At the nearby *Phoenix* landing site, smaller polygon centers are typically composed of a higher fraction of fine-grained material with larger rocks sometimes interspersed throughout polygon centers, but generally concentrated along polygon margins. The location of the *Phoenix* spacecraft suggests that the centers and margins of larger polygons visible in HiRISE imagery should be visible from the landing site, however the distinction between the large polygon centers and margins is not clear at ground level. This suggests that while some compositional and physical variation may exist between the large polygon centers and margins, the visual distinction that is observed from orbit is likely driven largely by albedo variations from the material composition of the centers and margins. While the subdued landscape of Vastitas Borealis made for an ideal landing site for the *Phoenix* spacecraft, the subdued topography yielded some ambiguity in quantifying surface roughness between polygon centers and margins. The observations at the *Phoenix* landing site underscore the limitations of applying this technique at other locations where the differences between polygon centers and margins were more subdued, such as Lethe Vallis, Vastitas Borealis Site 1, and Utopia Rupes Site 1.

4.2 Processing Observations, Limitations, and Provenance

HiRISE imagery and the resulting DTMs from stereopairs provide an unprecedented level of detail that has enabled morphological investigations of Mars for over 16 years. For example, HiRISE imagery has led to the discovery and ongoing monitoring of small-scale surface processes such as recurring slope linea (McEwen et al, 2011; Dundas et al, 2017) and the camera is currently engaged in monitoring ongoing seasonal changes across the planet (e.g. Knightly et al, 2019). Despite these capabilities, there are limitations to the accuracy and utility of the data at extremely small scales. The scale limitations were known at the start of this project, so while morphometric details are detectable in high-relief features, the analysis of low-relief features is an exercise of ascertaining DTM quality. As noted previously, small-scale cross-hatching that appeared in DTMs built using the ASP strongly interfered with the analysis of smaller polygons.

Existing programs and toolkits are utilized throughout every step of the process, eliminating the need for developing task-specific scripts for the project. While alternative workflows incorporating customizable code were explored (e.g. in Python and R), performing the data analysis using existing tools delivered consistent results. For dataset provenance, all DTMs and DTM-derived datasets were generated based on the stereo images specified in Table 1. Workflows supporting the multiscale surface roughness calculations in QGIS were saved as .JSON files to permit easier data re-processing in the future. In a similar manner, workflows using the Zonal Statistics toolkit for exporting surface roughness datasets and other morphometric parameters from QGIS were saved as .JSON files to enable rapid re-processing in the future.

4.3 Future Work

The ultimate objective of further evaluation of surface roughness parameters for patterned ground is to ascertain the extent to which surface morphology is reflective of subsurface conditions, such as the presence of nature of ground ice. Data from SHARAD and MARSIS is only capable of resolving cryogenic features deeper than 15 m bgs (Seu et al, 2006). The extent to which there is communication between surface morphology and cryogenic processes > 15 m bgs is likely limited, so gaining a better understanding of the relationship between surface morphology and near-surface (< 15 m bgs) cryosphere is required. Additional analog field work that incorporates co-located morphological and subsurface ground penetrating radar (GPR) surveys may provide useful data in the interim. If a connection between surface roughness and the cryosphere (or level of activity of patterned ground) cannot be established, the baseline parameters of the MSR evaluations performed in this project may be useful in supporting the identification and characterization of safe landing zones for future surface missions.

5.0 Conclusion

Patterned ground was evaluated at ten locations on Mars using a combination of imagery and digital terrain models generated from HiRISE stereo-pair imagery. There were two primary purposes for evaluating the patterned ground: to perform a morphometric analysis using standardized parameters to enable comparisons with previous and future studies of patterned ground and to perform a surface roughness evaluation in conjunction with the morphometric analysis to ascertain if roughness parameters could be associated with feature-scale details. Sites that had greater topographic relief (e.g. Utopia Planitia, Deuteronlius Mensae) produced more definitive surface roughness results than sites with low topographic relief (e.g. Vastitas Borealis and the *Phoenix* Landing Site). The results demonstrate the applicability of this multiscale surface roughness approach to future sites, however inspection of HiRISE DTM topographic surfaces prior to performing a surface roughness analysis is required to assess DTM quality. Future applications of this technique in areas with topographically distinct patterned in conjunction with an analysis of subsurface radar data could provide new insight into the nature, activity, and stability of the near-subsurface water ice table.

References

Arvidson, R.E., Bonitz, R.G., Robinson, M.L., Carsten, J.L., Volpe, R.A., Trebi-Ollennu, A., Mellon, M.T., Chu, P.C., Davis, K.R., Wilson, J.J., Shaw, A.S., Greenberger, R.N., Siebach, K.L., Stein, T.C., Cull, S.C., Goetz, W., Morris, R.V., Ming, D.W., Keller, H.U., Lemmon, M.T., Sizemore, H.G., and Mehta, M. 2009. Results from the Mars Phoenix Lander Robotic Arm experiment. Journal of Geophysical Research. 114, E00E02.

Ascione, A., Cinque, A., Miccadei, E., Villani, F., and Berti, C. 2008. The Pli-Quaternary uplift of the Apennine chain: new data from the analysis of topography and river valleys in Central Italy. Geomorphology, 102, p. 105-108. DOI:10.1016/j.geomorph.2007.07.022

Balme, M.R., Gallagher, C.J., and Hauber, E. 2013. Morphological evidence for geologically young thaw of ice on Mars: A review of recent studies using high-resolution imaging data. Progress in Physical Geography. 37 (3). 289-324.

Balme, M.R., Gallagher, C.J., Murray, J.B., and Muller, J.P. 2009. Sorted stone circles in Elysium Planitia, Mars: Implications for recent martian climate. Icarus. 200, 30-38.

Barrett, A. M., Balme M. R., Patel, M. R., and Hagermann, A. 2017. Clastic patterned ground in Lomonosov crater, Mars: examining fracture controlled formation mechanisms. Icarus. 295, 125-139.

Barrett, A.M., Balme, M.R., Patel, M.R., and Hagermann, A. 2018. The distribution of putative periglacial landforms on the martian northern plains. Icarus. 314, 133-148.

Brooker, L.M., Balme, M.R., Conway, S.J., Hagermann, A., Barrett, A.M., Collins, G.S., and Soare, R.J. 2018. Clastic polygonal networks around Lyot crater, Mars: Possible formation mechanisms from morphometric analysis.

Broxton, M.J. and Edwards, L.J. 2008. The Ames Stereo Pipeline: Automated 3D surface reconstruction from orbital imagery. Lunar and Planetary Science Conference XXXIX. Abstract 2419.

Bryson, K.L., Chevrier, V., Sears, D.W.G., and Ulrich, R. 2008. Stability of ice on Mars and the water vapor diurnal cycle: Experimental study of the sublimation of ice through a fine-grained basaltic regolith. Icarus. 196, 446-458.

Buczkowski, D.L., Seelos, K.D., and Cooke, M.L. 2012. Giant polygons and circular graben in western Utopia basin, Mars: Exploring possible formation mechanisms. Journal of Geophysical Research. 117, E08010.

Burr, D.M., Soare, R.J., Wan Bun Tseung, J.M., Emery, J.P. 2005. Young (late-Amazonian), near-surface, ground ice features near the equator, Athabasca Valles, Mars. Icarus. 178, 56-73.

Cao, W. and Cai, Z. 2018. Improved Multiscale Roughness Algorithm for Lunar Surface. IEEE Journal of Selected Topics in Applied Earth Observations and Remote Sensing. 11 (7), 2336-2345.

Cao, W., Cai, Z., and Tang, Z. 2015. Lunar surface roughness based on multiscale morphological method. Planetary and Space Science. 108, 13-23.

Costard, F., Forget, F., Mangold, N., and Peulvast, J. P. 2002. Formation of Recent Martian Debris Flows by Melting of Near-Surface Ground Ice at High Obliquity. Science. 295, 110-113.

Dundas, C.M., McEwen, A.S., Chojnacki, M., Milazzo, M.P., Byrne, S., McElwaine, J.N., and Urso, A. Granular flows at recurring slope linea on Mars indicate a limited role for liquid water. Nature Geoscience, 10, 903-907. DOI:10.1038/s41561-017-0012-5

El-Maarry, M.R., Markiewicz, W.J., Mellon, M.T., Goetz, W., Dohm, J.M., and Pack, A. 2010. Crater floor polygons: Desiccation patterns of ancient lakes on Mars? Journal of Geophysical Research, 115, E10006. DOI:

El-Maarry, M.R., Kodikara, J., Wijessoriya, S., Markiewicz, W.J., and Thomas, N. 2012. Desiccation mechanism for formation of giant polygons on Earth and intermediate-sized polygons on Mars: Results from a pre-fracture model. Earth and Planetary Science Letters, 323-324, 19-26. DOI:

El-Maaryy, M.R., Pemmerol, A., and Thomas, N. 2013. Analysis of polygonal cracking patterns in chloride-bearing terrains on Mars: Indicators of ancient playa settings. Journal of Geophysical Research: Planets, 118, 2263-2278. DOI:

El-Maarry, M.R., Watters, W., McKeown, N.K., Carter, J., Dobrea, N., Bishop, J.L., Pommerol, A., and Thomas, N. 2014. Potential desiccation cracks on Mars: A synthesis from modeling, analogue-field studies, and global observations. Icarus, 241, 248-268. DOI:

El-Maary, M.R., Watters, W.A., Yoldi, Z., Pommerol, A., Fischer, D., Eggenberger, U., and Thomas, N. 2015. Field investigation of dried lakes in western United States as an analogue to desiccation fractures on Mars. Journal of Geophysical Research: Planets, 120, 2241-2257. DOI:

Florinsky, I.V. 2017. An illustrated introduction to general geomorphometry. Progress in Physical Geography. 41 (6), 723-752.

Florinsky, I.V. 2018. Multiscale geomorphometric modeling of Mercury. Planetary and Space Science. 151, 56-70.

Gallagher, C., Balme, M.R. Conway, S.J., and Grindrod, P.M. 2011. Sorted clastic stripes, lobes, and associated gullies in high-latitude craters on Mars: Landforms indicative of very recent, polycyclic ground-ice thaw and liquid flows. Icarus. 211, 458-471.

Haltigin, T.W., Pollard, W.H., Dutilleul, P., Osinski, G.R., and Koponen, L. 2014. Co-evolution of polygonal and scalloped terrains, southwestern Utopia Planitia, Mars. Earth and Planetary Science Letters. 387, 44-54.

Hepburn, A.J., Holt, T., Hubbard, B., and Ng, F. 2019. Creating HiRISE digital elevation models for Mars using the open-source Ames Stereo Pipeline. Geoscientific Instrumentation Methods and Data Systems. 8, 293-313.

Hiesinger, H. and Head, J.W. 2000. Characteristics and origin of polygonal terrain in southern Utopia Planitia, Mars: Results from Mars Orbiter Laser Altimeter and Mars Orbiter Camera Data. Journal of Geophysical Research. 105, No. E5, 11,999-12,022.

Kerber, L., Dickson, J.L., Head, J.W., and Grosfils, E.B. 2017. Polygonal ridge networks on Mars: Diversity of morphologies and the special case of the Eastern Medusae Fossae Formation. Icarus. 281, 200-219.

Knightly, J.P., Fusco, M., Farnsworth, K., and Chevrier, V.F. 2019. Temporal Variations in Martian Swiss Cheese Terrain. Lunar and Planetary Science Conference L, Abstract Number 2187.

Korteniemi, J. and Krselavsky, M. A. 2013. Patterned ground in martian high northern latitudes: Morphology and age constraints. Icarus. 225, 960-970.

Kossacki, K.J. and Karmkiewicz, W.J. 2009. Small-scale trench in the north polar region of Mars: Evolution of surface frost and ground ice concentration. Icarus. 199, 75-85.

Kreslavsky, M.A., Head, J.W., and Marchant, D.R. 2006. Periods of active permafrost layer formation during the geological history of Mars: Implications for circum-polar and mid-latitude surface processes. Planetary and Space Science. 56. 289-302

Levy, J., Head, J., and Marchant, D. 2009. Thermal contraction crack polygons on Mars: Classification, distribution, and climate implications from HiRISE observations. Journal of Geophysical Research. 114, E01007.

Levy, J.S., Head, J.W., Marchant, D.R., Dickson, J.L., and Morgan, G.A. 2009. Geologically recent gully-polygon relationships on Mars: Insights from the Antarctic Dry Valleys on the roles of permafrost, microclimates, and water source for surface flow. Icarus. 201, 113-126.

Levy, J.S., Head, J.W., and Marchant, D.R. 2009. Cold and dry processes in the Martian Arctic: Geomorphic observations at the Phoenix landing site and comparisons with terrestrial cold desert landforms. Geophysical Research Letters. 36. L21203.

Lindsay, J.B., Newman, D.R., and Francioni, A. 2019. Scale-Optimized Surface Roughness for Topographic Analysis. Geosciences. 9, 322.

Luchitta, B.K. 1983. Permafrost on Mars: Polygonally Fractured Ground. Permafrost: Fourth Internation Conference Proceedings, 744-749.

Mangold, N., Maruice, S., Feldman, W.C., Costard, F., and Forget, F. 2004. Spatial relationships between patterned ground and ground ice detected by the Neutron Spectrometer on Mars. Journal of Geophysical Research. 109, E08001.

Mangold, N. 2005. High latitude patterned grounds on Mars: Classification, distribution and climate control. Icarus. 174, 336-359.

Marchant, D.R., Lewis, A.R., Phillips, W.M., Moore, E.J., Souchez, R.A., Denton, D.H., Sugden, D.E., Potter Jr., N., and Landis, G.P. 2002. Formation of patterned ground and sublimation till over Miocene glacier ice in Beacon Valley, southern Victoria Land, Antarctica. Geological Society of America Bulletin, 114, 6, 718-730.

McEwen, A.S., Ojha, L., Dundas, C.M., Mattson, S.S., Byrne, S., Wray, J.J., Cull, S.C., Murchie, S.L., Thomas, N., and Gulick, V.C. 2011. Seasonal Flows on Warm Martian Slopes. Science, 333, 740-743. DOI:10.1126/science.1204816

Mellon, M. T., Arvidson, R. E., Marlow, J. L., Phillips, R. J., and Asphaug, E. 2008. Periglacial landforms at the Phoenix landing site and the northern plains of Mars. Journal of Geophysical Resarch. 113, E00A23.

Mellon, M. T., Arvidson, R. E., Sizemore, H. G., Searls, M. L., Blaney, D. L., Cull, S., Hecht, M.H., Heet, T.L., Keller, H.U., Lemmon, M.T., Markiewicz, W.J., Ming, D.W., Morris, R.V., Pike, W.T., and Zent, A.P. 2009. Ground ice at the Phoenix Landing Site: Stability state and origin. Journal of Geophysical Research. 114, E00E07.

Moratto, Z.M., Broxton, M.J., Beyer, R.A., Lundy, M., and Husmann, K. 2010. Ames Stereo Pipeline, NASA's Open Source Automated Stereogrammetry Software. Lunar and Planetary Science Conference 41, abstract #2364.

Morgan, G.A., Putzig, N.E., Perry, M.R., Sizemore, H.G., Bramson, A.M., Petersen, E.I., Bain, Z.M., Baker, D.M.H., Mastroguiseppe, M., Hoover, R.H., Smith, I.B., Pathare, A., Dundas, C.M., and Campbell, B.A. 2021. Availability of subsurface water-ice resources in the northern mid-latitudes of Mars. Nature Astronomy, 5, p. 230-236. DOI:10.1038/s41550-020-01290-z

Nakamura, T. and Tajika, E. 2003. Climate change of Mars-like planets due to obliquity variations: implications for Mars. Geophysical Research Letters. 30 (13). 1685.

Oehler, D.Z. and Allen, C.C. 2012. Giant Polygons and Mounds in the Lowlands of Mars: Signatures of an Ancient Ocean? Astrobiology. 12 (6), 601-615.

Oehler, D.Z., Mangold, N., Hallet, B., Fairén, Le Deit, L., Williams, A.J., Sletten, R.S., and Martínez-Frías. 2016. Origin and significance of decameter-scale polygons in the lower Peace Vallis fan of Gale crater, Mars. Icarus. 277, 56-72.

Orloff, T., Kreslavsky, M., and Asphaug, E. 2013. Distribution of polygon characteristic scale in Martian patterned terrain in the northern hemisphere using the Fourier transform. Journal of Geophysical Research: Planets. 118, 1558-1566.

Orloff, T.C., Kreslavksy, M.A., and Asphaug, E.I. 2013. Possible mechanism of boulder clustering on Mars. Icarus. 225, 992-999.

Pechmann, 1980 – origin of polygonal troughs in northern plains of Mars

Renno et al, 2009. Physical and Thermodynamical Evidence for Liquid Water on Mars? Lunar and Planetary Science Conference 40. Abstract Number 1440.

Seibert, N.M. and Kargel, J.S. 2001. Small-Scale Martian Polygonal Terrain: Implications for Liquid Surface Water. Geophysical Research Letters. 28 (5), 899-902.

Séjourné, A., Costard, F., Swirad, Z.M., Łosiak, A., Bouley, S., Smith, I., Balme, M.R., Orgel, C., Ramsdale, J.D., Hauber, E., Conway, S.J., van Gasselt, S., Reiss, D., Johnsson, A., Gallagher, C., Skinner, J.A., Kereszturi, Á, and Platz, T. 2019. Grid Mapping the Northern Plains of Mars: Using Morphotype and Distribution of Ice-Related Landforms to Understand Multiple Ice-Rich Deposits in Utopia Planitia. Journal of Geophysical Research: Planets. 124, 483-503.

Shaw, A., Arvidson, R.E., Bonitz, R., Carsten, J., Keller, H.U., Lemmon, M.T., Mellon, M.T., Robinson, M., and Trebi-Ollennu, A. 2009. Phoenix soil physical properties investigation. Journal of Geophysical Resarch. 114, E00E05.

Shean, D.E., Alexandrov, O., Moratto, Z., Smith, B.E., Joughin, I.R., Porter, C.C., and Morin, P.J. 2016. An automated, opne-source pipeline for mass production of digital elevation models (DEMs) from very high-resolution commercial stereo satellite imagery. ISPRS Journal of Photogrammetry and Remote Sensing, 116.

Sizemore, H. G., Mellon, M. T., Searls, M. L., Lemmon, M. T., Zent, A. P., Heet, T. L., Arvidson, R. E., Blaney, D. L., and Keller, H. U. 2010. In situ analysis of ice table depth variations in the vicinity of small rocks at the Phoenix landing site. Journal of Geophysical Research. 115, E00E09.

Sletten, R.S., Hallet, B., and Fletcher, R.C. 2003. Resurfacing time of terrestrial surfaces by the formation and maturation of polygonal patterned ground. Journal of Geophysical Research. 108 (E4), 8044.

Smith, P.H., Tamppari, L.K., Arvidson, R.E., Bass, D., Blaney, D., Boynton, W.V., Carswell, A., Catling, D.C., Clark, B.C., Duck, T., DeJong, E., Fisher, D., Goetz, W., Gunnlaugsson, H.P., Hecht, M.H., Hipkin, V., Hoffman, J., Hviid, S.F., Keller, H.U., Kounaves, S.P., Lange, C.F., Lemmon, M.T., Madsen, M.B., Markiewicz, W.J., Marshall, J., McKay, C.P., Mellon, M.T., Ming, D.W., Morris, R.V., Pike, W.T., Renno, N., Staufer, U., Stoker, C., Taylor, P., Whiteway, J.A., and Zent, A.P. 2009. H_2O at the Phoenix Landing Site. Science. 325, 58-61

Soare, R.J., Conway, S.J., Williams, J.-P., Gallagher, C., and McKeown, L.E. 2020. Possible (closed system) pingo and ice-wedge/thermokarst complexes at the mid latitudes of Utopia Planitia, Mars.

Soare, R. J., Conway, S. J., and Dohm, J. M. 2014. Possible ice-wedge polygons and recent landscape modification by “wet” periglacial processes in and around the Argyre impact basin, Mars. Icarus. 233, 214-228.

Soare, R. J., Conway, S. J., Gallagher, C., and Dohm, J. M. 2016. Sorted (clastic) polygons in the Argyre region, Mars, and possible evidence of pre- and post-glacial periglaciation in the Late Amazonian Epoch. Icarus. 264, 184-197.

Seu, R., Phillips, R.J., Biccari, D., Orosei, R., Masdea, A., Picardi, G., Safaeinili, A., Campbell, B.A., Plaut, J.J., Marinagneli, L., Smrekar, S., and Nunes, D.C. 2006. SHARAD sounding radar on the Mars Reconnaissance Orbiter. Journal of Geophysical Research, 112, E05S05. DOI:10.1029/2006JE002745

Taud, H. and Parrot, F. 2005. Measurement of DEM roughness using the local fractal dimension. Géomorphologie. 4, 327-338.

Ulrich, M., Hauber, E., Herzschuh, U., Hartel, S., Shirrmesiter, L. (2011). Polygon pattern geomorphometry on Svalbard (Norway) and western Utopia Planitia (Mars) using high-resolution stereo remote-sensing data. Geomorphology, 134, 197-216.

Yoshikawa, K. 2003. Origin of the polygons and the thickness of Vastitas Borealis Formation in Western Utopia Planitia on Mars. Geophysical Research Letters. 30 (12), 1603.

Chapter 4

Thermal and Morphometric Observations of Patterned Ground in the Haughton Impact Structure on Devon Island, Nunavut, Canada

Knightly, J.P.[1], Dixon, J.C.[1], Chevrier, V.F.[1]

[1]University of Arkansas, Center for Space and Planetary Sciences, Fayetteville, AR 72701

1. Introduction

The vicinity surrounding Haughton Impact Structure (HIS) provides a unique setting as the largest accessible terrestrial periglacial impact crater, leading to its extensive utilization as an Earth-Mars analog site (Osinski et al., 2001; Lee et al., 2001; Lee and Osinski, 2005; Osinski and Lee, 2005; Osinski et al. 2005; Godin et al., 2019). Dated at approximately 21 to 39 million years old (Sherlock et al., 2005; Young et al., 2013; Erickson et al., 2021), the geology within the crater consists of lacustrine silt, sand, and clay deposits within the upper Haughton Formation overlying impact-derived polymict breccias in the lower Haughton Formation (Osinski and Lee, 2005). The lacustrine deposits originate from a post-impact intracrater lake that featured attendant ouflow channels (Osinski and Lee, 2005), lesser versions of which presently exit the HIS and flow northeast before emptying into the Arctic Ocean at Thomas Lee Inlet.

The Haughton impact structure is situated in an active periglacial environment on Devon Island in the Canadian high arctic (Osinski et al, 2005). The HIS remains one of the best-preserved impact craters owing to relatively cold and dry polar desert conditions that have persisted since its formation (Osinski et al 2005b). Long-term climate data is sparse for the HIS and Devon Island in general, however detailed observations recorded at the Truelove Lowlands approximately 150 km east of HIS provide some context. The modern climate at the HIS is classified as a polar desert that receives approximately 185 mm of precipitation annually, of which roughly 30% is liquid, primarily during the short arctic summer (Ryden, 1977). The combination of mean annual climate conditions, abundance of active periglacial features, geologically recent glacial activity, and the remnants of an intracrater lake make the Haughton impact structure an ideal setting to conduct Earth-Mars analog studies of periglacial morphologies that occur on both planets.

Patterned ground morphology has been extensively studied in the field (Washburn, 1956; Kessler and Werner, 2003; Watanabe et al 2013; Watanabe et al 2017; Uxa et al, 2017). Terrestrial patterned ground has also been utilized as an analog for patterned ground on Mars (Marchant et al, 2002; Mangold, 2005; Levy et al, 2008; Levy et al, 2009a; Levy et al, 2009b; Ulrich et al, 2011; Haltigin et al, 2012; Mellon et al, 2014; Soare et al, 2014; Soare et al, 2016; Barrett et al, 2018; Brooker et al 2018). Modeling patterned ground formation and development on both planets has continued (Ray et al, 1983; Daanen et al, 2008; Peterson and Krantz, 2002; Peterson, 2011). Additional field parameters are necessary in order to refine computational models for patterned ground development (Fisher et al, 2016; Watanabe et al, 2017).

Observations from the *Phoenix* mission indicate that contemporary modification of patterned ground on Mars likely occurs via sublimation-driven processes as subsurface ground ice is currently in vapor-diffusive equilibrium with the atmosphere (Mellon et al., 2009). It has been proposed that periods of high obliquity could result in an increase in atmospheric pressure and temperature enabling polygon modification via periglacial (freeze-thaw) processes to occur on Mars (Laskar et al., 2004; Soare et al., 2014). Further calibration of active layer thermal properties in periglacially-modified patterned ground would therefore benefit modeling efforts to constrain the conditions leading to the onset of periglacial processes on Mars. Analog evaluations of the thermal properties of both smaller-scale features (such as hummocks, stone circles, stone nets) and larger-scale features (such as ice-wedge polygons) would help capture the range of polygon morphologies that are observed on Mars today.

To provide additional measurements to support future modeling efforts, this project collected in-situ datalogged and point observations of the temperature and moisture conditions of the active layer at a variety of sites comprising small- and large-scale patterned ground on Devon Island in the Canadian high arctic. These temperature and moisture observations are used in tandem with measurements collected to derive the thermal properties of material sampled from patterned ground margins and centers during local summer and peak active layer development. Examining the morphology and thermal conditions within individual patterned ground landforms during the terrestrial arctic summer provided data during the seasonal thawing period, an important window of time to understand while testing the wet periglaciation hypothesis for patterned ground development on Mars.

2. Site Selection

The field work for this project was conducted during summer 2017 as a project involved with the Mars 160 Mission Simulation at The Mars Society's Flashline Mars Arctic Research Station (FMARS) located near 75.4312° north, 89.8233° west on Haynes Ridge, located on the west-northwest rim of the HIS (Figure 4-1). As a mixed human-studies and field research analog, most field work at FMARS was conducted under Mars-mission constraints, including the notable requirement that field science activities be conducted while donning a mock spacesuit. Field measurements were collected over a period of 27 days from 19 July to 14 August 2017 at field-selected sites using the methods described below. Field site locations and descriptions are listed in Table 4-1 and presented in Figure 4-1.

2.1 Patterned Ground Site Beneath Slopewash Streaks

An initial reconnaissance of the area near FMARS identified irregular stone nets downgradient of the station and near the terminus of seasonal slopewash streaks resulting from the melting of seasonal snowpack accumulated in a sheltered area below Haynes Ridge (Figure 4-2). Slopewash is a periglacial fluvial process that is prevalent across the Canadian high arctic (Lewkowicz, 1977). The slopewash streaks below FMARS were studied over the course of the simulation as "wet" analogs for their similarities to slope streaks and recurring slope linea (RSL) on Mars (Clarke et al., 2018). Gullies, potentially formed via dry or wet fluvial processes, have been studied for their spatial relationship to patterned ground on Earth and Mars (Levy et al, 2009). It has been previously noted that gullies and polygonal ground occur in close spatial proximity at several locations on Mars and gully/polygon analogs have been studied both on Devon Island (Lee et al., 2001) and in Antarctica (Levy et al., 2009) to further evaluate this spatial relationship.

A series of sorted stone nets located downgradient of and adjacent to slopewash streaks were identified for studying subsurface moisture and thermal conditions along patterned ground margins and centers. The setting was used as a hypothetical analog for the interaction between patterned ground and “wet-formation” slope streaks (Kreslavsky et al, 2009) and RSL (Bhardwaj

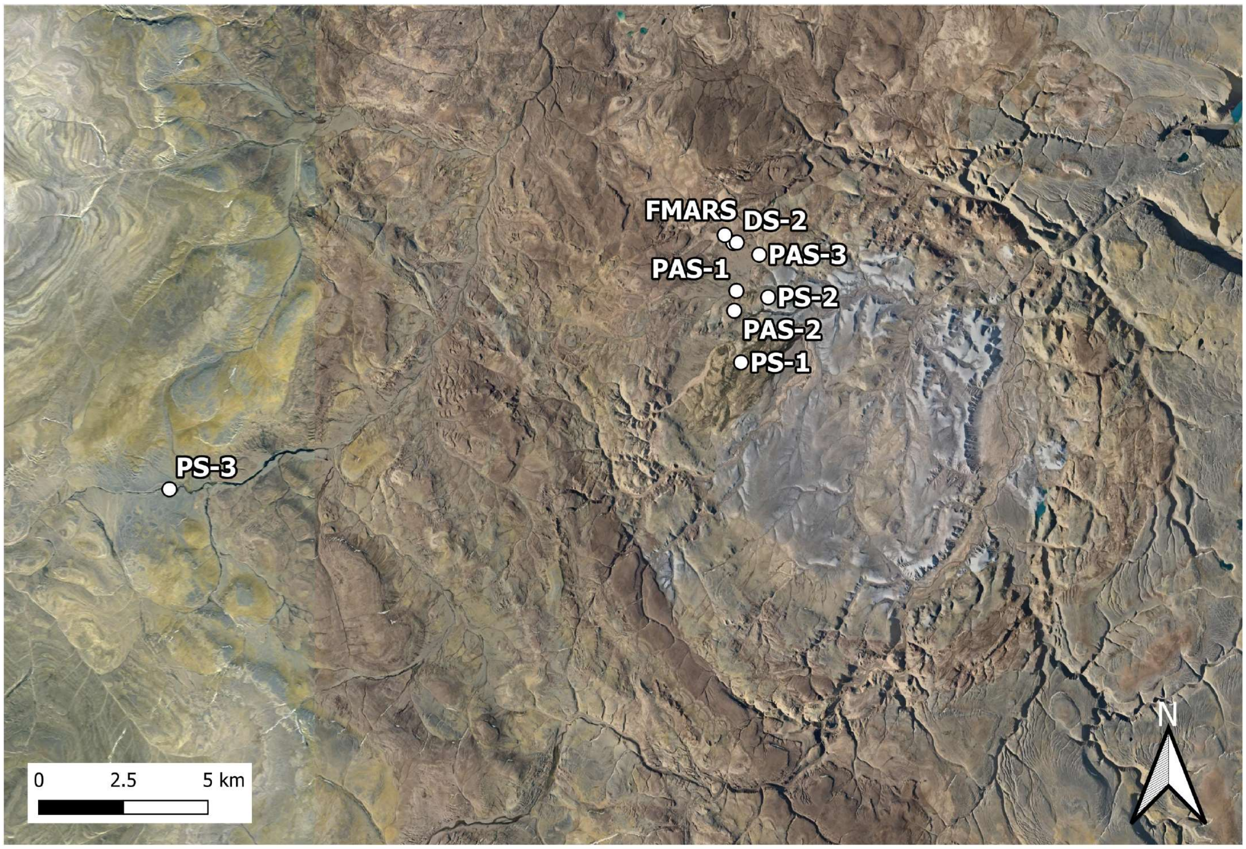

Figure 4-1 – Haughton Impact Structure and Study Area Location. Overview of the 2017 field season study locations within and near the Haughton Impact Structure relative to FMARS. Abbreviations: DS = Datalogger Station. FMARS = Flashline Mars Arctic Research Station. PAS = *Phoenix* Analog Site. PS = Polygon Site.

et al, 2017) on Mars. This potential relationship was evaluated through a literature review following the completion of fieldwork and is detailed in the discussion section.

2.2 Patterned Ground (*Phoenix* Analog) Sites

The *Phoenix* mission to Mars explored an area of patterned ground near its landing site in Vastitas Borealis in the north polar high latitudes (Mellon et al., 2008; Mellon et al., 2009; Shaw et al., 2009; Smith et al., 2009). The landing site was selected for morphological similarities to terrestrial patterned ground, to which Devon Island is referenced among several analogs used in the lead-up to the mission (Keller et al, 2008). While it detected the presence of subsurface water ice (Smith et al., 2009), the *Phoenix* mission did not find evidence to support the recent or contemporary development of a seasonal wet active active layer (Mellon et al., 2009). However, a “wet active layer” formation hypothesis operable during periods of high obliquity has persisted (Kreslavsky et al., 2008; Soare et al., 2014; Soare et al., 2016). To better characterize the thermal and environmental setting of patterned ground occurring within an active wet periglacial regime, three additional sites were selected in the field based on visual morphological similarities at the surface to the *Phoenix* landing site (Figure 4-3).

While the term “polygon” is used colloquially throughout much of the *Phoenix*-mission literature, the patterned ground in the vicinity of the landing site can also be described as hummocks with higher centers and lower margins. Hummocky patterned ground occurs in abundance across Devon Island, so the process of locating appropriate analog sites was limited primarily by their location to FMARS, the relative sorting and distribution of gravels at the surface, and the approximate dimensions and shapes of the hummocks in each area of interest. The hummocks at the *Phoenix* landing site have a generally smooth appearance due to the presence of fine-grained regolith at the surface with some gravels and boulders interspersed primarily along

Table 4-1

Slopewash Streak and Data Logger Locations

Location ID	GPS Coordinates		Location Description
	°North	°West	
DS-1A	75.4291	-89.8152	Patterned ground center. Silty/gravel patterned ground fed by meltwater runoff
DS-1B	75.4291	-89.8153	Patterned ground margin. Silty/gravel patterned ground fed by meltwater runoff
DS-2A	75.4292	-89.8116	Patterned ground margin. Sandy/gravel patterned ground fed by meltwater runoff
DS-2B	75.4292	-89.8116	Patterned ground center. Sandy/gravel patterned ground fed by meltwater runoff
DS-3	75.4292	-89.8137	Slightly patterned ground located about halfway between DS-1 and DS-2
Background	75.4289	-89.8136	Sandy ground just south of and in between DS-1 and DS-2. Non-patterned ground
MWS-1	75.4309	-89.8219	Silty ground just below the current extent of crater rim snow pack
MWS-2	75.4304	-89.8205	Halfway down meltwater streak
MWS-3	75.4299	-89.8178	Base of meltwater streak along the margin of solifluction lobe
MWS-4	75.4293	-89.8155	Halfway between termination of meltwater and DS-1
MWS-5	75.4293	-89.8123	Halfway between termination of meltwater and DS-2

Patterned Ground – Point of Interest Locations

Location ID	GPS Coordinates		Location Description
	°North	°West	
PAC-1	75.4190	-89.8136	Grey colored limestone mounds. Slightly graded slope between FMARS and Trinity Creek
PAC-2	75.4118	-89.8126	Color sorted mounds (yellow and dark gey) along hillslope off ATV trail leading to Polygons and Gemini Hills
PAS-1	75.4165	-89.8120	Same as PAC-1, location of first trench excavation on 7/25/17
PAS-2	75.4113	-89.8142	Same as PAC-2, location of second trench excavation 7/26/17
PAS-3	75.4260	-89.7882	Grey colored limestone hummocky mounds. Slightly graded slope leading towards stream, biofilm along margins
PSA	75.3979	-89.8073	Large ice-wedge polygons. Approximately 15-30 meters across on average, half meter rise between tops/margins.

Polygon Sample Locations

Location ID	GPS Coordinates		Location Description
	°North	°West	
PSA-P1	75.3978	-89.8062	Middle of polygon
PSA-P2	75.3979	-89.8061	Halfway between middle of polygon and north margin
PSA-P3	75.3979	-89.8061	Halfway along north margin of polygon. S-series along sidewall of polygon
PSA-P4	75.3979	-89.8061	Middle of trough between polygons
PSA-P5	75.3978	-89.8063	Halfway along south margin of polygon
PSA-P6	75.3978	-89.8065	Southwest corner of polygon
PSA-P7	75.3979	-89.8059	Northeast corner of polygon
PSA-P8	75.3979	-89.8057	Middle of trough intersection to the northeast of the polygon
PSA-P9	75.3978	-89.8061	Halfway between middle and northeast corner of polygon
PSA-T1	75.3988	-89.8122	Hill at northwest end of transect above polygon field
PSA-T2	75.3985	-89.8117	Northwest bank of stream
PSA-T3	75.3985	-89.8113	Mid-stream
PSA-T4	75.3985	-89.8100	Southeast bank of stream
PSA-T5	75.3983	-89.8099	Polygon margin, along the northwestern edge of the polygon field
PSA-T6	75.3980	-89.8087	Polygon center
PSA-T7	75.3977	-89.8057	Intersection of polygon margins
PSA-T8	75.3975	-89.8047	Polygon margin, along the southeastern edge of the polygon field
PSA-T9	75.3974	-89.8045	Mid-stream
PSA-T10	75.3973	-89.8044	Southeast bank of stream
PSA-T11	75.3972	-89.8035	Hill at southeast end of transect above polygon field

Notes

DS = Datalogger Site

FMARS = Flashline Mars Arctic Research Station

MWS = Meltwater (Slopewash) Streak

PAC = *Phoenix* Analog Candidate

PAS = *Phoenix* Analog Site

PSA = Polygon Site A

P# = Polygon Sample Number

T# = Transect Sample Number

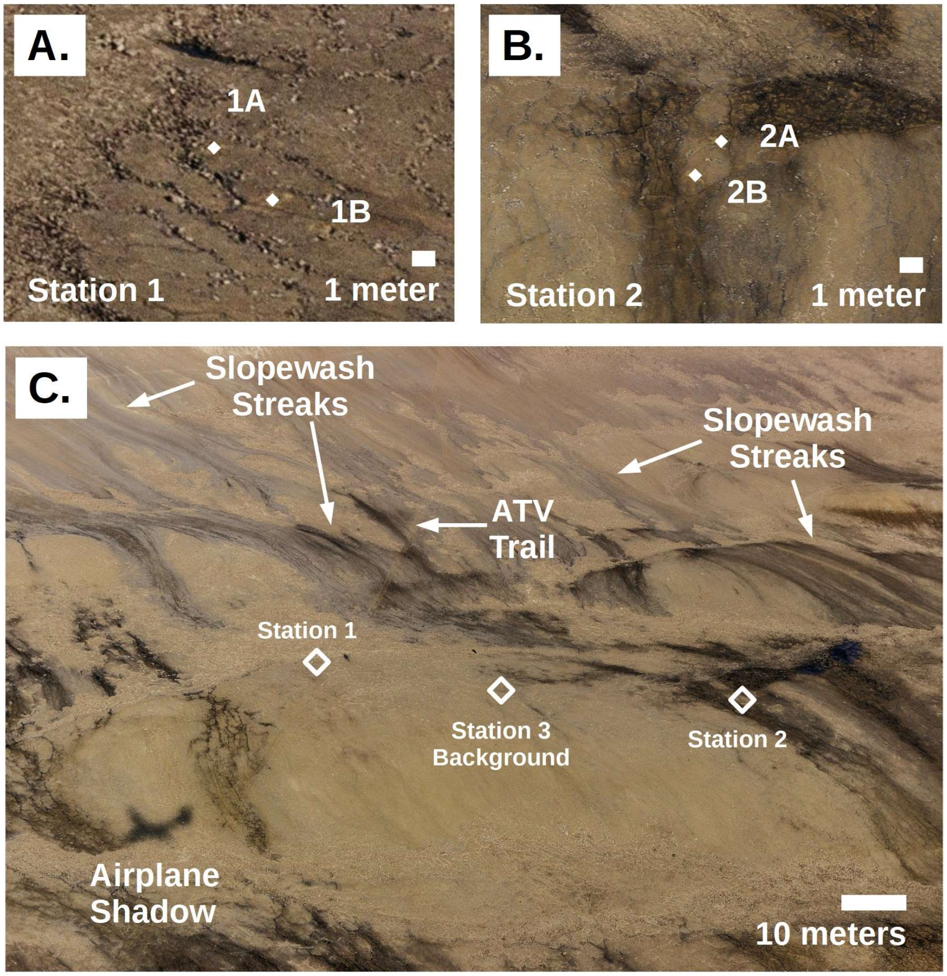

Figure 4-2 – Datalogger Station and Slopewash Streak Locations. A.) Zoomed in view from an aerial photo of Station 1 and the approximate locations of probe deployment locations 1A and 1B. Displaced soil from the installation and retrieval of the dataloggers is visible near the indicated points. B.) Zoomed in view of Station 2 and the approximate locations of probe deployment points 2A and 2B. A rock cairn that was supporting the datalogger station is visible between the indicated points. C.) View of the datalogger monitoring site and the positions of Stations 1, 2, and 3. Station 3 collected atmospheric background measurements between Stations 1 and 2. The proximity of slopewash streaks originating upgradient of the datalogger stations is apparent, with Station 1 located outside of a slopewash pathway and Station 2 located in the middle of a slopewash streak.

the margins. The topology of the water ice boundary beneath large rocks at the *Phoenix* landing site was examined as a potential gauge for patterned ground activity by looking for depressions in the ice directly beneath the rocks (Sizemore et al., 2010). The selection of analog features for further sampling and study on Devon Island involved identifying candidate locations with relatively larger boulders at the surface that could facilitate an examination of potential differences in topology at the permafrost-active layer boundary.

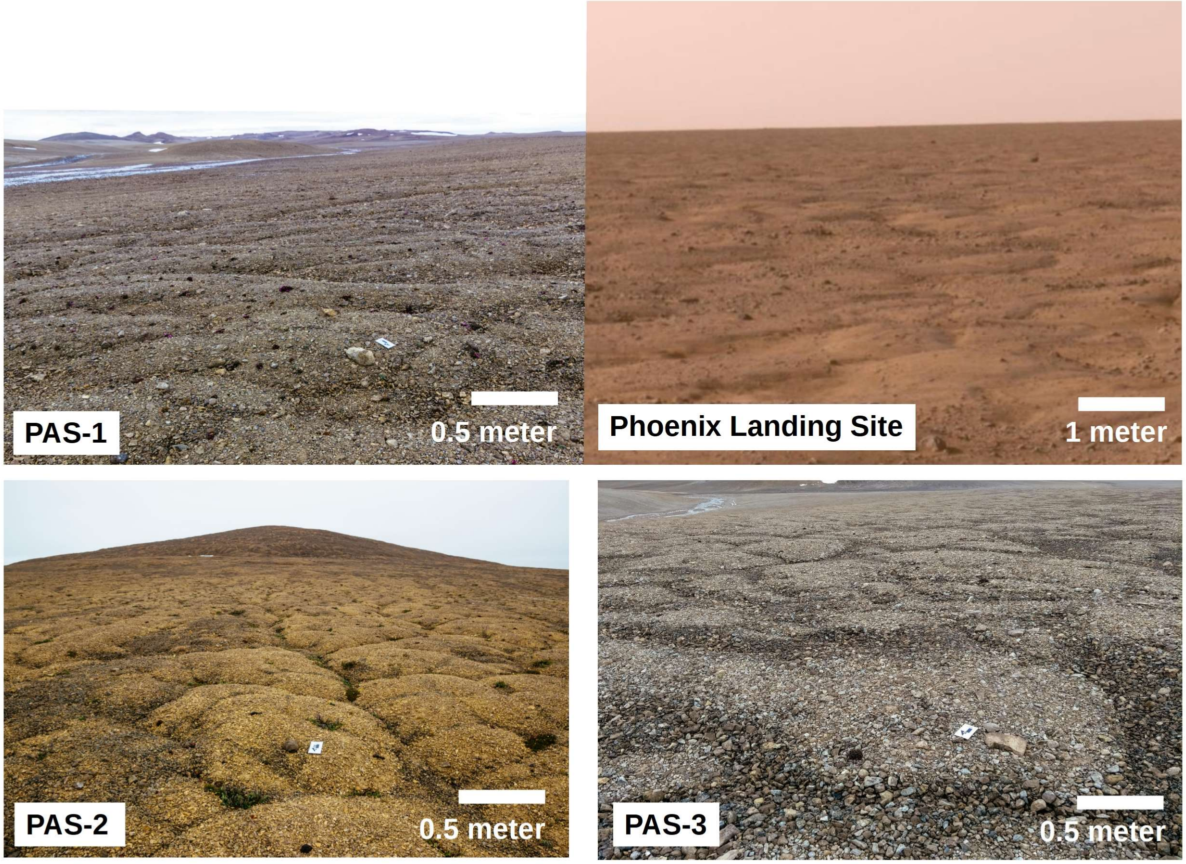

Figure 4-3 – *Phoenix* Analog Sites (PAS). The morphological similarities of PAS 1, 2, 3 to the *Phoenix* landing site. While the hummocks observed within the Haughton Impact Structure of approximately similar dimensions to the hummocks observed near the *Phoenix* lander, the small-scale patterned ground observed within the crater was overwhelmingly composed of larger-grained gravels with interstitial sand relative to finer-grained regolith observed on Mars.

The hummocks within the HIS generally contain a higher gravel fraction than the hummocks at the *Phoenix* landing site. The process of site selection thus focused on finding analogues with similar relative dimensions to hummocks at the *Phoenix* landing site and the presence of larger boulders distributed across the feature. The three sites that were selected were based off a ground-level reconnaissance of the area near FMARS that occurred shortly after the start of the mission simulation in late July (Figure 4-3). The site locations are detailed in Table 4-1 and are located within the Trinity Creek watershed and are located within fluvial glacial deposits that overlie the Allen Bay Formation (Osinski and Lee, 2005). The field investigation and analysis of these sites is further described in Sections 3.3 and 4.3, respectively.

2.3 Ice-Wedge Polygon Sites

An ice-wedge polygon site was selected prior to mobilizing to the field based on available satellite imagery of the HIS. The site is centered near 75.3979°N, -89.8061°W to the west of Rabbit Run Creek with distal portions of the site extending northwest towards West Rhinoceros Creek. The site is located within lacustrine sediments of the Haughton Formation that were deposited in a post-impact crater lake. The site has also been investigated during previous Mars analog field work activities (Osinski and Lee, 2005).

A notable characteristic of polygons throughout the HIS and across Devon Island is their near-ubiquitous proximity to surface water features, including streams and ponds (Figure 4-4). The polygons bear a striking resemblance to intracrater polygons on Mars that have been utilized in previous Earth-Mars analogue research activities (Burr et al, 2005; Ulrich et al, 2011; Haltigin et al, 2012; Soare et al 2014). The presence of intracrater polygon networks on Mars, particularly in the low-lying center of craters, could provide evidence of active (wet) periglacial conditions during periods of high obliquity (Costard et al, 2002; Kreslavsky et al, 2008, Soare et al, 2014; Soare et al; 2016).

3. Methods

3.1 Morphometric Characterization

There were three flights between Resolute Bay, Cornwallis Island and the HIS on Devon Island over the course of mobilizing and demobilizing for field work in 2017. Photographs were taken during each of the flights on 3 July, 15 July, and 17 August to document changes in the periglacial landscape during a 45-day period that spanned the peak warm period for the year. Conditions between the 3 July and 17 August flights were the most pronounced and while some differences were noted between 3 July and 15 July, partially overcast skies prevented the collection of more detailed observations on the 15 July flight. Clear ground conditions on the 17 August flight permitted photo documentation of patterned ground and polygonal terrain along a transect corresponding to the direct flight path towards Resolute Bay to the southwest. Aerial photos were later georeferenced and georectified against satellite imagery enabling approximate feature measurements to be gathered using the open-source QGIS software. While the photos aren’t as precisely georeferenced as they would be through a formal survey, there is precedent and value in utilizing opportunistic photogrammetry from overflights to derive morphometric observations from aerial photos (Girod et al, 2017). Procedures and metrics utilized to characterize feature morphology are detailed in Table 4-2 and are modeled after similar studies conducted by Ulrich et al (2011), Uxa et al (2017), and Brooker et al (2018).

The same procedures employed with the georeferenced aerial photos were also applied to feature measurements using satellite imagery. High-resolution satellite imagery of across Devon Island is sparse, however 0.5m-resolution imagery is available in the vicinity of the HIS. While the spatial resolution does not permit accurate measurements of smaller-scale patterned ground, larger polygons and their associated margins are discernible, enabling an approximation of their dimensions.

Digital elevation models (DEMs) to 2-meter resolution are available for free download via the ArcticDEM database supported by the Polar Geospatial Center (Porter et al., 2018). A multiscale surface roughness (MSSR) analysis was performed to assess the viability of using the DEM for deriving fine-scale micromorphological data. The MSSR analysis was performed using a tool included with the Whitebox plugin which integrates with both QGIS and ESRI ArcMap (Lindsay et al, 2019). The results of the MSSR analysis are presented in Table 4-3 and reveal that the 2-meter DEM resolution is insufficient for detecting and correlating feature-scale changes in surface morphology on larger features to regional satellite imagery, however the DEM resolution allows for quantifying approximate values for the slope and slope aspect of feature clusters.

3.2 Active Layer Datalogger Stations

One of the instruments on board the *Phoenix* spacecraft was the Thermal and Electrical Conductivity Probe (TECP), designed to assess the thermal and hydrological properties of the regolith and atmosphere at the landing site (Zent et al., 2009). Results from TECP found the dry regolith overlying ground ice is a good thermal insulator with an average thermal conductivity of 0.085 W/mK and an average heat capacity of 1.05 x 10^6 J/m^3K (Zent et al., 2010). Due to a suspected open circuit in the instrument, TECP data has been re-evaluated and re-calibrated (Rivera-Valentin and Chevrier, 2015; Zent et al., 2016). Despite this, the present-day conditions on the Martian surface are well-constrained in that they are incompatible with sustaining wet periglacial environments. Assessing the thermal properties of terrestrial patterned ground is an important step to understanding the behavior of postulated wet periglacials environment on Mars under periods of high obliquity.

A field-hardened thermal conductivity meter was not identified prior to commencing field work, so an alternative experiment was developed to assess the thermal properties of the patterned ground within Haughton Crater. In-situ temperature and moisture measurements were collected using HOBO H21-USB datalogger stations paired with HOBO S-TMB-M002

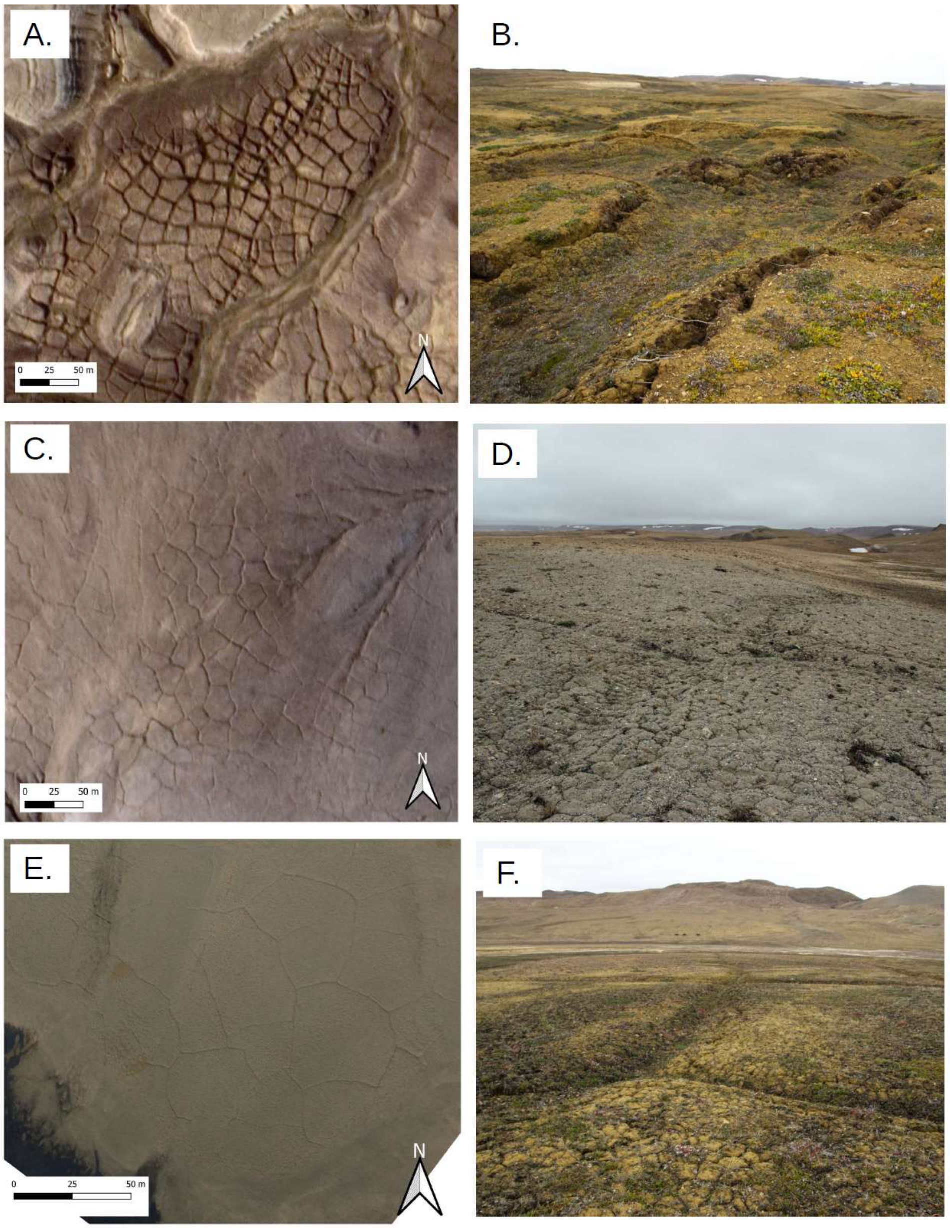

Figure 4-4 – Polygon Site 1 (PS-1) satellite image (A) and ground-level photo taken from near the middle of the site (B). PS-2 satellite image (C) and ground level photo of subdued polygons taken from a distal portion along the northwest margin of the site. Ground-level photos of polygons at PS-2 (D). PS-3 aerial photo captured on the departure flight from Devon Island on 17 August 2017 (E). While no ground-level photos were acquired of PS-3, it is likely that polygon morphology at the surface resembles a combination of the PS-2 polygons in image (D) and subdued polygons along a distal portion of the PS-1 site (F).

Table 4-2

Morphometric Parameters			
Parameter	**Data Source**	**Derived Using**	**Description**
Vegetation	Aerial/Satellite Imagery, Ground Observations	Visual observations	Rated by: None, Sparse, Moderate, and Dense
Length (m)	Aerial or satellite imagery	Field Calculator in QGIS	Length of the longest axis of the feature
Width (m)	Aerial or satellite imagery	Field Calculator in QGIS	Length of the shortest axis of the feature
Perimeter (m)	Aerial or satellite imagery	Field Calculator in QGIS	The sum total length of all sides
Area (m^2)	Aerial or satellite imagery	Field Calculator in QGIS	The area of the feature
Long axis orientation (°)	Aerial or satellite imagery	Field Calculator in QGIS	The orientation of the longest feature axis measured between 0 and 180 degrees from true north
Size (m)	Aerial or satellite imagery	LibreOffice Calc	$\sqrt{(4A/\pi)}$ where A is the feature area
Circularity	Aerial or satellite imagery	LibreOffice Calc	$(4\pi A)/p^2$ where A is the feature area and P is the feature perimeter. 0 indicates an elongated ellipse and 1 indicates a circle
Mean slope (°)	2m ArcticDEM	Spatial Analyst Tool in ArcMap	The mean slope across the area of the feature
Mean aspect (°)	2m ArcticDEM	Spatial Analyst Tool in ArcMap	The mean slope aspect across the area of the feature

The selected parameters are based on those used by Ulrich et al (2011) and Brooker et al (2018). Feature = Patterned ground or ice-wedge polygon.

temperature and S-SMD-M005 10HS soil moisture probes. Soil measurements were collected at one minute intervals throughout a 27-day observational period. The temperature and moisture probes were deployed within the active layer that was present at the start of the simulation, which extended from the surface to between 0.35 to 0.45 meters in depth, the encountered depths to permafrost at the time of datalogger deployment. A schematic of each datalogger station setup is detailed in Figure 4-5. A HOBO Pro v2 atmospheric station placed between the two datalogger stations recorded atmospheric temperature and moisture conditions at five-minute intervals throughout the 27-day period. To complement the other measurements collected by TECP and other instruments on board *Phoenix*, electrical conductivity and soil pH measurements were collected at the surface and deployment depth at each datalogger point. The thermal properties of samples collected at each datalogger location were evaluated under laboratory conditions following the mission simulation, as described in Section 3.4.

Table 4-3 (Part 1 of 3)

Multiscale Surface Roughness Analysis of 2m ArcticDEM											
		Cell Filtering Radius									
Location	Feature ID	5 Magnitude	5 Scale	10 Magnitude	10 Scale	20 Magnitude	20 Scale	30 Magnitude	30 Scale	40 Magnitude	40 Scale
Datalogger Site A	A	0.247	4	0.668	9	0.824	19	1.069	29	1.255	39
	B	0.191	4	0.645	9	0.823	19	1.073	29	1.280	39
	C	0.251	4	0.683	9	0.808	19	1.061	29	1.219	39
	D	0.414	4	0.727	9	0.821	19	1.069	29	1.215	39
	E	0.500	4	0.776	9	0.826	19	1.064	29	1.172	39
	F	0.225	4	0.621	9	0.780	19	1.058	29	1.212	39
	G	0.272	4	0.686	9	0.788	19	1.050	29	1.178	39
	H	0.326	4	0.721	9	0.809	19	1.051	29	1.175	39
	I	0.446	4	0.746	9	0.820	19	1.056	29	1.169	39
	J	0.473	4	0.788	7.8	0.825	19	1.041	29	1.131	39
	K	0.535	4	0.818	8.0	0.831	13.5	1.046	29	1.129	39
	L	0.290	4	0.683	9	0.782	19	1.041	29	1.154	39
	M	0.336	4	0.738	9	0.798	19	1.034	29	1.135	39
	N	0.382	4	0.766	9	0.816	19	1.034	29	1.131	39
	O	0.525	4	0.798	8.4	0.829	18.3	1.054	29	1.145	39
	Center Averages	0.361	4	0.724	8.8	0.812	18.6	1.053	29	1.180	39
	Margin	0.348	4	0.718	8.9	0.811	18.8	1.053	29	1.182	39
Location	Feature ID	5 Magnitude	5 Scale	10 Magnitude	10 Scale	20 Magnitude	20 Scale	30 Magnitude	30 Scale	40 Magnitude	40 Scale
Datalogger Site 2	A	0.571	4	1.132	9	1.253	12.6	1.253	12.6	1.253	12.6
	AA	0.522	4	0.928	9	0.932	12.5	0.961	29	0.961	29
	B	0.540	4	1.118	9	1.357	12.3	1.357	12.3	1.357	12.3
	BB	0.577	4	0.875	9	0.933	17.8	0.946	25.5	0.950	36.3
	C	0.465	4	1.077	9	1.126	11	1.126	11	1.126	11
	CC	0.576	4	1.092	9	1.121	11	1.121	11	1.121	11
	D	0.569	4	1.173	9	1.194	10	1.194	10	1.194	10
	E	0.621	4	1.124	9	1.134	10.7	1.134	10.7	1.134	10.7
	F	0.690	4	1.141	8.3	1.142	9.7	1.142	9.7	1.142	9.7
	G	0.468	4	0.981	9	1.055	12.3	1.055	12.3	1.055	12.3
	H	0.507	4	0.982	9	1.062	12	1.062	12	1.062	12
	I	0.563	4	1.060	9	1.090	10.5	1.090	10.5	1.090	10.5
	J	0.604	4	1.081	9	1.091	10	1.091	10	1.091	10
	K	0.679	4	1.087	9	1.106	11	1.106	11	1.106	11
	L	0.707	4	1.100	8.3	1.120	11.3	1.120	11.3	1.120	11.3
	M	0.730	4	1.094	8.5	1.124	12	1.124	12	1.124	12
	N	0.715	4	1.106	8.9	1.142	13.0	1.142	13.0	1.142	13.0
	O	0.737	4	1.088	9	1.103	10.5	1.103	10.5	1.103	10.5
	P	0.665	4	1.121	9	1.162	12.6	1.162	12.6	1.162	12.6
	Q	0.605	4	1.126	9	1.148	10.2	1.148	10.2	1.148	10.2
	R	0.516	4	1.031	9	1.042	10.3	1.042	10.3	1.042	10.3
	S	0.446	4	0.912	9	0.988	12	0.990	17.7	1.012	26
	T	0.467	4	0.961	9	1.007	11	1.007	11	1.017	25.7
	U	0.457	4	0.949	9	0.994	11	0.994	11	1.002	25.3
	V	0.485	4	0.957	9	0.976	10.6	0.982	18.2	0.990	29.2
	W	0.525	4	0.950	9	0.952	9.3	0.968	29	0.972	31.3
	X	0.578	4	1.027	9	1.032	10	1.032	10	1.032	17.7
	Y	0.649	4	1.058	8.7	1.060	9	1.060	9	1.060	9
	Z	0.612	4	1.042	9	1.048	9.9	1.048	9.9	1.048	9.9
	Center Averages	0.581	4	1.047	8.9	1.086	11.2	1.088	13.2	1.090	15.6
	Margin	0.562	4	1.036	8.9	1.092	11.9	1.094	13.7	1.096	16.3

Table 4-3 (Part 2 of 3)

Multiscale Surface Roughness Analysis of 2m ArcticDEM											
		Cell Filtering Radius									
Location	Feature ID	5 Magnitude	5 Scale	10 Magnitude	10 Scale	20 Magnitude	20 Scale	30 Magnitude	30 Scale	40 Magnitude	40 Scale
Polygon Site 1	A	0.233	4	0.434	8.9	0.751	19	1.221	29	1.715	39
	A1	0.231	4	0.539	9	0.899	19	1.178	29	1.905	39
	B	0.460	4	1.003	9	1.976	19	2.535	29	2.946	39
	B1	0.222	4	0.512	9	0.868	19	1.293	29	1.936	39
	C	0.518	4	1.239	9	2.162	19	2.520	29	2.962	39
	C1	0.213	4	0.461	9	0.822	19	1.354	29	1.846	39
	D	0.468	4	1.363	9	2.193	19	2.487	29	2.890	39
	D1	0.200	4	0.553	9	0.870	19	1.495	29	1.959	39
	E	0.272	4	0.782	9	1.479	19	1.995	29	2.370	39
	E1	0.211	4	0.628	9	1.075	19	1.563	29	2.032	39
	F	0.265	4	0.660	9	1.481	19	2.067	29	2.365	39
	F1	0.324	4	0.676	9	1.028	19	1.459	29	1.876	39
	F1	0.321	4	0.623	9	1.011	19	1.434	29	1.840	39
	G	0.170	4	0.562	9	1.400	19	2.065	29	2.365	39
	G1	0.231	4	0.557	9	0.958	19	1.427	29	1.845	39
	H	0.195	4	0.433	9	0.984	19	1.614	29	2.159	39
	H1	0.162	4	0.419	9	1.042	19	1.506	29	1.977	39
	I	0.303	4	0.565	9	0.909	19	1.517	29	2.155	39
	I1	0.186	4	0.556	9	1.232	19	1.652	29	2.031	39
	J	0.191	4	0.401	9	0.653	19	1.173	29	1.980	39
	J1	0.295	4	1.100	9	1.516	19	1.856	29	2.059	39
	K	0.147	4	0.410	9	0.707	19	1.236	29	2.001	39
	K1	0.323	4	0.881	9	1.484	17.1	1.713	29	1.981	39
	L	0.281	4	0.572	9	1.183	19	1.786	29	2.246	39
	L1	0.361	4	0.999	9	1.557	16.9	1.686	29	2.005	39
	M	0.303	4	0.719	9	0.933	18.6	1.491	29	2.045	39
	M1	0.279	4	0.684	9	1.503	19.0	1.706	29	2.101	39
	N	0.237	4	0.513	9	0.784	19	1.190	29	1.916	39
	N1	0.300	4	1.063	9	1.807	19	2.005	29	2.232	39
	O	0.156	4	0.359	9	0.619	19	1.047	29	1.837	39
	O1	0.386	4	1.242	9	2.025	19	2.196	29	2.328	39
	P	0.143	4	0.394	9	0.593	19	1.067	29	1.752	39
	P1	0.451	4	1.438	9	1.843	18.3	1.975	27.9	2.137	39
	Q	0.249	4	0.559	9	0.750	19	1.027	29	1.770	39
	Q1	0.530	4	1.364	9	1.792	17.8	1.885	27.6	2.069	39
	R	0.413	4	0.931	9	0.961	10.8	1.321	29	1.924	39
	R1	0.439	4	1.227	9	1.715	19	1.965	29	2.132	39
	S	0.326	4	0.717	9	0.945	19	1.164	29	1.818	39
	S1	0.235	4	0.689	9	1.476	19	1.899	29	2.188	39
	T	0.308	4	0.735	9	0.896	19	1.107	29	1.768	39
	T1	0.381	4	0.890	9	1.437	18.7	1.567	29	1.923	39
	U	0.222	4	0.533	9	0.760	19	1.054	29	1.738	39
	V	0.166	4	0.426	9	0.631	19	1.144	29	1.698	39
	W	0.192	4	0.369	8.9	0.641	19	1.333	29	1.736	39
	X	0.181	4	0.385	8.9	0.835	19	1.429	29	1.892	39
	Y	0.249	4	0.437	8.9	0.686	19	1.314	29	1.718	39
	Z	0.205	4	0.448	9	0.833	19	1.168	29	1.799	39
	Center Averages	0.279	4	0.703	9.0	1.164	18.7	1.572	28.9	2.042	39
	Margin	0.276	4	0.673	9.0	1.152	18.7	1.594	29.0	2.073	39

Table 4-3 (Part 3 of 3)

Multiscale Surface Roughness Analysis of 2m ArcticDEM											
		Cell Filtering Radius									
Location	Feature ID	5 Magnitude	5 Scale	10 Magnitude	10 Scale	20 Magnitude	20 Scale	30 Magnitude	30 Scale	40 Magnitude	40 Scale
Polygon Site 2	2A	0.230	4	0.442	9	0.636	19	0.728	29	0.887	39
	2B	0.223	4	0.481	9	0.639	19	0.781	29	0.926	39
	2C	0.227	4	0.409	8.7	0.528	19	0.721	29	0.890	39
	2D	0.176	4	0.361	9.0	0.541	19	0.665	29	0.786	39
	2E	0.224	4	0.439	8.9	0.472	14.3	0.585	27.7	0.710	39
	2F	0.249	4	0.398	8.5	0.476	16.6	0.598	29	0.696	39
	2G	0.240	4	0.454	9.0	0.471	11.5	0.498	24.6	0.612	39
	2H	0.165	4	0.350	9.0	0.416	18.6	0.509	29	0.618	39
	2I	0.246	4	0.407	8.6	0.501	19	0.580	29	0.675	39
	2J	0.178	4	0.449	9	0.564	18.7	0.659	29	0.777	39
	2K	0.235	4	0.464	9	0.581	19	0.722	29	0.842	39
	Center Averages	0.218	4.000	0.423	8.9	0.530	17.6	0.641	28.5	0.765	39
	Margin	0.211300035	4	0.4175983239	8.895759717	0.524262629	17.69140165	0.6397289589	28.41990577	0.7636061022	39
Location	Feature ID	5 Magnitude	5 Scale	10 Magnitude	10 Scale	20 Magnitude	20 Scale	30 Magnitude	30 Scale	40 Magnitude	40 Scale
Polygon Site 3	3A	0.276	4	0.480	8.7	0.497	11.0	0.505	19.3	0.627	39
	3B	0.186	4	0.361	8.7	0.459	18.0	0.530	29.0	0.611	39
	3C	0.182	4	0.462	9	0.566	15.3	0.580	21.8	0.617	39
	3D	0.233	4	0.459	9	0.576	18.8	0.603	24.9	0.630	39
	3E	0.342	4	0.620	8.7	0.660	13.2	0.667	15.6	0.676	28
	3F	0.271	4	0.613	9	0.626	11.4	0.647	23.4	0.712	39
	3G	0.345	4	0.636	8.8	0.652	11.0	0.657	14.9	0.700	39
	3H	0.185	4	0.447	9.0	0.550	15.3	0.570	23.0	0.633	39
	3I	0.177	4	0.440	9	0.600	18.5	0.645	28.4	0.736	39
	3J	0.278	4	0.569	8.8	0.618	14.8	0.683	26.0	0.745	39
	Center Averages	0.248	4	0.509	8.9	0.580	14.7	0.609	22.6	0.669	37.9
	Margin	0.236	4	0.499	8.9	0.578	14.8	0.606	23.0	0.665	35.9

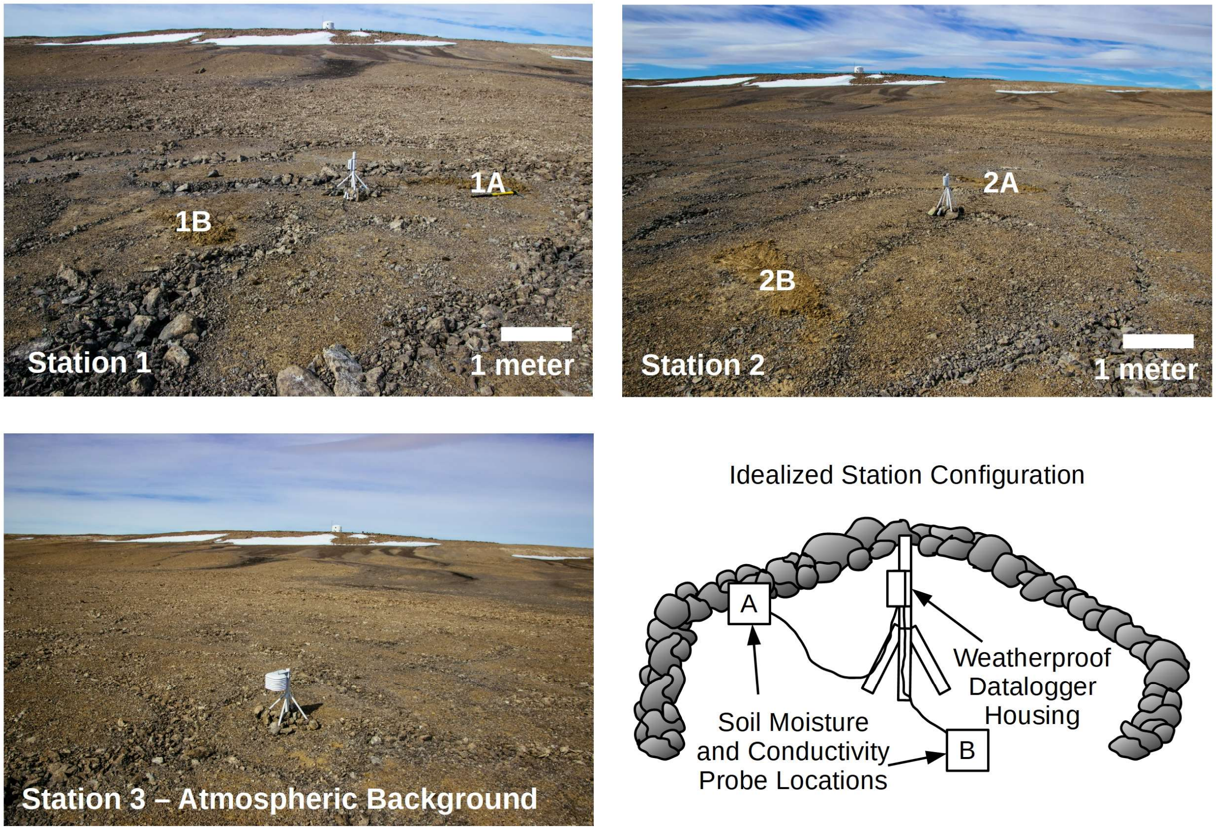

Figure 4-5 – Datalogger Station Configurations and Schematic. Final deployment configurations of Stations 1, 2, and 3. An annotated idealized station configuration highlighting the components of the datalogger setup. Slopewash streaks are visible on the hillslope in the background of the Station 1, 2, and 3 images. FMARS is visible at the crest of the hill and is located due northwest of each station.

3.3 Patterned Ground In-Situ Thermal Observations and Sampling

Trenches were excavated into the active layer until permafrost was encountered at each of the three patterned ground sites that were selected in the field. In smaller hummocks and stone nets, a singular trench was excavated straddling the margin and extending towards the center of the feature in order to obtain a stratigraphic and cryogenic cross section. In a similar manner, three trenches were excavated to permafrost in polygon centers and margins at the ice-wedge polygon site. A trench was excavated near the high-center of a representative polygon and following a transect extending laterally from the center, a second trench was excavated on the slope straddling the polygon center and margin, and a third trench was excavated at the lowest point of the polygon margin (trough).

In-situ temperature and electrical conductivity measurements were collected using a Hanna Groline HI98331 Direct Soil Conductivity and Temperature meter. The approximate moisture content and pH was measured using a mechanical Kelway Model HB-2 probe. When insterted into soil, the Kelway Model HB-2 works by converting a small flow of current between two metal plates into an approximate pH and moisture reading in terms of relative percent saturation. Temperature, electrical conductivity, moisture, and pH readings were taken at 10 cm intervals with depth in the trench and a final series of readings were collected at the base of the trench once the permafrost contact was reached. Thermal gradients were calculated by taking the difference between the surface temperature at the temperature at the base of the trench divided by the depth of the trench. Temperatures approaching 0°C were presumed to have reached the active layer/permafrost boundary.

Previous work has examined soil composition and pedogensis on Devon Island and the relationship between intracrater and noncrater soils. Comparisons are frequently drawn between prior work at the Devon Plateau and Truelove Lowland approximately 150 km east of the study area at the HIS (Lev and King, 1999; Ugolini et al, 2006). The vicinity near the ice-wedge polygons in the Haughton Formation has previously been described as analogous to the Truelove Lowland for similarities in both soil composition as well as the diversity of fauna present at these polar oases (Bliss 1977; Cockell and Lee, 2001). Soil conditions were noted during the excavation and representative samples were collected at each measuring point for further characterization under stable laboratory settings following the conclusion of field work. Samples were collected at intervals ranging from every 10 cm to every 25 cm depending on feature composition (sites with a higher fraction of medium to large gravels were more difficult to accurately sample at smaller intervals). Sample descriptions were recorded using Unified Soil Classification System (USCS) methodologies.

One of the objectives of the project was to look for topological variations across the permafrost boundary in relation to large boulders positioned at the surface. The presence of perched water at the active layer-permafrost contact in combination with a high fraction of very coarse gravels throughout the features prevented the collection of measurements of the permafrost boundary that were accurate enough to yield insight into topological differences of the permafrost boundary in relation to the presence of overlying boulders at the surface. The depth to permafrost within each trench was defined as the point at which the shovel used for trenching experienced increased resistance due to the presence of frozen ground and at which the temperature of interstitial sand and clay within the gravel matrix approached or reached 0°C.

3.4 Post-Field Thermal Measurements of Samples

Confirmation samples were collected at each measuring point to allow for measurements under controlled laboratory settings in the future as needed to address any follow-up questions. Following the conclusion of the Devon Island field work in 2017, obtaining the specific thermal conductivity, diffusivity, and specific heat capacity of each measuring location was desired. A TEMPOS Thermal Properties Analyzer was utilized to record measurements of these parameters from the retained field samples. Thermal measurements of the dried and unconsolidated samples were recorded at ambient room temperature of approximately 20 to 24°C and under ambient atmospheric humidity conditions. The size and portability of the TEMPOS Thermal Properties Analyzer is well-suited to field data collection and the same or a similar instrument is recommended if similar field work is conducted in the future.

The TEMPOS Thermal Properties Analyzer (manufactured under compliance with ISO 9001:2015) utilizes a variation of the dual probe heat pulse (DPHP) method in which a short burst of heat is generated by one needle and the resulting temperature change is detected by an adjacent thermistor needle (Campbell 1985). On the TEMPOS Thermal Properties Analyzer, the two needles are 3 cm long and spaced 6 mm apart on the SH-3 attachment used for this project.

The SH-3 attachment is inserted into each soil sample and the automated DPHP test is initiated and uses a manufacturer-programmed algorithm (Equations 1 and 2) based on modeling by Knight et al, 2012. The TEMPOS and SH-3 attachment measured the thermal conductivity, diffusivity, and specific heat capacity of each sample over a two-minute period.

The two-minute measurement period is optimized in the design of the TEMPOS unit, with the smaller needles requiring less time to gather a measurement while also minimizing thermally-induced water movement resulting from heating the sample. Current is applied to the heater needle for 30 seconds (s) and the temperature of the sample is monitored for another 90 s following the heater needle shut off. The observed ΔT from the 90 s observation period is used to solve for D and k, as q, r, t, th, and Ei are known. Once Equation 1 and Equation 2 have been solved for D and k, the specific heat capacity can be calculated using Equation 3.

To ensure consistent measurement procedures for all samples, sample materials were transferred into a 250 mL vial and measured at a consistent table-top location at an ambient room temperature between 20 and 24°C. While the moisture content of the samples was less than field conditions at the time of collection, no attempt was made to re-saturate the samples due to inherent variations that would arise, including discrepancies between in-situ factors such as the natural compression, available pore-space of the sample locations, and external environmental influences such as atmospheric temperature and humidity. We therefore treat the results derived from the laboratory thermal measurements of the samples as an unsaturated, dry baseline.

$$\Delta T = \left(\frac{q}{4\pi k}\right) Ei\left(\frac{-r^2}{4Dt}\right) \qquad t \le t_h \qquad \textbf{Equation 1}$$

$$\Delta T = \left(\frac{q}{\pi k}\right)\left\{ Ei\left[\frac{-r^2}{4D\left(t-t_h\right)}\right] - Ei\left[\frac{-r^2}{4Dt}\right]\right\} \qquad t > t_h \qquad \textbf{Equation 2}$$

$$\rho C = \frac{k}{D} \qquad \textbf{Equation 3}$$

ΔT is the temperature rise at the measuring needle,

q is the heat input at the heated needle (W/m),

k is the thermal conductivity (W/mK),

r is the distance from the heated needle to the measuring needle,

D is the thermal diffusivity (m^2/s),

t is time (s),

t_h is the heating time (s), and

E_i is the exponential integral and is approximated using polynomials (Abramowitz and Stegun 1972).

Equations 1 through 3, as presented in the TEMPOS Manual and based on modeling by Knight et al., 2012.

4. Results

4.1 Morphometric Characterization

4.1.1 Aerial Observations of Datalogger Sites

The 3 July flight was the initial attempt to land at FMARS that was ultimately aborted due to saturated ground conditions that prevented safe landing. While circling FMARS to look for a landing site, several photographs were taken of the research station and surrounding area, including an area of patterned ground that would ultimately serve as the location for Datalogger Station 1, as described in Section 3.2. Figure 4-6 details a comparison of the observed changes in the ground conditions at the Datalogger Site four days prior to the deployment of the datalogger stations and three days following their retrieval.

The photos highlight a few key changes that occurred at the site. The first is the near total melting of the remaining snow pack, reflecting conditions that were observed island-wide. All but the deepest or most sheltered areas of snow near the datalogger sites had melted by the 17 August departure. The second notable difference is the change in albedo resulting from the drying of the ground surface and decrease in surface flow stemming from snowmelt runoff. While some changes in surface color and albedo are semi-permanent as the result of the variable deposition darker or lighter colored sediments across the slopewash streaks, much of the color variability between the two images is associated with changes in surface soil moisture content between the beginning and ending of the monitored period. A third difference between the two images is the addition of a looped ATV track through one of the snow slopewash streaks. The track reflects a change in semi-permanent ground conditions, transitioning from relatively drier surface conditions near where Station 1 was deployed to fully saturated ground conditions within the snow slopewash streak. The fully saturated ground conditions were confirmed by nearly entrapping an ATV before executing a U-turn back to dry ground.

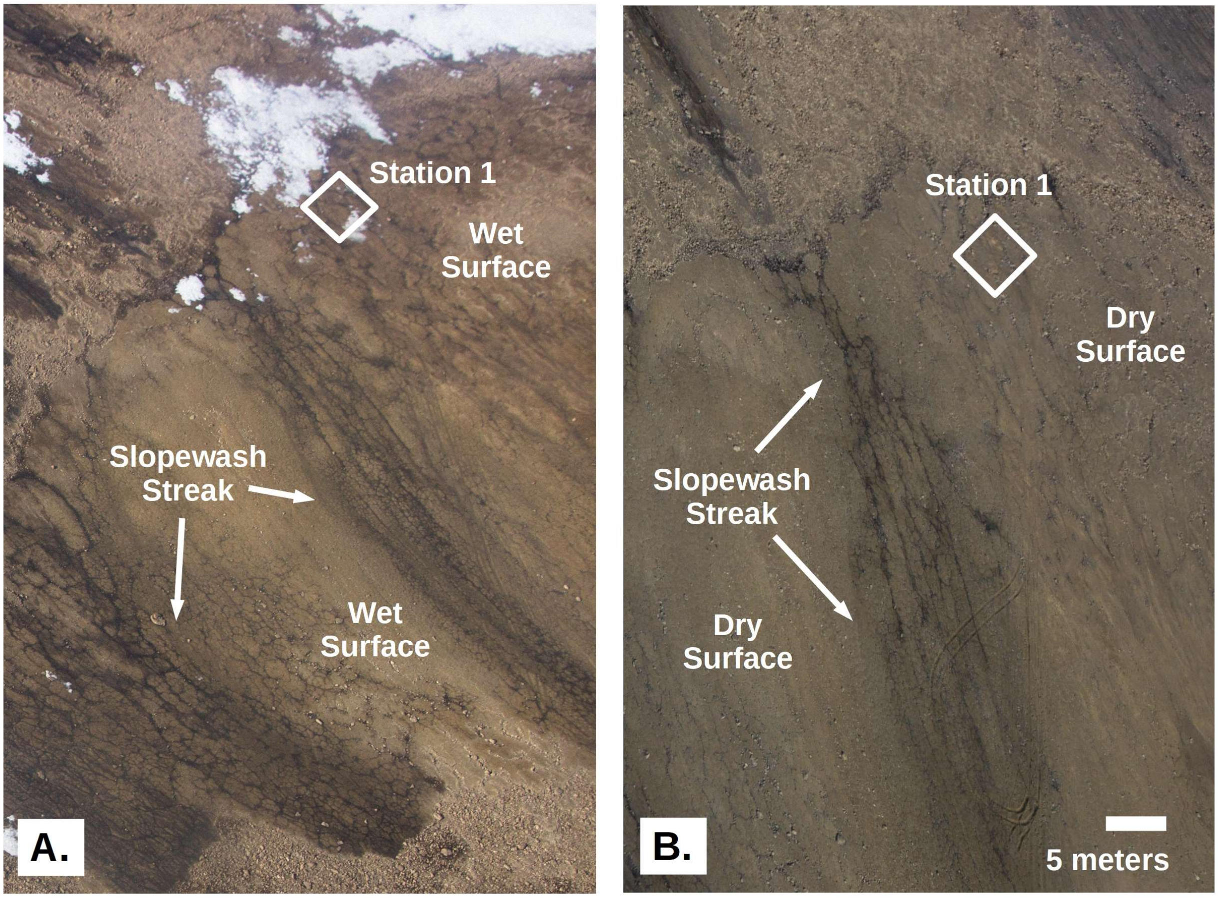

Figure 4-6 – Wet vs Dry Comparison of Datalogger Station 1. A.) Image captured on 3 July of the Station 1 location prior to datalogger deployment. Residual snow is visible at the surface near the station deployment location and the slopewash streaks are prominently visible. B.) Image captured on 17 August following the retrieval of the dataloggers. All remaining snow near the dataloggers has melted and while still visible, the slopewash streaks have started to lighten in appearance due to reduced water flow.

While patterned ground is prevalent throughout the area, patterned ground with the most distinct boundaries occurs within the saturated zones within and downgradient of the slopewash streaks. These boundaries are possibly more distinct due to a few reasons: the presence of larger gravels to boulders along the margins, continued water flow across the monitored period that maintained saturated (and darker) conditions along the margins, and the accumulation of a biofilm on the surface of rocks along the margins were recurrent surface water flow provides a suitable environment for biological activity.

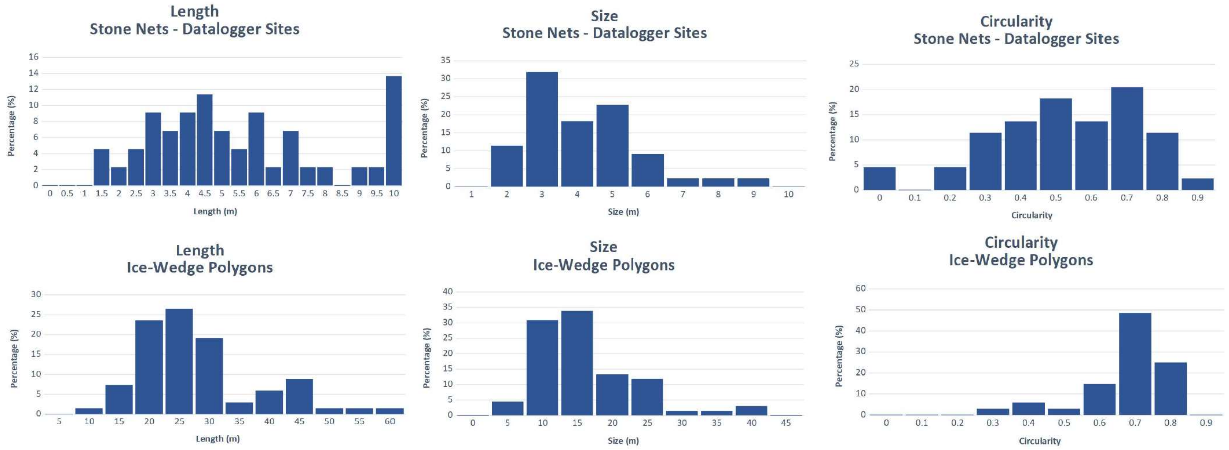

Figure 4-7 – Histograms for the datalogger sites (DS-1 and DS-2; top row) and ice-wedge polygon sites (PS-1, PS-2, and PS-3; bottom row).

Morphometric parameters and topographic properties were calculated using georeferenced aerial photos of the site captured on 17 August and projected onto the underlying 2m ArcticDEM of the area. The morphometric observations are presented in Table 4-4 and histograms in Figure 4-7. A total of 15 patterned ground features were surveyed at Datalogger Site 1 and a total of 29 features were surveyed at Datalogger Site 2. The variation in the total number of surveyed features was determined by the lateral extent of patterned ground surrounding each datalogger station and the spatial resolution of the aerial photos of each site. Individual patterned ground features at Datalogger Site 2 were on average twice as large as patterned ground at Datalogger Site 1 (14.83 m^2 and 7.03 m^2, respectively). Correspondingly, the average slope across DS-2 was nearly twice that of DS-1 (1.413 deg. and 0.785 deg. respectively). The lower slope at DS-1 translated to a wider differential between feature orientation (173 deg off north) and the average slope aspect of the site (238 deg off north). The higher slope at DS-2 translated to nearly identical average feature orientations (148 deg) and average slope aspect (146 deg). The circularity of features at DS-1 (0.636) were similar though slightly more circular relative to the features at DS-2 (0.525) which were more elongated due to the steeper slope.

4.1.2 Aerial Observations of Polygonal Terrain

Ground conditions during the 17 August flight permitted photo documentation of patterned ground and polygonal terrain morphologies along a southwestwardly flight transect covering approximately 70 km of Devon Island's land area. A shallow ice-wedge polygon site located approximately 18 km southwest of FMARS was documented well enough to enable aerial photos to be georeferenced against a lower-resolution satellite image of Devon Island (Polygon Site 3 - PS-3). These polygons are similar in morphology to shallow polygons that were noted while conducting an early reconnaissance to identify patterned ground sites for additional study. Satellite imagery was utilized to measure features at PS-1 and PS-2. The PS-1, PS-2, and PS-3 measurements were projected onto the underlying 2m ArcticDEM of the area. Morphometric observations for these features are presented in Table 4-4 and histograms in Figure 4-7.

A total of 47 polygons were surveyed at PS-1; 11 polygons were surveyed at PS-2; and 10 polygons were surveyed at PS-3. On average, polygon centers at PS-1 were approximately 20.7 m in length with an average size of 13.3 m. The polygons at PS-2 are slightly larger relative to PS-1, with an average center length of approximately 32.6 m and 23 m in size. The polygon centers at PS-3 are quite large in comparison to the other sites. Center length is approximately 40.4 m across the long axis with a size of 30.7 m – twice as large as the polygons at PS-1 (Table 4-4).

4.2 Active Layer Datalogger Stations

4.2.1 Active Layer Soil Classifications

Samples were collected at each datalogger location to facilitate post-field analysis as needed. The samples are fully characterized along with all samples collected during the study in Table 4-5. In general, the collected samples indicate the presence of a poorly to well graded sand matrix across each patterned ground feature and represents the interstitial matrix among larger gravels and boulders within the feature. There was no strong correlation between the gravel fraction and location on the feature (margin vs center) of each sample, however this discrepancy is possibly tied to the size of gravels and boulders along the patterned ground margins that could not be collected for practical reasons. Larger gravels ranging from approximately 5 to 30 cm were observed along the feature margins at each datalogger site. The distribution of larger gravels along the margins translated to higher hydraulic conductivity that was detected in the moisture observations from the active layer datalogger stations.

Table 4-4 (Part 1 of 3)

Morphometric Observations												
Location	Feature ID	Notes	Vegetation	Width (m)	Length (m)	Long-Axis Orientation (°)	Slope Aspect (°)	Slope (°)	Perimeter (m)	Area (m²)	Size	Circularity
Datalogger Site 1	A		None	1.676	4.326	33.163	202.389	0.783	10.756	6.318	2.836	0.686
	B		None	2.058	3.718	155.907	201.588	1.004	10.079	7.06	2.998	0.873
	C		None	1.743	3.396	28.82	218.283	0.861	8.296	4.473	2.386	0.817
	D		None	1.357	2.375	16.064	141.770	0.315	6.176	2.537	1.797	0.836
	E		None	0.557	3.582	27.848	157.574	0.367	15.202	6.199	2.809	0.337
	F		None	1.286	5.993	172.322	203.056	1.039	14.523	9.104	3.405	0.542
	G		None	1.777	4.589	135.739	227.753	0.967	11.08	6.467	2.870	0.662
	H	Dataloggers	None	0.685	6.972	11.868	244.974	0.820	22.538	16.051	4.521	0.397
	I		None	0.721	4.258	169.163	279.749	0.357	14.213	7.233	3.035	0.450
	J		None	1.309	2.826	11.215	292.106	0.829	8.882	3.739	2.182	0.596
	K		None	1.353	4.019	126.29	329.308	0.592	9.927	4.18	2.307	0.533
	L		None	1.414	4.831	150.835	233.378	1.025	13.091	10.089	3.584	0.740
	M		None	1.588	4.818	149.109	254.619	1.158	12.387	7.353	3.060	0.602
	N		None	1.412	7.254	179.339	267.995	1.161	17.414	12.9	4.053	0.535
	O		None	1.181	1.589	158.839	320.347	0.499	4.926	1.812	1.519	0.938
	Center Averages		None	1.341	4.303	101.768	238.326	0.785	11.966	7.034	2.891	0.636
	Margin		None	--	--	--	228.510	0.833	66.084	187.256	--	--
Location	Feature ID	Notes	Vegetation	Width (m)	Length (m)	Long-Axis Orientation (°)	Slope Aspect (°)	Slope (°)	Perimeter (m)	Area (m²)	Size	Circularity
Datalogger Site 2	A		None	2.751	7.19	135.716	253.319	1.912	18.005	16.059	4.522	0.623
	AA		None	0.821	1.691	142.125	167.285	1.937	4.129	1.026	1.143	0.756
	B		None	2.659	11.259	161.122	243.660	1.217	31.06	43.857	7.473	0.571
	BB		None	0.922	21.993	145.239	170.450	1.631	67.562	36.274	6.796	0.100
	C		None	1.713	7.001	25.635	137.202	1.238	23.39	21.585	5.242	0.496
	CC		None	1.202	5.478	107.209	109.531	2.472	13.414	8.83	3.353	0.617
	D		None	0.464	7.831	47.028	112.784	2.568	22.358	15.164	4.394	0.381
	E		None	0.549	6.479	154.231	107.630	2.300	21.404	13.205	4.100	0.362
	F		None	1.484	4.596	156.507	130.113	1.475	14.188	12.606	4.006	0.787
	G		None	2.534	5.136	179.173	138.778	1.451	14.792	12.661	4.015	0.727
	H		None	1.473	8.307	3.508	129.367	2.001	25.625	22.313	5.330	0.427
	I		None	1.008	6.317	46.97	107.529	2.099	26.924	16.196	4.541	0.281
	J		None	2.17	4.279	159.726	93.717	1.790	10.729	6.961	2.977	0.760
	K		None	1.105	3.382	141.228	98.413	1.553	7.994	3.091	1.984	0.608
	L		None	1.677	2.803	150.336	114.340	1.283	7.195	3.47	2.102	0.842
	M		None	0.87	5.953	173.874	147.855	0.766	14.023	5.569	2.663	0.356
	N		None	0.742	3.981	168.182	212.246	0.758	9.684	3.863	2.218	0.518
	O		None	1.743	5.182	100.483	176.336	0.209	12.517	9.108	3.405	0.731
	P		None	1.311	9.775	144.347	256.481	1.288	23.48	24.813	5.621	0.566
	Q		None	1.173	3.484	133.399	284.647	1.297	8.663	4.346	2.352	0.728
	R		None	1.378	6.331	4.509	88.676	1.345	17.45	12.644	4.012	0.522
	S		None	1.138	6.296	132.818	138.493	1.602	16.634	10.732	3.697	0.487
	T		None	2.409	4.911	141.128	115.770	1.128	13.186	11.186	3.774	0.808
	U		None	1.634	9.452	134.183	113.584	0.825	9.156	5.039	2.533	0.755
	V		None	0.61	3.156	141.13	120.089	1.002	22.399	17.769	4.756	0.445
	W		None	0.514	13.655	136.1	148.465	1.269	7.575	1.978	1.587	0.433
	X		None	0.194	13.655	136.1	82.617	1.037	30.647	6.032	2.771	0.081
	Y		None	1.061	15.189	135.735	52.828	0.821	32.901	21.803	5.269	0.253
	Z	Dataloggers	None	2.789	13.135	144.683	196.730	0.697	32.526	62	8.885	0.736
	Center Averages		None	1.383	7.514	123.532	146.515	1.413	19.297	14.834	3.964	0.525
	Margin		None	--	--	--	--	1.401	172.838	702.647	--	--

Table 4-4 (Part 2 of 3)

Location	Feature ID	Notes	Vegetation	Width (m)	Length (m)	Long-Axis Orientation (°)	Slope Aspect (°)	Slope (°)	Perimeter (m)	Area (m²)	Size	Circularity
Polygon Site 1	A	Samples and Trenches	Moderate	13.6	24.378	162.736	145.934	1.373	64.355	249.458	17.822	0.757
	A1		Moderate	5.696	8.902	171.736	147.773	1.143	22.894	29.207	6.098	0.700
	B		Moderate	7.29	12.948	177.871	76.785	3.104	38.307	95.713	11.039	0.820
	B1		Moderate	8.421	14.709	23.048	133.221	0.326	41.78	119.94	12.358	0.863
	C		Moderate	8.329	19.046	99.073	213.182	1.717	55.998	206.403	16.211	0.827
	C1		Moderate	8.403	14.131	32.915	184.475	1.082	38.644	85.55	10.437	0.720
	D		Moderate	11.98	20.965	171.223	325.839	3.431	55.385	204.389	16.132	0.837
	D1		Moderate	9.672	20.067	168.828	196.719	0.770	52.534	166.195	14.547	0.757
	E		Moderate	8.305	25.885	162.289	104.186	1.132	68.693	316.5	20.074	0.843
	E1		Moderate	7.619	20.725	169.464	167.534	1.373	49.366	119.518	12.336	0.616
	F		Moderate	5.77	25.248	172.833	92.788	1.339	61.86	227.309	17.012	0.746
	F1		Moderate	7.81	22.631	170.865	182.831	1.729	64.79	262.71	18.289	0.786
	F1		Moderate	10.53	25.064	135.796	152.087	2.337	66.417	155.113	14.053	0.442
	G		Moderate	3.866	28.543	134.721	85.559	1.337	94.639	289.027	19.183	0.406
	G1		Moderate	9.901	18.007	154.065	152.250	2.154	49.177	150.683	13.851	0.783
	H		Moderate	11.988	26.875	72.295	124.879	1.428	70.235	317.344	20.101	0.808
	H1		Moderate	5.948	18.527	177.259	165.483	2.675	41.347	81.947	10.215	0.602
	I		Moderate	6.105	22.308	162.804	116.042	1.965	62.6	252.777	17.940	0.811
	I1		Moderate	5.108	24.645	147.23	168.348	2.391	74.385	209.647	16.338	0.476
	J		Moderate	5.843	20.39	64.239	102.104	1.448	57.259	192.596	15.660	0.738
	J1		Moderate	8.227	17.683	112.424	168.145	1.948	46.305	128.06	12.769	0.751
	K		Moderate	5.438	14.003	166.794	117.390	1.274	40.223	106.685	11.655	0.829
	K1		Moderate	11.778	19.828	51.451	135.050	1.928	57.191	200.714	15.986	0.771
	L		Moderate	5.403	20.723	1.089	142.649	1.126	59.043	189.786	15.545	0.684
	L1		Moderate	5.696	27.292	163.984	219.479	1.853	96.888	320.189	20.191	0.429
	M		Moderate	8.063	16.366	174.478	138.099	1.302	44.643	126.363	12.684	0.797
	M1		Moderate	11.146	23.332	160.915	143.855	1.522	63.7	260.826	18.223	0.808
	N		Moderate	11.93	25.812	81.885	108.729	1.181	68.309	302.367	19.621	0.814
	N1		Moderate	12.193	21.861	167.121	148.976	2.325	65.343	254.669	18.007	0.750
	O		Moderate	10.21	22.279	143.535	128.807	1.450	57.974	214.086	16.510	0.800
	O1		Moderate	4.963	22.832	12.448	163.476	3.755	51.267	77.245	9.917	0.369
	P		Moderate	10.415	19.523	37.419	132.210	1.635	51.363	165.514	14.517	0.788
	P1		Moderate	16.851	29.567	6.403	189.247	3.732	82.3	382.903	22.080	0.710
	Q		Moderate	5.982	18.593	16.612	125.602	1.893	51.874	163.382	14.423	0.763
	Q1		Moderate	11.772	26.822	17.404	153.367	2.749	66.218	223.678	16.876	0.641
	R		Moderate	12.517	19.811	145.323	153.411	2.159	54.629	179.872	15.133	0.757
	R1		Moderate	6.912	14.42	39.987	189.441	3.850	44.158	127.562	12.744	0.822
	S		Moderate	2.094	17.613	134.547	171.815	0.895	40.745	48.639	7.870	0.368
	S1		Moderate	9.681	17.613	134.547	193.069	3.459	71.4	279.042	18.849	0.688
	T		Moderate	5.767	25.24	134.131	110.973	0.780	41.981	91.961	10.821	0.656
	T1		Moderate	11.2	17.197	141.391	160.615	2.403	35.966	80.715	10.138	0.784
	U		Moderate	12.068	18.316	158.399	128.446	1.628	49.506	154.353	14.019	0.791
	V		Moderate	7.848	18.243	169.114	127.370	1.846	46.276	119.868	12.354	0.703
	W		Moderate	13.07	20.301	158.972	149.512	1.640	53.544	178.39	15.071	0.782
	X		Moderate	9.462	21.196	163.543	166.246	2.433	52.701	164.894	14.490	0.746
	Y		Moderate	10.26	23.517	157.998	128.370	1.922	59.687	207.63	16.259	0.732
	Z		Moderate	8.724	19.15	157.323	136.206	1.152	48.946	142.436	13.467	0.747
	Center Averages		Moderate	8.763	20.705	122.139	150.395	1.874	56.018	183.486	13.334	0.700
	Margin		Moderate	--	--	--	137.506958	1.720	2952.207	4450.161	--	--

Table 4-4 (Part 3 of 3)

Location	Feature ID	Notes	Vegetation	Width (m)	Length (m)	Long-Axis Orientation (°)	Slope Aspect (°)	Slope (°)	Perimeter (m)	Area (m²)	Size	Circularity
Polygon Site 2	2A		Sparse	21.661	22.768	152.844	199.427	4.610	66.045	302.146	19.614	0.870
	2B		Sparse	11.259	35.941	136.657	199.427	4.192	95.458	437.454	23.601	0.603
	2C		Sparse	16.903	35.628	138.703	199.427	3.435	88.516	483.355	24.808	0.775
	2D		Sparse	14.412	40.006	175.486	199.427	3.021	109.102	555.722	26.600	0.587
	2E		Sparse	29.03	32.068	63.351	199.427	2.703	90.895	516.541	25.645	0.786
	2F		Sparse	8.859	43.572	152.139	199.427	2.347	109.337	500.611	25.247	0.526
	2G		Sparse	18.925	23.037	52.033	199.427	2.320	65.313	299.264	19.520	0.882
	2H		Sparse	20.994	40.379	148.5	199.427	2.238	102.455	667.124	29.145	0.799
	2I		Sparse	12.635	19.584	170.437	199.427	1.927	49.831	154.983	14.047	0.784
	2J		Sparse	20.316	35.863	5.711	199.427	3.335	89.591	497.913	25.179	0.780
	2K		Sparse	14.811	30.008	19.195	199.427	4.024	77.331	301.187	19.583	0.633
	Center Averages		Sparse	17.255	32.623	110.460	199.427	3.105	85.807	428.755	22.999	0.730
	Margin		Sparse	--	--	--	199.427	3.099	405.129	6969.041	--	--
Location	Feature ID	Notes	Vegetation	Width (m)	Length (m)	Long-Axis Orientation (°)	Slope Aspect (°)	Slope (°)	Perimeter (m)	Area (m²)	Size	Circularity
Polygon Site 3	3A		Limited to None	15.722	40.779	65.254	231.439	0.571	102.601	583.464	27.256	0.696
	3B		Limited to None	22.076	44.077	67.355	122.625	0.407	123.347	979.37	35.312	0.809
	3C		Limited to None	22.942	42.574	35.218	120.018	0.535	105.734	646.016	28.680	0.726
	3D		Limited to None	20.559	46.172	86.219	111.866	0.552	108.535	662.121	29.035	0.706
	3E		Limited to None	30.045	59.991	140.231	158.076	0.872	158.719	1499.415	43.693	0.748
	3F		Limited to None	16.289	25.924	122.099	136.739	0.721	76.432	327.882	20.432	0.705
	3G		Limited to None	18.511	27.798	30.293	198.041	0.530	87.786	410.178	22.853	0.669
	3H		Limited to None	32.927	52.606	140.466	156.071	0.512	151.657	1520.949	44.006	0.831
	3I		Limited to None	16.818	25.503	22.551	180.847	0.386	84.898	438.097	23.618	0.764
	3J		Limited to None	26.16	38.079	45.478	170.321	0.738	112.172	822.892	32.369	0.822
	Center Averages		Limited to None	22.205	40.350	75.516	158.604	0.582	111.188	789.038	30.725	0.748
	Margin		Limited to None	--	--	--	157.330	0.614	1457.03	1237.312	--	--

4.2.2 Active Layer Datalogger Observations

Active layer diurnal temperature and moisture conditions were collected via the small-scale patterned ground dataloggers near FMARS. Active layer conditions from each datalogger station are detailed in Table 4-6 and Figures 4-8 and 4-9. The temperature gradient at each datalogger location was recorded during deployment and recorded in Table 4-7. The highest observed atmospheric temperature of 11.25°C occurred on 22 July 2017 was at the upper end of normal climate conditions for the summer in Resolute Bay, the closest location with aggregated historical climate data, located approximately 168 km to the west southwest. A secondary high temperature of 10.76°C occurred on 12 August and was followed by the lowest temperature of the monitoring period, which bottomed out at -2.07°C on 14 August following the passage of a cold front.

The average atmospheric relative humidity (RH) across the monitoring period was 92.87% and ranged from about 68.19% to 100%. The lowest RH of approximately 68% occurred on 23 July following the passage of a front that brought the first rain event of the period on 22 July and brought colder and drier conditions in its wake. A written log of weather observations was maintained and updated four times per day at regular intervals in order to relate atmospheric temperature and moisture measurements to prevailing weather conditions. The RH reached 100% on several occasions and often corresponded with periods of precipitation that mostly consisted of rain, however snow was observed on a few occasions. The relatively high atmospheric humidity is interpreted to be a result of the summertime polar maritime climate and a persistent weather pattern that generated several rain and snow events during the course of the field event.

The average active layer temperature across all measuring points at 0.45 m below ground surface (bgs) was 2.01°C, approximately 2.5°C cooler than the average observed atmospheric temperature of 4.58°C. The moisture content across all measuring points occurred within a narrow range averaging 0.3742 m^3/m^3 (37.42%) compared to the average atmospheric relative humidity of 92.87%. Minor fluctuations of the soil moisture content correspond well with observed rain events during the monitoring period. Samples collected at the datalogger sites and other locations throughout the HIS were observed to undergo thixotropic separation when exposed to vibration, such as when samples were transported back to FMARS on extended ATV rides and when soils were exposed to repeated motion or pressure while excavating trenches and sampling. The relative stability of the soil moisture observations indicate that the active layer just above the contact with permafrost was near a fully saturated condition throughout the entire monitoring period.

Table 4-5 (Part 1 of 2)

Patterned Ground Samples			Primary Constituents and Characteristics by USCS Field Methodology							
Location ID	Depth (m)	Location	Type	Munsell Color	Color Name	Plasticity	Stiffness	Grain Size	Grading	Proportion
DS-1A 20170719	0.45	Patterned ground center. Silty/gravel patterned ground fed by meltwater runoff	Sand	10YR7/3	Very Pale Brown	NA	Soft, no cohesion	1/8”-1/2” subrounded, fine grained	Poorly graded	99% sand, trace gravel
DS-1A 20170814	0	Patterned ground center. Silty/gravel patterned ground fed by meltwater runoff	Sand	10YR6/3	Pale Brown	NA	Soft, no to low cohesion	Fine grained, 1/8”-1/2” subrounded	Poorly graded	99% sand, trace gravel
DS-1B 20170719	0.35	Patterned ground margin. Silty/gravel patterned ground fed by meltwater runoff	Sand	10YR7/3	Very Pale Brown	NA	Soft, no cohesion	Fine grained, 1/8”-3/4” subrounded	Poorly graded	>95% sand, <5% gravel
DS-2A 20170719	0.45	Patterned ground margin. Sandy/gravel patterned ground fed by meltwater runoff	Sand/Gravel	10YR7/3	Very Pale Brown	NA	Soft, no cohesion	Fine grained, 1/4”-1.5” sunbangular	Well graded	>85% sand, <15% gravel
DS-2B 20170719	0.45	Patterned ground center. Sandy/gravel patterned ground fed by meltwater runoff	Sand/Gravel	10YR6/4	Light Yellowish Brown	NA	Soft, low cohesion	Fine grained, 1/4”-2” subangular to subrounded	Well graded	>90% sand, <10% gravel
DS-2B 20170814	0	Patterned ground center. Sandy/gravel patterned ground fed by meltwater runoff	Sand	10YR7/3	Very Pale Brown	NA	Soft, no cohesion	Fine grained, 1/8”-1/4” subrouneded	Poorly graded	99% sand, trace gravel
Background	0	Sandy ground just south of and in between Stations A and B. Non-patterned ground	Clay	10YR7/3	Very Pale Brown	Medium plasticity	Soft, medium cohesion	1/8”-1” rounded	Well graded	>90% clay, <10% gravel
PAS-1-1	0	PG Center – Surface	Gravel	5Y5/4	Olive	Non plastic	NA	1/8-1/2” subround	Well graded	>95% gravel, <5% coarse sand/silt
PAS-1-2	0.5	PG Center – 0.5 m bgs	Gravel	5Y5/4	Olive	Non plastic	NA	1/8-1/2” subangular	Well graded	>99%
PAS-2-1-Clay	0.55	PG Center – 0.5 m bgs	Gravel	10YR6/4	Light Yellowish Brown	Non plastic	NA	1/8-1” subround to subangular	Well graded	>95%
PAS-2-1-Gravel	0.55	PG Center – 0.5 m bgs	Gravel	10YR6/4	Light Yellowish Brown	Non plastic	NA	1/8”-1” subangular to angular	Well graded	>98%
PAS-2-2	0	PG Center – Surface	Gravel	10YR6/4	Light Yellowish Brown	Non plastic	NA	1/8”-1/2” sub rounded	Well graded	>85%
PAS-2-20 Normal	20	PG Center – 0.2 m bgs	Gravel	10YR6/4	Light Yellowish Brown	Non plastic	NA	1/8”-1” subround to subangular	Well graded	>98% gravel, <2% clay
PAS-2-20 Stain	20	PG Center – 0.2 m bgs	Gravel	10YR6/4	Light Yellowish Brown	Non plastic	NA	1/8”-3/4” rounded to subangular	Well graded	>98% gravel, <2% clay
PAS-2-50 Beneath Rock	50	PG Center – 0.5 m bgs	Gravel	10YR6/4	Light Yellowish Brown	Non plastic	NA	1/8”-1/2” sub angular	Well graded	>95% gravel, <5% clay
PAS-2-50 Beneath Margin	50	PG Margin – 0.5 m bgs	Gravel	10YR6/4	Light Yellowish Brown	Non plastic	NA	1/8”-2” subround to angular	Well graded	100.00%
PAS-3 Margin	0	PG Margin – Surface	Gravel	10YR5/2	Grayish Brown	NA- Dolomite	NA	1/4”-2” angular	Well graded	100.00%
PAS-3 Under Rock	0	PG Center – Surface	Gravel	10YR5/2	Grayish Brown	NA- Dolomite	NA	1/8”-1” subangular to angular	Well graded	100.00%
PAS-3-1	0.1	PG Center – 0.1 m bgs	Gravel	10YR5/3	Brown	NA	NA	1/4”-1” rounded to subrounded	Well graded	>80% gravel, <20% clay
PAS-3-2	0.2	PG Center – 0.2 m bgs	Gravel	10YR5/3	Brown	NA	NA	1/4”-1.5” rounded to subrounded	Well graded	>80% gravel, <20%clay/fines
PAS-3-3	0.3	PG Center – 0.3 m bgs	Gravel	10YR5/3	Brown	NA	NA	1/4”-3/4” subangular to subrounded	Well graded	>80% gravel, <20%clay/fines
PAS-3-4	0.4	PG Center – 0.4 m bgs	Sand/Gravel	10YR5/3	Brown	NA	NA	Fine to medium, 1/2”-1” rounded	Well graded sand, poorly graded gravel	>95% sand, <5% gravel
PAS-3-5	0.5	PG Center – 0.5 m bgs	Gravel	10YR5/3	Brown	NA	NA	1/4”-1.5” subangular to rounded	Well graded	>90% gravel, <10% sand
PAS-3-6	0.6	PG Center – 0.6 m bgs	Gravel	10YR5/3	Brown	NA	NA	1/4”-2” angular to rounded	Well graded	>90% gravel, <10% fines
PAS-3-7	0	PG Center – Surface	Gravel/Clay	10YR6/3	Pale Brown	Low plasticity	Soft, low cohesion	1/4”-1” subangular to rounded	Well graded	>80% gravel, <15% clay, <5% sands/fines
PSA-P1-0	0	Polygon Center – Surface	Clay	10YR5/4	Yellowish Brown	Low plasticity	Soft, no choesion	NA	NA	>90% clay, <10% fine sand
PSA-P1-10	10	Polygon Center – 0.1 m bgs	Sand	10YR5/4	Yellowish Brown	None	Soft, no cohesion	Fine	Poor	>80% sand, <20% silt
PSA-P1-20	20	Polygon Center – 0.2 m bgs	Sand	10YR5/4	Yellowish Brown	Low plasticity	Soft, no to low cohesion	Fine	Poor	>60% sand, <40% clay
PAS-P1-30	30	Polygon Center – 0.3 m bgs	Sand	10YR5/4	Yellowish Brown	None	NA	Fine-medium grained	Well graded	100.00%
PSA-P1-40	40	Polygon Center – 0.4 m bgs	Sand	10YR5/4	Yellowish Brown	Low plasticity	Soft, low cohesion	Fine-medium grained	Well graded	>60% sand, <40% clay
PSA-P1-50	50	Polygon Center – 0.5 m bgs	Sand	10YR5/4	Yellowish Brown	NA	NA	Fine-medium grained	Well graded	50.00%
PSA-P2	0	Polygon Midway	Clay	10YR5/4	Yellowish Brown	Medium plasticity	Soft, low cohesion	NA	NA	>90% clay, <10% fine sand
PSA-P3	0	Polygon Margin	Sand	10YR5/4	Yellowish Brown	Low plasticity	Soft, no cohesion	Fine	Poor	>90% sand, <10% clay
PSA-P3S-10	10	Polygon Margin – 0.1 m bgs	Peat	5YR2.5/2	Dark Reddish Brown	None	Soft, no choesion	NA	NA	100.00%
PSA-P3S-20	20	Polygon Margin – 0.2 m bgs	Peat	5YR2.5/2	Dark Reddish Brown	None	Soft, no choesion	NA	NA	100.00%
PSA-P3S-30	30	Polygon Margin – 0.3 m bgs	Peat	5YR2.5/2	Dark Reddish Brown	None	Soft, no choesion	NA	NA	100.00%
PSA-P3ST-0	0	Polygon Margin Trench – Surface	Clay	10YR5/4	Yellowish Brown	Low plasticity	Soft, no-low cohesion	Fine	poor	>80% clay, <20% sand
PSA-P3ST-10	10	Polygon Margin Trench – 0.1 m bgs	Sand	10YR4/4	Dark Yellowish Brown	NA	NA	Fine and 1” rounded	Poor	99% sand, trace gravel
PSA-P3ST-25	25	Polygon Margin Trench – 0.25 m bgs	Clay/Peat	10YR4/3	Brown	Medium plasticity	Soft, low cohesion	NA	NA	>75% clay, <25% peat
PSA-P3ST-50	50	Polygon Margin Trench – 0.5 m bgs	Peat	10YR3/2	Very Dark Grayish Brown	NA	Soft, low cohesion	NA	NA	100.00%

Table 4-5 (Part 2 of 2)

Patterned Ground Samples			Primary Constituents and Characteristics by USCS Field Methodology							
Location ID	Depth (m)	Location	Type	Munsell Color	Color Name	Plasticity	Stiffness	Grain Size	Grading	Proportion
PSA-P4-0	0	Polygon Trough	Clay	10YR4/4	Dark Yellowish Brown	Medium plasticity	Medium stiff, medium cohesion	NA	NA	100.00%
PSA-P4-10	10	Polygon Trough – 0.1 m bgs	Clay	10YR5/4	Yellowish Brown	High plasticity	Very stiff, medium cohesion	NA	NA	>90% clay, <10% fine sand
PSA-P4-20	20	Polygon Trough – 0.2 m bgs	Clay	10YR5/4	Yellowish Brown	Medium to high plasticity	Medium stif, medium cohesion	NA	NA	>80% clay, <20% fine sand
PSA-P4-30	30	Polygon Trough – 0.3 m bgs	Clay	10YR5/4	Yellowish Brown	Medium plasticity	Medium stiff, low cohesion	NA	NA	>75% clay
PSA-P4-40	40	Polygon Trough – 0.4 m bgs	Clay	10YR5/4	Yellowish Brown	Medium plasticity	Medium stiff, low cohesion	NA	NA	>75% clay
PSA-P4-50	50	Polygon Trough – 0.5 m bgs	Clay	10YR5/4	Yellowish Brown	High plasticity	Medium stiff, low cohesion	NA	NA	>75% clay
PSA-P5	0	Polygon Margin	Clay	10YR4/3	Brown	Low plasticity	Soft, low cohesion	Fine sand	Poor	>60% clay, <40% sand
PSA-P6	0	Polygon Corner	Peat	10YR3/4	Dark Yellowish Brown	None	Soft, no cohesion	NA	NA	>60% peat
PSA-P7	0	Polygon Corner	Peat	7.5YR2.5/2	Very Dark Brown	None	Soft, no cohesion	NA	NA	>90% peat, <10% fine sand
PSA-P8	0	Polygon Trough Intersection	Clay	10YR4/3	Brown	Low plasticity	Soft, medium cohesion	NA	NA	>95% clay, <5% find sand/silt
PSA-P9	0	Polygon Midway	Clay	10YR5/3	Brown	Medium plasticity	Medium stiff, low-medium cohesion	NA	NA	>90% clay, <10% fine sand
PSA-T1	0	Hill at northwest end of transect above polygon field	Clay	10YR6/2	Light Brownish Gray	High plasticity	Very stiff, high cohesion	NA	NA	100.00%
PSA-T2	0	Northwest bank of stream	Clay	10YR5/3	Brown	High plasticity	Very stiff, high cohesion	NA	NA	100.00%
PSA-T3	0	Mid-stream	Clay	10YR4/3	Brown	Medium plasticity	Medium stiff, medium cohesion	NA	NA	>80% clay
PSA-T4	0	Southeast bank of stream	Clay	10YR5/4	Yellowish Brown	High plasticity	Medium stiff, high cohesion	NA	NA	100.00%
PSA-T5	0	Polygon margin, along the northwestern edge of the polygon field	Clay	10YR5/3	Brown	High plasticity	Medium stiff, high cohesion	NA	NA	100.00%
PSA-T6	0	Polygon center	Clay/Silt	10YR4/4	Dark Yellowish Brown	Medium plasticity	Medium stiff, low cohesion	NA	NA	50/50
PSA-T7	0	Intersection of polygon margins	Silt	10YR4/6	Dark Yellowish Brown	Low plasticity	Soft, no cohesion	1/4"-1.5" subrounded	Well graded	>95% silt, <5% gravel
PSA-T8	0	Polygon margin, along the southeastern edge of the polygon field	Clay	10YR4/3	Brown	High plasticity	Low stiff/soft, high cohesion	NA	NA	99% clay with trace fine sand
PSA-T9	0	Mid-stream	Gravel	10YR4/3	Brown	NA	NA	Coarse sand to 1", subround	Well graded	>90% gravel, <10% sand
PSA-T10	0	Southeast bank of stream	Clay	10YR5/4	Yellowish Brown	High plasticity	Medium stiff, high cohesion	NA	NA	100.00%
PSA-T11	0	Hill at southeast end of transect above polygon field	Gravel	10YR4/3	Brown	NA	NA	1/8"-1", subangular to subrounded	Well graded	>95% gravel, <5% clay
PSA-Dessicated Crust-Margin	0	Desiccation “polygon” margin	Clay	10YR5/4	Yellowish Brown	Medium plasticity	Low stiff, medium cohesion	NA	NA	>98% clay, <2% gravel
PSA-Dessicated Crust-Center	0	Desiccation “polygon” center	Clay	10YR5/4	Yellowish Brown	Low plasticity	Soft, medium cohesion	NA	NA	>98% clay, <2% gravel

Notes

DS = Datalogger Site
FMARS = Flashline Mars Arctic Research Station
MWS = Meltwater Streak
PAS = Phoenix Analog Site
PSA = Polygon Site A
P-# = Polygon Sample Number
T-# = Transect Sample Number

Table 4-6 (Part 1 of 3)

Meltwater Streak and Datalogger Station Soil Measurements									
Location ID	**Date**	**Time**	**Depth (m)**	**Soil pH**	**Water pH**	**Percent Moisture**	**Temperature (ºC)**	**Electrical Conductivity (mS/cm)**	**Visible Moisture**
DS-1A	07/19/2017	1335	0.45	6.8	NA	50	1.9	0.06	Wet
	07/20/2017	1439	0	6.8	NA	65	7.7	0.05	Moist
	07/23/2017	1410	0	NA	7.0	NA	NA	NA	Underwater
DS-1B	07/19/2017	1315	0.35	6.8	NA	55	1.3	0.06	Wet
	07/20/2017	1442	0	6.2	NA	65	6.4	0.05	Wet
	07/23/2017	1415	0	NA	6.0	NA	NA	NA	Underwater
Background	07/20/2017	1515	0	6.6	NA	45	7.1	0.02	Dry
	07/23/2017	1421	0	NA	NA	NA	NA	NA	Dry
DS-2A	07/19/2017	1420	0.45	6.8	NA	40	0.8	0.05	Wet
	07/20/2017	1459	0	7.0	NA	30	7.1	0.03	Moist
	07/23/2017	1427	0	NA	6.0	NA	NA	NA	Underwater
DS-2B	07/19/2017	1405	0.45	7.0	NA	30	0.7	0.03	Wet
	07/20/2017	1504	0	6.8	NA	40	6.9	0.02	Moist
	07/23/2017	1431	0	NA	NA	NA	NA	NA	Moist
MWS-1	07/20/2017	1410	0	6.6	NA	55	3.3	0.05	Wet/Water on Surface
	07/23/2017	1348	0	NA	6.0	NA	NA	NA	Wet/Water on Surface
MWS-2	07/20/2017	1422	0	6.4	NA	50	7	0.03	Wet/Water on Surface
	07/23/2017	1353	0	NA	6.0	NA	NA	NA	Underwater
MWS-3	07/20/2017	1428	0	6.4	NA	50	7.4	0.03	Wet
	07/23/2017	1358	0	NA	5.0	NA	NA	NA	Underwater
MWS-4	07/20/2017	1436	0	6.8	NA	50	7.8	0.04	Moist
	07/23/2017	1403	0	NA	6.0	NA	NA	NA	Underwater
MWS-5	07/20/2017	1520	0	7.0	NA	30	8.1	0.04	Moist
	07/23/2017	1436	0	NA	6.0	NA	NA	NA	Underwater

Table 4-6 (Part 2 of 3)

Phoenix Analog Sites – Patterned Ground Soil Measurements

Location ID	Date	Time	Depth (m)	Soil pH	Water pH	Percent Moisture	Temperature (ºC)	Conductivity (mS/cm)	Visible Moisture
PAS-1-1	07/25/2017	1533	0	6.8	NA	80	5.4	0.04	Moist
PAS-1-2	07/25/2017	1536	0.5	7.0**	NA	0**	1.3	0.01	Wet/Gravel
PAS-2-1-G	07/26/2017	1506	0.55	NA	NA	NA	1.6	0.08	Underwater/ Gravel
	07/26/2017	1509	0.55	NA	6.0	NA	NA	NA	Underwater/ Gravel
PAS-2-1-C	07/26/2017	1527	0.55	NA	NA	NA	1.7	0.04	Underwater/ Clay
PAS-2-2	07/26/2017	1507	0	6.4	NA	65	5.9	0.10	Moist
PAS-3-1	08/07/2017	1352	0.1	6.9	NA	30	5.5	0.01	Moist***
PAS-3-2	08/07/2017	1402	0.2	6.8	NA	25	4.1	0.03	Moist***
PAS-3-3	08/07/2017	1413	0.3	6.6	NA	40	4.0	0.02	Moist***
PAS-3-4	08/07/2017	1428	0.4	6.6	NA	40	3.0	0.02	Moist***
PAS-3-5	08/07/2017	1441	0.5	6.8	NA	30	2.5	0.04	Moist***
PAS-3-6	08/07/2017	1500	0.6	6.7	NA	40	1.1	0.03	Moist***
PAS-3-7	08/07/2017	1502	0	6.9	NA	30	6.6	0.01	Moist***

Table 4-6 (Part 3 of 3)

Polygon Soil Measurements									
Location ID	**Date**	**Time**	**Depth (m)**	**Soil pH**	**Water pH**	**Percent Moisture**	**Temperature (ºC)**	**Conductivity (mS/cm)**	**Visible Moisture**
P-1-0	08/09/2017	1645	0	6	NA	80	6	0.15	Moist
P-1-10	08/09/2017	1646	0.1	6.4	NA	60	5.4	0.08	Moist
P-1-25	08/09/2017	1647	0.25	6.6	NA	50	3.3	0.06	Moist
P-1-50	08/09/2017	1648	0.5	6.6	NA	50	0.7	0.06	Moist
P-2	08/09/2017	1649	0	5.6	NA	100*	5.4	0.21	Moist
P-3	08/09/2017	1650	0	6.0	NA	100*	5.6	0.15	Moist
P-4-0	08/09/2017	1651	0	5.8	NA	100*	5.2	0.21	Moist
P-4-10	08/09/2017	1653	0.1	5.4	NA	100*	3.7	0.31	Wet
P-4-25	08/09/2017	1654	0.25	5.4	NA	100*	2.1	0.23	Wet
P-4-50	08/09/2017	1655	0.5	5.3	NA	100*	0.2	0.48	Saturated
P-5	08/09/2017	1700	0	6.4	NA	70	5.8	0.05	Moist
P-6	08/09/2017	1701	0	6	NA	100*	5.9	0.36	Moist
P-7	08/09/2017	1658	0	6	NA	100*	5.6	1.06	Moist
P-8	08/09/2017	1659	0	5.4	NA	100*	5.5	0.30	Moist
P-9	08/09/2017	1657	0	5	NA	100*	5.5	0.80	Moist

Notes

* - Kelway pegged out past 100% moisture content on these readings. P-5 reading was towards the end of the measurements and seemed normal and verification with locations in P-1 were similar to original readings.

** - Gravel was measured using soil Kelway pH/moisture probe that requires firm contact with silt or clay for accurate readings. There was not enough soil matrix in the gravel for these field readings to be considered accurate.

*** - Samples were moist on collection, but on arrival to FMARS they had compacted and the water had separated out through a suspected thyxiotropic process that resulted from vibrations induced by rough ATV trail conditions. This would indicate that the samples were at their saturation point when collected and that the measured moisture content is probably lower than the actual moisture state at collection.

DS = Datalogger Site

MWS = Meltwater Streak

NA – Not Available – data point not collected due to either environmental or equipment limitations

PAS = *Phoenix* Analog Site

PSA = Polygon Site A

P-# = Polygon Sample Number

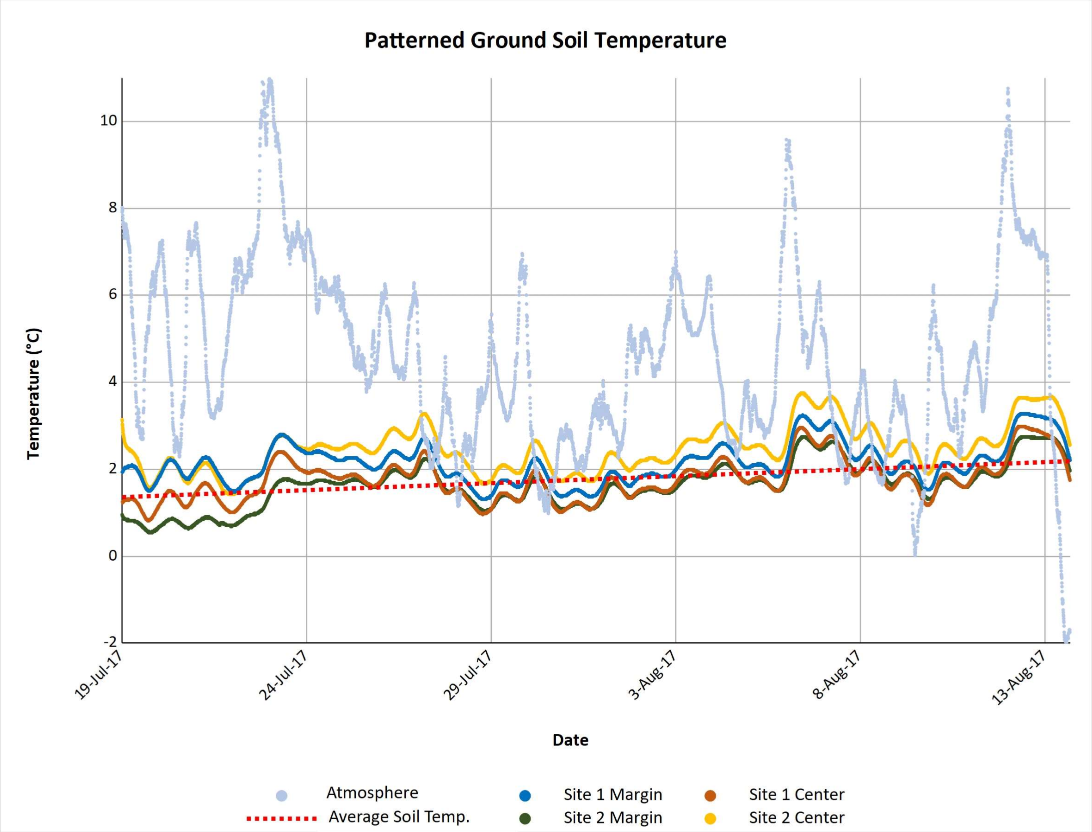

Figure 4-8 – Patterned Ground Soil Temperature. Datalogger temperature observations from Stations 1 and 2. Diurnal temperature trends are evident and there was an approximately 5 to 7 hour lag in temperature response between atmospheric fluctuations detected at the surface and the corresponding temperature change from the temperature sensors at the active layer-permafrost boundary approximately 0.35 to 0.45 meters bgs. The final drop in air temperature prior to retrieval represents the passage of a cold front that brought temperatures below zero for the only sustained period of the study.

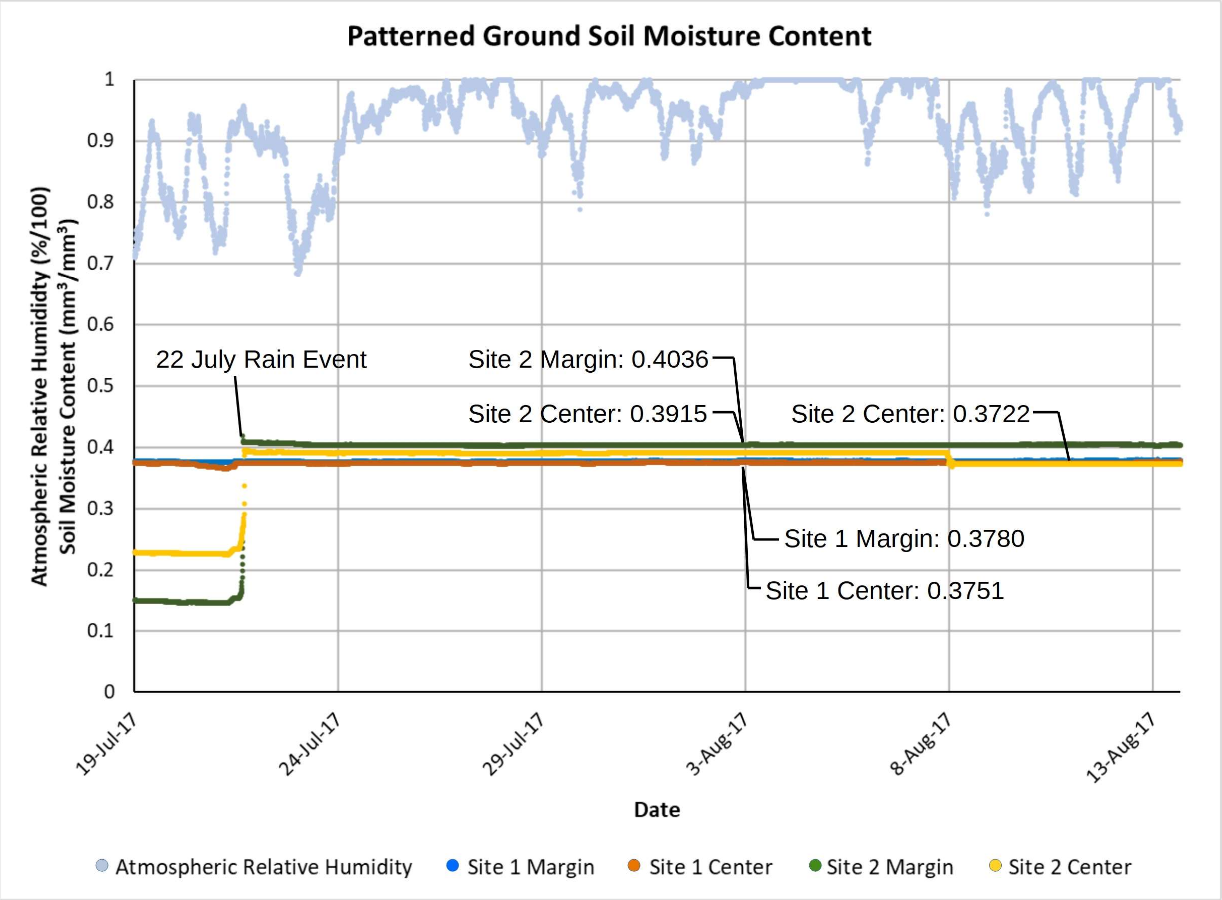

Figure 4-9 – Patterned
Ground Soil Moisture Content. Datalogger moisture observations from Stations 1 and 2 relative to atmospheric relative humidity. All of the soil moisture dataloggers recorded saturated conditions of approximately 0.37 to 0.40 mm^3/mm^3 for the majority of the observational period. Fluctuations at Station 2 represent an influx of water moving downgradient along a slopewash streak during a rain event on 22 July.

4.3 In-Situ Thermal Observations and Sampling

4.3.1 “*Phoenix* Analog” Patterned Ground Sites

Results are summarized in Table 4-6 and sample descriptions associated with each in-situ measurement point are described in Table 4-5. Since measurements were recorded over the span of peak summertime heating on Devon Island, the active layer was in an observed state of expanding saturation with depth throughout the period that made sustained direct measurements at the permafrost/active layer boundary difficult.

The average depth to permafrost across all sites was observed to be near 0.54 m below ground surface (bgs) with a range of 0.35 to 0.45 m near the start of the field event to 0.50 to 0.60 m at the end of the field event. An average of pH = 6.2 was observed across all sample locations. Average electrical conductivity was observed to be 0.18 mS/cm. When observed, standing water in trenches had an average pH = 6.0.

An average active layer temperature of 4.01°C was observed across all sites from the near surface (0.10 m) to the local permafrost contact. The temperature gradient was recorded across the sites and the estimated depth to permafrost was compared to the observed depth based on temperature and the presence of ice. The temperature gradients are detailed in Table 4-7 and a detailed temperature profile from PAS-3 is displayed in Figure 4-10. Soil samples were collected at each field measuring point and transported to the lab for further analysis following the conclusion of the Mars 160 simulation. Soil classification descriptions are provided for each sample in Table 4-5 following USCS methodologies. Located within fluvio-glacial deposits, the *Phoenix* Analog Sites were predominantly gravel-rich with lesser fractions of sand and clay occupying interstitial space between gravels. This helps to explain the higher hydraulic conductivity observed at the active layer-permafrost contact that resulted in standing water accumulating at the base of trenches excavated at PAS-2 and PAS-3.

Table 4-7

Thermal Gradient/Permafrost Depth Calculations

Location ID	Date	Depth (m)	Temperature (ºC)	Gradient (ºC/m)	Estimated Permafrost Depth (m)	Depth/Permafrost Difference (m)
A-1	07/19/17	0.45	1.9	12.89	0.60	0.15
	07/20/17	0	7.7			
A-2	07/19/17	0.35	1.3	14.57	0.44	0.09
	07/20/17	0	6.4			
C-3	07/19/17	0.45	0.8	14	0.51	0.06
	07/20/17	0	7.1			
C-4	07/19/17	0.45	0.7	13.78	0.50	0.05
	07/20/17	0	6.9			
PHX-1	07/25/17	0.5	1.3	8.2	0.66	0.16
	07/25/17	0	5.4			
PHX-2	07/26/17	0.55	1.6	7.82	0.75	0.20
	07/26/17	0	5.9			
PHX-3	08/07/17	0.6	1.1	9.17	0.72	0.12
	08/07/17	0	6.6			

Thermal Gradient and Permafrost Depth Calculations and Confirmation

Location ID	Date	Depth (m)	Temperature (ºC)	Gradient (ºC/m)	Estimated Permafrost Depth (m)	Measured Depth to Permafrost (m)
PSA-P1	08/10/17	0	6	10.60	0.57	0.55
	08/10/17	0.5	0.7			
PSA-P3	08/10/17	0	5.6	10.30	0.50	0.50 (near margin) To 0.55 (near PSA-P3-0)
	08/12/17	0.55	NM			
PSA-P4	08/10/17	0	5.2	10.00	0.52	0.50
	08/10/17	0.5	0.2			

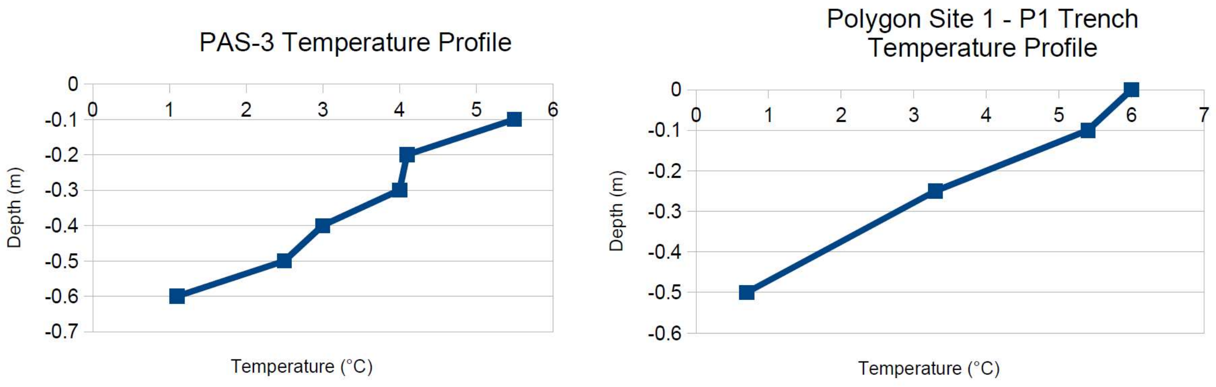

Figure 4-10 – Trench Temperature Gradients. A comparison of the observed temperature profiles in trenches excavated at PAS-3 and Polygon Site 1. Over the relatively small depth interval, the temperature profiles follow a nearly linear trend from the surface to the permafrost contact with the active layer.

4.3.2 Ice-Wedge Polygons

Larger ice-wedge polygons were generally composed of finer-grained silts, sands, and clays that are typical of the lacustrine deposits in the Haughton Formation. Samples collected at PS-1 demonstrate that the centers were largely composed of sand and clay mixtures and the margins extending into the troughs were composed of clay and peat (Table 4-5). The site location between two creeks means the area is apparently susceptible to high water events and flooding, with standing water evident during two separate visits to the site on non-consecutive days. A variety of small woody shrubs (arctic willow) appeared to preferentially to occupy the polygon high centers with flowering plants and grasses occupying the lower-lying troughs. It is possible that the variable thickness and penetration of roots from different plant species could provide variable controls on polygon erosion and degradation.

Polygon morphology at PS-1 was varied, but the majority comprised high centered polygons with scarps abruptly dropping approximately 1 to 1.5 m from the centers to the adjacent margins (Figure 4-11). In-situ measurements are presented in Table 4-6. Permafrost was encountered at a near uniform depth of approximately 0.5 m during trenching and sampling activities. Distinct soil horizons were observed in a trench excavated along the margin of one polygon where cryoturbation has resulted in the upturning of clay and peat into the sand-rich polygon center (Figure 4-12).

While samples were only collected at PS-1, a brief traverse across PS-2 highlighted the contrast in composition across features between the two sites (Figure 4-4 – images B and D). PS-2 is uniformly composed of a clay/gravel admixture that makes for difficult travel by foot and has a storied reputation for bogging down wayward all-terrain vehicles. The shallow transition from polygon centers to margins at PS-2 is subtle and comparable to shallow polygons along the distal edge of PS-1 (Figure 4-11, Image B). PS-3 was only viewed from the air on the departure flight leaving Devon Island and it appears to have a predominantly clay surface composition, similar to PS-2 (Figure 4-4).

4.4. Post-Field Thermal Measurements of Samples

Laboratory-collected thermal conductivity, specific heat capacity, and diffusivity measurements were recorded for most confirmation samples collected at in-situ measuring points within excavated trenches. These results are summarized in Table 4-8. Average thermal conductivity values of 0.6711 W m^{-1} K^{-1}, heat capacity of 1.62 x 10^6 J m^{-3} K^{-1}, and electrical conductivity of 0.13 mS cm^{-1} were observed across all of the patterned ground and ice-wedge polygon sites. These results are compared to the average thermal properties measured by the *Phoenix* spacecraft in Table 4-8. A full tabulation of the laboratory thermal measurements are provided in Appendix A.

Table 4-8

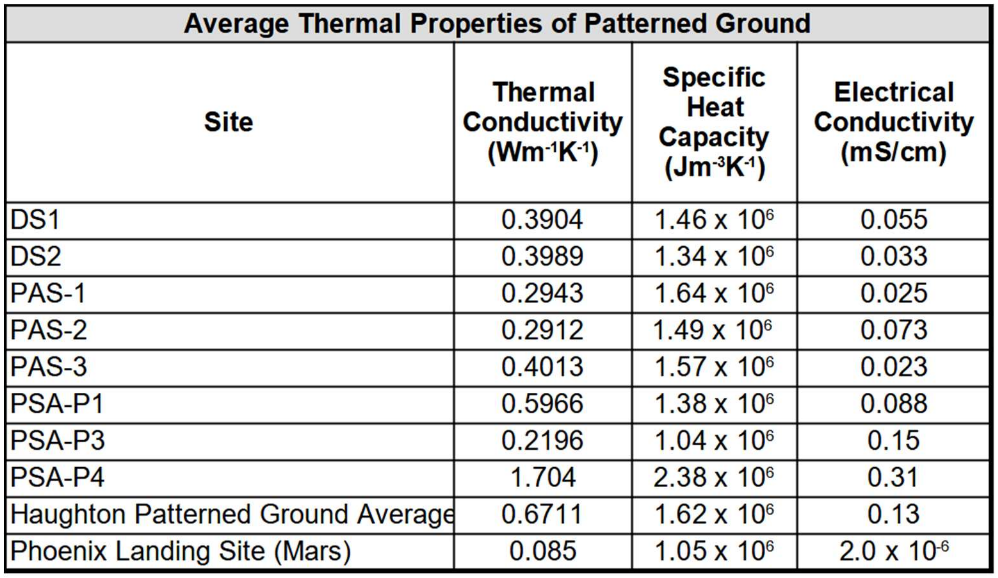

Average Thermal Properties of Patterned Ground

Site	Thermal Conductivity ($Wm^{-1}K^{-1}$)	Specific Heat Capacity ($Jm^{-3}K^{-1}$)	Electrical Conductivity (mS/cm)
DS1	0.3904	1.46 x 10^6	0.055
DS2	0.3989	1.34 x 10^6	0.033
PAS-1	0.2943	1.64 x 10^6	0.025
PAS-2	0.2912	1.49 x 10^6	0.073
PAS-3	0.4013	1.57 x 10^6	0.023
PSA-P1	0.5966	1.38 x 10^6	0.088
PSA-P3	0.2196	1.04 x 10^6	0.15
PSA-P4	1.704	2.38 x 10^6	0.31
Haughton Patterned Ground Average	0.6711	1.62 x 10^6	0.13
Phoenix Landing Site (Mars)	0.085	1.05 x 10^6	2.0 x 10^{-6}

Figure 4-13 provides a breakdown of the thermal conductivity (K), diffusivity (D), and specific heat capacity (C) measurements of the samples relative to feature type, composition, and depth of sample collection. Sample composition was the strongest factor controlling variations in thermal properties. Clay (generally associated with the larger ice-wedge polygons) registered consistently higher thermal conductivity, diffusivity, and specific heat capacity measurements. While there was some interplay among sand and gravel samples, the thermal properties of gravel-rich hummocks and sand-rich polygon centers were similar across all metrics. Figure 4-14 provides a comparison of the field and laboratory-measured thermal properties of the patterned ground sites. Samples collected at the Datalogger Sites exhibited the most consistent field and laboratory-derived metrics across the depth profile.

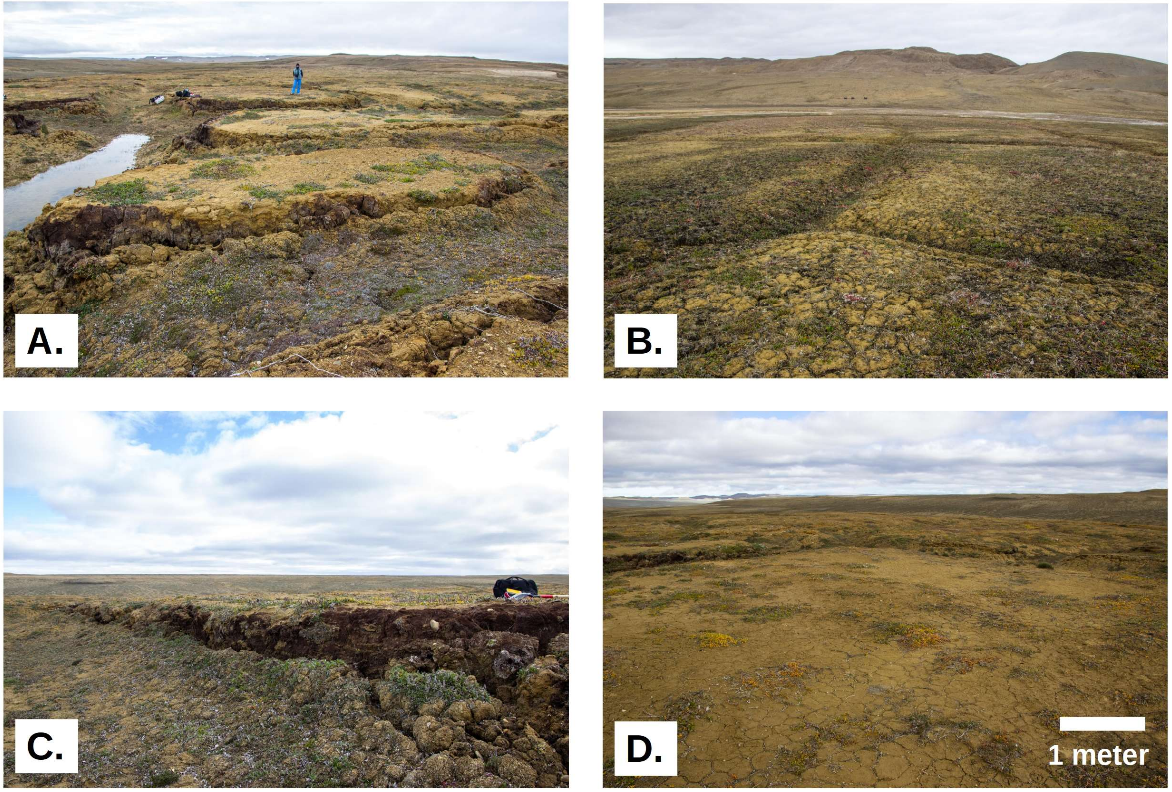

Figure 4-11 – Polygon Site 1 Morphology. A.) Several polygons are visible extending from the foreground towards the horizon. Ponding water is visible in the polygon margin (trough) on the left-hand side of the image. Mars 160 crew member Anastasiya Stepanova for scale. B.) Subdued polygon morphology along a distal portion of the site. C.) View looking southeast towards the northern margin of Polygon A – the primary polygon that was the target of trenching and sampling activities. D.) View looking northeast across the center of Polygon A. Small dessication polygons are visible across the surface and were ubiquitous across the observed polygon centers. Vegetation was prevalent throughout the polygon site.

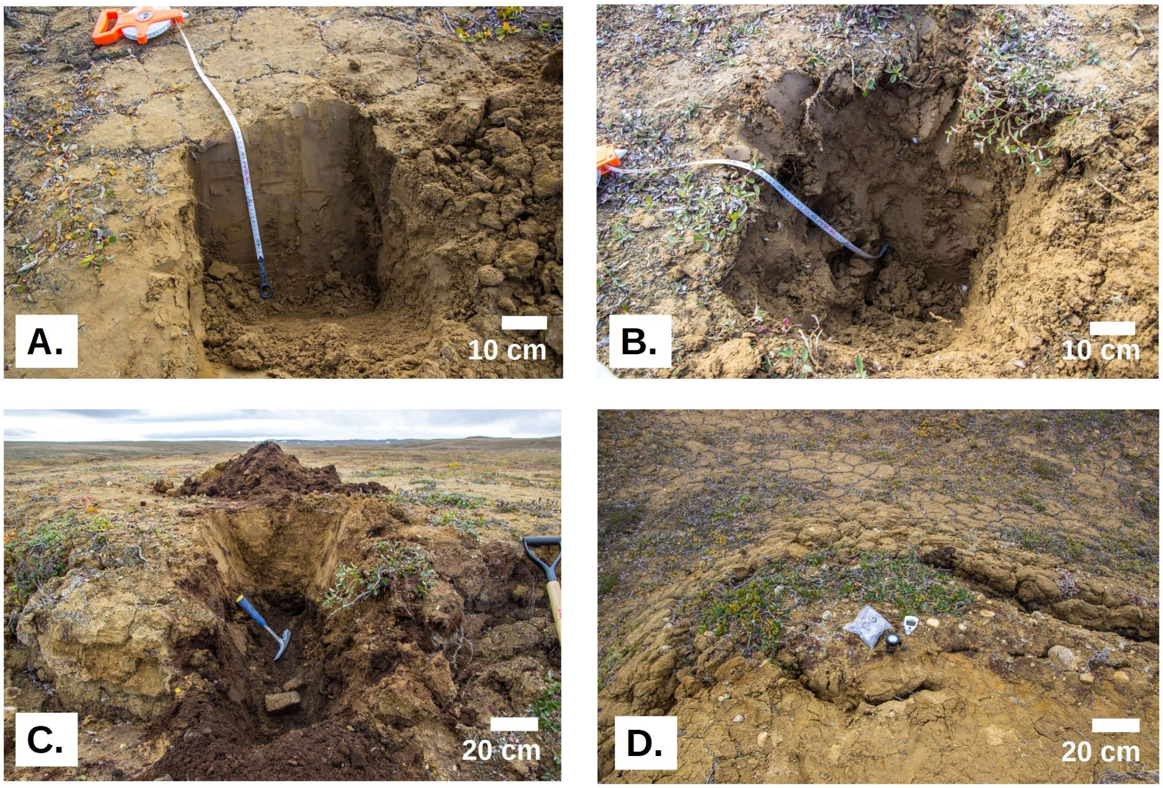

Figure 4-12 – Polygon Site 1 Trenching and Sampling Photos. A.) Trench excavated into the center of Polygon A and the collection of sample PSA-P1. Permafrost contact at 0.5 m bgs. B.) Trench excavated in the trough north of Polygon A and the collection of sample PSA-P4. Permafrost contact at 0.5 m bgs. C.) Trench excavated along the marginal slope leading from the Polygon A center towards the northern trough. The permafrost contact reflected the ground surface gradient and maintained a consistent, curved profile approximately 0.5 to 0.55 m bgs across the trench. D.) The location of sample PSA-P6 with the Hanna temperature/electrical conductivity and Kelway pH probes shown in a deployed configuration collecting in-situ measurements.

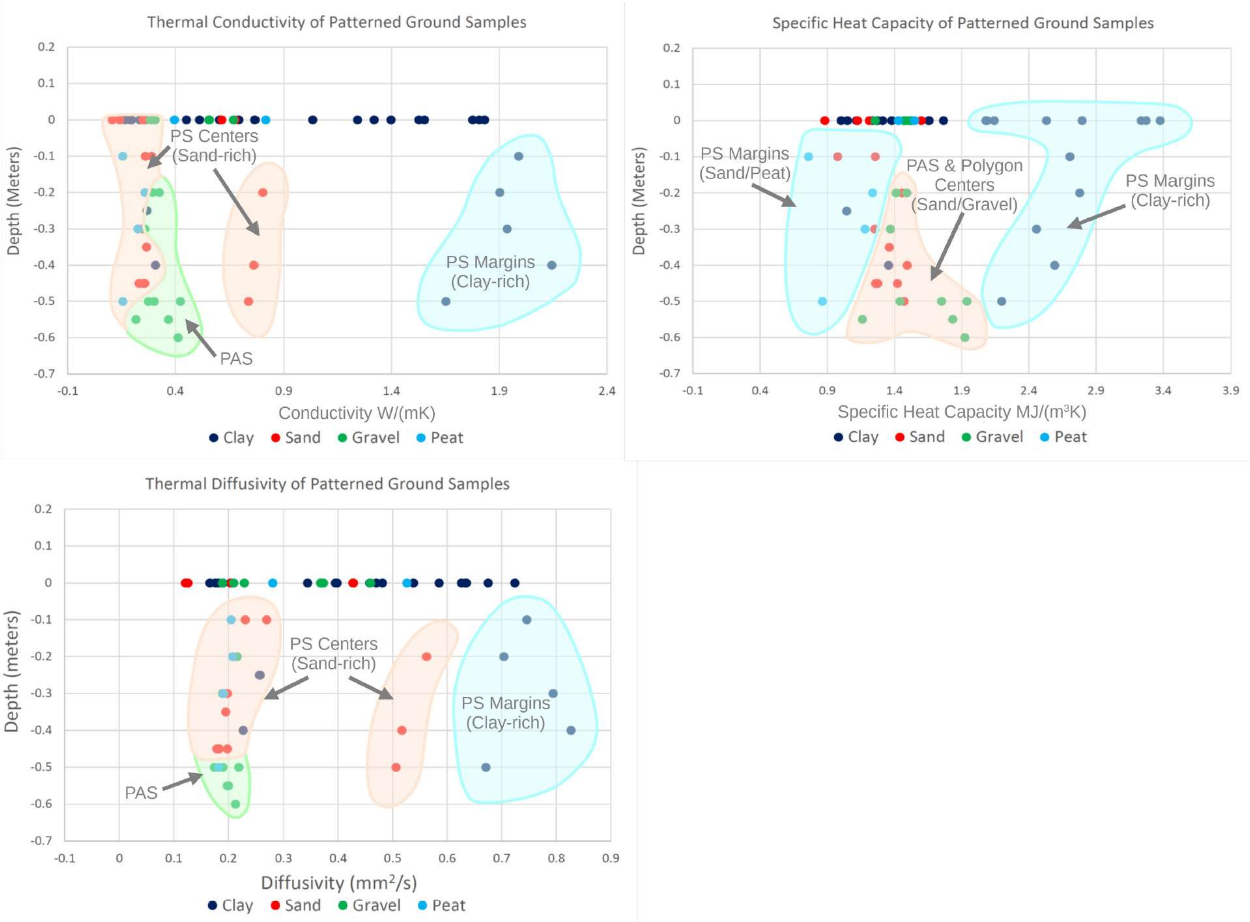

Figure 4-13 – Thermal Properties (Lab Measured) Relative to Feature Morphology. The distribution of laboratory measured thermal properties of samples collected at patterned ground and ice-wedge polygon locations within the Haughton Impact Structure. While the general distribution of laboratory-measured thermal properties could remain similar relative to theoretical field-measured thermal properties, the exact values will differ due to variations in moisture content, pore space (soil compaction), and prevailing environmental conditions at the time of measurement, including atmospheric temperature and relative humidity. While no firm conclusions can be derived from this dataset in its present form, it is hoped that by making the data freely available it can serve as a comparative dataset to future field-collected measurements or provide input values for future modeling efforts. Tabulated data is presented in full in Appendix A.

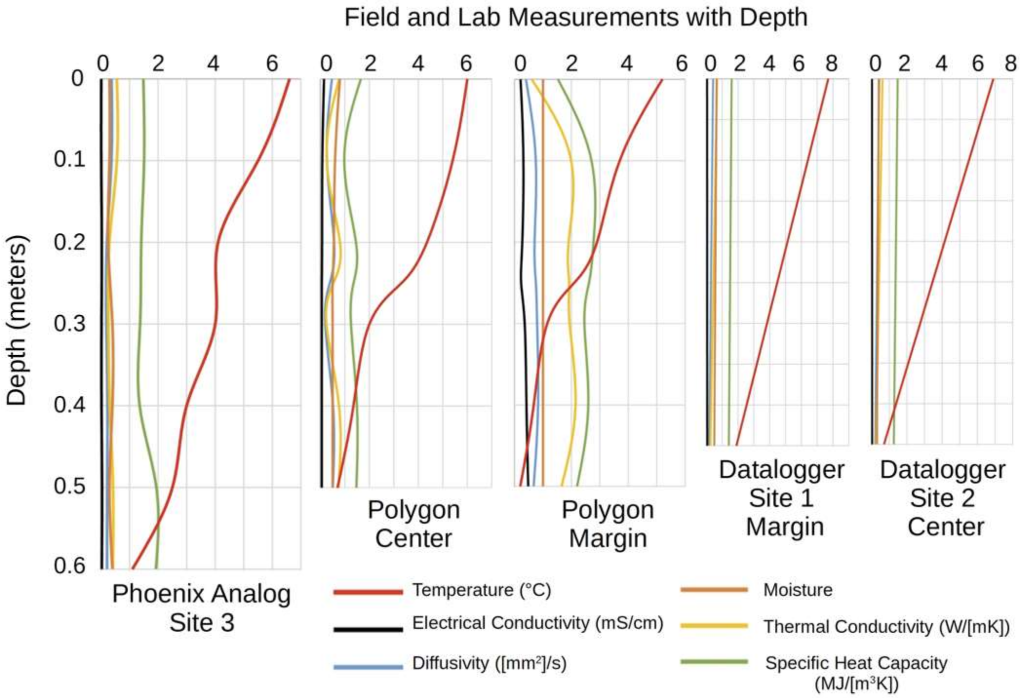

Figure 4-14 – Thermal Properties with Depth. A comparison of field-measured (in-situ) temperature, electrical conductivity, and moisture with the laboratory-measured thermal conductivity, diffusivity, and specific heat capacity of samples collected at each location.

5. Discussion

5.1 Morphometric Observations

Aerial and satellite imagery overlying the 2m ArcticDEM were used to support the morphometric characterization of patterned ground at the datalogger sites and the ice-wedge polygon sites within and near the HIS. In general, both smaller scale patterned ground and larger ice-wedge polygons were shown to have a mean long axis orientation that were approximately similar to the mean slope aspect of the study sites. The morphometric observations as a whole were similar to those collected in a previous field analog study in Svalbard by Ulrich et al (2011). Deriving finer-scale measurements of the micromorphologies of the features presented here would require the collection of high resolution imagery or performing a surface LiDAR survey of the study sites.

5.2 Thermal Observations

An early objective of the field study was to collect thermal analog measurements corresponding to data collected during the *Phoenix* mission to Mars. The results of these observations are informative of the approximate properties of the soil conditions and how they relate to feature morphology. While the thermal properties relative to feature morphology displayed in Figure 4-13 could remain similar relative to theoretical field-measured thermal properties, the exact values will differ due to variations under actual field conditions. The application of this dataset to *Phoenix* observations can serve as a starting point for analog comparisons, however more data would need to be collected in the field under varying seasonal conditions and states of active layer evolution. A comparative dataset from a hyperarid polar environment such as the Antarctic Dry Valleys would also be informative for a full comparison to the *Phoenix* dataset to be made.

5.3 Slopewash Streaks and Patterned Ground – Slope Streak or RSL Connection?

The connection between patterned ground and gullies on Mars has been a well-researched topic over the past decade (Levy et al, 2009; Gallagher et al, 2011), however a potential association (or lack thereof) between patterned ground and slope streaks and RSL has not been extensively explored. The utilization of the slopewash streaks below FMARS as Mars analogs are discussed in Clarke et al. 2018. The observation of biological communities (biofilms) growing on the surface of gravels within the slopewash streak underlies potential astrobiological implications if water or water-brines are involved in the formation of recurring-slope linea (RSL) or slope streaks on Mars.

One variation of the wet-origin hypothesis for RSL formation suggests that the absorption and melting of near-surface ground ice results in percolating surface flows of water brine that are metastable for brief periods of time under favorable eutectic temperature (T_e) conditions (McEwen et al., 2011). The resulting hypothetical brine flows discolor the surface by either wetting the regolith or by triggering the downslope movement of overlying light-colored regolith and subsequent exposure of darker-colored underlying regolith. The initially darker streaks fade with time as lighter-colored dust is deposited across the surface until a new RSL streak appears and the cycle is repeated.

As detailed in Clarke et al, 2018, the slopewash streaks below FMARS in Haughton Crater exhibited a similar behavior of darkening and lightening over the course of the simulation. The color changes in the slopewash streaks were due to three observed factors: moisture content (wet or dry), changes in sediment loading within the water flowing downslope, and the presence of biological communities (biofilm) that coat gravels and boulders within the slopewash flow pathway. Due to the presence of permafrost across the intracrater environment, patterned ground was observed to develop along the margins and terminal deposits associated with the slopewash streaks. The boundary between the slopewash streaks and patterned ground roughly corresponds with where the slope of the ground surface decreases from a steeper slope (slopewash streaks) to a shallower slope (patterned ground). As with other slopewash streaks studied throughout the arctic, the FMARS streaks are fed through a combination of snowmelt and active layer discharge (Wilkinson and Bunting, 1975; Lewkowicz, 1977). The contribution of infiltration between the slopewash streak discharge and patterned ground was observed during a sitewide increase in active layer saturation resulting from a rain event on 22 July 2017 (Figure 4-9).

As with the slopewash streaks in the HIS, RSL and slope streaks have been observed to occur off martian crater rims. With the presence of at least a seasonal near-surface ground ice reservoir serving as one of the requirements for the “wet” RSL hypothesis, the presence of patterned ground or periglacial modification in the vicinity of RSL could further support the wet formation hypothesis. Under volatile conditions that frequently reach the T_e for potential brine solutions, the freezing, thawing, and subsequent sublimation of water solutions would be expected to leave markers in addition to RSL. Similar hypotheses are proposed for wet mechanisms behind the development of slope streaks (Ferris et al, 2002). Patterned ground would be expected in high latitude areas of Mars where the presence of subsurface water ice is capable of supporting transient seeps that trigger slope streak or RSL formation.

The zone of distribution for known RSL are broadly centered across the equator with furthest extents ranging between approximately +/- 60° latitude (Bhardwaj et al, 2017). The highest density distribution of slope streaks ranges between approximately +/- 40° latitude (Bhardwaj et al, 2019). In contrast, patterned ground distribution on Mars has a strong observed limit between the poles and 50° and 55° latitude (Mangold, 2005). Therefore, known slope streak populations do not overlap with the known extent of patterned ground distribution. However, there is a narrow range between approximately +/- 50° and 60° latitude where the known distributions of RSL and patterned ground do overlap. While the identification of patterned ground in the vicinity of recurring slope linea on Mars has not be identified or studied, the interplay between slopewash streaks and patterned ground as seen at the datalogger site on Devon Island could serve as a saturated end-member analog for potential interactions between wet RSL and patterned ground on Mars.

6. Conclusions

Active patterned ground and ice-wedge polygons represent the ubiquitous periglacial processes that have modified the Haughton Impact Structure. The presence of patterned ground and polygon networks in Martian impact craters that are co-located with suspected near-subsurface ground ice offer the intriguing hypothesis that a warmer Martian climate during periods of high obliquity could support similar landscape evolution as viewed in the HIS. However, observations of patterned ground morphology and the interplay with slopewash streaks and other periglacial processes in the HIS underscore the large role that liquid water plays in shaping the intracrater landscape over a short window of time every summer. The observations demonstrate the thermal response between the atmosphere and active layer at patterned ground sites in the vicinity of perennial slopewash streaks pathways. Potential applications of these results include being utilized as variables to assist with computational model development and validation for terrestrial patterned ground formation and evolution; serving as an Earth-Mars analog for patterned ground on Mars during high obliquity climate conditions; and serving as an Earth-Mars analog for patterned ground in the vicinity of gullies, recurring slope linea, and other fluvio-periglacial processes.

7. Limitations

As a mixed human-studies and field research analog, most of the fieldwork for this project was conducted under Mars-mission constraints, which included the notable requirement that field science activities were required to be conducted while donning a mock spacesuit. Field work was originally scheduled to begin concurrently with the planned start of the Mars 160 Mission Simulation around 1 July, yielding approximately 48 days to conduct an extended campaign to monitor active layer development in ice-wedge polygons located approximately 4 km south of FMARS. A series of weather-related delays forced a late arrival to FMARS on 15 July. It was not initially possible to reach an ice-wedge polygon site that was identified prior to the start of the Mars 160 simulation due to poor ground conditions throughout the crater, so the scope of work was adjusted and transformed into an opportunistic study of in-situ temperature and moisture conditions of the active layer in irregular stone nets near FMARS. These stone nets are located downgradient of and adjacent to slopewash streaks that serve as an analog for understanding the subsurface moisture and thermal conditions in this unique environment. Three additional sites were selected in the field based on feature morphology. Once ground conditions permitted deep travel into Haughton Crater, the original ice-wedge polygon site was assessed during two separate excursions. The extraction flight was on August 17, which provided a total of 25 days to gather in-situ observations.

Trenches were excavated into the active layer to the contact with permafrost at each patterned ground site. In smaller hummocks and stone nets, a singular trench was excavated straddling the margin and extending towards the center of the feature in order to obtain a stratigraphic and compositional cross section. Due to active layer development that resulted in saturated soils in response to seasonally warm temperatures, water perched on top of the permafrost contact was occasionally encountered in the trenches. As an electronic pH meter was not available, pH strips were used to test the water. Additional in-situ thermal properties (including thermal conductivity, diffusivity, and specific heat capacity) were not collected as there was no awareness during project planning of the existence or availability of a field-hardened instrument that would enable the collection of consistent measurements under field conditions. Thermal properties were analyzed under laboratory conditions and represent a dry, unconsolidated baseline for the gathered samples. There was some variation across the in-situ and laboratory measurements of the polygon and *Phoenix* Analog sites, however the trends are inconsistent between features of similar composition and morphology. A larger sample size and collecting in-situ measurements of all metrics from similar features would be required to derive firm conclusions in the future.

References

Barrett, A.M., Balme, M.R., Patel, M.R., and Hagermann, A. 2018. The distribution of putative periglacial landforms on the martian northern plains. Icarus. 314, 133-148. DOI:10.1016/j.icarus.2018.05.032

Bhardwaj, A., Sam, L., Martin-Torres, F.J., Zorzano, M.P., and Fonseca, R.M. 2017. Martian slope streaks as plausible indicators of transient water activity. Nature Scientific Reports. 7, 7074. DOI:10.1038/s41598-017-07453-9.

Bhardwaj, A., Sam, L., Martin-Torres, F.J., and Zorzano, M.P. 2019. Are Slope Streaks Indicative of Global-Scale Aqueous Processes on Contemporary Mars? Reviews of Geophysics, 57, 48-77. DOI:10.1029/2018RG000617

Brooker, L.M., Balme, M.R., Conway, S.J., Hagermann, A., Barrett, A.M., Collins, G.S., and Soare, R.J. 2018. Clastic polygonal networks around Lyot crater, Mars: Possible formation mechanisms from morphometric analysis. Icarus. 302, 386-406.

Burr, D.M., Soare, R.J., Wan Bun Tseung, J.M., and Emery, J.P. 2005. Young (late Amazonian), near-surface, ground ice features near the equator, Athabasca Valles, Mars. Icarus. 178, 56-73. DOI: 10.1016/j.icaurs.2005.04.012

Campbell, G.S. 1985. Soil Physics with BASIC: Transport Models for Soil-Plant Systems. Elsevier, New York.

Clarke, J.D.A., Knightly, P., and Rupert, S. 2018. Melt-water formed dark streaks on slopes of Haughton crater as possible Mars analogues. International Jounral of Astrobiology. 1-9.

Cockell, C.S. and Lee, P. 2002. The biology of impact craters – a review. Biological Review. 77, 279-310. DOI: 10.1017/S146479310100584X

Costard, F., Forget, F., Mangold, N., and Peulvast, J.P. 2002. Formation of Recent Martian Debris Flows by Melting of Near-Surface Ground Ice at High Obliquity. Science. 295, 110-113. DOI: 10.1126/science.1066698

Erickson, T.M., Kirkland, C.L., Jouradn, F., Schmieder, M., Hartnady, M.I.H., Cox, M.A., and Timms, N.E. 2021. Resolving the age of the Haughton impact structure using coupled Ar-40/Ar-39 and U-Pb geochronology. Geochimica Et Cosmochimica Acta. 204, 68-82. DOI: 10.1016/j.gca.2021.04.008

Ferris, J.C., Dohm, J.M., Baker, V.R., and Maddock, T. 2002. Dark slope streaks on Mars: Are aqueous processes involved? Geophysical Research Letters, 29(10), 1490. DOI:10.1029/2002GL014936

Fisher, D.A., Lacelle, D., Pollard, W., Davila, A., and McKay, C.P. 2016. Ground surface temperature and humidity, ground temperature cycles, and the ice table depths in University Valley, McMurdo Dry Valleys of Antarctica. Journal of Geophysical Research: Earth Surface. DOI: 10.1002/2016JF004054

Gallagher, C., Balme, M.R., Conway, S.J., and Grindrod, P.M. 2011. Sorted clastic stripes, lobes and associated gullies in high-latitude craters on Mars: Landforms indicative of very recent, polycyclic ground-ice thaw and liquid flows. Icarus. 211, 1, 458-471. DOI:10.1016/j.icarus.2010.09.010

Girod, L., Nuth, C., Kääb, A., Etzelmüller, B., and Kohler, J. 2017. Terrain changes from images acquired on opportunistic flights by SfM photogrammetry. The Cryosphere. 11, 827-840. DOI: 10.5194/tc-11-827-2017.

Haltigin, T.W., Pollard, W.H., Dutilleul, P., and Osinski, G.R. 2012. Geometric Evolution of Polygonal Terrain Networks in the Canadian High Arctic: Evidence of Increasing Regularity Over Time. Permafrost and Periglacial Processes. 23, 178-186. DOI: 10.1002/ppp.1741

Keller, H.U., Goetz, W., Hartwig, H., Hviid, S.F., Kramm, R., Markiewicz, W.J., Reynolds, R., Shinohara, C., Smith, P., Tanner, R., Woida, P., Woida, R., Bos, B.J., and Lemmon, M.T. Phoenix Robotic Arm Camera. Journal of Geophysical Research. 113, E00A17. DOI: 10.1029/2007JE003044.

Kessler, M.A. and Werner, B.T. 2003. Self-Organization of Sorted Patterned Ground. Science. 299, 380-383.

Knight, J.H., Kluitenberg, G.J., Kamai, T., and Hopmans, J.W. 2012. Semianalytical solution for dual-probe heat-pulse applications that accounts for probe radius and heat capacity. Vadose Zone Journal. 11, No. 2.

Kreslavsky, M. A., Head, J. W., and Marchant D. R. 2008. Periods of active permafrost layer formation during the geological history of Mars: Implications for circum-polar and mid-latitude surface processes. Planetary and Space Science. 56, 289-302.

Kreslavsky, M.A. and Head, J.W. 2009. Slope streaks on Mars: A new “wet” mechanism. Icarus. 201, 517-527. DOI: 10.1016/j.icarus.2009.01.026

Lee, P. and Osinski, G. R. 2005. The Haughton-Mars Project: overview of science investigations at the Haughton impact structure and surrounding terrains, and relevance to planetary studies. Meteoritics and Planetary Science. 40(12), 1755-1758

Lev, A. and King, R.H. 1999. Spatial Variation of Soil Development in a High Arctic Soil Landscape, Truelove Lowland, Devon Island, Nunavut, Canada. Permafrost and Periglacial Processes. 10, 289-307.

Levy, J.S., Head, J.W., and Marchant, D.R. 2008. The role of thermal contraction crack polygons in cold-desert fluvial systems. Antarctic Science. 20, 6. 565-579. DOI: 10.1017/S0954102008001375

Levy, J., Head, J., and Marchant, D. 2009a. Thermal contraction crack polygons on Mars: Classification, distribution, and climate implications from HiRISE observations. Journal of Geophysical Research. 114, E01007. DOI: 10.1029/2008JE003273

Levy, J.S., Head, J.W., Marchant, D.R., Dickson, J.L., & Morgan, G.A. (2009). Geologically recent gully-polygon relationships on Mars: Insights from the Antarctic Dry Valleys on the roles of permafrost, microclimates, and water sources for surface flow. *Icarus*, 201, 113-126.

Lewkowicz, A.G. (1977). Slopewash processes in an arctic tundra environment, Banks Island, N.W.T. Master of Arts Dissertation, University of Ottawa.

Mangold, N., Maurice, S., Feldman, W.C., Costard, F., and Forget, F. 2004. Spatial relationships between patterned ground and ground iced detected by the Neutron Spectrometer on Mars. Journal of Geophysical Research. 109, E08001. DOI: 10.1029/2004JE002235

Mangold, N. 2005. High latitude patterned grounds on Mars: Classification, distribution and climate control. Icarus. 174, 336-359.

Marchant, D.R., Lewis, A.R., Phillips, W.M., Moore, E.J., Souchez, R.A., Denton, G.H., Sugden, D.E., Potter Jr., N., and Landis, G.P. 2002. Formation of patterned ground and sublimation till over Miocene glacier ice in Beacon Valley, southern Victoria Land, Antarctica. Geological Society of America Bulletin. 114, 6, 718-730.

McEwen, A. S., Ojha, L., Dundas, C.M., Mattson, S.S., Byrne, S., Wray, J.J., Cull, S.C., Murchie, S.L., Thomas, N., and Gulick, V.C. 2011. Seasonal Flows on Warm Martian Slopes. Science. 333, 740.

Mellon, M. T., Arvidson, R. E., Marlow, J. L., Phillips, R. J., and Asphaug, E. 2008. Periglacial landforms at the *Phoenix* landing site and the northern plains of Mars. Journal of Geophysical Resarch. 113, E00A23.

Mellon, M. T., Arvidson, R. E., Sizemore, H. G., Searls, M. L., Blaney, D. L., Cull, S., et al. 2009. Ground ice at the *Phoenix* Landing Site: Stability state and origin. Journal of Geophysical Research. 114, E00E07.

Mellon, M.T., Mckay, C.P., and Heldmann, J.L. 2014. Polygonal ground in the McMurdo Dry Valleys of Antarctica and its relationship to ice-table depth and the recent Antarctic climate history. Antarctic Science. 26, 4, 413-426. DOI: 10.1017/S0954102013000710

Ojha, L., McEwen, A., Dundas, C., Byrne, S., Mattson, S., Wray, J., Masse, M., and Schaefer, E. 2014. HiRISE observations of Recurring Slope Linea (RSL) during southern summer on Mars. Icarus. 231, 365-376. DOI: 10.1016/j.icarus.2013.12.021

Orloff, T., Kreslavsky, M., and Asphaug, E. 2013. Distribution of polygon characteristic scale in Martian patterned ground terrain in the northern hemisphere using Fourier transform. Journal of Geophysical Research-Planets. 118, 7, 1558-1566. DOI: 10.1002/jgre.20111

Osinski, G. R. and Lee, P. 2005a. Intra-crater sedimentary deposits at the Haughton impact structure, Devon Island, Canadian High Arctic. Meteoritics and Planetary Science. 40(12), 1887-1899.

Osinski, G. R., Lee, P., Spray, J. G., Parnell, J., Lim, D. S. S., Bunch, T. E., Cockell, C. S., and Glass, B. 2005b. Geological overview and cratering model for Haughton impact structure, Devon Island, Canadian High Arctic. Meteoritics and Planetary Science. 40(12), 1759-1776.

Osinski, G. R. and Spray, J. G. 2001. Impact-generated carbonate melts: evidence from the Haughton Structure, Canada. Earth and Planetary Science Letters. 194(1-2), 17-29.

Peterson, R.A. and Krantz, W.B. 2002. A mechanism for differential frost heave and its implications for patterned-ground formation. Journal of Glaciology, 69-80.

Peterson, R.A. 2011. Assessing the role of differential frost heave in the origin of non-sorted circles. Quaternary Research. 75. 325-333. DOI: 10.1016/j.yqres.2010.08.003

Ray, R.J., Krantz, W.B., Caine, T.N., and Gunn, R.D. 1983. A model for sorted patterned-ground regularity. Journal of Glaciology. 29, 102, 317-337.

Rivera-Valentin, E. G. and Chevrier, V. F. 2015. Revisiting the *Phoenix* TECP data: Implications for regolith control of near-surface humidity on Mars. Icarus. 253, 156-158.

Ryden, B.E. 1977. Hydrology of Truelove Lowland. L.C. Bliss. *Truelove Lowland, Devon Island, Canada: A High Arctic Ecosystem.* 107-135. The University of Alberta Press.

Shaw, A., Arvidson, R.E., Bonitz, R., Carsten, J., Keller, H.U., Lemmon, M.T., Mellon, M.T., Robinson, M., and Trebi-Ollennu, A. 2009. *Phoenix* soil physical properties investigation. Journal of Geophysical Research. 114, E00E05.

Sherlock, S. C., Kelley, S. P., Parnell, J., Green, P., Lee, P., Osinski, G. R., and Cockell, C. S. 2005. Re-evaluating the age of the Haughton impact event. Meteoritics and Planetary Science. 40(12), 1777-1787.

Sizemore, H. G., Mellon, M. T., Searls, M. L., Lemmon, M. T., Zent, A. P., Heet, T. L., Arvidson, R. E., Blaney, D. L., and Keller, H. U. 2010. In situ analysis of ice table depth variations in the vicinity of small rocks at the *Phoenix* landing site. Journal of Geophysical Research. 115, E00E09.

Smith, P.H., Tamppari, L.K., Arvidson, R.E., Bass, D., Blaney, D., Boynton, W.V., Carswell, A., Catling, D.C., Clark, B.C., Duck, T., DeJong, E., Fisher, D., Goetz, W., Gunnlaugsson, H.P., Hecht, M.H., Hipkin, V., Hoffman, J., Hviid, S.F., Keller, H.U., Kounaves, S.P., Lange, C.F., Lemmon, M.T., Madsen, M.B., Markiewicz, W.J., Marshall, J., McKay, C.P., Mellon, M.T., Ming, D.W., Morris, R.V., Pike, W.T., Renno, N., Staufer, U., Stoker, C., Taylor, P., Whiteway, J.A., and Zent, A.P. 2009. H2O at the Phoenix Landing Site. Science. 325. 58-61.

Soare, R. J., Conway, S. J., and Dohm, J. M. 2014. Possible ice-wedge polygons and recent landscape modification by “wet” periglacial processes in and around the Argyre impact basin, Mars. Icarus. 233, 214-228.

Soare, R. J., Conway, S. J., Gallagher, C., and Dohm, J. M. 2016. Sorted (clastic) polygons in the Argyre region, Mars, and possible evidence of pre- and post-glacial periglaciation in the Late Amazonian Epoch. Icarus. 264, 184-197.

Ugolini, F.C., Corti, G., and Certini, G. 2006. Pedogenesis in the sorted patterned ground of Devon Plateau, Devon Island, Nunavut, Canada. Geoderma. 136, 87-106. DOI: 10.1016/j.geoderma.2006.03.030

Ulrich, M., Hauber, E., Herzschuh, U., Hartel, S., Shirrmesiter, L. (2011). Polygon pattern geomorphometry on Svalbard (Norway) and western Utopia Planitia (Mars) using high-resolution stereo remote-sensing data. Geomorphology, 134, 197-216.

Uxa, T., Mida, P., and Křížek, M. 2017. Effect of Climate on Morphology and Development of Sorted Circles and Polygons. Permafrost and Periglacial Processes. 28, 663-674. DOI: 10.1002/ppp.1949

Washburn, A.L. 1956. Classification of patterned ground and review of suggested origins. Bulletin of the Geological Society of America. 67, 823-866.

Watanabe, T., Matsuoka, N., and Christiansen, H.H. 2013. Ice- and Soil-Wedge Dynamics in the Kapp Linne Area, Svalbard, Investigated by Two- and Three-Dimensional GPR and Ground Thermal and Acceleration Regimes. Permafrost and Periglacial Proccesses. 24, 39-55. DOI: 10.1002/ppp.1767

Watanabe, T., Matsuoka, N., Christiansen, H.H., and Cable, S. 2017. Soil Physical and Environmental Conditions Controlling Patterned-Ground Variability at a Continuous

Permafrost Site, Svalbard. Permafrost and Periglacial Processes. 28, 433-445. DOI:10.1002/ppp.1924

Wilkinson, T.J. and Bunting, B.T. 1975. Overland transport of sediment by rill water in a periglacial environment in the Canadian high arctic. Geografiska Annaler. Series A, Physical Geogrpahy. 57, 1. 105-116.

Wilson, J.T., Eke, V.R., Massey, R.J., Elphic, R.C., Feldman, W.C., Maurice, S., and Teodoro, L.F.A. 2018. Equatorial locations of water on Mars: Improved resolution maps based on Mars Odyssey Neturon Spectrometer data. Icarus. 299, 148-160. DOI: 10.1016/j.icarus.2017.07.028

Young, K.E., van Soest, M.C., Hodges, K.V., Watson, E.B., Adams, B.A., and Lee, P. 2013. Impact thermocrhonology and the age of Haughton impact structure, Canada. Geophysical Research Letters. 40, 3836-3840. DOI: 10.1002/grl.50745

Zent, A. P. et al. 2009. Thermal and Electrical Conductivity Probe (TECP) for *Phoenix*. Journal of Geophysical Research. 114, E00A27.

Zent, A. P. et al. 2010. Initial results from the thermal and electrical conductivity probe (TECP) on *Phoenix*. Journal of Geophysical Research. 115, E00E14.

Zent, A. P., Hecht, M. H., Hudson, T. L., Wood, S. E., and Chevrier, V. F. 2016. A revised calibration function and results for the *Phoenix* mission TECP relative humidity sensor. Journal of Geophysical Research: Planets. 121, 626-651.

Chapter 5

A Comparison of Morphometric and Surface Roughness Parameters of Terrestrial and Martian Patterned Ground with Implications for Recent Periglacial Activity on Mars

Knightly, J.P., Tullis, J., Dixon, J.C., Chevrier, V.F.

[1]University of Arkansas, Center for Space and Planetary Sciences, Fayetteville, AR 72701

1.0 Introduction

The primary objective of this comparative analysis is to determine if morphometric and surface roughness observations of active and putative relict terrestrial patterned ground can provide insight into the possibility of historical wet periglacial modification of patterned ground on Mars. This work is summarized in the following subsections and was accomplished by:

1. Identifying a potential data gap in the absence of relict terrestrial patterned ground in previous Earth-Mars analog studies
2. Identifying and implementing appropriate data collection and processing methodologies, including the use of uncrewed aerial vehicle surveys, photogrammetric processing, and a novel application of a multiscale surface roughness evaluation technique
3. Evaluating terrestrial analog data for morphometric properties that could provide insight into the present condition of the surveyed polygons
4. Evaluating Mars datasets for morphometric properties that could provide insight into the present condition of the surveyed polygons and to constrain the detection limitations of small-scale features in high resolution digital terrain models
5. Comparing the evaluated datasets and identifying future applications of the developed techniques

2.0 Discussion of Surface Roughness Analysis Techniques

There are a wide range of applications for surface roughness in terrestrial and planetary sciences. Before undertaking a discussion of surface roughness derivation and analysis techniques, it is important to understand the underlying reasons that surface roughness may be derived. Smith (2014) provides an overview of surface roughness applications in remote sensing and Earth sciences and categorizes applications of surface roughness into three general categories: using roughness as a variable (e.g. in mapping landforms), as a surrogate for less measurable variables (e.g. estimating the resistance to flow), or as an indicator of near-surface processes (e.g. aeolian and glacial landscape modification). While the lack of standardization of surface roughness parameters in remote sensing and Earth sciences have previously been identified (Fassnacht et al, 2009), any contemporary standardization could restrict future applications that may require the use of different roughness parameters to address specific applications. Therefore, it is advantageous to have a multitude of roughness parameters available, however the chosen parameter space should be compatible with the available datasets and appropriate for the problem being addressed.

2.1 Types of Surface Roughness Parameters

Smith, 2014 further categorizes the techniques for quantifying surface roughness into four spaces defined by amplitude, spacing, hybrid, and multi-scale parameters. Key concepts from Smith, 2014 are summarized in the following subsections.

2.1.1 Roughness from Amplitude Parameters

Amplitude parameters are most often used when quantifying roughness as it imparts resistance to fluid flow (water or air) over the surface. A central component of amplitude parameters is the evaluation of neighboring and extreme characteristics (such as the topographic height of peaks and depth of pits) and can be achieved through several different methods. The first is the incorporation of discrete parameters such as grain size profiles and protrusion measures (Gomez, 1993). A second method would be to evaluate neighborhood elevation differences, such as evaluating the maximum elevation difference between three adjacent points on a profile or by evaluating the root mean square (RMS) difference between the elevation of one cell and the elevation of neighboring cells in an array (Riley et al, 1999). A third method involves evaluating probability statistics, such as the standard deviation of elevation (Ascione et al, 2008). Equation 1 presents a simplified representation of deriving the standard deviation of elevation for a DTM using the ArcGIS Focal Statistics calculator where:

$$\frac{(\text{"}Mean\ DTM\text{"} - \text{"}DTM\text{"})}{\text{"}Range\ DTM\text{"}} = Standard\ Deviation\ of\ Elevation \qquad (1)$$

Due to the scale-dependency of surface roughness parameterization, the proper application of amplitude parameters such as the standard deviation of elevation relies upon previous evaluation of the surface so that an appropriate scale can be applied for calculations.

2.1.2 Roughness from Spacing Parameters

Spacing parameters focus entirely on the horizontal scale of surface deviations, rather than the vertical scale evaluated by other methodologies. Central to this method is feature spacing (such as the distance between peaks, pits, and other points of inflection), feature length, and feature radius of curvature. A zero-crossing wavelength analysis is a useful spacing method in areas with coarse resolution lacking previous determinations of surface roughness by counting the number of upcrossings (or peaks) of a roughness profile along a reference line (Clifford et al, 1992). However, difficulty may arise when comparing datasets at fundamentally different scales (such as between UAS and satellite-acquired datasets) where topographic peaks in a UAS survey may represent individual rocks and gravels and satellite data may only detect topographic peaks at a feature-scale.

2.1.3 Roughness from Hybrid Parameters

Hybrid parameters are strongly dependent on feature and dataset scale, which frequently results in an increase in surface roughness values in response to higher resolution datasets. This can be beneficial when assessing complexity ratios such as profile tortuosity and porosity. Standard deviation of elevation and RMS slope based on the deviation and separation of two points also fall into this category. Additional hybrid parameters include assessing aspect variability via Eigenvalue ratios and Laplacian operators and using parameters of fitted Gaussian distributions.

2.1.4 Roughness from Multi-Scale Parameters

Multi-scale parameters can fall under two separate subcategories. The first subcategory is performing multi-scale analyses as part of a broader statistical analysis of a dataset. This can involve performing space-scale, geostatistics, fractal, spectral, and wavelet analyses. The second subcategory of multi-scale parameters involves performing multiple iterations of the previously summarized amplitude, spacing, and hybrid parameters at varying scales. For this project, calculating the standard deviation of elevation as an amplitude parameter at a fixed scale is insufficient to account for variations in feature scale and spatial resolutions across different datasets. Accordingly, a set of multi-scale parameters and associated procedures were implemented in the evaluation of the UAS and HiRISE datasets as detailed in Chapter 2.

2.2 Surface Roughness Applications in Planetary Science

Aerial and satellite-borne photogrammetry have been used extensively in terrestrial applications dating to the inception of each respective imaging platform. Previous photogrammetric applications in planetary science include evaluations of the surface roughness of Mercury using stereo imagery acquired from the MErcury Surface, Space ENvironment, GEochemistry, and Ranging (MESSENGER) mission (Florinsky, 2018). Many planetary science applications of surface roughness have utilized laser or radar-derived terrain models of the subject planetary body. For example, previous work examining the roughness of the lunar surface used a laser altimetry-derived terrain models (Cao et al, 2015; Cao and Cai, 2018) and the surface roughness of Venus has been evaluated using radar-derived terrain models from the Magellan spacecraft (Byrnes and Crown, 2002).

Several datasets have historically been utilized to perform surface roughness analyses of the Martian surface. Early surface roughness evaluations of Mars used Arecibo radar data to estimate the average surface roughness at a regional scale (e.g. Harmon, 1997). The arrival of the Mars Orbiter Laser Altimeter (MOLA) on the Mars Global Surveyor (MGS) spacecraft enabled the development of a high-resolution global elevation model (Smith et al, 2001) and supported subsequent surface roughness analyses capable of deriving refined roughness parameters at a kilometer-scale (Kreslavsky and Head, 2000). While some limited photogrammetric studies had been applied to Mars imagery, the development of the global MOLA DEM enabled the creation of refined photogrammetric DEMs using imagery extending back to the Viking missions (Baratoux et al, 2001). MOLA DTMs have also supported the derivation of surface roughness parameters from radar-based instruments, including Shallow Radar (SHARAD) data (Campbell et al, 2013) and Mars Advanced Radar for Subsurface and Ionosphere Sounding (MARSIS) data (Campbell et al, 2018).

While surface roughness evaluations using laser altimetry and radar have broad utility (such as simultaneously evaluating surface roughness and radar reflectors for subsurface features, as with SHARAD and MARSIS), there are inherent scale limitations that prevent the analysis of smaller-scale features that may otherwise be visible in high-resolution imagery. Satellite-borne photogrammetry of other planetary bodies has been possible from the earliest days of the space program, however the initial utility of roughness evaluations from photogrammetrically-derived DTMs was limited by sensor specifications, the resulting spatial resolution of image datasets, and the scarcity or complexity of the computational resources required for data processing. The advent of high-resolution imaging of planetary surfaces with instruments such as HiRISE and the High Resolution Stereo Camera (HRSC) has provided an opportunity to examine smaller-scale topographic details that would otherwise not be possible to evaluate from planet-wide datasets (e.g. MOLA). Surface roughness and related photoclinometry analyses of HRSC-derived DTMs (Cord et al, 2007) and HiRISE-derived DTMs (Li et al, 2011; Beyer and Kirk, 2012; Beyer, 2017; Kirk et al, 2021; Pardo-Iguzquiza and Dowd, 2022) have validated the principal of using high-resolution photogrammetry to derive surface roughness on scales of meters to tens of meters. The application of these techniques have been previously used for purpose of technique validation and landing site characterization, however using meter-scale DTMs to evaluate the surface roughness of patterned ground has not been previously been explored.

3.0 Implications for High-Resolution Digital Terrain Modeling of Mars

Increased interest in the utilization of high-resolution DTMs in the analysis of planetary datasets corresponds with the growing availability of high-resolution datasets and the affordability of the computational resources required to facilitate their analysis. While LiDAR datasets have been traditionally relied upon for performing surface roughness evaluations at kilometer-scales (e.g. Kreslavsky and Head, 2000; Cao et al, 2015; Lindsay et al, 2019), photogrammetry has been increasingly incorporated to evaluate the surface roughness of planetary datasets (e.g. Florinsky, 2018; Guo et al, 2021).

HiRISE has proven to be one of the most prolific and successful instruments sent beyond Earth orbit, generating over 100 terabytes of data since its 2006 arrival at Mars. The fortune of several mission extensions means that HiRISE continues to produce vast quantities of data that will take many decades to fully process and evaluate. A central philosophy in planetary science is to utilize existing datasets as frequently and often as possible and to explore unanticipated applications of existing datasets to address outstanding questions. In this regard, it is important to understand the underlying goals of the instrument, the basic technical specifications, and the functional limitations for the application of surface roughness analytical techniques to HiRISE DTMs.

3.1 HiRISE Basics

The structure of HiRISE consists of 1.4 m long, 0.7 m diameter flight structure that houses a 0.5 m, f/24 aperture telescope. HiRISE uses 14 separate linear-array charge-coupled device

(CCD) sensors capable of capturing the spectral range from 400 to 1000 nm (visible blue, green, and red to near infrared). This linear array can achieve a ground sample distance of 0.3 m/pixel from a 300 km altitude over the highest resolution image swaths (McEwen et al, 2007).

3.2 Peering through the Static: Processing Challenges Associated with Meter-Scale Digital Terrain Models

Under best-case imaging scenarios and processing workflows, HiRISE DTMs derived from stereo pair imagery can resolve surface topography with an accuracy of 0.25 m (Kirk et al, 2008). Instrument design and performance must be accounted for in processing workflows and final dataset interpretation. As scale plays a central role in surface roughness evaluations, a key objective to determining the applicability of roughness derived from HiRISE DTMs is establishing the measurement scale limit, below which instrument noise interferes with the quantification of topographic roughness variations. There are advanced workflows within ISISv3 (and SOCET SET/SOCET GXP) that are capable of correcting HiRISE-derived datasets to remove scan lines and other operational artifacts that are present in raw imagery (Kirk et al, 2008). While these workflows are useful for smoothing stitched images and the resulting DTMs, they come at the expense of smoothing fine-scale topography that may otherwise be detectable in uncorrected datasets. The concern with smoothing associated with photogrammetric algorithms originated from the initial processing of UAV datasets from Utah and Iceland in Agisoft Metashape and Pix4D. A comparison of centimeter-scale features at sites processed using both programs revealed that the Pix4D algorithm had a tendency to “smooth” smaller features that could propagate into subsequent surface roughness analyses. Workflows (and program algorithms) that could have resulted in smoothing smaller features were not employed over the course of this project to preserve meter to submeter scale feature resolution in UAV and HiRISE-derived DTMs and to ascertain the degree of interference from instrument noise.

Understanding that imaging artifacts would be present in resulting HiRISE DTMs in the absence of further processing, the analysis of DTMs was performed to avoid the most obvious imaging artifacts. For example, features delineated at Vastitas Broealis near the *Phoenix* landing site in a SOCET SET-derived DTM and features delineated at Lethe Vallis in an ASP-derived DTM were selected to avoid the most obvious camera scan lines.

3.3 Future Applications

A successor to HiRISE is not under active development or funding by NASA at the present time. Since its launch in 2005, MRO and HiRISE have operated far longer than the original design life of five Earth years. Signs of age are starting to appear on both MRO and HiRISE, ranging from declining performance of the gyroscopes used to orient the spacecraft (NASA press release, 2018a) and blurring of HiRISE imagery that has been intermittently detected since around 2017 (NASA press release, 2018b). Despite increasing signs of age and the potential for declining performance, recent mission extensions call for MRO and HiRISE to continue operation through at least the mid to late 2020’s. Several mission concepts have been proposed that would provide replacement capabilities for HiRISE at Mars, however none of the concepts are currently funded. As it generally takes around 5 years to propose, design, build, and launch new spacecraft to Mars, it is reasonable to estimate that a potential successor would not launch until the 2026 launch window at the earliest. Therefore, the techniques described in this study will have utility in analyzing small-scale features using HiRISE DTMs throughout much of the coming decade and beyond.

4.0 Terrestrial Investigations in this Study

A total of 23 sites comprising 849 polygons in the Uinta Mountains, Utah, U.S.A. and the Westfjords and Highlands, Iceland were evaluated for this study. The analysis of these sites are discussed in Chapter 2 and key outcomes that apply to the study of patterned ground on Mars are summarized in the following subsections.

4.1 Summary of Investigations

Uncrewed aerial system (UAS) surveys were performed to gather site imagery to perform a visual analysis of polygon morphometry. The UAS orthoimagery was then photogrammetrically transformed into DTMs for each respective site, followed by performing a multiscale surface roughness analysis using the Whitebox Tools extension in QGIS. The primary objective of these surveys was to validate a novel application of a multiscale surface roughness (MSR) algorithm to UAS-derived digital terrain data of active and potentially relict patterned ground. The secondary objective of the UAS surveys is the application of UAS survey results as a terrestrial analog for patterned ground on Mars to ascertain if feature morphometry and surface roughness can be used as predictive variables for determining if patterned ground was formed through (relict) “wet” periglacial processes or through (active) “dry” sublimation processes.

4.2 Conclusions

In addressing the primary objective, the project successfully validated the application of the Whitebox Tools MSR algorithm in the analysis of nearly 850 patterned ground features that were delineated using a combination of UAS orthoimagery and DTMs. The scale-dependency of the MSR algorithm was evaluated by adjusting the focal radius of each MSR analysis and by varying the scale of input datasets. For example, UAS surveys were performed over similar types of patterned ground at different altitudes ranging from 7.5 m to 120 m above ground level. Scale-dependent changes in surface roughness were also observed across common polygon regions (e.g. centers and margins) among different types of polygon morphologies at fixed survey altitudes. For example, a strong association between high and low surface roughness values in polygon centers and margins were noted in higher relief features such as stone circles (with centers composed of small gravels and margins composed of larger gravels and boulders) and ice wedge polygons (with prominent topographic variations between relatively smooth centers and eroded margins). Weaker associations of specific surface roughness values were observed in low relief polygons or features with a uniform composition.

For the secondary objective, there was not enough data to ascribe specific surface roughness parameters to active or relict patterned ground. Relict sites were selected based on the best available data at the time which suggested that alpine patterned ground sites in the Uinta Mountains, Utah (Munroe, 2007) and Westfjords, Iceland (Etzelmüller et al, 2007) were the best candidates for studying well-preserved relict patterned ground. Field observations including microsorting of small pebbles from needle ice formation, isotherms in trenches that suggested sporadic permafrost could be possible, and gelic behavior of soils in conjunction with work that was published following the completion of field work (Emmert, 2020 and Morino et al, 2021) called into question the initial estimation that patterned ground at the Westfjords site was relict. Seasonal modification of patterned ground in the Uinta Mountains cannot be fully ruled out either as modification resulting from the freezing of soils in winter, followed by a summer thaw cannot be fully ruled out. However, the presence of extensive vegetation and mature soils as described by Munroe (2007) support a higher probability that the site is periglacially inactive, even if it may be cryogenically active during seasonal transitions. Despite the higher probability of both Icelandic sites representing active sites and the probability of seasonal cryogenic activity in the Uinta Mountains, the observations from the UAV surveys provide important observational parameters for patterned ground morphology that can serve as a baseline for future studies.

5.0 Martian Investigations in this Study

A total of 10 sites comprising 1,093 polygons were evaluated for this study. The analysis of these sites is discussed in Chapter 3 and the key outcomes are summarized here.

5.1 Summary of Investigations

HiRISE DTMs were built using a workflow in the Ames Stereo Pipeline to evaluate sites with stereo image coverage that have not previously been translated into DTMs. A morphometric analysis was performed on patterned ground in the resulting processed HiRISE images. The HiRISE DTMs were then evaluated using the same multiscale surface roughness workflow leveraging the Whitebox Tools extension in QGIS. The primary objective was to validate a novel application of a multiscale surface roughness algorithm to HiRISE DTMs that provide coverage of different patterned ground morphologies on Mars. The secondary objective is to leverage the results of the multiscale surface roughness analysis of the HiRISE DTMs in comparison with the results of the UAS surveys to ascertain if patterned ground morphometry and surface roughness on Mars can be used as predictive variables for determining if patterned ground was formed through (relict) “wet” periglacial processes or through (active) “dry” sublimation processes.

5.2 Conclusions

In addressing the primary objective, the project successfully validated the application of the Whitebox Tools MSR algorithm in the analysis of over 1,000 patterned ground features that were delineated using a combination of HiRISE images and DTMs. The scale-dependency of the MSR algorithm was evaluated by adjusting the focal radius of each MSR analysis. At most sites there were discernible and consistent differences in surface roughness between polygon centers and margins, however the magnitude of the surface roughness differences varied according to feature scale. Topographically well-defined polygons scored higher in a principal component analysis (PCA) of the resulting MSR datasets, in contrast to topographically poorly-defined polygons that scored lower in the PCA.

The second objective was partially addressed through the outcome of first objective. The results of the morphometric surveys were comparable to similar studies evaluating patterned ground on Mars (primarily Ulrich et al, 2011 and Brooker et al, 2018). The introduction of the MSR analysis was partially successful and established constraints for determining what types of features are appropriate for evaluating using the MSR technique. Surface roughness and morphometric parameters alone were not sufficient for developing predictions of historical “wet” or “dry” activity associated with the evaluated patterned ground sites. The comparison of the MSR analysis of the HiRISE DTMs and UAS surveys and the role of terrestrial analogs in assessing patterned ground activity on Mars will be explored in Section 7. The future work required to fully address the secondary objective will be outlined in Section 8.

6.0 Implications for Recent Periglacial Processes on Mars

The primary combined objective of the comparative analysis between the UAS surveys and HiRISE site surveys is an evaluation of the parameters that were utilized and a determination of the applicability of morphometric parameters and multiscale surface roughness evaluations derived from HiRISE DTMs. The secondary objective is to determine if morphometric and MSR analyses can ascertain potential differences between “wet” periglacial and “dry” sublimation modification of Martian patterned ground.

6.1 Comparison of Terrestrial UAS Surveys to HiRISE DTMs of Mars

The overarching purpose of any planetary science terrestrial analog study is to provide high resolution insight into processes that can’t be easily studied on other worlds. There are three general considerations when comparing the UAS and HiRISE datasets in this study: dataset scale, feature scale, and feature morphology.

6.1.1 Dataset Scale

In this regard, the primary limitation to terrestrial data analysis is technological in nature. Conversely, the limitations of comparing terrestrial datasets to analogous planetary landforms or processes are also technological in nature and dictated by the resolution and sensitivity of instrument data returned to Earth. UAS surveys have expanded the potential to gather high-resolution imagery to facilitate morphometric surveys at centimeter-scale resolution, rapidly exceeding previous imaging capabilities that were available at the turn of the century. HiRISE provides imagery with a spatial resolution down to 25 cm per pixel. While exceeding the capabilities of most commercially available high-resolution terrestrial satellite imagery by 25 to 75 cm, HiRISE imagery is only directly comparable to UAS datasets when UAS imagery is collected by either a lower-resolution sensor or with a high-resolution sensor at a high survey altitude. The highest resolution UAS survey performed at 7.5 m agl at FPG-X25 provides a spatial resolution of approximately 0.34 cm/pixel and most surveys performed at 80 m agl have a spatial resolution of approximately 2.6 cm/pixel.

The multiscale surface roughness evaluations of both the terrestrial and Martian sites did, however, demonstrate the utility of the technique in characterizing larger areas at scales appropriate for each respective sensor. As previously indicated, the primary limitation to future applications of this technique on terrestrial datasets is the spatial resolution of the sensor. The highest resolution survey at FPG-X25 provides detail sufficient to distinguish the location of small gravels across polygon centers, margins, and border regions, which holds implications for microtopographic monitoring of polygon evolution and associating surface morphometry with underlying processes (such as annual freeze-thaw cycles and permafrost degradation due to climate change). In comparison, multiscale surface roughness evaluations of HiRISE datasets are more sensitive to feature scale and morphometry for establishing appropriate survey parameters.

6.1.2 Feature Scale

Due to scale limitations, the detectability and morphometric characterization of smaller features using HiRISE datasets can present a challenge. For example, small-scale patterned ground near the *Phoenix* landing site is roughly 2-3 m in size as measured by surface imagery from the spacecraft, comparable in size to much of the small-scale patterned ground observed at the Flateyri, Iceland site. UAS image resolution enabled the clear delineation of polygon centers, margins, and sub-regions such as borders along the center/margin contact where compositional changes in gravel size distribution were observed. In contrast, resolving clear boundaries between polygons in HiRISE imagery near the *Phoenix* landing site was a challenge and resulted in the delineation of larger small polygons (> 5 m in size) that, if higher resolution imagery were available, would likely be revealed as clusters of small polygons of 2-3 m in size. While larger polygons are not nearly as impacted by this effect, the broadest areas of polygon centers and margins are most likely to be geologically stable in comparison to feature margins where rocks or regolith are more likely to shift due to changes in slope imparted by erosion, freeze-thaw cycles, or sublimation-driven modification (e.g. ice-wedge polygons in the Highlands, Iceland and polygons in Utopia Planitia). Even where there is high contrast along polygon center and margin boundaries in HiRISE data, delineating these zones as a separate "boundary" region would result in datasets as narrow as perhaps 4 pixels (1 m ground distance) which is insufficient for performing multiscale surface roughness analyses that require a minimum of 3 neighboring pixels for a first order filter radius and 5 neighboring pixels for a second order filter radius.

The effect of feature scale can be countered in all terrestrial applications by using sensors with higher spatial resolution or performing surveys closer to the ground surface. In HiRISE surveys, feature scale must be large enough to perform several incremental steps of the multiscale surface roughness evaluation. In general, features between 5-10 m in size represent the lowermost bounds of detecting distinct roughness variations. While larger features are more likely to resolve distinct variations in roughness and other morphometric parameters, larger features that are topographically subdued or indistinct performed poorly, indicating that feature morphology also plays an important role.

6.1.3 Feature Morphology

Topographically subdued, small-scale patterned ground is ubiquitous to the permafrost regions of Earth, however in some cases larger-scale ice-wedge polygons with prominent topographic provinces between feature centers and margins may develop. In a similar manner, small-scale and topographically subdued patterned ground pockmarks the high latitudes of Mars but is sometimes punctuated by larger polygons featuring prominent topographic variations between polygon centers and margins. Topographically prominent polygons provided the clearest distinctions between surface roughness of polygon centers and margins, such as those evaluated near Lyot Crater, Utopia Planitia, and Utopia Rupes Sites 1 and 2.

Among the larger polygons that were evaluated, features at the Utopia Planitia and Utopia Rupes Sites 1 and 2 are most morphologically similar to polygons evaluated in the Highlands, Iceland and on Devon Island, Nunavut, Canada (Figure 6-1). Variations in vegetation coverage between polygons on Devon Island and Iceland can be used as a proxy for periglacial activity, as increased vegetation has been tied to decreased rates of cryoturbation at relict sites (Munroe, 2007). Ascertaining feature activity would require subsurface investigations using ground-penetrating radar or more extensive trenching, however the variations in vegetation density and changes to surface topography suggest that surface roughness may be a viable parameter for evaluating feature activity if associated permafrost baselines can be established.

While fine-scale morphometric parameters for the Devon Island polygons were not collected, imagery from the ground surface provides insight into topographic variations that are apparent in HiRISE imagery and DTMs for the Utopia Planitia polygons. The Devon Island polygons appear to be experiencing active modification and feature degradation and the presence of ice at the surface inside polygon margins at Utopia Planitia suggest that at least cryogenic processes are active in the area. It is suspected that the distinct surface roughness parameters at the Utopia Planitia and Utopia Rupes sites can be attributed to topographic variations between polygon centers and margins that are similar to what was seen on Devon Island. If sublimation or cryogenic processes are particularly active at these sites, variations in surface roughness may provide a useful metric for change detection (feature erosion or modification) and evaluating the seasonality and mechanics of such processes (i.e. sublimation or thermal contraction).

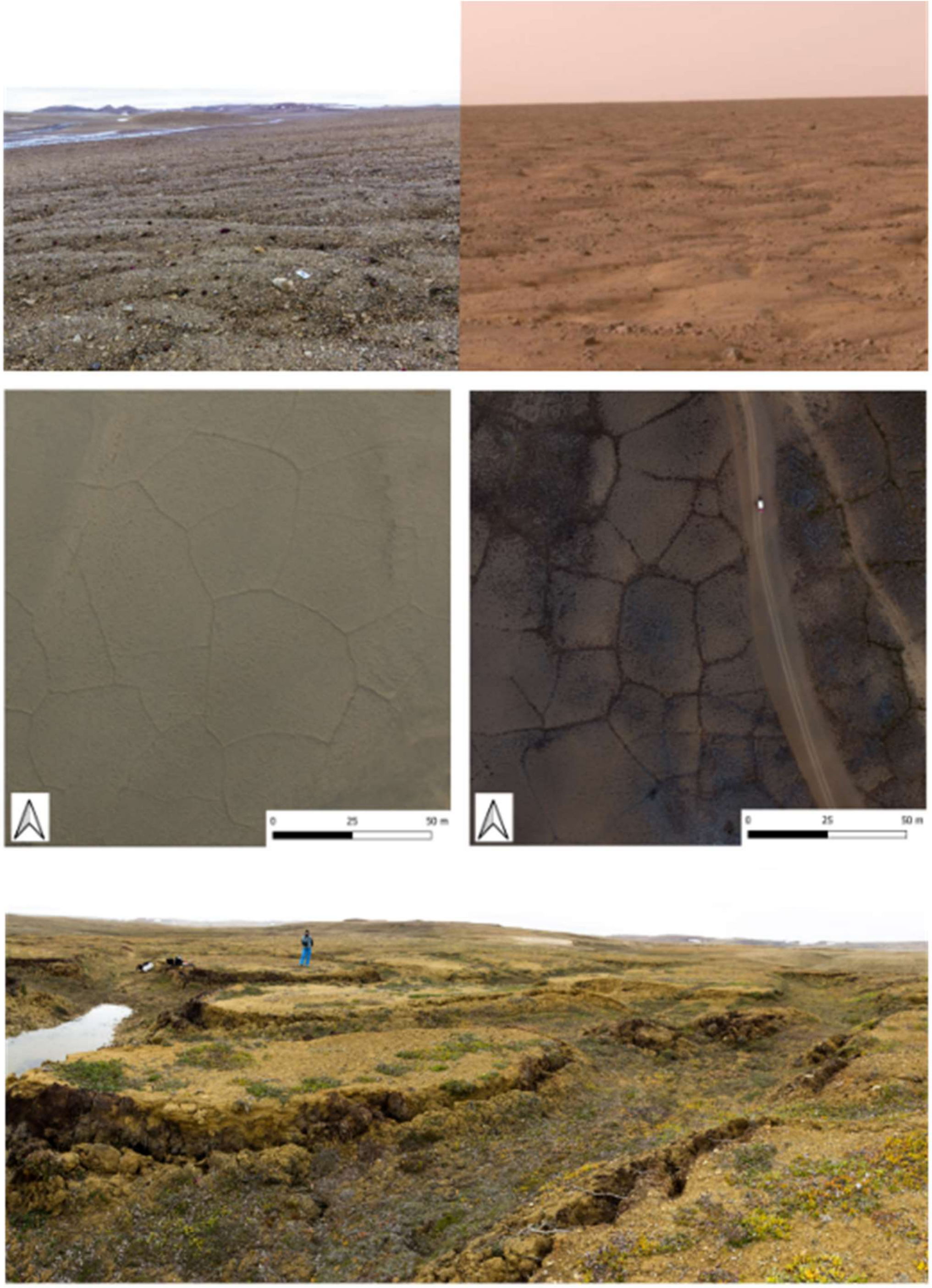

Figure 5-1. Top: Side-by-side view of topographically subdued polygons on Devon Island and the Phoenix landing site. Middle: Comparison of non-vegetation polygons on Devon Island and vegetated polygons in Iceland of similar morphology and scale. Vegetation and variations in surface roughness may provide insight into the degree of present-day cryogenic activity. Bottom: Degraded polygons on Devon Island may provide the best analog for high-relief polygons observed in Utopia Planita and Utopia Rupes.

6.2 Modern Periglacial Activity on Mars: The Verdict from Available Data

Subsurface water ice is known to exist across the high northern latitudes of Mars. Water ice was discovered and analyzed at a depth of approximately 4 cm bgs by the *Phoenix* spacecraft at its landing site in Vastitas Borealis, approximately 1-2 km away from sites evaluated in this project. In addition, suspected water ice is visible outcropping at the surface in polygon margins at the Utopia Planitia site evaluated in this project. Taken in combination with observations from GRS observations, there is a very high probability that shallow subsurface water ice is present at many of the remaining sites evaluated in this study. Rocks in the vicinity of the *Phoenix* spacecraft were observed to influence the topology of the underlying ice, depressing the ice table by several centimeters resulting from sublimation via vapor diffusion (Sizemore et al, 2010). Changes in ice table topology could therefore influence the positioning of rocks at the surface across polygon centers and margins and provide potential paleoclimate indicators for the onset of periglacial (freeze-thaw) conditions during previous periods of high obliquity.

The largest unknown at the start of the project was the detectability of microtopographic variations from HiRISE DTMs and differentiating surface changes with instrument noise. While surface roughness parameters are reasonably detectable in topographically prominent or high contrast polygons, the underlying processes of larger polygons are not well constrained to provide a definitive conclusion on the degree of water ice activity. The data collected and analyzed through this project provides a framework for performing future work that may fully address the question of historical periglacial activity on Mars.

6.3 Future Work

The results of this project lay the groundwork for future evaluations of terrestrial and Martian patterned ground. While many of the project objectives were achieved in terms of developing an approach for evaluating the surface roughness of terrestrial and Martian patterned ground using photogrammetric techniques, there are key limitations to the resulting data analysis that will benefit from future work. Among the terrestrial sites that were studied, the nature and extent of periglacial and frost-driven processes at the putative relict sites is not well constrained and would benefit from the collection of more extensive in-situ environmental measurements (such as the soil temperature, moisture, and thermal properties that were evaluated in patterned ground on Devon Island in Chapter 1) and trenching work performed in conjunction with ground-penetrating radar (GPR) surveys to constrain the depth to either local permafrost or bedrock at each site. The incorporation of a LiDAR survey would enable the development of centimeter to millimeter-scale DTMs in support of higher-resolution feature-scale morphometric analyses.

The collection of high-resolution imagery from follow-up UAV surveys with the addition of ground control points will also enable a more comprehensive analysis of the slope and slope aspect of each site to evaluate the slope dependency of the morphometric parameters discussed in Chapter 2. The follow-up UAV surveys would also focus on key reference sites that are representative of each of the identified polygon subpopulations such that more surveys could be performed at different UAV altitudes at a fewer number of sites. Increasing the diversity of flight altitudes for each survey from a singular altitude at each site (e.g. 80 m) to several incremental altitudes (e.g. 7.5 m, 25 m, 50 m, 100 m, etc.) would enable a more comprehensive evaluation of the scale-dependency of the surface roughness parameters associated with patterned ground. The additional UAV and LiDAR DTMs could be compared with associated GPR data to ascertain if surface roughness and other morphometric parameters can be used as predictive variables for the presence, extent, and activity level of permafrost. These observations would be directly useful in support of ongoing evaluations that seek to quantify the nature and extent of subsurface ground ice on Mars with implications ranging from constraining historical climate conditions to identifying potential resources to support crewed exploration of the Martian surface (Petersen and Holt, 2021).

Historical analog site selection has largely been based on the previous experiences of project investigators and the accessibility of analog sites. Since every spacecraft launched towards Mars has originated from space programs based in countries located in the northern hemisphere, the corresponding distribution of supporting investigators and their preferred analog sites are concentrated to the global north as well. While there are substantial logistical challenges to reaching sites in Antarctica, future research that expands on these results by incorporating sites in the ADV should be a priority given they share the closest known physical and environmental characteristics to Martian patterned ground. An application of the in-situ environmental monitoring and geospatial (morphometric and surface roughness) techniques at these sites in comparison with other terrestrial and Martian sites would be beneficial for isolating differences between sublimation and freeze-thaw driven terrestrial processes, which may in turn provide additional insight to formation mechanisms of patterned ground on Mars.

From a quantitative perspective, the optimized scale parameters identified through the course of the work also provides a basis for performing detailed surface roughness evaluations that expand on other parameters. For example, there may be a benefit to identifying an appropriate method for building a graphical representation of the Hurst exponent over both terrestrial and Martian datasets to further standardize comparative roughness evaluations of polygonal terrain on both planets (e.g. Guo et al, 2021). The Hurst exponent is based partially on calculating the RMS of a surface roughness dataset. The resulting Hurst exponent is a unitless variable that provides a more uniform characterization of rough surfaces independent of scale. Effective Hurst exponent calculations rely on previous characterizations of the investigated surface, for which this work may serve as a useful baseline.

7.0 Conclusions

There were three main objectives with this project: to perform a morphometric analysis of patterned ground at terrestrial and Martian sites using established methods; to perform a multiscale surface roughness analysis of patterned ground at terrestrial and Martian sites; and to perform a comparative analysis of the terrestrial and Martian sites to determine if feature morphometry and surface roughness could serve as predictive variables for diagnosing the level of present-day activity of patterned ground on Mars at a feature scale. The project successfully identified correlations between morphometric variables and the surface roughness of some patterned ground sites on Earth and Mars, with some limitations. The resolution of surface roughness parameters was greatly reduced in some lower resolution UAS surveys that were flown over 80 m agl above subdued or homogenous patterned ground on Earth. Polygons with a high contrast in composition or prominent topographic variations between centers and margins were well-resolved in both lower resolution UAS surveys (>80 m agl) in addition to high resolution surveys performed closer to the ground (7.5 m agl). A similar trend in high contrast or prominent feature resolution and detectability was observed in HiRISE DTMs. Surface roughness evaluations of topographically prominent polygons in regions such as Utopia Planitia where there are known subsurface water ice reservoirs and limited surface ice exposures may provide additional insight into the near-subsurface cryosphere of Mars in future work evaluating the astrobiological potential of the cryosphere and for work characterizing potential resources for crewed missions.

References

Addinsoft (2022). XLSTAT statistical and data analysis solution. New York, USA. https://www.xlstat.com/en.

Ascione, A., Cinque, A., Miccadei, E., Villani, F., and Berti, C. 2008. The Pli-Quaternary uplift of the Apennine chain: new data from the analysis of topography and river valleys in Central Italy. Geomorphology, 102, p. 105-108. DOI:10.1016/j.geomorph.2007.07.022

Baratoux, D., Delacourt, C., and Allemand, P. 2001. High-resolution digital elevation models derived from Viking Orbiter images: Method and comparison with Mars Orbiter Laser Altimeter Data. Journal of Geophysical Research, 106, E12, 32,927-32,941. DOI: 10.1029/2000JE001454

Balme, M.R., Gallagher, C.J., and Hauber, E. 2013. Morphological evidence for geologically young thaw of ice on Mars: A review of recent studies using high-resolution imaging data. Progress in Physical Geography. 37 (3). 289-324.

Balme, M.R., Gallagher, C.J., Murray, J.B., and Muller, J.P. 2009. Sorted stone circles in Elysium Planitia, Mars: Implications for recent martian climate. Icarus. 200, 30-38.

Barrett, A.M., Balme, M.R., Patel, M.R., and Hagermann, A. 2018. The distribution of putative periglacial landforms on the martian northern plains. Icarus. 314, 133-148.

Beyer, R.A. and Kirk. R.L. 2012. Meter-Scale Slopes of Candidate MSL Landing Sites form Point Photoclinometry. Space Science Reviews, 170, 1-4, 775-791. DOI:10.1007/s11214-012-9925-x

Beyer, R.A. Meter-Scale Slopes of Candidate InSight Landing Sites from Point Photoclinometry. Space Science Reviews, 211, 1-4, 97-107. DOI:10.1007/s11214-016-0287-7

Brooker, L.M., Balme, M.R., Conway, S.J., Hagermann, A., Barrett, A.M., Collins, G.S., and Soare, R.J. 2018. Clastic polygonal networks around Lyot crater, Mars: Possible formation mechanisms from morphometric analysis.

Broxton, M.J. and Edwards, L.J. 2008. The Ames Stereo Pipeline: Automated 3D surface reconstruction from orbital imagery. Lunar and Planetary Science Conference XXXIX. Abstract 2419.

Byrnes, J.M. and Crown, D.A. 2002. Morphology, stratigraphy, and surface roughness properties of Venusian lava flow fields. Journal of Geophysical Research, Vol. 107, No. E10, 5079. DOI:10.1029/2001JE001828

Cao, W. and Cai, Z. 2018. Improved Multiscale Roughness Algorithm for Lunar Surface. IEEE Journal of Selected Topics in Applied Earth Observations and Remote Sensing. 11 (7), 2336-2345.

Cao, W., Cai, Z., and Tang, Z. 2015. Lunar surface roughness based on multiscale morphological method. Planetary and Space Science. 108, 13-23.

Campbell, B.A., Putzig, N.E., Carter, L.M., Morgan, G.A., Phillips, R.J., and Plaut, J.S. 2013. Roughness and near-surface density of Mars from SHARAD radar echoes. Journal of Geophysical Research: Planets, 118, 436-450. DOI:10.1002/jgre.20050

Campbell, B.A., Schroeder, D.M., and Whitten, J.L. 2018. Mars radar clutter and surface roughness characteristics from MARSIS data. Icarus, 299, 22-30. DOI:10.1016/j.icarus.2017.07.011

Cord, A., Baratoux, D., Mangold, N., Martin, P., Pinet, P., Greeley, R., Costard, F., Masson, P., Foing, B., and Neukum, G. Surface roughness and geological mapping at subhectometer scale from the High Resolution Stereo Camera onboard Mars Express. Icarus, 191, 1, 38-51. DOI:10.1016/j.icarus.2007.04.029

Costard, F., Forget, F., Mangold, N., and Peulvast, J. P. 2002. Formation of Recent Martian Debris Flows by Melting of Near-Surface Ground Ice at High Obliquity. Science. 295, 110-113.

Clifford, N.J., Robert, A., and Richards, K.S. 1992. Estimation of flow resistance in gravel-bedded rivers: A physical explanation of the multiplier of roughness length. Earth Surface Processes and Landforms, 17, 2, p. 111-126. DOI:10.1002/esp.3290170202

Emmert, A.A. 2020. The Internal Structure of Periglacial Landforms: Assessments of Subsurface Variations in Permafrost-related and Frost-related Phenomena by Multi-dimensional Geophysical Investigations. Dissertation, Julius-Maximilians-Universität Würzbürg.

Etzelmüller, B., Farbrot, H. Guđmundsson, A., Humlum, O., Tveito, O.E., and Björnsson, H. 2007. The Regional Distribution of Mountain Permafrost in Iceland. Permafrost and Periglacial Processes. 18. 185-199.

Fassnacht, S.R., Stednick, J.D., Deems, J.S., and Corrao, M.V. 2009. Metrics for assessing snow surface roughness from digital imagery. Water Resources Research, 45, W00D31. DOI:10.1029/2008WR006986

Florinsky, I.V. 2017. An illustrated introduction to general geomorphometry. Progress in Physical Geography. 41 (6), 723-752.

Florinsky, I.V. 2018. Multiscale geomorphometric modeling of Mercury. Planetary and Space Science. 151, 56-70.

Gallagher, C., Balme, M.R. Conway, S.J., and Grindrod, P.M. 2011. Sorted clastic stripes, lobes, and associated gullies in high-latitude craters on Mars: Landforms indicative of very recent, polycyclic ground-ice thaw and liquid flows. Icarus. 211, 458-471.

Gomez, B. 1993. Roughness of Stable, Armored Gravel Beds. Water Resources Research, 29, 11, 3631-3642. DOI:10.1029/93WR01490

Guo, D., Fa, W., Wu, B., Li, Y., and Liu, Y. 2021. Millimeter- to Decimeter-Scale Surface Roughness of the Moon at the Chang'e-4 Exploration Region. Geophysical Research Letters, 48, e2021GL094931. DOI:10.1029/2021GL094931

Haltigin, T.W., Pollard, W.H., Dutilleul, P., Osinski, G.R., and Koponen, L. 2014. Co-evolution of polygonal and scalloped terrains, southwestern Utopia Planitia, Mars. Earth and Planetary Science Letters. 387, 44-54.

Harmon, J.K. 1997. A radar study of the Chryse region, Mars. Journal of Geophysical Research, 102, E2, 4081-4095. DOI: 10.1029/96JE01953

Hepburn, A.J., Holt, T., Hubbard, B., and Ng, F. 2019. Creating HiRISE digital elevation models for Mars using the open-source Ames Stereo Pipeline. Geoscientific Instrumentation Methods and Data Systems. 8, 293-313.

Hiesinger, H. and Head, J.W. 2000. Characteristics and origin of polygonal terrain in southern Utopia Planitia, Mars: Results from Mars Orbiter Laser Altimeter and Mars Orbiter Camera

Kirk, R.L., Howington-Kraus, E., Rosiek, M.R., Anderson, J.A., Archinal, B.A., Becker, K.J., Cook, D.A., Galuszka, D.M., Geissler, P.E., Hare, T.M., Homberg, I.M., Keszthelyi, L.P., Redding, B.L., Delamere, W.A., Gallagher, D., Chapel, J.D., Eliason, E.M., King, R., and McEwen, A.S. 2008. Ultrahigh resolution topographic mapping of Mars with MRO HiRISE stereo images: Meter-scale slopes of candidate Phoenix landing sites. Journal of Geophysical Research, 113, E00A24. DOI:10.1029/2007JE003000

Kirk, R.L., Mayer, D.P., Fergason, R.L., Redding, B.L., Galuszka, D.M., Hare, T.M., and Gwinner, K. 2021. Evaluating Stereo Digital Terrain Model Quality at Mars Rover Landing Sites with HRSC, CTZ, and HiRISE Images. Remote Sensing, 13, 3511. DOI:10.3390/rs13173511

Kossacki, K.J. and Karmkiewicz, W.J. 2009. Small-scale trench in the north polar region of Mars: Evolution of surface frost and ground ice concentration. Icarus. 199, 75-85.

Kreslavsky, M.A. and Head, J.W. 2000. Kilometer-scale roughness of Mars: Results from MOLA data analysis. Journal of Geophysical Research, 105, E11, 26,695-26,711. DOI: 10.1029/2000JE001259

Kreslavsky, M.A., Head, J.W., and Marchant, D.R. 2006. Periods of active permafrost layer formation during the geological history of Mars: Implications for circum-polar and mid-latitude surface processes. Planetary and Space Science. 56. 289-302

Levy, J., Head, J., and Marchant, D. 2009. Thermal contraction crack polygons on Mars: Classification, distribution, and climate implications from HiRISE observations. Journal of Geophysical Research. 114, E01007.

Levy, J.S., Head, J.W., Marchant, D.R., Dickson, J.L., and Morgan, G.A. 2009. Geologically recent gully-polygon relationships on Mars: Insights from the Antarctic Dry Valleys on the roles of permafrost, microclimates, and water source for surface flow. Icarus. 201, 113-126.

Levy, J.S., Head, J.W., and Marchant, D.R. 2009. Cold and dry processes in the Martian Arctic: Geomorphic observations at the Phoenix landing site and comparisons with terrestrial cold desert landforms. Geophysical Research Letters. 36. L21203.

Li, R., Hwangbo, J., Chen, Y., and Di, K. 2011. Rigorous Photogrammetric Processing of HiRISE Stereo Imagery for Mars Topographic Mapping. IEEE Transactions on Geoscience and Remote Sensing, 49, 7. DOI:10.1109/TGRS.2011.2107522

Lindsay, J.B., Newman, D.R., and Francioni, A. 2019. Scale-Optimized Surface Roughness for Topographic Analysis. Geosciences. 9, 322.

Luchitta, B.K. 1983. Permafrost on Mars: Polygonally Fractured Ground. Permafrost: Fourth Internation Conference Proceedings, 744-749.

Mangold, N., Maruice, S., Feldman, W.C., Costard, F., and Forget, F. 2004. Spatial relationships between patterned ground and ground ice detected by the Neutron Spectrometer on Mars. Journal of Geophysical Research. 109, E08001.

Mangold, N. 2005. High latitude patterned grounds on Mars: Classification, distribution and climate control. Icarus. 174, 336-359.

McEwen, A.S., Eliason, E.M., Bergstrom, J.W., Bridges, N.T., Hansen, C.J., Delamere, W.A., Grant, J.A., Gulick, V.G., Herkenfhoff, K.E., Keszthelyi, L., Kirk, R.L., Mellon, M.T., Squyres, S.W., Thomas, N., and Weitz, C.M. 2007. Mars Reconnaissance Orbiter's High Resolution Imaging Science Experiment (HiRISE). Journal of Geophysical Research, 112, E05S02. DOI:10.1029/2005JE002605

Mellon, M. T., Arvidson, R. E., Marlow, J. L., Phillips, R. J., and Asphaug, E. 2008. Periglacial landforms at the Phoenix landing site and the northern plains of Mars. Journal of Geophysical Resarch. 113, E00A23.

Mellon, M. T., Arvidson, R. E., Sizemore, H. G., Searls, M. L., Blaney, D. L., Cull, S., Hecht, M.H., Heet, T.L., Keller, H.U., Lemmon, M.T., Markiewicz, W.J., Ming, D.W., Morris, R.V., Pike, W.T., and Zent, A.P. 2009. Ground ice at the Phoenix Landing Site: Stability state and origin. Journal of Geophysical Research. 114, E00E07.

Morino, C., Conway, S.J., Balme, M.R., Helgason, J.K., Þorsteinn, S., Jordan, C., Hillier, J., and Argles, T. 2021. The impact of ground-ice thaw on landslide geomorphology and dynamics: two case studies in northern Iceland. Landslides.

Munroe, J.S. 2007. Properties of Alpine Soils Associated with Well-Developed Sorted Polygons in the Uinta Mountains, Utah, U.S.A. Arctic, Antarctic, and Alpine Research. 39:4. 578-591.

Nakamura, T. and Tajika, E. 2003. Climate change of Mars-like planets due to obliquity variations: implications for Mars. Geophysical Research Letters. 30 (13). 1685.

NASA. 2018. Mars Reconnaissance Orbiter Preparing for Years Ahead, Press Release. 9 Feb. https://www.nasa.gov/feature/jpl/mars-reconnaissance-orbiter-preparing-for-years-ahead

NASA. 2018. Slight Blurring in Newer Image from Mars Orbiter, Press Release. 9 Feb. https://mars.nasa.gov/resources/21490/slight-blurring-in-newer-image-from-mars-orbiter/?site=insight

Oehler, D.Z. and Allen, C.C. 2012. Giant Polygons and Mounds in the Lowlands of Mars: Signatures of an Ancient Ocean? Astrobiology. 12 (6), 601-615.

Oehler, D.Z., Mangold, N., Hallet, B., Fairén, Le Deit, L., Williams, A.J., Sletten, R.S., and Martínez-Frías. 2016. Origin and significance of decameter-scale polygons in the lower Peace Vallis fan of Gale crater, Mars. Icarus. 277, 56-72.

Orloff, T., Kreslavsky, M., and Asphaug, E. 2013. Distribution of polygon characteristic scale in Martian patterned terrain in the northern hemisphere using the Fourier transform. Journal of Geophysical Research: Planets. 118, 1558-1566.

Orloff, T.C., Kreslavksy, M.A., and Asphaug, E.I. 2013. Possible mechanism of boulder clustering on Mars. Icarus. 225, 992-999.

Pardo-Iguzquiza, E. and Dowd, P.A. 2022. Fractal analysis of the Martian landscape: A study of kilometre-scale topographic roughness. Icarus, 372, 114727. DOI:10.1016/j.icarus.2021.114727

Pechmann, 1980 – origin of polygonal troughs in northern plains of Mars

Petersen, E.I. and Holt, J.W. 2021. Surface Roughness Prevents Radar Penetration of Some Martian Debris-Covered Glaciers. IEEE Transactions on Geoscience and Remote Sensing, 60, 5104307, DOI:10.1109/TGRS.2021.3094762.

Riley, S.J., DeGloria, S.D., and Elliot, R. 1999. A Terrain Ruggedness Index That Quantifies Topographic Heterogeneity. Intermountain Journal of Sciences, 5, 1-4.

Seibert, N.M. and Kargel, J.S. 2001. Small-Scale Martian Polygonal Terrain: Implications for Liquid Surface Water. Geophysical Research Letters. 28 (5), 899-902.

Séjourné, A., Costard, F., Swirad, Z.M., Łosiak, A., Bouley, S., Smith, I., Balme, M.R., Orgel, C., Ramsdale, J.D., Hauber, E., Conway, S.J., van Gasselt, S., Reiss, D., Johnsson, A., Gallagher, C., Skinner, J.A., Kereszturi, Á, and Platz, T. 2019. Grid Mapping the Northern Plains of Mars: Using Morphotype and Distribution of Ice-Related Landforms to Understand Multiple Ice-Rich Deposits in Utopia Planitia. Journal of Geophysical Research: Planets. 124, 483-503.

Shaw, A., Arvidson, R.E., Bonitz, R., Carsten, J., Keller, H.U., Lemmon, M.T., Mellon, M.T., Robinson, M., and Trebi-Ollennu, A. 2009. Phoenix soil physical properties investigation. Journal of Geophysical Resarch. 114, E00E05.

Sizemore, H. G., Mellon, M. T., Searls, M. L., Lemmon, M. T., Zent, A. P., Heet, T. L., Arvidson, R. E., Blaney, D. L., and Keller, H. U. 2010. In situ analysis of ice table depth variations in the vicinity of small rocks at the Phoenix landing site. Journal of Geophysical Research. 115, E00E09.

Sletten, R.S., Hallet, B., and Fletcher, R.C. 2003. Resurfacing time of terrestrial surfaces by the formation and maturation of polygonal patterned ground. Journal of Geophysical Research. 108 (E4), 8044.

Smith, D.E., Zuber, M.T., Frey, H.V., Garvin, J.B., Head, J.W., Muhleman, D.O., Pettengill, G.H., Phillips, R.J., Solomon, S.C., Zwally, H.J., Banerdt, W.B., Duxbury, T.C., Golombek, M.P., Lemoine, F.G., Neumann, G.A>, Rowlands, D.D., Aharonson, O., Ford, P.G., Ivanov, A.B., Johnson, C.L., McGovern, P.J., Abshire, J.B., Afzal, R.S., and Sun, X. 2001. Mars Orbiter

Laster Altimeter: Experiment summary after first year of global mapping of Mars. Journal of Geophysical Research, 106, E10, 23,689-23,722. DOI: 10.1029/2000JE001364

Smith, M.W. 2014. Roughness in the Earth Sciences. Earth-Science Reviews, 136, p. 202-225. DOI:10.1016/j.earscirev.2014.05.016

Smith, P.H., Tamppari, L.K., Arvidson, R.E., Bass, D., Blaney, D., Boynton, W.V., Carswell, A., Catling, D.C., Clark, B.C., Duck, T., DeJong, E., Fisher, D., Goetz, W., Gunnlaugsson, H.P., Hecht, M.H., Hipkin, V., Hoffman, J., Hviid, S.F., Keller, H.U., Kounaves, S.P., Lange, C.F., Lemmon, M.T., Madsen, M.B., Markiewicz, W.J., Marshall, J., McKay, C.P., Mellon, M.T., Ming, D.W., Morris, R.V., Pike, W.T., Renno, N., Staufer, U., Stoker, C., Taylor, P., Whiteway, J.A., and Zent, A.P. 2009. H_2O at the Phoenix Landing Site. Science. 325, 58-61

Soare, R.J., Conway, S.J., Williams, J.-P., Gallagher, C., and McKeown, L.E. 2020. Possible (closed system) pingo and ice-wedge/thermokarst complexes at the mid latitudes of Utopia Planitia, Mars.

Soare, R. J., Conway, S. J., and Dohm, J. M. 2014. Possible ice-wedge polygons and recent landscape modification by “wet” periglacial processes in and around the Argyre impact basin, Mars. Icarus. 233, 214-228.

Soare, R. J., Conway, S. J., Gallagher, C., and Dohm, J. M. 2016. Sorted (clastic) polygons in the Argyre region, Mars, and possible evidence of pre- and post-glacial periglaciation in the Late Amazonian Epoch. Icarus. 264, 184-197.

Taud, H. and Parrot, F. 2005. Measurement of DEM roughness using the local fractal dimension. Géomorphologie. 4, 327-338.

Ulrich, M., Hauber, E., Herzschuh, U., Hartel, S., Shirrmesiter, L. (2011). Polygon pattern geomorphometry on Svalbard (Norway) and western Utopia Planitia (Mars) using high-resolution stereo remote-sensing data. Geomorphology, 134, 197-216.

Yoshikawa, K. 2003. Origin of the polygons and the thickness of Vastitas Borealis Formation in Western Utopia Planitia on Mars. Geophysical Research Letters. 30 (12), 1603.

Appendix A

Thermal Properties of Soil Samples Collected in Patterned Ground at Haughton Crater on Devon Island, Nunavut, Canada

Room Temperature Thermal Analysis

	SH-3							TR-3					
	Date	Time	T – Celsius		D	C	K	Date	Time	T – Celsius		K	R
			Initial	2 min	(mm²)/s	MJ/(m³K)	W/(mK)			Initial	1 min	W/(mK)	Cm/W
Mars Controls													
Simulant													
JSC Mars 1	12/21/18	1500	NA	NA	0.117	0.8355	0.0975	NA	NA	NR	NR	NR	NR
	12/21/18	1506	21.378	23.77	0.120	0.8602	0.1028	12/21/18	1527	22.399	28.41	0.0701	14.26
	12/21/18	1509	22.125	23.79	0.120	0.9127	0.1095	12/21/18	1530	22.953	28.57	0.0774	12.92
	12/21/18	1513	21.882	23.79	0.124	0.8704	0.1081	12/21/18	1537	23.039	28.74	0.0746	13.41
		Averages	21.795	23.78	0.121	0.8811	0.1068		**Averages**	22.797	28.57	0.0740	13.53
MMS – Fine	12/21/18	1546	21.614	22.91	0.121	1.1224	0.1357	12/21/18	1602	21.944	29.05	0.0607	16.48
	12/21/18	1548	21.488	22.95	0.125	1.1430	0.1426	12/21/18	1607	22.400	28.36	0.0772	12.95
	12/21/18	1554	21.984	23.19	0.133	1.1084	0.1469	12/21/18	1612	22.643	28.71	0.0697	14.35
		Averages	21.695	23.02	0.126	1.1246	0.1417		**Averages**	22.329	28.71	0.0692	14.59

Devon Island Samples	SH-3							TR-3					
Sample ID	Date	Time	T – Celsius		D	C	K	Date	Time	T – Celsius		K	R
			Initial	2 min	(mm²)/s	MJ/(m³K)	W/(mK)			Initial	1 min	W/(mK)	Cm/W
DS-1A 20170719	12/22/18	1405	14.763	16.64	0.176	1.5058	0.2657						
	12/22/18	1427	19.939	20.97	0.181	1.4154	0.2566						
	12/22/18	1435	20.752	21.72	0.160	1.4066	0.2251						
	12/22/18	1438	21.189	22.03	0.191	1.6001	0.3061						
	12/22/18	1509	21.965	22.78	0.188	1.6188	0.3047						
	12/22/18	1512	22.233	23.23	ddd	1.2035	0.2351						
	12/22/18	1516	22.646	22.60	0.177	1.2006	0.2122						
		Averages	20.498	21.42	0.179	1.4215	0.2579						
DS-1A 20170814	12/22/18	1542	21.125	21.54	0.491	1.5083	0.7402	12/22/18	1602	22.165	26.84	0.1788	5.59
	12/22/18	1545	21.520	21.97	0.338	1.7673	0.5972	12/22/18	1605	22.416	26.32	0.3112	3.21
	12/22/18	1549	21.863	21.90	0.452	1.4896	0.6730	12/22/18	1611	22.523	29.76	0.0731	13.69
	12/22/18	1553	21.811	22.32	0.458	1.3468	0.6168	12/22/18	1617	22.544	29.05	0.1012	9.88
	12/22/18	1556	22.125	22.53	0.398	1.8832	0.7493	12/22/18	1624	22.578	29.07	0.1013	9.87
		Averages	21.689	22.05	0.427	1.5990	0.6753		**Averages**	22.445	28.21	0.1531	8.45
DS-1B 20170719	12/22/18	1608	22.307	23.42	0.187	1.2401	0.2320						
	12/22/18	1613	22.784	23.60	0.191	1.2888	0.2461						
	12/22/18	1620	22.779	23.55	0.183	1.4835	0.2721						
	12/22/18	1627	22.929	23.59	0.219	1.4305	0.3136						
		Averages	22.700	23.54	0.195	1.3607	0.2660						
DS-2A 20170719	12/22/18	1633	22.526	23.55	0.180	1.2790	0.2307						
	12/22/18	1637	22.759	23.79	0.205	1.1390	0.2338						
	12/22/18	1641	23.125	23.97	0.163	1.4048	0.2280						
		Averages	22.803	23.77	0.183	1.2743	0.2308						
DS-2B 20170719	12/22/18	1646	22.527	23.47	0.201	1.2999	0.2610						
	12/22/18	1648	23.063	23.90	0.187	1.2903	0.2419						
	12/22/18	1654	23.250	24.11	0.206	1.1842	0.2444						
		Averages	22.947	23.83	0.198	1.2581	0.2491						
DS-2B 20170814	12/22/18	1711	22.421	22.81	0.339	1.7054	0.5788	12/22/18	1722	22.756	27.70	0.1070	9.35
	12/22/18	1713	22.474	22.89	0.406	1.5192	0.6171	12/22/18	1724	23.106	28.26	0.1602	6.24
	12/22/18	1717	22.568	22.98	0.540	1.2036	0.6494	12/22/18	1731	23.497	27.64	0.2891	3.46
	12/22/18	1742	23.546	23.99	0.367	1.4382	0.5273	12/22/18	1736	23.359	29.30	0.1144	8.74
	12/22/18	1746	23.653	24.08	0.447	1.2883	0.5754	12/22/18	1740	23.395	26.96	0.3168	3.16
		Averages	22.488	22.89	0.428	1.4761	0.6151		**Averages**	23.120	27.87	0.1854	6.35
Background	12/23/18	943	22.668	23.64	0.198	1.1442	0.2268						
	12/23/18	948	22.980	23.81	0.188	1.3778	0.2593						
	12/23/18	953	23.247	24.20	0.183	1.1908	0.2182						
		Averages	22.965	23.88	0.190	1.2376	0.2348						

Devon Island Samples	SH-3							TR-3					
Sample ID	Date	Time	T – Celsius		D	C	K	Date	Time	T – Celsius		K	R
			Initial	2 min	(mm²)/s	MJ/(m³K)	W/(mK)			Initial	1 min	W/(mK)	Cm/W
PAS-1-1	12/27/18	1450	20.910	21.91	0.200	1.1582	0.2316						
	12/27/18	1454	21.300	22.17	0.188	1.7938	0.3373						
	12/27/18	1457	21.437	22.24	0.180	1.6346	0.2934						
		Averages	21.216	22.11	0.189	1.5289	0.2874						
PAS-1-2	12/22/18	1803	23.927	25.01	0.167	1.5483	0.2580						
	12/22/18	1807	24.254	25.25	0.142	1.9972	0.2844						
	12/22/18	1811	24.834	25.69	0.212	1.7043	0.3609						
		Averages	24.338	25.32	0.174	1.7499	0.3011						
PAS-2-1 Clay	12/27/18	1603	20.238	21.09	0.191	1.8680	0.3566						
	12/27/18	1607	20.258	20.93	0.182	1.7377	0.3165						
	12/27/18	1611	20.575	21.17	0.227	1.8937	0.4304						
		Averages	20.357	21.06	0.200	1.8331	0.3678						
PAS-2-1 Gravel	12/22/18	1750	23.553	24.59	0.289	0.8844	0.2552						
	12/22/18	1754	23.927	24.76	0.150	1.6755	0.2511						
	12/22/18	1758	24.204	25.61	0.155	0.9232	0.1431						
		Averages	23.895	24.99	0.198	1.1610	0.2165						
PAS-2-2	12/27/18	1520	19.218	20.16	0.266	1.1519	0.3067						
	12/27/18	1523	19.460	22.32	0.192	1.5399	0.2964						
	12/27/18	1527	19.916	20.69	0.172	1.8325	0.3147						
		Averages	19.531	21.06	0.210	1.5081	0.3059						
PAS-2-20 Normal	12/23/18	1000	22.759	23.79	0.180	1.2728	0.2289						
	12/23/18	1004	23.359	24.42	0.278	1.5921	0.4429						
	12/23/18	1008	23.819	24.78	0.189	1.6074	0.3038						
		Averages	23.312	24.33	0.216	1.4908	0.3252						
PAS-2-20 Beneath Margin	12/23/18	1014	22.918	23.90	0.196	1.8181	0.3559						
	12/23/18	1020	23.211	24.55	0.191	0.9917	0.1897						
	12/23/18	1024	23.354	Not recorded	0.184	1.5111	0.2782						
		Averages	23.161	24.23	0.190	1.4403	0.2746						
PAS-3-1	12/23/18	1158	22.942	23.51	0.333	1.3342	0.4444						
	12/23/18	1203	23.088	23.36	0.377	1.8930	0.7142						
	12/23/18	1207	23.078	23.50	0.395	1.3039	0.5152						
		Averages	23.036	23.46	0.368	1.5104	0.5579						
PAS-3-2	12/23/18	1210	22.866	23.59	0.221	1.3346	0.2950						
	12/23/18	1213	23.186	23.92	0.202	1.4688	0.2965						
	12/23/18	1218	23.142	23.88	0.205	1.4310	0.2937						
		Averages	23.065	23.80	0.209	1.4115	0.2951						
PAS-3-3	12/23/18	1144	22.923	23.71	0.170	1.3975	0.2369						
	12/23/18	1149	23.093	23.81	0.200	1.5009	0.2995						
	12/23/18	1153	23.256	24.12	0.197	1.2106	0.2385						
		Averages	23.091	23.88	0.189	1.3697	0.2583						
PAS-3-4	12/23/18	1108	22.973	23.78	0.215	1.3281	0.2855						
	12/23/18	1113	23.371	23.99	0.217	1.3520	0.2937						
	12/23/18	1116	23.480	24.08	0.248	1.3865	0.3432						
		Averages	23.275	23.95	0.227	1.3555	0.3075						
PAS-3-5	12/27/18	1435	19.414	20.04	0.224	1.7466	0.3912						
	12/27/18	1438	19.581	20.18	0.227	1.9634	0.4462						
	12/27/18	1442	19.907	20.48	0.205	2.1067	0.4324						
		Averages	19.634	20.23	0.219	1.9389	0.4233						

Devon Island Samples	SH-3							TR-3					
Sample ID	Date	Time	T – Celsius		D	C	K	Date	Time	T – Celsius		K	R
			Initial	2 min	(mm²)/s	MJ/(m³K)	W/(mK)			Initial	1 min	W/(mK)	Cm/W
PAS-3-6	12/27/18	1621	21.693	22.12	0.230	2.0750	0.4763	12/27/18	1635	21.311	25.78	0.1923	5.20
	12/27/18	1626	21.669	22.22	0.190	1.7398	0.3308	12/27/18	1639	21.288	24.79	0.2968	3.37
	12/27/18	1630	21.806	22.31	0.219	1.9577	0.4282	12/27/18	1643	21.308	24.74	0.3485	2.87
		Averages	21.723	22.22	0.213	1.9242	0.4118		Averages	21.302	25.10	0.2792	3.81
PAS-3-7	12/23/18	1031	23.210	23.55	0.368	1.5465	0.5696	12/23/18	1053	23.116	28.23	0.1732	5.77
	12/23/18	1044	22.600	23.03	0.359	1.3186	0.4730	12/23/18	1056	23.124	27.45	0.2407	4.15
	12/23/18	1050	23.029	23.37	0.393	1.5879	0.6233	12/23/18	1102	23.443	26.89	0.3710	2.70
		Averages	22.946	23.32	0.373	1.4843	0.5553		Averages	23.228	27.52	0.2616	4.21
PSA-P1-0	12/23/18	1229	22.918	23.40	0.361	1.5649	0.5648						
	12/23/18	1233	23.054	23.41	0.450	1.9934	0.8971						
	12/23/18	1237	22.949	23.33	0.598	1.4049	0.8396						
		Averages	22.974	23.38	0.470	1.6544	0.7672						
PSA-P1-10	12/23/18	1257	21.943	22.86	0.247	1.0552	0.2602						
	12/23/18	1304	22.252	23.15	0.301	0.7939	0.2386						
	12/23/18	1308	22.429	23.14	0.260	1.0820	0.2809						
		Averages	22.208	23.05	0.269	0.9770	0.2599						
PSA-P1-20	12/23/18	1841	22.821	23.11	0.630	1.4063	0.8858	12/23/18	1858	22.605	25.44	0.4740	2.11
	12/23/18	1845	22.679	23.05	0.674	1.3294	0.8966	12/23/18	1901	22.668	24.81	0.8228	1.22
	12/23/18	1849	22.580	22.99	0.383	1.6314	0.6256	12/23/18	1906	22.732	25.03	0.5905	1.69
		Averages	22.693	23.05	0.562	1.4557	0.8027		Averages	22.668	25.09	0.6291	1.67
PSA-P1-30	12/23/18	1853	22.165	23.26	0.201	1.2336	0.2482	12/23/18	1916	22.669	26.96	0.1621	6.17
	12/23/18	1908	22.579	23.64	0.198	1.2560	0.2485	12/23/18	1919	22.900	27.13	0.1537	6.51
	12/23/18	1912	22.937	23.84	0.195	1.2676	0.2471	12/23/18	1924	22.996	27.41	0.1484	6.74
		Averages	22.560	23.58	0.198	1.2524	0.2479		Averages	22.855	27.17	0.1547	6.47
PSA-P1-40	12/23/18	1927	22.503	22.97	0.380	1.6178	0.6143	12/23/18	2002	22.604	24.85	0.6323	1.58
	12/23/18	1931	22.632	23.04	0.620	1.3742	0.8518	12/23/18	2004	22.812	26.16	0.3447	2.90
	12/23/18	1935	22.674	23.13	0.552	1.4880	0.8219	12/23/18	2008	23.042	26.03	0.4192	2.39
		Averages	22.603	23.05	0.517	1.4933	0.7627		Averages	22.819	25.68	0.4654	2.29
PSA-P1-50	12/23/18	1938	22.605	23.11	0.463	1.3868	0.6427	12/23/18	1951	22.936	25.27	0.6079	1.65
	12/23/18	1942	22.838	23.23	0.488	1.7532	0.8550	12/23/18	1954	22.929	25.23	0.7031	1.42
	12/23/18	1946	22.863	23.28	0.566	1.2722	0.7197	12/23/18	1959	23.051	25.66	0.5125	1.95
		Averages	22.769	23.21	0.506	1.4707	0.7391		Averages	22.972	25.39	0.6078	1.67
PSA-P2	12/23/18	1242	22.788	23.28	0.332	1.1491	0.3817	12/23/18	1254	22.756	27.83	0.1637	6.11
	12/23/18	1246	22.626	23.11	0.386	1.5124	0.5838	12/23/18	1301	22.772	26.49	0.2934	3.41
	12/23/18	1249	22.689	23.10	0.386	1.4742	0.5691	12/23/18	1310	22.788	25.80	0.4480	2.23
		Averages	22.701	23.16	0.368	1.3786	0.5115		Averages	22.772	26.71	0.3017	3.92
PSA-P3	12/23/18	1314	22.515	23.34	0.214	1.2925	0.2769	12/23/18	1327	22.556	26.89	0.1655	6.13
	12/23/18	1317	22.745	23.59	0.197	1.2351	0.2433	12/23/18	1333	22.753	27.00	0.1633	6.13
	12/23/18	1322	22.656	23.74	0.206	1.1067	0.2279	12/23/18	1338	22.575	27.15	0.1619	6.18
		Averages	22.639	23.56	0.206	1.2114	0.2494		Averages	22.628	27.01	0.1636	6.15
PSA-P3ST-10	12/23/18	1639	22.773	23.68	0.214	1.1601	0.2482	12/23/18	1703	22.495	26.54	0.1759	5.69
	12/23/18	1646	22.797	23.60	0.263	1.2425	0.3271	12/23/18	1706	22.569	26.69	0.1758	5.69
	12/23/18	1651	22.839	23.67	0.215	1.3672	0.2946	12/23/18	1710	22.746	26.90	0.1772	5.64
		Averages	22.803	23.65	0.231	1.2566	0.2900		Averages	22.603	26.71	0.1763	5.67
PSA-P3S-20	12/23/18	1329	22.340	23.94	0.213	0.7524	0.1602						
	12/23/18	1335	22.678	24.21	0.192	0.8023	0.1538						
	12/23/18	1340	22.795	24.29	0.201	0.7258	0.1457						
		Averages	22.604	24.15	0.202	0.7602	0.1532						

Devon Island Samples	SH-3							TR-3					
Sample ID	Date	Time	T – Celsius		D	C	K	Date	Time	T – Celsius		K	R
			Initial	2 min	(mm²)/s	MJ/(m³K)	W/(mK)			Initial	1 min	W/(mK)	Cm/W
PSA-P3S-30	12/23/18	1504	22.295	23.34	0.196	1.1408	0.2233	12/23/18	1528	22.485	26.71	0.1607	6.22
	12/23/18	1509	22.560	23.63	0.198	1.1626	0.2305	12/23/18	1533	22.524	26.84	0.1525	6.56
	12/23/18	1515	22.142	23.36	0.180	1.2345	0.2225	12/23/18	1539	22.600	26.75	0.1656	6.04
		Averages	22.332	23.44	0.191	1.1793	0.2254		**Averages**	22.536	26.77	0.1596	6.27
PSA-P3ST-0	12/23/18	1355	22.703	23.60	0.211	1.2473	0.2629						
	12/23/18	1400	22.782	Not recorded	0.201	1.2268	0.2469						
	12/23/18	1405	22.856	23.62	0.200	1.3426	0.2684						
		Averages	22.780	23.61	0.204	1.2722	0.2594						
PSA-P3S-10	12/23/18	1549	22.761	24.22	0.208	0.7856	0.1630	12/23/18	1615	23.008	28.94	0.0744	13.45
	12/23/18	1555	22.913	24.39	0.188	0.7788	0.1464	12/23/18	1620	23.016	28.91	0.0729	13.72
	12/23/18	1600	22.915	24.42	0.219	0.7143	0.1564	12/23/18	1626	23.124	29.00	0.0792	12.63
		Averages	22.863	24.34	0.205	0.7596	0.1553		**Averages**	23.049	28.95	0.0755	13.27
PSA-P3ST-25	12/23/18	1623	22.923	23.87	0.259	1.0591	0.2738	12/23/18	1649	22.659	27.44	0.1348	7.42
	12/23/18	1629	22.803	23.74	0.251	1.0472	0.2627	12/23/18	1655	22.522	27.57	0.1384	7.23
	12/23/18	1634	22.988	23.88	0.261	1.0246	0.2675	12/23/18	1658	22.981	27.60	0.1417	7.06
		Averages	22.905	23.83	0.257	1.0436	0.2680		**Averages**	22.721	27.54	0.1383	7.24
PSA-P3ST-50	12/23/18	1606	22.754	24.31	0.171	0.8798	0.1504	12/23/18	1632	22.698	28.83	0.0740	13.51
	12/23/18	1611	22.944	Not recorded	0.199	0.7838	0.1560	12/23/18	1637	23.037	28.92	0.0750	13.33
	12/23/18	1617	22.922	24.41	0.175	0.9240	0.1618	12/23/18	1643	22.952	28.23	0.0904	11.06
		Averages	22.873	24.36	0.182	0.8625	0.1561		**Averages**	22.896	28.66	0.0798	12.63
PSA-P4-0	12/27/18	706	18.800	19.32	0.418	1.3417	0.5606						
	12/27/18	710	19.049	19.51	0.382	1.5693	0.5998						
	12/27/18	714	18.980	19.42	0.393	1.6608	0.6519						
		Averages	18.943	19.42	0.398	1.5239	0.6041						
PSA-P4-10	12/27/18	721	18.985	19.13	0.668	3.1928	2.1168						
	12/27/18	724	18.973	19.20	0.860	2.3542	2.0249						
	12/27/18	735	19.081	19.39	0.711	2.5683	1.8268						
		Averages	19.013	19.24	0.746	2.7051	1.9895						
PSA-P4-20	12/27/18	800	20.075	20.14	0.794	2.4375	1.9366						
	12/27/18	803	19.900	20.08	0.518	3.3501	1.7353						
	12/27/18	812	19.626	19.77	0.799	2.5455	2.0328						
		Averages	19.867	20.00	0.704	2.7777	1.9016						
PSA-P4-30	12/27/18	816	19.372	19.59	0.870	2.0726	1.8025	12/27/18	829	19.476	21.27	0.7599	1.32
	12/27/18	821	19.359	19.59	0.756	2.9170	2.2054	12/27/18	832	19.493	21.01	1.2667	0.79
	12/27/18	826	19.424	19.69	0.756	2.3809	1.8001	12/27/18	835	19.546	20.40	1.7429	0.57
		Averages	19.385	19.62	0.794	2.4568	1.9360		**Averages**	19.505	20.89	1.2565	0.89
PSA-P4-40	12/27/18	903	19.029	19.18	0.828	2.6658	2.2078	12/27/18	936	18.912	20.08	1.1952	0.84
	12/27/18	927	18.798	18.98	0.824	2.5037	2.0626	12/27/18	939	19.005	19.91	1.4605	0.68
	12/27/18	930	18.876	19.10	0.828	2.6075	2.1595	12/27/18	943	19.179	20.50	1.7150	0.58
		Averages	18.901	19.09	0.827	2.5923	2.1433		**Averages**	19.032	20.16	1.4569	0.70
PSA-P4-50	12/27/18	739	19.093	19.35	0.703	2.4343	1.7120						
	12/27/18	747	19.440	19.73	0.610	1.9137	1.6760						
	12/27/18	750	19.451	19.68	0.699	2.2446	1.5680						
		Averages	19.328	19.59	0.671	2.1975	1.6520						
PSA-P5 (U1)	12/23/18	1530	22.618	23.95	0.160	0.9898	0.1582	12/23/18	1546	22.479	27.50	0.1183	8.45
	12/23/18	1536	22.837	24.10	0.167	1.0018	0.1674	12/23/18	1552	22.547	27.97	0.1096	9.13
	12/23/18	1542	22.935	24.13	0.172	1.0153	0.1745	12/23/18	1557	22.672	27.40	0.1435	6.97
		Averages	22.797	24.06	0.166	1.0023	0.1667		**Averages**	22.566	27.62	0.1238	8.18
PSA-P6 (U3)	12/23/18	1446	21.880	22.33	0.541	1.6125	0.8721	12/23/18	1507	22.332	25.00	0.3866	2.59
	12/23/18	1451	22.016	22.40	0.520	1.4512	0.7551	12/23/18	1513	22.363	25.48	0.3345	2.99
	12/23/18	1456	22.116	22.52	0.518	1.5851	0.8210	12/23/18	1520	22.470	25.43	0.3850	2.60
		Averages	22.004	22.42	0.526	1.5496	0.8161		**Averages**	22.388	25.30	0.3687	2.73
PSA-P7	12/23/18	1344	22.636	23.29	0.223	1.6249	0.3631	12/23/18	1358	22.644	26.22	0.2388	4.19
	12/23/18	1347	22.552	23.31	0.320	1.3726	0.4396	12/23/18	1403	22.694	27.28	0.1834	5.45
	12/23/18	1351	22.640	23.36	0.298	1.2862	0.3835	12/23/18	1409	22.728	25.60	0.3430	2.92
		Averages	22.609	23.32	0.280	1.4279	0.3954		**Averages**	22.689	26.37	0.2551	4.19

Devon Island Samples	SH-3							TR-3					
Sample ID	Date	Time	T – Celsius		D	C	K	Date	Time	T – Celsius		K	R
			Initial	2 min	$(mm^2)/s$	$MJ/(m^3K)$	W/(mK)			Initial	1 min	W/(mK)	Cm/W
PSA-P3S-30	12/23/18	1504	22.295	23.34	0.196	1.1408	0.2233	12/23/18	1528	22.485	26.71	0.1607	6.22
	12/23/18	1509	22.560	23.63	0.198	1.1626	0.2305	12/23/18	1533	22.524	26.84	0.1525	6.56
	12/23/18	1515	22.142	23.36	0.180	1.2345	0.2225	12/23/18	1539	22.600	26.75	0.1656	6.04
		Averages	22.332	23.44	0.191	1.1793	0.2254		Averages	22.536	26.77	0.1596	6.27
PSA-P3ST-0	12/23/18	1355	22.703	23.60	0.211	1.2473	0.2629						
	12/23/18	1400	22.782	Not recorded	0.201	1.2268	0.2469						
	12/23/18	1405	22.856	23.62	0.200	1.3426	0.2684						
		Averages	22.780	23.61	0.204	1.2722	0.2594						
PSA-P3S-10	12/23/18	1549	22.761	24.22	0.208	0.7856	0.1630	12/23/18	1615	23.008	28.94	0.0744	13.45
	12/23/18	1555	22.913	24.39	0.188	0.7788	0.1464	12/23/18	1620	23.016	28.91	0.0729	13.72
	12/23/18	1600	22.915	24.42	0.219	0.7143	0.1564	12/23/18	1626	23.124	29.00	0.0792	12.63
		Averages	22.863	24.34	0.205	0.7596	0.1553		Averages	23.049	28.95	0.0755	13.27
PSA-P3ST-25	12/23/18	1623	22.923	23.87	0.259	1.0591	0.2738	12/23/18	1649	22.659	27.44	0.1348	7.42
	12/23/18	1629	22.803	23.74	0.251	1.0472	0.2627	12/23/18	1655	22.522	27.57	0.1384	7.23
	12/23/18	1634	22.988	23.88	0.261	1.0246	0.2675	12/23/18	1658	22.981	27.60	0.1417	7.06
		Averages	22.905	23.83	0.257	1.0436	0.2680		Averages	22.721	27.54	0.1383	7.24
PSA-P3ST-50	12/23/18	1606	22.754	24.31	0.171	0.8798	0.1504	12/23/18	1632	22.698	28.83	0.0740	13.51
	12/23/18	1611	22.944	Not recorded	0.199	0.7838	0.1560	12/23/18	1637	23.037	28.92	0.0750	13.33
	12/23/18	1617	22.922	24.41	0.175	0.9240	0.1618	12/23/18	1643	22.952	28.23	0.0904	11.06
		Averages	22.873	24.36	0.182	0.8625	0.1561		Averages	22.896	28.66	0.0798	12.63
PSA-P4-0	12/27/18	706	18.800	19.32	0.418	1.3417	0.5606						
	12/27/18	710	19.049	19.51	0.382	1.5693	0.5998						
	12/27/18	714	18.980	19.42	0.393	1.6608	0.6519						
		Averages	18.943	19.42	0.398	1.5239	0.6041						
PSA-P4-10	12/27/18	721	18.985	19.13	0.668	3.1928	2.1168						
	12/27/18	724	18.973	19.20	0.860	2.3542	2.0249						
	12/27/18	735	19.081	19.39	0.711	2.5683	1.8268						
		Averages	19.013	19.24	0.746	2.7051	1.9895						
PSA-P4-20	12/27/18	800	20.075	20.14	0.794	2.4375	1.9366						
	12/27/18	803	19.900	20.08	0.518	3.3501	1.7353						
	12/27/18	812	19.626	19.77	0.799	2.5455	2.0328						
		Averages	19.867	20.00	0.704	2.7777	1.9016						
PSA-P4-30	12/27/18	816	19.372	19.59	0.870	2.0726	1.8025	12/27/18	829	19.476	21.27	0.7599	1.32
	12/27/18	821	19.359	19.59	0.756	2.9170	2.2054	12/27/18	832	19.493	21.01	1.2667	0.79
	12/27/18	826	19.424	19.69	0.756	2.3809	1.8001	12/27/18	835	19.546	20.40	1.7429	0.57
		Averages	19.385	19.62	0.794	2.4568	1.9360		Averages	19.505	20.89	1.2565	0.89
PSA-P4-40	12/27/18	903	19.029	19.18	0.828	2.6658	2.2078	12/27/18	936	18.912	20.08	1.1952	0.84
	12/27/18	927	18.798	18.98	0.824	2.5037	2.0626	12/27/18	939	19.005	19.91	1.4605	0.68
	12/27/18	930	18.876	19.10	0.828	2.6075	2.1595	12/27/18	943	19.179	20.50	1.7150	0.58
		Averages	18.901	19.09	0.827	2.5923	2.1433		Averages	19.032	20.16	1.4569	0.70
PSA-P4-50	12/27/18	739	19.093	19.35	0.703	2.4343	1.7120						
	12/27/18	747	19.440	19.73	0.610	1.9137	1.6760						
	12/27/18	750	19.451	19.68	0.699	2.2446	1.5680						
		Averages	19.328	19.59	0.671	2.1975	1.6520						
PSA-P5 (U1)	12/23/18	1530	22.618	23.95	0.160	0.9898	0.1582	12/23/18	1546	22.479	27.50	0.1183	8.45
	12/23/18	1536	22.837	24.10	0.167	1.0018	0.1674	12/23/18	1552	22.547	27.97	0.1096	9.13
	12/23/18	1542	22.935	24.13	0.172	1.0153	0.1745	12/23/18	1557	22.672	27.40	0.1435	6.97
		Averages	22.797	24.06	0.166	1.0023	0.1667		Averages	22.566	27.62	0.1238	8.18
PSA-P6 (U3)	12/23/18	1446	21.880	22.33	0.541	1.6125	0.8721	12/23/18	1507	22.332	25.00	0.3866	2.59
	12/23/18	1451	22.016	22.40	0.520	1.4512	0.7551	12/23/18	1513	22.363	25.48	0.3345	2.99
	12/23/18	1456	22.116	22.52	0.518	1.5851	0.8210	12/23/18	1520	22.470	25.43	0.3850	2.60
		Averages	22.004	22.42	0.526	1.5496	0.8161		Averages	22.388	25.30	0.3687	2.73
PSA-P7	12/23/18	1344	22.636	23.29	0.223	1.6249	0.3631	12/23/18	1358	22.644	26.22	0.2388	4.19
	12/23/18	1347	22.552	23.31	0.320	1.3726	0.4396	12/23/18	1403	22.694	27.28	0.1834	5.45
	12/23/18	1351	22.640	23.36	0.298	1.2862	0.3835	12/23/18	1409	22.728	25.60	0.3430	2.92
		Averages	22.609	23.32	0.280	1.4279	0.3954		Averages	22.689	26.37	0.2551	4.19

Notes

Average/final measurement

Not enough sample volume to collect accurate measurements using the TR-3 probe

DS = Datalogger Site

FMARS = Flashline Mars Arctic Research Station

MWS = Meltwater Streak

PAS = Phoenix Analog Site

PSA = Polygon Site A

P-# = Polygon Sample Number

T-# = Transect Sample Number

U# = U-qualifier denotes sample labels were damaged during transport. Samples were re-identified based on context clues from adjacent samples and from field notes